Dissertation

submitted to the
Combined Faculties for the Natural Sciences and for Mathematics
of the
Ruperto-Carola University of Heidelberg, Germany
for the degree of

Doctor of Natural Sciences

presented by
Dipl.-Phys. David Berge
born in Berlin

Oral examination: 15 February 2006

A detailed study of

The gamma-ray supernova remnant
RX J1713.7−3946

with

H.E.S.S.

Referees: Prof. Dr. Werner Hofmann
Prof. Dr. Thomas Lohse

Abstract

The H.E.S.S. telescope system – an array of four imaging atmospheric Čerenkov telescopes situated in Namibia – aims at exploring non-thermal processes in the universe by means of very-high-energy (VHE) gamma rays. Its large field of view combined with unprecedented sensitivity enables detailed spectral and morphological studies of extended VHE gamma-ray sources. The shell-type supernova remnant RX J1713.7−3946 is such a source. It is located in the Galactic plane, constellation scorpius, and has a diameter of 1°. H.E.S.S. observations of this source were conducted in 2003, 2004, and 2005. A thorough discussion of the methodology of the analysis of (extended) VHE gamma-ray sources is given. The systematic uncertainties involved in different stages of the analysis are explored. Detailed morphological and spectral studies reveal the VHE aspects of RX J1713.7−3946. Gamma rays are detected throughout the whole remnant. The emission resembles a shell structure strikingly similar to the X-ray image. The differential gamma-ray spectrum is measured over a large energy range, no spatial variation is found. The data recorded in three different years are in good agreement. The origin of the gamma-ray emission is discussed for a leptonic and a hadronic scenario. The latter case is favoured, but no decisive conclusion can be drawn.

Kurzfassung

H.E.S.S. ist ein Experiment zur Messung hochenergetischer Gammastrahlung. Es besteht aus vier abbildenden Čerenkov Teleskopen und wird im Khomas Hochland in Namibia betrieben. Das grosse Gesichtsfeld und die hohe Empfindlichkeit der Teleskope sind sehr gut dafür geeignet, ausgedehnte Quellen kosmischer Gammastrahlung zu beobachten. Der Supernova Überrest RX J1713.7−3946, der sich im Sternbild des Skorpion befindet, ist solch eine Quelle. Beobachtungen mit H.E.S.S. wurden in den Jahren 2003, 2004 und 2005 durchgeführt. Vor den Ergebnissen wird die Datenanalyse Schritt für Schritt erklärt. Es wird sowohl die Methodik der Analyse ausgedehnter Quellen hochenergetischer Gammastrahlung diskutiert, als auch systematische Fehler abgeschätzt. Schliesslich werden die Ergebnisse der Analyse präsentiert. Alle Regionen des Überrests emittieren Gammastrahlung. Das Bild zeigt eine schalenartige Struktur mit stärkerer Emission von der Nord-West Seite und ähnelt stark der Messung im Röntgenbereich. Das Spektrum wurde über einen sehr grossen Energiebereich gemessen, die Form des Spektrums variiert nicht in verschiedenen Regionen von RX J1713.7−3946. Im Vergleich liefern die verschiedenen Datensätze, aufgenommen in drei Jahren, kompatible Ergebnisse. Der Ursprung der Gammastrahlung wird innerhalb eines leptonischen und eines hadronischen Szenarios diskutiert. Letzteres passt eher zu den Daten, definitive Schlüsse lassen sich jedoch nicht ziehen.

Contents

List of Figures

List of Tables

1 Gamma-ray astronomy and the quest for the origin of Galactic cosmic rays

The history of cosmic rays begins in the early nineteen hundreds when it was realised that electroscopes discharged even if they were kept shielded from natural sources of radioactivity. 1912 it was Victor Franz Hess who discovered in balloon ascents that the ionisation even increases when going up in the atmosphere. He found that electroscopes discharged twice as fast at 5300 meters altitude than at sea level and attributed this to extraterrestrial radiation of very high penetration power – the cosmic rays (Hess 1912). His discovery initiated an era of cosmic-ray research and paved the way for the development of the field of particle physics. Particles like the positron, kaons, or pions were all discovered by means of cosmic rays and it was only in the nineteen fifties that man-made accelerators had developed to the point where high energies, available up to then only in cosmic rays, could be produced.

Today it is well established that an intense flux of charged and neutral cosmic particles exists. The Earth's atmosphere is hit by these particles at the rate of about 1000 per square metre per second (Gaisser 1990). The energy spectrum measured to date ranges over ten decades up to the highest energies around 10^{20} eV. For most parts the spectrum is well described by a single power law with index -2.7. The cosmic-ray spectrum reveals two distinct features, the "knee" and the "ankle" at $\sim 10^{15}$ eV and $\sim 10^{18}$ eV, respectively. At the knee the spectrum steepens, at the ankle it hardens again. It is generally believed that cosmic rays up to the knee are of Galactic origin, whereas beyond the ankle they are produced and accelerated outside the Galactic disk. Cosmic rays arrive isotropically at Earth. Extrapolating from the locally, directly measured flux to the entire Galactic disk, an average energy density of ~ 1 eV/cm^3 is estimated. The abundance of cosmic rays is measured up to the knee, the main components are protons (80%) and α-particles (18%), heavier nuclei, electrons and positrons (together $\sim 1.8\%$) resulting in a large fraction of 99.8% of the cosmic rays being charged particles.

Despite almost one century of cosmic-ray research, we are still lacking decisive proof of what the sources of this high-energy radiation in the Galaxy are. The main obstacle is the diffusion of charged particles in the interstellar magnetic fields. Once the cosmic rays are injected into the interstellar medium at the acceleration site, they are deflected by Lorentz forces thereby loosing directional information. From the isotropically arriving charged radiation no information about the source direction can be inferred on Earth. This problem may be overcome by means of neutral messenger particles which do not suffer from deflection in magnetic fields, namely gamma rays and neutrinos. They account for the remaining 0.2% of cosmic radiation incident at Earth. While the conceptual proof of the experimental techniques of neutrino-based astronomy is still missing today, gamma-ray astronomy is already a discipline in its own right. The origin of Galactic cosmic rays is one of its main incentives.

1.1 Production processes of very-high-energy gamma rays

From the power-law shape of the cosmic-ray spectrum and the extremely high energies it is evident that the radiation originates from non-thermal acceleration processes rather than from black-body radiation of thermal processes. The hottest objects observed in the universe emit thermal radiation with energies extending up to the hard X-ray range of ≈ 10 keV. Hence, any radiation exceeding these energies must be created in non-thermal processes. Very-high-energy (VHE) gamma rays[1] provide ideal characteristics for the study of such non-thermal acceleration processes in the Galaxy. They are abundantly produced in interactions of highly energetic particles with ambient radiation fields and matter of the interstellar medium. In addition, they propagate freely through interstellar space, unperturbed by magnetic fields. On Galactic scales they do not suffer from absorption by infrared and optical photon background fields.

The two most important processes for the generation of VHE gamma rays are Inverse Compton (IC) scattering and neutral pion decay following proton-proton interactions. IC gamma rays are produced in interactions of energetic particles – mostly electrons, IC scattering of protons is suppressed by a factor of $(m_\mathrm{e}/m_\mathrm{p})^4$ – with the ambient background fields, the 2.7 K cosmic microwave background, and the diffuse Galactic radiation of star light and dust photons. Since these background fields are omnipresent, this process is very effective in producing gamma rays whenever high-energy particles are created. If VHE gamma rays of TeV energies are generated by multi-TeV electrons, the same electrons produce synchrotron radiation of X-ray energies in the presence of magnetic fields. A relation between typical energies E_γ of the IC gamma rays and ϵ_X of the synchrotron X-rays generated by a multi-TeV electron is given in Aharonian (2004):

$$E_\gamma \simeq 2 \left(\frac{\epsilon_\mathrm{X}}{0.1\ \mathrm{keV}}\right) \left(\frac{\mathrm{B}}{10\ \mu\mathrm{G}}\right)^{-2}\ \mathrm{TeV}\,. \tag{1.1}$$

The ratio of the synchrotron and IC fluxes depends mostly on the ambient magnetic field, to first order not on the spectral shape of the primary electrons:

$$\frac{f_\mathrm{IC}(E_\gamma)}{f_\mathrm{sy}(\epsilon_\mathrm{X})} \simeq 0.1 \left(\frac{B}{10\mu\mathrm{G}}\right)^{-2}\ . \tag{1.2}$$

Therefore, with a synchrotron X-ray flux measurement one can approximately derive an IC gamma-ray flux value expected for a given magnetic field strength B.

When searching for hints of the hadronic component of Galactic cosmic rays, the main channel of interest is the meson-decay channel. Relativistic protons and heavier nuclei produce VHE gamma rays in inelastic interactions with ambient target material via production and subsequent decay of secondary pions, kaons, and hyperons. The most important process is the decay of π^0-mesons, $pp \to \pi^0 \to \gamma\gamma$, which occurs if the kinetic energy of the protons exceeds a threshold of $E_\mathrm{kin} \approx 0.3$ GeV. A simple formalism that allows to calculate the emissivity of gamma rays through the π^0 channel, $q_\gamma(E_\gamma)$, is given in Aharonian & Atoyan (2000):

$$q_\gamma(E_\gamma) = 2 \int_{E_\mathrm{min}}^{\infty} \frac{q_\pi(E_\pi)}{\sqrt{E_\pi^2 - m_\pi^2 c^4}}\, \mathrm{d}E_\pi\ , \tag{1.3}$$

---

[1] Gamma rays with energies exceeding a few tens of GeV are usually referred to as very-high-energy gamma rays.

with $E_{\rm min} = E_\gamma + m_\pi^2 c^4/4E_\gamma$. m_π is the π_0-meson rest mass. The emissivity of secondary particles from inelastic proton-proton interactions can be calculated from accelerator measurements, in Aharonian & Atoyan (2000) (Eq. (22)) it is given as:

$$q_\pi(E_\pi) = \frac{c n_{\rm H}}{K_\pi}\,\sigma_{\rm pp}\left(m_{\rm p}c^2 + \frac{E_\pi}{K_\pi}\right) n_{\rm p}\left(m_{\rm p}c^2 + \frac{E_\pi}{K_\pi}\right)\,. \tag{1.4}$$

$\sigma_{\rm pp}$ is the total cross section for inelastic *pp* collisions, $n_{\rm H}$ the ambient density, and K_π is the mean fraction of the kinetic energy of the proton, $E_{\rm kin} = E_{\rm p} - m_{\rm p}c^2$, transferred to the secondary meson per collision. $n_{\rm p}(E_{\rm p})$ is the energy distribution of the parent protons.

In a broad region from GeV to TeV energies, $K_\pi \approx 0.17$, which includes ≈ 6% contribution from the neutral η-meson. The cross section for the inelastic interaction rises from the threshold $E_{\rm th} \approx 0.3$ GeV rapidly to 28–30 mb. At energies beyond 2 GeV, $\sigma_{\rm pp}$ increases logarithmically with energy. It is approximated:

$$\sigma_{\rm pp}(E_{\rm p}) \approx 30\ (0.95 + 0.06 \ln(E_{\rm kin}/1\ {\rm GeV}))\ {\rm mb} \tag{1.5}$$

for $E_{\rm kin} \geq 1$ GeV, $\sigma_{\rm pp} = 0$ else.

A handy expression for the proton cooling time through the π^0-decay channel can now be derived. It is energy-independent above 1 GeV because of the almost constant cross section. Taking an average value of $\sigma_{\rm pp}$ =40 mb one finds (Aharonian & Atoyan 2000):

$$t_{\rm pp} = (n_0 \sigma_{\rm pp} f c)^{-1} \approx 5.3 \times 10^7 \left(\frac{n}{1\,{\rm cm}^{-3}}\right)^{-1}\ {\rm yr}\,. \tag{1.6}$$

The coefficient of inelasticity, $f \approx 0.5$, takes into account that on average the proton loses half of its energy per interaction. That fact that the cooling time is almost independent of energy above 1 GeV means that the initial proton acceleration spectrum remains almost unchanged. The gamma-ray spectrum almost repeats the parent proton spectrum, with a factor of $\sim K_\pi$ lower energies. It is hence demonstrated that VHE gamma rays, generated in inelastic *pp* collisions, carry crucial information about the primary nucleonic cosmic rays.

There is another process that generates VHE gamma rays in interactions with matter, non-thermal Bremsstrahlung of relativistic electrons. However, assuming the local electron-to-proton ratio, π_0-production dominates over the bremsstrahlung contribution at high energies, even more so if this contribution is further suppressed by synchrotron and IC losses of the high-energy electrons.

1.2 VHE gamma rays from shell-type supernova remnants – the case of RX J1713.7−3946

It is commonly believed that the only sources capable of supplying enough energy output to power the flux of Galactic cosmic rays are supernova explosions (e.g., Ginzburg & Syrovatskii 1964). At the present time there are two main arguments for this hypothesis: firstly, estimates of the power required to sustain the observed nuclear Galactic cosmic-ray population show that about 10% of the mechanical energy released by the population of

Galactic supernovae would suffice, or, in other words, that supernova remnants could be the sources of the Galactic cosmic rays if the average acceleration efficiency in a remnant is about 10%. Secondly, a rather well developed theoretical framework for the acceleration mechanism, diffusive shock acceleration (for reviews see eg, Blandford & Eichler 1987; Jones & Ellison 1991; Malkov & O'C Drury 2001), exists and it indeed predicts acceleration efficiencies in excess of 10%.

The best way of proving unequivocally the existence of VHE particles, electrons or hadrons, in the shells of supernova remnants (SNRs) is the detection of VHE (about 100 GeV up to a few tens of TeV) gamma rays produced either via IC scattering of VHE electrons off ambient photons or in interactions of nucleonic cosmic rays with ambient matter. As was argued already in Drury et al. (1994), a system of imaging atmospheric Cherenkov telescopes with a large field of view provides the most powerful measurement technique for extended nearby SNRs at these very high energies. One should note that there exist two other experimental approaches to trace VHE cosmic rays, the detection of X-rays, which suggests the presence of VHE electrons (Koyama et al. 1995), and of high-energy neutrinos, which probe exclusively nuclear particles.

A prime candidate for gamma-ray observations is the SNR RX J1713.7−3946, in particular because of its close association with dense molecular clouds along the line of sight (Fukui et al. 2003; Moriguchi et al. 2005), which might suggest a scenario of a supernova shell overtaking dense molecular clouds, leading to a detectable VHE gamma-ray signal from hadronic interactions, as described theoretically in Aharonian et al. (1994). RX J1713.7−3946, situated in the Galactic plane, constellation Scorpius, was discovered in soft X-rays (0.1-2.4 keV) in 1996 in the ROSAT all-sky survey (Pfeffermann & Aschenbach 1996). It was found to be roughly elliptical in shape with a maximum extent of 70′. Bright X-ray emission dominantly from its western shell was measured with an X-ray flux between 0.1-2.4 keV of 4.4×10^{-10} erg cm^{-2} s^{-1}, ranking it among the brightest Galactic SNRs in this energy band. A follow-up pointed observation was then carried out which revealed the image shown in Fig. 1.1 (Slane et al. 1999). The entire remnant was mapped with good angular resolution. The spectral results were inconclusive due to the restricted energy range of ROSAT. With ASCA the northwest part of the source was covered serendipitously in the ASCA Galactic plane survey (Koyama et al. 1997) in 1996, and was then re-observed in a pointed observation campaign in 1997 (Slane et al. 1999) covering the SNR almost completely. The ASCA image in a restricted energy range of 1-5 keV is shown in Fig. 1.1, in the top right corner. The X-ray spectra were found to be featureless extending to the 10 keV range, the highest energies accessible to ASCA. Line emission was not detected, the spectra were well described by absorbed power laws. The most plausible explanation of the hard X-ray emission is that it is of non-thermal origin, namely synchrotron radiation of 100-TeV electrons (Koyama et al. 1995). The existence of such highly energetic electrons makes it very likely that also hadronic cosmic rays are accelerated to such high energies in this object providing further support to the expectation of RX J1713.7−3946 being a VHE gamma-ray emitter. X-ray observations have also been conducted with Chandra and XMM with their superior angular resolution. The images are shown in Fig. 1.1, bottom row. Chandra observed a small region in the bright northwestern part of the SNR (Uchiyama et al. 2003; Lazendic et al. 2004). Despite distinct brightness variations within this small field, the corresponding X-ray spectra were all found to be well described by power-law models with similar absorbing column densities and photon indices, albeit

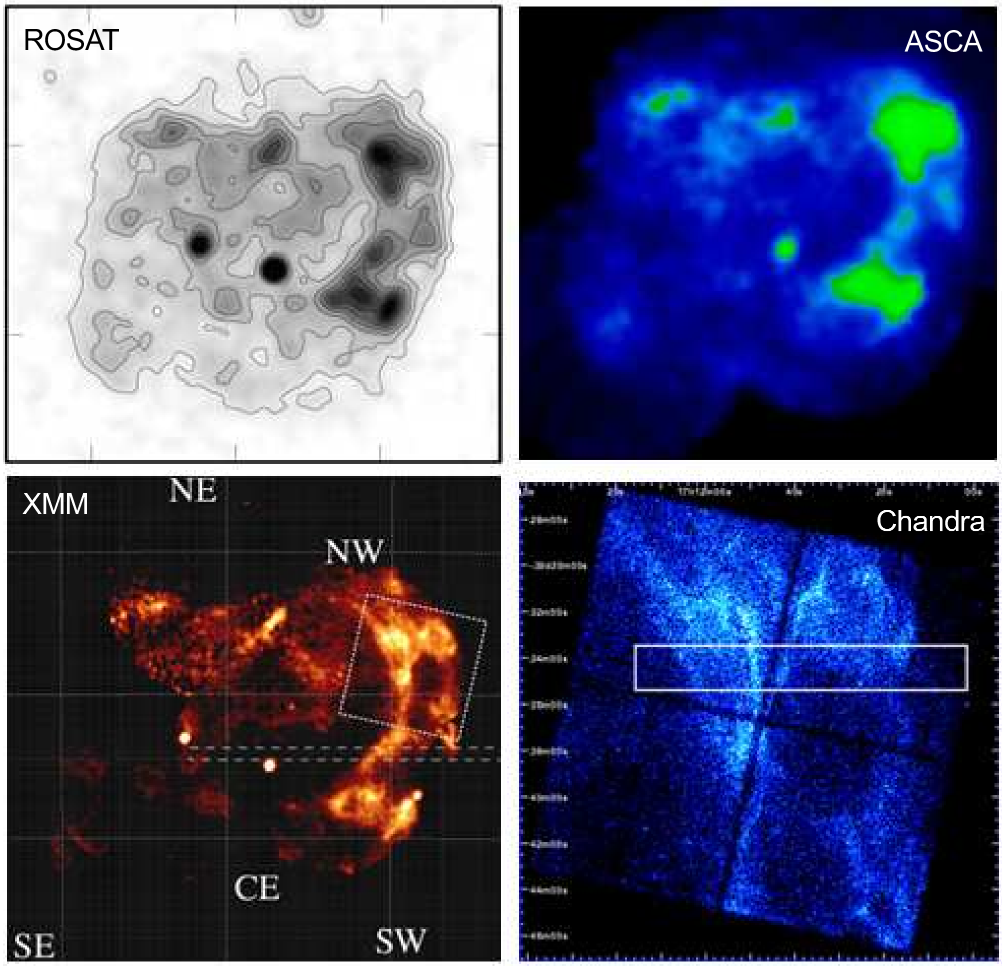

Figure 1.1: X-ray images of RX J1713.7−3946 are shown. The ROSAT image is shown in the upper left corner (0.1-2.4 keV) (Slane et al. 1999). The ASCA image (upper right corner) in the 1-5 keV band (Uchiyama et al. 2002) reveals similar morphological features. The soft band of XMM (0.7-2.0 keV) (Hiraga et al. 2005) is shown in the bottom left corner. Complex filamentary structures are resolved particularly in the bright western portion of the SNR. Marked as white dashed square is the $17' \times 17'$ Chandra field of view, the corresponding image (1-5 keV) is shown in the bottom right-hand corner (Uchiyama et al. 2003).

with rather large statistical uncertainties. XMM covered the remnant almost completely in five pointings (Cassam-Chenaï et al. 2004a; Hiraga et al. 2005). Also on this much larger scale, a highly inhomogeneous and complex morphology was found in the western part of the SNR with two narrow rims resembling a double-shell structure running from north to south. The (non-thermal) X-ray spectra, when fit with a power law, exhibit strong variations in photon index across the remnant ($1.8 < \Gamma < 2.6$) and the hydrogen column density N_H was found to vary significantly (0.4×10^{22} cm$^{-2} \leq N_\mathrm{H} \leq 1.1 \times 10^{22}$ cm^{-2}). The spectra of the central and the western parts differ clearly at low energies, possibly indicating an increase in column density of $\Delta N_\mathrm{H} \approx 0.4 \times 10^{22}$ cm^{-2} towards the west. Furthermore, a positive correlation between X-ray brightness and absorption was interpreted as being due to the shock front of RX J1713.7−3946 impacting a molecular cloud in the west which was assumed to be responsible for the absorption. Further support for this scenario is lent by CO line emission observations with the NANTEN telescope (Fukui et al. 2003; Moriguchi et al. 2005), which suggest that the SNR is interacting with molecular clouds in this region at a distance of 1 kpc from the Solar System. The intensity distribution of CO emission in the corresponding velocity range is shown in Fig. 1.2. The regions of RX J1713.7−3946 that exhibit the brightest X-ray emission coincide with the densest molecular clouds. Hence it was argued that the non-thermal X-ray emission is possibly associated with interactions between the cloud and the western part of the SNR shell.

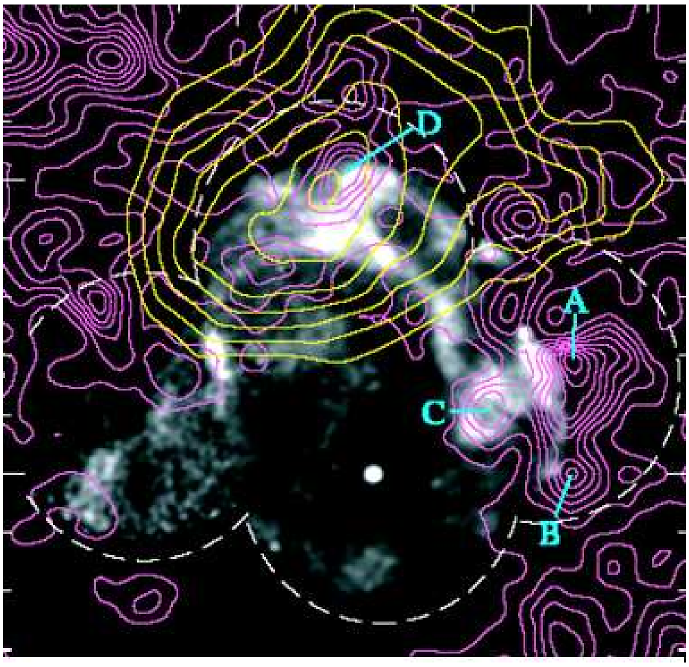

Figure 1.2: The intensity distribution of CO ($J = 1 - 0$) emission (Fukui et al. 2003) (in units of $\mathrm{K\ km\ s^{-1}}$) is shown as purple contours, superimposed on the XMM soft-band image. The CO distribution is derived by integrating the CO spectra in the velocity range from $-11\ \mathrm{km\ s^{-1}}$ to $-3\ \mathrm{km\ s^{-1}}$ (which corresponds to $0.4\ \mathrm{kpc}$ to $1.5\ \mathrm{kpc}$ in space). CANGAROO significance contours of TeV gamma-ray emission (Enomoto et al. 2002) is also shown.

Age and distance of the SNR are under debate and have been revised quite a few times. Initially, Koyama et al. (1997) had derived a distance of 1 kpc and correspondingly an age of about 1000 years from the column density towards the source as estimated from ASCA X-ray observations. Slane et al. (1999) on the other hand have derived a larger distance of 6 kpc (corresponding to an age of about 10 000 years) based on the possible association of RX J1713.7−3946 with a molecular cloud in this region and the HII region G347.6 + 0.2 to its northwest. Both the latest XMM and NANTEN findings are consistent with the remnant being closer, at 1 kpc, which might support the hypothesis of Wang et al. (1997), that RX J1713.7−3946 is the remnant of an AD393 guest star. They searched historical records of Chinese astronomers and found three mentions of a guest star which appeared in the tail of constellation Scorpius, close to the actual position of RX J1713.7−3946. The ancient record of Shen (500) in Sung Shu (History of the Sung Dynasty) is shown in

Fig. 1.3, where he noted:

> “A guest star appeared within the asterism Wei during the second lunar month of the eighteenth year of the Tai-Yuan reign period (February 27–March 28, AD393), and disappeared during the ninth lunar month (October 22–November 19, AD393).”

Other references are given in Wang et al. (1997). The *asterism Wei* is shown in Fig. 1.4, on the right-hand side. The word “Wei” means that it looks like the tail of a dragon, hence the stars indicated in the figure correspond to the stars that form the constellation Scorpius, an image of which can be seen in Fig. 1.4 (left). The stars that form Scorpius are highlighted, the approximate position of RX J1713.7−3946 is marked by a red cross. From the positional coincidence, Wang et al. (1997) suggested the AD393 guest star to be the supernova that created the remnant of RX J1713.7−3946.

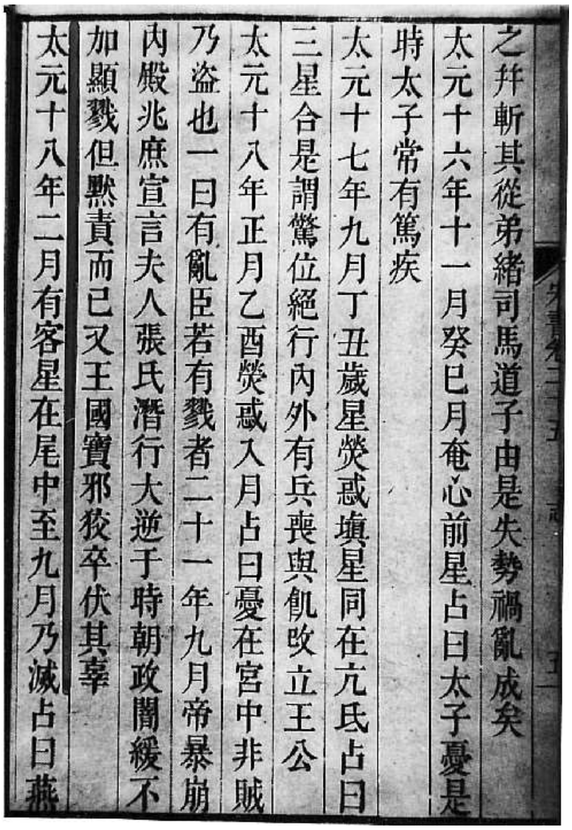

之幷斬其從弟緒司馬道子由是失勢禍亂成矣

太元十六年十一月癸巳月奄心前星占曰太子憂是時太子常有篤疾

太元十七年九月丁丑歲星熒惑填星同在亢氐占曰三星合是謂驚位絕行內外有兵喪與飢改立王公

太元十八年正月乙酉熒惑入月占曰憂在宮中非賊乃盜也一曰有亂臣若有戮者二十一年九月帝暴崩內殿兆庶宣言夫人張氏潛行大逆于時朝政闇緩不加顯戮但默責而已又王國寶邪狡卒伏其辜

太元十八年二月有客星在尾中至九月乃滅占曰燕

Figure 1.3: Historical record of the AD393 guest star in Sung Shu (Shen 500), taken from Wang et al. (1997).

The suggested relatively young age of the SNR is supported by the high surface brightness of this object in non-thermal X-rays, which suggests that it is close to the evolutionary phase where the shocks are most powerful. While hardly a conclusive argument, this implies that the remnant is observed at the sweep-up time when the ejecta are interacting with approximately their own mass of swept-up ambient material and the energy flux

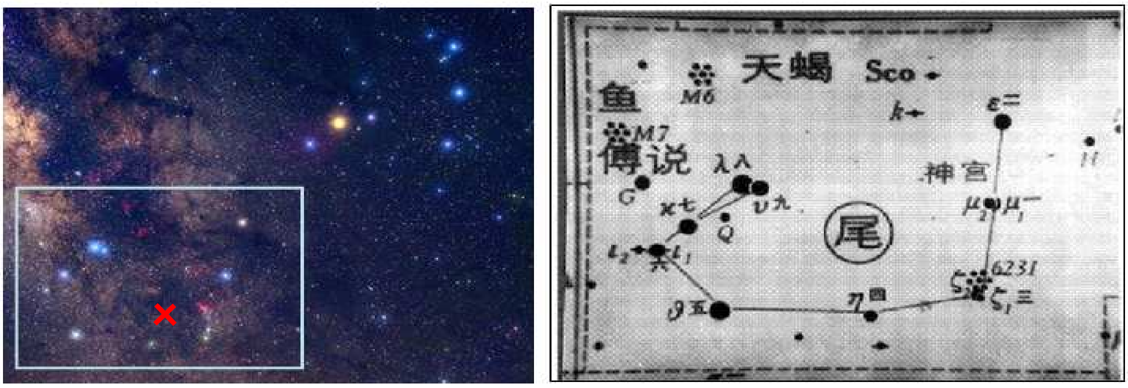

Figure 1.4: Left: Optical image of the Constellation Scorpius. The stars that form the constellation are highlighted. The approximate position of RX J1713.7−3946 is marked with a red cross. The rectangle is the area pictured in the ancient image drawn on the **right** (from Wang et al. 1997), which shows the *asterism Wei*. The Chinese character in the circle is “Wei”, which means “tail”.

through the shocks (both forward and reverse) peaks. Normally this would be at an age of a few hundred to a thousand years, which indeed supports the closer distance estimate.

The radio emission of RX J1713.7−3946 is very faint (Lazendic et al. 2004) which puts it into a peculiar class of shell-type SNRs with dominantly non-thermal X-ray and only very faint radio emission. The only other known object of this type is RX J0852.0−4622 (G266.2−1.2) (Aschenbach 1998; Slane et al. 2001).

RX J1713.7−3946 was detected in VHE gamma rays by the CANGAROO collaboration in 1998 (Muraishi et al. 2000) and re-observed by CANGAROO-II in 2000 and 2001 (Enomoto et al. 2002). Recently H.E.S.S., a new array of imaging atmospheric Cherenkov telescopes operating in Namibia, has confirmed the detection (Aharonian et al. 2004b). This was the first independent confirmation of VHE gamma-ray emission from an SNR shell. Furthermore, the H.E.S.S. measurement provided the first ever resolved gamma-ray image at very high energies. The complex morphology of RX J1713.7−3946 was clearly unraveled. Deep follow-up observations confirmed the previous measurement and enabled detailed spatially resolved studies (Aharonian et al. 2005a). Together with the H.E.S.S. detection of RX J0852.0−4622 (Aharonian et al. 2005c) there are currently two spatially resolved VHE gamma-ray SNRs with a shell-like structure which agrees well with that seen in X-rays. These two objects may well be the brightest SNRs in the VHE gamma-ray domain in the whole sky; anything equally bright in the Northern sky would have been clearly seen in the Milagro survey (Atkins et al. 2004), and the H.E.S.S. Galactic plane survey (Aharonian et al. 2005e) reveals no SNRs brighter than RX J1713.7−3946 or RX J0852.0−4622 in the region covered.

It is worth mentioning that there are two more shell-type SNRs which have been reported to emit TeV gamma rays. One is the remnant of SN 1006, which was claimed by CANGAROO (Tanimori et al. 1998), but could not be confirmed with H.E.S.S. (Aharonian et al. 2005f). The other one is Cassiopeia A (Aharonian et al. 2001), a classical core-collapse SNR, whose northern location makes it inaccessible to H.E.S.S..

The interpretation of the gamma-ray emission mechanisms for RX J1713.7−3946 has been the subject of debate. From their flux level, the CANGAROO collaboration interpreted in Muraishi et al. (2000) the gamma rays as IC emission, whereas in Enomoto et al. (2002), after re-observations with CANGAROO-II, neutral pion decay was put forward as an explanation instead. The proposed model was then heavily disputed by Reimer & Pohl (2002) and Butt et al. (2002) because of its conflict in the GeV regime with the flux of the nearby EGRET source 3EG 1714−3857 (Hartman et al. 1999). Further attempts to model the broadband spectrum of RX J1713.7−3946 were undertaken (e.g., Ellison et al. 2001; Uchiyama et al. 2003; Pannuti et al. 2003; Lazendic et al. 2004). However, they did not result in unequivocal conclusions concerning the acceleration mechanisms of the highest-energy particles or the origin of the VHE gamma rays from this source.

This work is about the H.E.S.S. observations of RX J1713.7−3946 conducted in three years. It is organised as follows: In Chapter 2, a brief introduction into the physics of air showers and the detection principle of Čerenkov telescopes is given followed by a description of the H.E.S.S. experiment. A detailed overview of the methodology of the analysis of H.E.S.S. data is given in Chapter 3, focussing especially on topics related to the analysis of *extended* VHE gamma-ray sources such as RX J1713.7−3946. Analysis results are finally summarised in Chapter 4. In a chronological manner, results are presented year by year followed by conclusions as they were appropriate by the time of analysing the different data sets. First the results of 2003 (published in Aharonian et al. 2004b) are given, followed by the analysis of 2004 (published in Aharonian et al. 2005a), which covers the main part of this chapter. Finally, first results from the 2005 data are presented and compared to the two preceding years.

2 The H.E.S.S. Experiment

Currently the most successful experimental technique for the detection of VHE gamma rays is the ground-based Imaging Atmospheric Čerenkov Technique (IACT). While the direct detection of cosmic gamma rays by satellite experiments dominates the field of gamma-ray astronomy for primary energies up to 10 GeV, higher-energy gamma rays are exceedingly difficult to detect with the few square metres detection area of satellite experiments due to the steep decline of the gamma-ray flux with energy. Therefore, for higher energies, indirect measurements by means of the earth's atmosphere are required. The IACT is one such indirect technique where one records images of air showers, generated during the absorption process of VHE gamma rays in the atmosphere, and deduces from them properties of the primary gamma ray. A brief summary of the relevant physical processes that lead to the formation of an air shower is given in Section 2.1. The differences of showers induced by hadronic cosmic rays, mostly protons, and gamma rays are discussed. Moreover, the formation and propagation of Čerenkov light in air during the shower development is described. Section 2.2 describes the IACT and points out the geometry of the mapping of Čerenkov light by *Čerenkov telescopes*. Finally, in Section 2.3, details about the H.E.S.S. experiment, which applies the IACT and is currently leading the field of VHE gamma-ray astronomy, are given.

2.1 Air showers

Whenever a high-energy cosmic-ray nucleus or photon hits the top of the terrestrial atmosphere it sets off a cascade of secondary particles, produced in interactions of the primary particle and in turn of the secondary particles with molecules and atoms in air. The cascade is called *airshower*. It can have two different components depending on the type of the primary particle. In case of a photon or an electron a shower of electromagnetic nature is initiated. In case of a nucleus, like for the overwhelming part of the cosmic rays, interactions via the strong and the weak force will occur beside the electromagnetic processes and hadronic as well as electromagnetic sub-showers evolve.

2.1.1 Electromagnetic showers

In case of an electromagnetic cascade three processes dominate the longitudinal shower development in the atmosphere. Bremsstrahlung and pair production cause the formation, ionisation of atoms the expiration of a shower. VHE gamma rays penetrating the atmosphere can convert into electron-positron pairs in the Coulomb field of atomic nuclei. The electrons[1] subsequently are deflected by nuclei and emit photons via Bremsstrahlung.

---

[1] Positrons will from now on not be treated separately and simply referred to as electrons.

Thus, both processes in turn set off an avalanche of particles and result in an electromagnetic air shower. The propagation of the shower continues until the mean particle energy drops below the critical energy $E_\mathrm{c} \approx 80$ MeV where the energy loss of electrons by ionisation of air molecules becomes dominant over Bremsstrahlung. The shower has reached its maximum particle number at this stage, no new particles will be created any more. Accordingly, all of the shower energy is eventually dissipated by ionisation of the medium, the shower is being absorbed.

The characteristic length scale of the interaction processes is given by the mean free path length. In case of Bremsstrahlung it is called radiation length X_0, usually measured in g cm^{-2}. It is the mean distance after which a high-energy electron loses all but $1/e$ of its initial energy E_0 by Bremsstrahlung:

$$\left(-\frac{dE}{dx}\right) = \frac{E_0}{X_0}\,. \tag{2.1}$$

$\frac{dE}{dx}$ is the energy loss of an electron due to Bremsstrahlung after traveling a distance x in matter. Integration of this equation yields:

$$E(x) = E_0 \cdot e^{-x/X_0}\,. \tag{2.2}$$

In air the radiation length amounts to $X_0 = 37.2\ \mathrm{g\,cm^{-2}}$. The corresponding e-folding distance for pair production of high-energy photons, the conversion length X_c, amounts to $\frac{9}{7}\,X_0$.

The predominant process determining the lateral shower development is multiple Coulomb scattering. A charged particle traversing air is deflected by many small-angle scatters. Most of this deflection stems from Coulomb scattering of electrons or photons off nuclei. Bremsstrahlung and pair production contribute to a lateral spread of the secondary particles with respect to the shower axis, too. An electron undergoing Bremsstrahlung radiates the photon in a cone in forward direction with an average opening angle of $\langle\Theta\rangle = 1/\gamma$, where γ is the Lorentz factor. Thus, for high-energy electrons the directional divergence from the shower axis originating from Bremsstrahlung is very small and can be neglected.

The Coulomb scattering distribution is well described by the theory of Molière (Bethe 1953). It has a roughly Gaussian shape for small scattering angles, but at larger angles it behaves like Rutherford scattering having longer tails than a Gaussian distribution. The lateral distribution of electromagnetic showers in different materials scales fairly accurately with the Molière radius R_mol which depends on the radiation length X_0 and the critical energy in a given material: $R_\mathrm{mol} = 0.0212\,\mathrm{GeV} \cdot X_0/E_\mathrm{c}$. In the atmosphere the distance corresponding to X_0 varies with the density, hence it is:

$$R_\mathrm{mol} = \frac{9.6\ \mathrm{g\,cm^{-2}}}{\rho_\mathrm{air}}\,. \tag{2.3}$$

At sea level R_mol is approximately 80 m (the values used to calculate R_mol are taken from Heck et al. (1998)).

On average, 90 % of the energy of a shower is deposited in a cylinder around the shower axis with radius R_mol. About 99 % is contained within $3.5\,R_\mathrm{mol}$.

The basic properties of the development of an electromagnetic shower can already be seen on the basis of a toy model introduced by Heitler (1954). Only Bremsstrahlung and pair production are considered for particle creation. It is assumed that both radiation and conversion length are equal, namely X_0, and that the energy is divided equally between the secondary particles after the passage of one length scale. Figure 2.1 illustrates the assumptions.

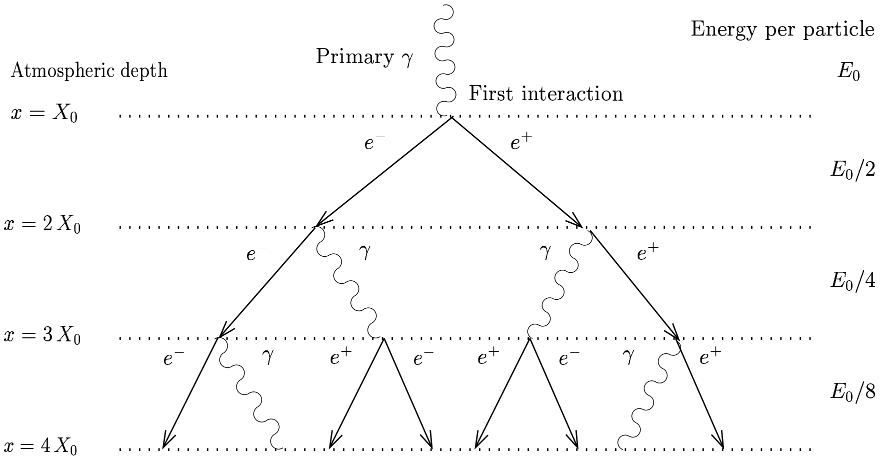

Figure 2.1: Simple model describing the development of an electromagnetic shower according to Heitler.

After $n = x/X_0$ branchings, x being the distance traveled along the shower axis in g cm^{-2}, the shower consists of $N(x) = 2^{x/X_0}$ particles each having an energy of $E(x) = E_0 \cdot 2^{-x/X_0}$. The depth of the shower maximum in the atmosphere, X_max, is then given by the expression:

$$E_0 \cdot 2^{-X_\mathrm{max}/X_0} \overset{!}{=} E_\mathrm{c} \quad \Rightarrow \quad X_\mathrm{max} = \frac{\ln E_0/E_\mathrm{c}}{\ln 2} \cdot X_0 \,. \tag{2.4}$$

From that one obtains the number of particles at the shower maximum to:

$$N_\mathrm{max} = 2^{X_\mathrm{max}/X_0} = \frac{E_0}{E_\mathrm{c}} \,. \tag{2.5}$$

Thus, this simple model predicts an exponential increase of the particle number in the initial phase of the shower development. The maximum amount of particles is proportional to the energy of the primary particle and the depth of the shower maximum grows logarithmically with the primary energy. These notions are found to be qualitatively true even when comparing them to more realistic approaches, which take energy loss processes during shower formation and other higher order interaction processes into account. For example, a 1 TeV gamma ray incident from zenith will create an air shower reaching its maximum X_max typically at ≈ 300 g cm^{-2} atmospheric depth which corresponds to a height of ≈ 10 km above sea level (asl).

2.1.2 Hadronic showers

Although the development of hadronic showers is similar to that of electromagnetic ones, both types differ significantly in some aspects. A cosmic-ray nucleus hitting the earth's atmosphere scatters inelastically on air nuclei and thereby produces mesons like pions and kaons as well as nucleons and hyperons. The induced air shower has two components, an electromagnetic and a hadronic component. The shower core consists of hadronic particles which constantly feed the electromagnetic component via decay of neutral and charged mesons. At each interaction, slightly more than a third of the energy is transformed to the electromagnetic part. Eventually most of the primary energy is transferred to electromagnetic sub-showers. The main energy losses are due to neutrino and muon production, which escape the shower region, and ionisation of electrons.

To summarise, the prominent differences between electromagnetic and hadronic showers (due to the differences in the interaction processes) are:

- In hadronic showers a significant fraction of the primary energy is converted into long-lived muons and neutrinos. Additionally energy is dissipated in nucleus interactions. Thus, hadronic showers with threefold primary energy result in the same number of particles in the electromagnetic shower component as gamma-ray induced showers.
- The mean free path length for a proton of energy 1 TeV is $\approx 80\,\mathrm{g\,cm^{-2}}$, more than twice as large as the electromagnetic radiation length. Hadronic showers penetrate deeper into the atmosphere, the atmospheric depth of the shower maximum X_{max} is on average larger.
- The lateral development of electromagnetic showers is dominated by multiple Coulomb scattering. The mean scattering angle is rather small and so is the lateral extent of the shower. In comparison, the secondary particles involved in weak and strong interactions receive higher transverse momenta by inelastic scattering at extended target particles resulting in a much larger lateral extension of hadronic showers (see Fig. 2.2).
- Complex multi-particle processes in contrast to the dominant three-particle processes in electromagnetic showers cause larger fluctuations in hadronic showers and make them less regular (see Fig. 2.2).

2.1.3 Atmospheric Čerenkov light

Most secondary particles of extensive air showers have high-relativistic energies. Thus, charged shower particles will move with a velocity larger than the local phase velocity of light and emit Čerenkov radiation. A short review of the main features of the emission of Čerenkov light in the atmosphere important for the detection of air showers with Čerenkov telescopes will be given in the following.

The half-angle ϑ_{C} of the Čerenkov cone for a particle with velocity βc in a medium with refractive index n is given by

$$\cos\vartheta_{\mathrm{C}} = \frac{1}{\beta c}\,. \tag{2.6}$$

Since $\cos\vartheta_{\mathrm{C}}$ must be smaller than 1, a threshold velocity of $\beta_{\mathrm{t}} = 1/n$ exists for Čerenkov-light emission. The threshold energy depends on the mass of the particle m_0 and the refractive index n of the medium:

$$E_{\mathrm{min}} = \gamma_{\mathrm{min}}\, m_0\, c^2 = \frac{m_0\, c^2}{\sqrt{1-n^{-2}}}\,. \tag{2.7}$$

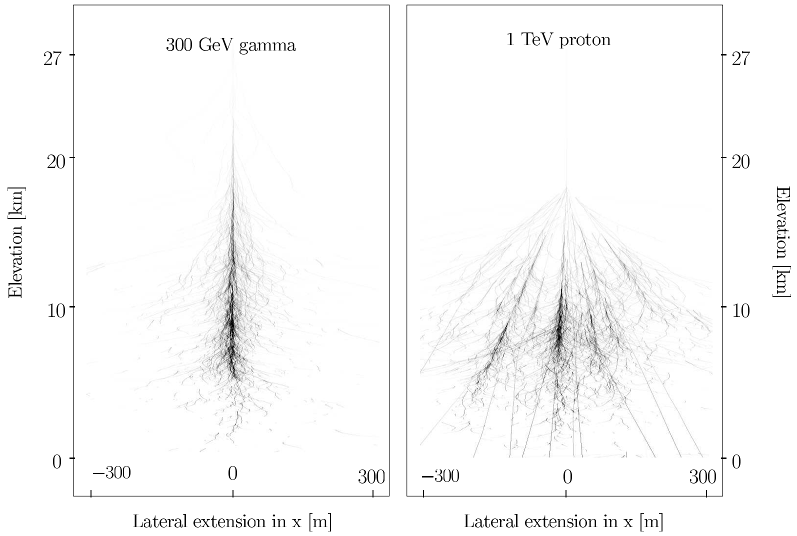

Figure 2.2: Comparison between electromagnetic and hadronic showers illustrating the longitudinal shower development. Shown are the tracks of individual secondary particles as projected into the (x,z) plane, taken from Monte Carlo simulations (Bernlöhr 2000). Note how compact electromagnetic showers are in comparison with hadronic showers.

Light particles such as electrons therefore dominate Čerenkov emission in air showers.

Since the density of air varies continuously with height, the refractive index varies, too. Hence, the threshold energy as well as the emission angle depend on the altitude in the atmosphere. With decreasing height, the density increases and also the refractive index. Under the simplified assumption of an isothermal atmosphere one can use the barometric formula for the density of air to express the dependence of the refractive index on the height in the atmosphere:

$$n(h) = n_0 \, e^{-h/h_0} \, , \qquad n_0 = 0.00029 \, , \; h_0 = 7250 \, \mathrm{m} \, . \tag{2.8}$$

Using Eq. (2.6) and Eq. (2.8) one can calculate the emission angle ϑ_C as a function of the height, as shown in Fig. 2.3.

Particles emit Čerenkov light on a narrow cone around their trajectory with an opening angle of $2\,\vartheta_\mathrm{C}$. On observation level this results in a roughly circular ring with Radius R_C given by

$$R = (h - h_\mathrm{obs}) \cdot \tan \vartheta_\mathrm{C} \equiv h' \cdot \tan \vartheta_\mathrm{C} \, , \tag{2.9}$$

where h_obs is the observation height asl. The change of R_C with the emission-height is shown in Fig. 2.3.

At observation level the light cones emitted by electrons in different heights superimpose resulting in an almost homogeneous light distribution in a circle with radii between 80 m and 150 m (in case of an electromagnetic shower) around the shower axis. The photons arrive within a very short time interval of a few nanoseconds. If all the particles emitting Čerenkov light would move parallel and close to the shower axis, there would be no light outside the maximum radius. However, due to multiple scattering (as mentioned above), the light distribution is smeared out. This can be seen in Figure 2.4 which compares light

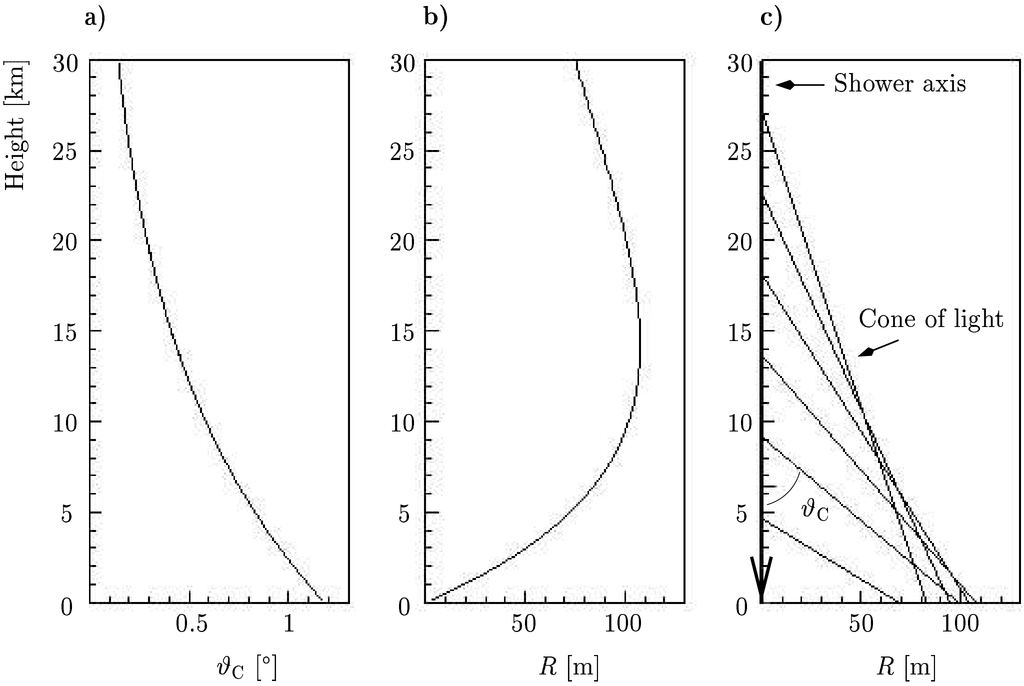

Figure 2.3: Shown in a) and b) are the dependencies of the Čerenkov emission angle ϑ_C and the Čerenkov-ring radius R_C on the emission height, respectively. The observation level is 2200 m asl. c) clarifies the geometry of the Čerenkov light cone emitted in different heights (picture taken from (Ulrich 1996)).

distributions on the ground for hadronic and electromagnetic showers. One can see the smearing effect for the electromagnetic shower, also the distinct circle of the maximum radius is visible. In contrast to that stands the image for the hadronic case which exhibits heterogeneous, asymmetric structures reflecting the differences in the shower development as described above. Faint circles originating from the various electromagnetic sub-showers occur.

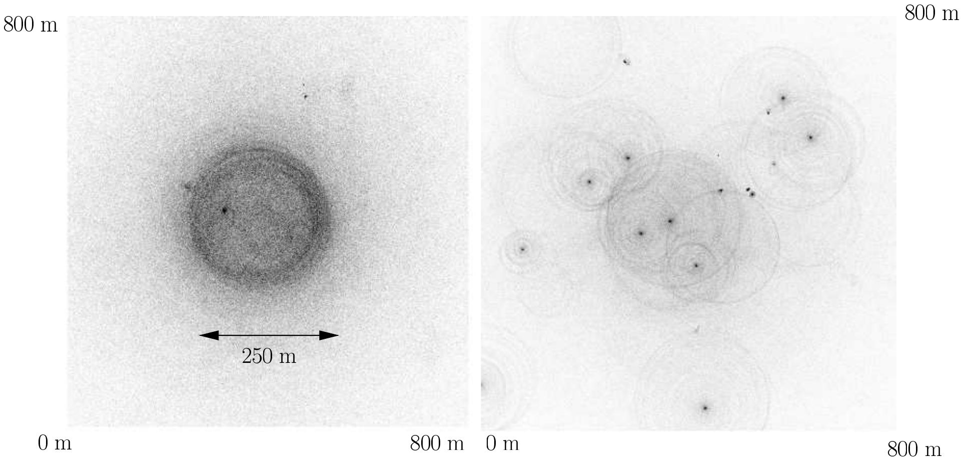

Figure 2.4: Simulated lateral Čerenkov light distributions on the ground are shown (Bernlöhr 2000). These pictures correspond to Figure 2.2.

Extinction of Čerenkov Light in the Atmosphere

The formation of Čerenkov light in the atmosphere ranges over several kilometres. On their way to the ground the photons undergo scattering and absorption processes leading to an exponential loss of intensity:

$$I(x) = I_0 \, e^{-\alpha x} \, . \tag{2.10}$$

α is called extinction coefficient and depends strongly on the wavelength. According to (Kyle 1991) light in the blue spectral range experiences the least extinction.

The three dominant sources of extinction are:

Rayleigh scattering: Scattering of photons on particles, which are small with respect to the photon's wavelength and which can be polarized by them, is called Rayleigh scattering. The extinction coefficient α_R is anti-proportional to the fourth power of the wavelength: $\alpha_\mathrm{R} \propto \lambda^{-4}$. Thus, mostly photons with small wavelengths are scattered.

Mie scattering: Photons are scattered on target particles like aerosols with dimensions similar to their wavelength. The dependency of the extinction coefficient on the wavelength is: $\alpha_\mathrm{M} \propto \lambda^{-1 \cdots -1.5}$.

Absorption by ozone: At wavelengths below 340 nm (Bernlohr 2000) ozone (O_3) is a very important absorber – not only in the ozone layer but even near ground. The fission of ozone, $O_3 + \gamma \rightarrow O_2 + O$, absorbs nearly all photons with wavelengths of 200–300 nm.

The total extinction can be described as a superposition of all three processes: $\alpha = \alpha_\mathrm{R} + \alpha_\mathrm{M} + \alpha_\mathrm{O}$. Especially the ozone absorption cuts off the spectrum at detection level at wavelengths of about 300 nm.

The number of photons emitted per unit path length x of a particle with charge ze and per unit wavelength λ of the photon is

$$\frac{d^2N}{dx d\lambda} = \frac{2\pi\alpha z^2}{\lambda^2} \left(1 - \frac{1}{\beta^2 n^2(\lambda)} \right) \, , \tag{2.11}$$

where α is the fine-structure constant. Due to the $1/\lambda^2$ dependence, the peak in the spectral Čerenkov-light distribution lies in the UV, where, as mentioned above, absorption processes in the atmosphere are strongest. Therefore, the maximum number of Čerenkovphotons reaching ground level is in the blue region of the visible electromagnetic spectrum, at wavelengths of about 330 nm. For a primary gamma ray of 1 TeV energy, about 100 Čerenkov photons per square metre reach ground level for an observation height of 2000 m asl.

Zenith-angle dependence of Čerenkov light-pool radius

So far the properties of the emission of atmospheric Čerenkov light in electromagnetic cascades were discussed for observations at zenith. As can be seen from the sketch in

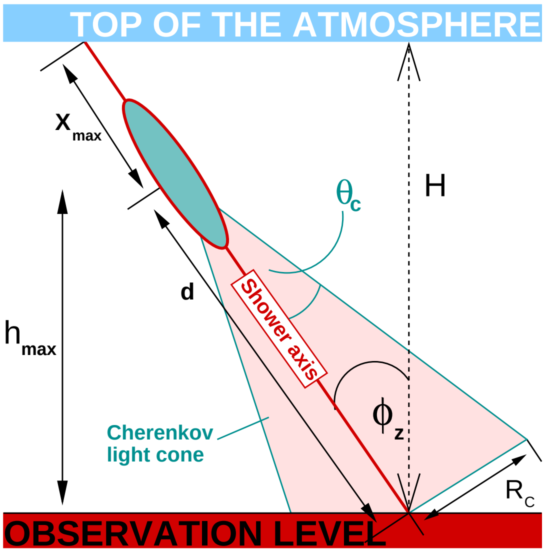

Figure 2.5: Sketch of Čerenkov light cone to explain the geometry. The Čerenkov light-cone radius on observation level depends on the cone–opening angle ϕ_z and the distance d that the Čerenkov light travels before reaching ground level. With increasing zenith angle, d increases, too, since X_max remains unchanged.

Fig. 2.5, there is one important effect that occurs with increasing zenith angle, and that is an increase of the distance d between the shower maximum and the impact point of the Čerenkov front on observation level. The formation of the shower depends mostly on the atmospheric depth traversed, the depth of the shower maximum X_max is to be understood as atmospheric depth along the shower axis. Therefore, with increasing zenith angle, the height of the shower maximum asl remains almost unchanged, but the Čerenkov light cone travels increasingly larger distances until the observation level is reached and widens correspondingly, the Čerenkov radius on ground (in a plane perpendicular to the shower axis) increases, too.

As is easily be understood from Fig. 2.5, the height of the shower maximum above observation level h_max can be approximately calculated as

$$h_\mathrm{max} = H - \cos\phi_\mathrm{z} \cdot X'_\mathrm{max} \,. \tag{2.12}$$

H is the height of the top of the atmosphere, ϕ_z is the zenith angle of the shower and X'_max is the distance in metres the shower has traversed when reaching its maximum, equivalent to X_max in units of $\mathrm{g\,cm^{-2}}$. The distance d between shower maximum and the impact point on ground is

$$d = \frac{h_\mathrm{max}}{\cos\phi_\mathrm{z}} \overset{(2.12)}{=} \frac{H}{\cos\phi_\mathrm{z}} - X'_\mathrm{max} \,. \tag{2.13}$$

Adopting eq. (2.9) with $\tan\vartheta_\mathrm{C} \approx \vartheta_\mathrm{C}$ one obtains the zenith-angle dependence of the Čerenkov light-cone radius on observation level:

$$R_\mathrm{C} = \left(\frac{H}{\cos\phi_\mathrm{z}} - X'_\mathrm{max} \right) \cdot \vartheta_\mathrm{C} \,. \tag{2.14}$$

Figure 2.6 illustrates the energy and zenith-angle dependence of the lateral Čerenkov-photon density on ground for electromagnetic showers. Shown is a quantity equivalent

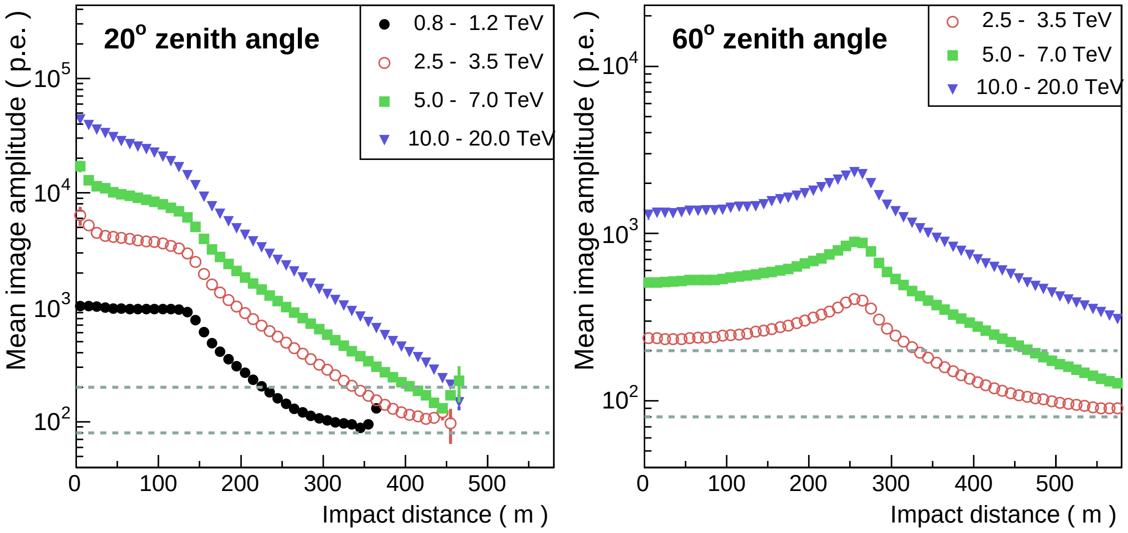

Figure 2.6: Shown is a quantity somewhat equivalent to the lateral Čerenkov-light distribution, the mean image amplitude measured with Čerenkov telescopes, for showers incident at 20° & 60° zenith angle. The horizontal dashed grey lines correspond to image amplitudes of 80 p.e. and 200 p.e., respectively, values which will be of importance later in Chapter 3.

to the photon density, the mean image amplitude in units of photo-electrons (p.e.), as measured with Čerenkov telescopes (see Section 2.2), as a function of the perpendicular distance between telescope and the shower axis. One can see the characteristic shape of the distributions. For moderate energies the photon density is constant up to a certain radius, for 20° zenith angle this radius is ≈ 130 m. Beyond it the density declines. In some cases one can also see the *Čerenkov shoulder*, just before starting to decline the density exhibits a local maximum or at least an edge. This position is normally referred to as (maximum) Čerenkov-cone radius R_C (used in Eq. 2.14). It is already apparent as maximum ring radius in Fig. 2.4. This feature appears if the shower maximum, where most of the Čerenkov emission takes place, is formed in heights where the effect that with increasing atmospheric depth the Čerenkov angle widens (due to the increasing density) is exactly cancelled by the fact that the Čerenkov cone has less distance to the ground to develop. This results then in a focussing effect on ground, Čerenkov light emitted in different heights is focussed onto equal Čerenkov-cone radii on ground, ≈ 150 m for small zenith angles. As can be seen from the figure, two effects are apparent with increasing energy: one is a general increase in Čerenkov light density on observation level, the other one is that the plateau and the Čerenkov shoulder are less pronounced. The shower maximum is formed deeper in the atmosphere, therefore the widening of the Čerenkov angle is not cancelled any more by the diminishing distance to ground level. The edge where the photon density starts to decline is washed out and eventually disappears completely, at very large energies (O(10 TeV) for 20° zenith angle, O(100 TeV) for 50° zenith angle) there is only a gradual decrease apparent with increasing distance to the shower axis.

The zenith-angle effect of the Čerenkov-cone radius as discussed above can also be seen when comparing the left-hand to the right-hand side of Fig. 2.6. At 20° zenith angle, for mean primary energies of 3 TeV, the maximum Čerenkov-cone radius is at ≈ 130 m, whereas at 60° zenith angle it is at ≈ 260 m, in reasonable accordance with Eq. 2.14. Note that for large zenith angles and similar energies, the Čerenkov shoulder is much clearer visible.

Čerenkov light is also emitted in hadronic showers. It can be either due to electromagnetic sub-showers, or due to secondary charged muons, $\mu^{\pm}$, which penetrate deep into the atmosphere and reach ground level because of small cross sections for interactions and their relatively long lifetime of 2.2×10^{-6} s. Given sufficient energy they emit Čerenkov light in a narrow cone around their path.

2.2 Imaging Atmospheric Čerenkov technique

The IACT makes use of the earth's atmosphere and the absorption processes of cosmic VHE gamma rays. It takes images of Čerenkov light emitted by secondary particles in air showers and has, due to the large extension of the Čerenkov light pool on observation level (cf. Section 2.1), a much larger detection area available compared to satellite experiments. The technique was pioneered by the Whipple collaboration (Weekes et al. 1989) who were the first to detect a source of VHE gamma rays with this technique, the Crab nebula, in 1989. The HEGRA collaboration (Daum et al. 1997) took the next step in 1996 with the installation of an array of Čerenkov telescopes to perform stereoscopic observations of air showers. This approach of simultaneous observations with more than one telescope has different advantages: the trigger threshold of the system can be lowered since a trigger coincidence of multiple telescopes can be required which drastically reduces random triggers of night-sky background (NSB) light and single-telescope triggers of local muons (the muons are called *local* because of their very narrow Čerenkov light cone, as mentioned in Section 2.1, which triggers only a single telescope). As a result the telescopes can be operated with reduced energy thresholds. Another advantage of having multiple views of the same air shower is that the amount of information is increased which improves the reconstruction of the shower geometry (and thereby the direction of the primary) and of the primary energy. Finally, viewing the shower from different sides improves the rejection of the dominant background, hadronic cosmic rays, given that on average gamma-ray induced showers are much more regular and symmetric than cosmic-ray showers. All of the experiments of the current generation of IACT experiments, H.E.S.S. (Hinton 2004), MAGIC (Lorenz 2004), VERITAS (Weekes et al. 2002), and CANGAROO-III (Kubo et al. 2004), take or plan to take the stereoscopic approach, aiming at energy thresholds of 50 GeV to 100 GeV. While the exact configuration and layout of the different experiments differ, the basic geometry and principles are the same and will be introduced in the following.

Čerenkov telescopes map the Čerenkov light of air showers with spherical or parabolic mirrors onto a camera in the focal plane of the mirrors. Since light rays viewed under the same opening angle are imaged onto the same point in the camera, the camera coordinate system is commonly defined as an angular system. In fact, Čerenkov telescopes measure the angular distribution of Čerenkov light from air showers.

The straight-forward mapping rule for a point (x, y, z) in the atmosphere from where a light ray hits the telescope mirrors reads:

$$\begin{pmatrix} u \\ v \end{pmatrix} = -\frac{f}{z} \begin{pmatrix} x \\ y \end{pmatrix} . \tag{2.15}$$

(u, v) are the resulting camera coordinates, f is the focal length the mirrors. The formation and orientation of the shower image in the camera can be understood by means of a simplified model, assuming that Čerenkov light is emitted isotropically along the shower axis. Figure 2.7 illustrates for this case the imaging of the shower axis into the camera, three points along the shower axis are mapped into the camera plane. The image of the shower axis in the focal plane (the "image axis") is a straight line which points towards the shower impact position on ground on one side. Light emitted from the shower axis in infinite height would be mapped onto a point $(-\theta_x, -\theta_y)$ in the focal plane. The point indicates the inclination of the shower axis with respect to the optical axis of the telescope. The image axis in the focal plane points on one side towards the image of the shower impact point on ground and on the other side towards the source position, given as inclination or offset angle relative to the telescope optical axis.

The shower maximum is typically in heights of 8 km to 12 km, accordingly most of the Čerenkov light is emitted in a narrow cylindrical region around the shower axis in that height. Figure 2.8 shows a sketch which explains the shape of the light distribution in a Čerenkov camera. On the left-hand side the plane spanned by the shower axis and

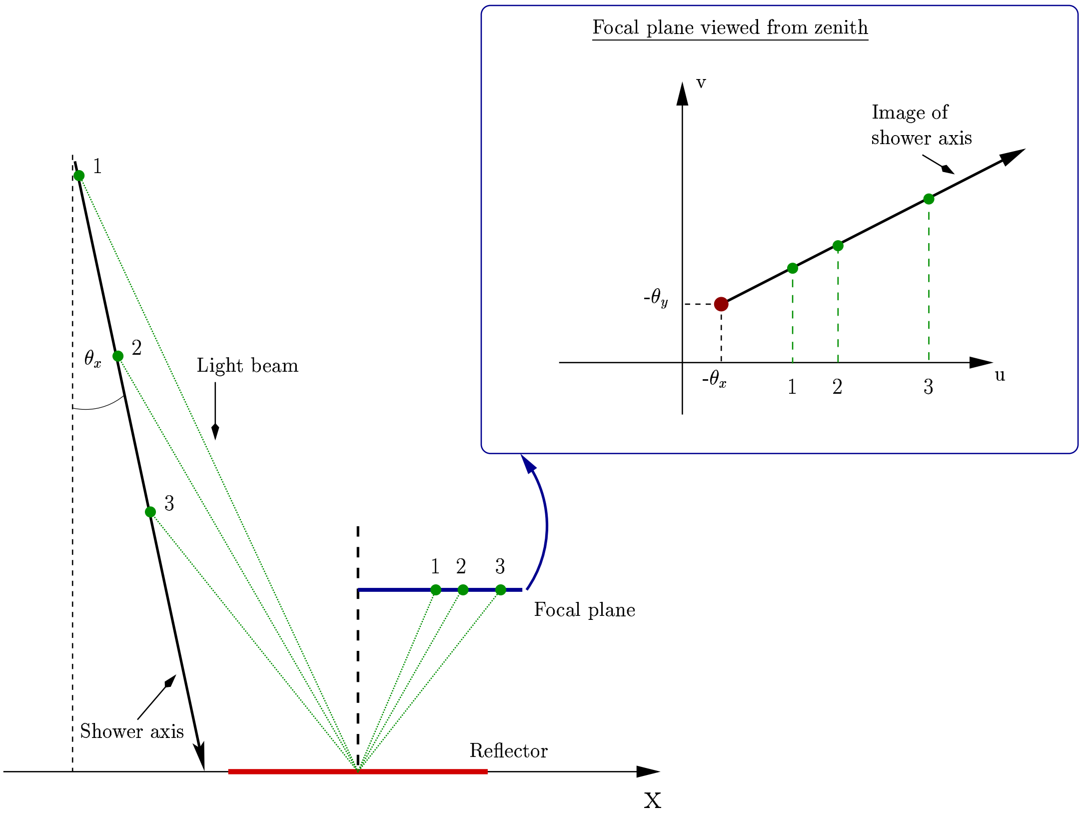

Figure 2.7: Sketched is the mapping of the shower axis into the focal plane of a telescope. As can be seen from the inset, the orientation of the image depends on the inclination of the shower with respect to the telescope optical axis.

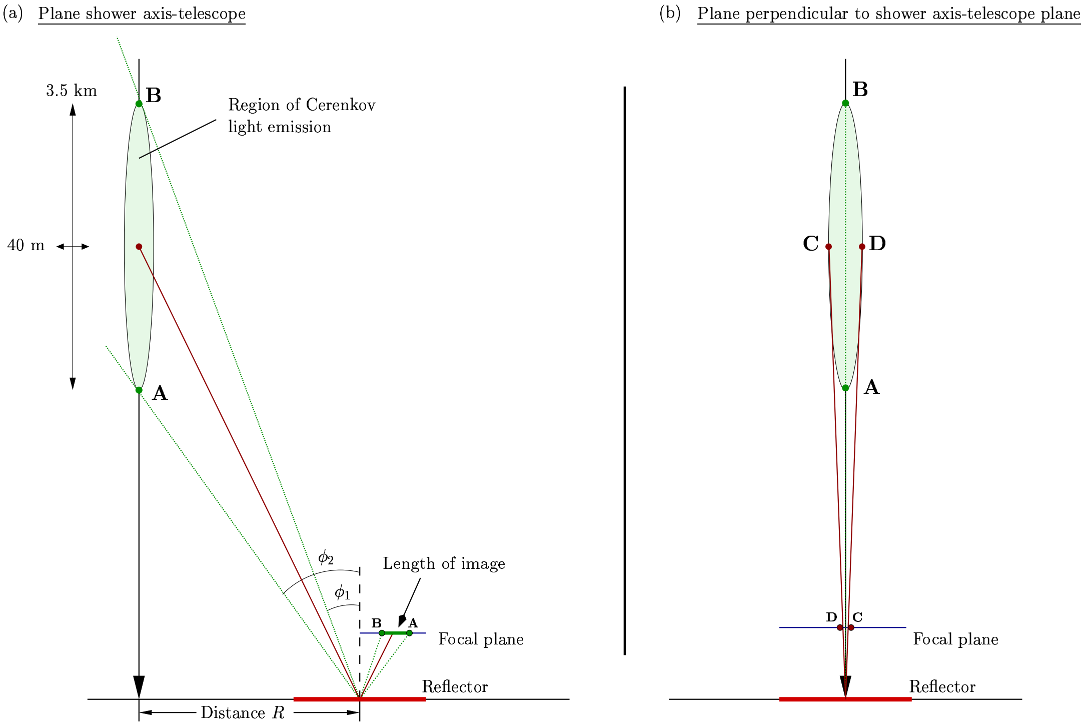

Figure 2.8: Sketch to explain basic dependencies between showers and camera images. (a) shows the view of the plane spanned by the shower axis and the telescope position. Length and position of the image are determined by $\Delta\phi = \phi_2 - \phi_1$ and R. (b) shows the perpendicular view from the telescope towards the shower, which determines the image width. Four points – A,B,C,D – are drawn and to be compared with Fig. 2.9.

the telescope is shown. The angle under which the elliptical emission region is viewed, $\Delta\phi = \phi_2 - \phi_1$, determines the length of the camera image, the distance R between telescope and shower axis determines the position of the image. If the shower moves further away from the telescope, the image will be elongated and move towards the outside of the camera. Figure 2.8 (b) shows the perpendicular view; the lateral extend of the shower determines the width of the camera image. The four points A,B,C,D are now also drawn in Fig. 2.9 (left), which sketches the corresponding camera image. The image is roughly elliptical in shape, its orientation is given by the image axis, which is, as discussed above, the image of the shower axis. Note that there are distortion effects, due to the non-linearity of the imaging as given by eq. (2.15) images are crushed towards the camera centre and stretched towards the outside.

Figure 2.9 (right) shows a simulated H.E.S.S. camera image of a shower from a 3 TeV gamma ray incident from zenith. The telescope was pointing directly to the source, the presumed source location coincides with the camera centre. One can indeed see the orientation of the image, it points to the camera centre, and it is roughly elliptical in shape and distorted.

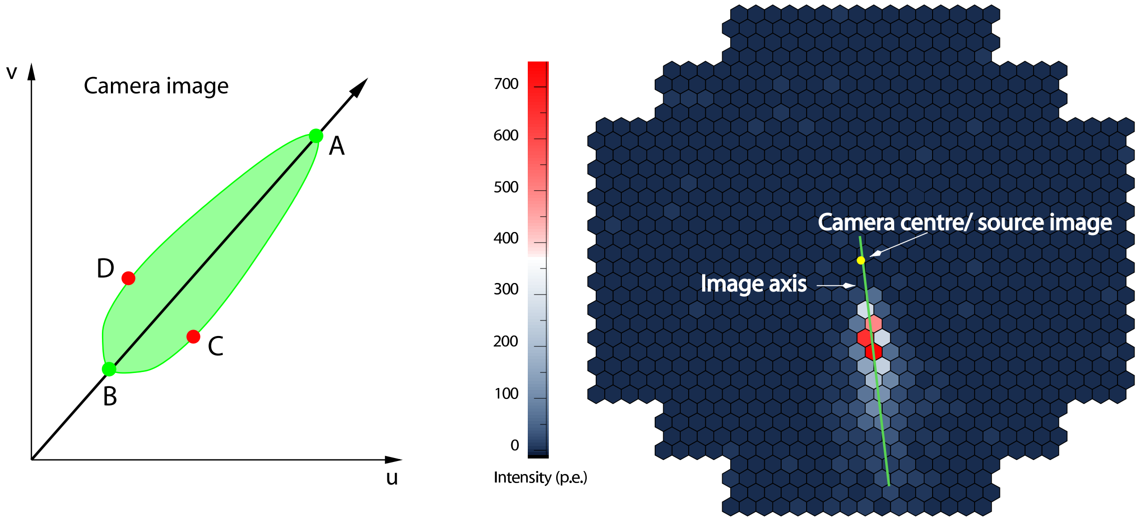

Figure 2.9: Left: Camera image corresponding to Fig. 2.8. The image shape is asymmetric due to the non-linear mapping. **Right:** H.E.S.S. camera image of a simulated, 3 TeV gamma ray. The camera centre and the image axis are indicated to guide the eye.

2.3 The H.E.S.S. telescope system

The High Energy Stereoscopic System (H.E.S.S.) is a system of four Čerenkov telescopes which employs the IACT. Its name is also a tribute to Victor Hess for his discovery of cosmic rays (see Introduction). The telescope array is situated in Namibia, in the Khomas Highland, at 23°16′ S 16°30′ E, 1800 m above sea level. The site location can be seen in Fig. 2.10. At a distance of about 100 km from the capital Windhoek, the area close to the Gamsberg is renowned for its excellent conditions for astronomical observations (Wiedner 1998). It was shown that 57% of the moon-less nights (only then are observations possible with IACT telescopes) were cloud-free and in 94% of these nights, the relative humidity was below 90%. These conditions, together with its height, the infrastructure, and its southern-hemisphere location made this site a good choice for building H.E.S.S., a telescope array in large parts devoted to the search for VHE gamma rays from Galactic sources. The central part of the Galactic plane culminates in the dry Namibian autumn and winter (that is, when optimum observation conditions are met) at zenith, enabling observations of a large number of potential gamma-ray sources including the SNR RX J1713.7−3946.

2.3.1 Telescopes

The first H.E.S.S. telescope started operation in summer 2002, in December 2003 the nominal four telescope of the first phase of H.E.S.S. were operational. Figure 2.11 shows an image of the complete H.E.S.S. array. The telescopes are arranged in a square of 120 m side length to provide stereoscopic views of showers. The spacing represents a compromise. On the one hand, large distances between telescopes are desirable because they provide good stereoscopic viewing conditions for close-by showers thereby easing shower reconstruction and increasing the collection area of the experiment. On the other hand, it was mentioned

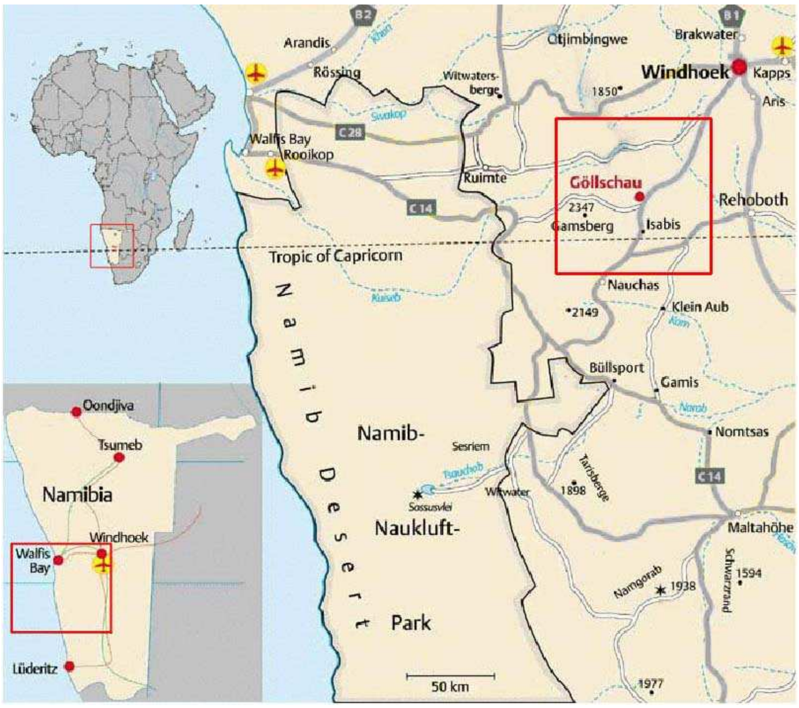

Figure 2.10: Location of the H.E.S.S. site in Namibia, at $23°16'$ S $16°30'$ E

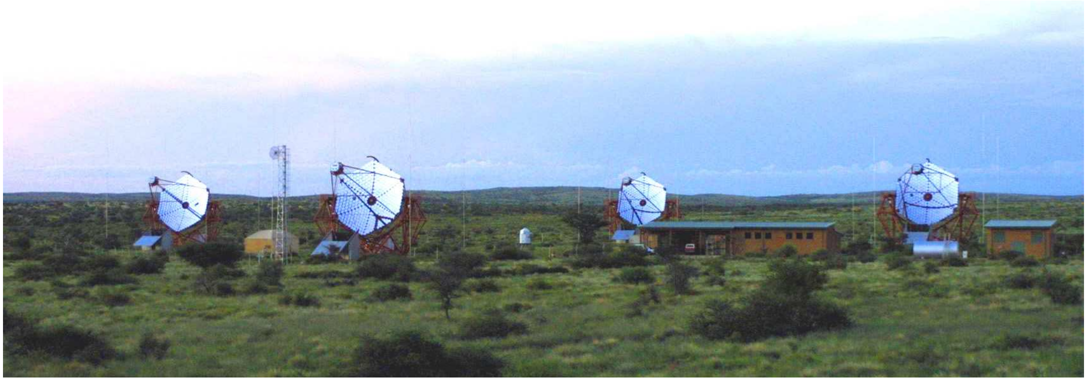

Figure 2.11: H.E.S.S. telescope array at nominal strength just after the installation of the last camera in December 2004.

that the area on ground illuminated by Čerenkov light of typical gamma-ray air showers is circular with diameter of ≈ 250 m. Therefore, increasingly larger distances between telescopes significantly reduces the rate at which multiple telescopes are illuminated by the same shower.

The telescopes as shown in Fig. 2.12, left-hand side, are an altitude-azimuth (alt-az) mount Davies-Cotton reflector (Davies & Cotton 1957). The mount rotates on a 13.6 m diameter circular azimuth rail. Friction drive systems acting on altitude rails at about 7 m radius from the axes control the movements in elevation. In both directions a telescope can move with a maximum angular velocity of 100°/min. Shaft encoders measure the actual position of the telescopes with mechanical accuracies for tracking of astronomical objects of better than 3″. Nevertheless, the precision of the absolute telescope pointing direction is dominated by systematic uncertainties induced by misalignments and deformation of the telescope structure. Currently the precision for locating gamma-ray sources in the sky is ≈ 30″. The reflector itself consists of 382 individual mirror segments mounted on the hexagonal dish with a flat-to-flat width of 12 m. The round mirrors (60 cm diameter) add up to a total reflector area of 107 m^2. The segments are made of ground glass, aluminised and quartz-coated. They are spherical mirrors arranged on a sphere with radius equal to the focal length $f = 15$ m.

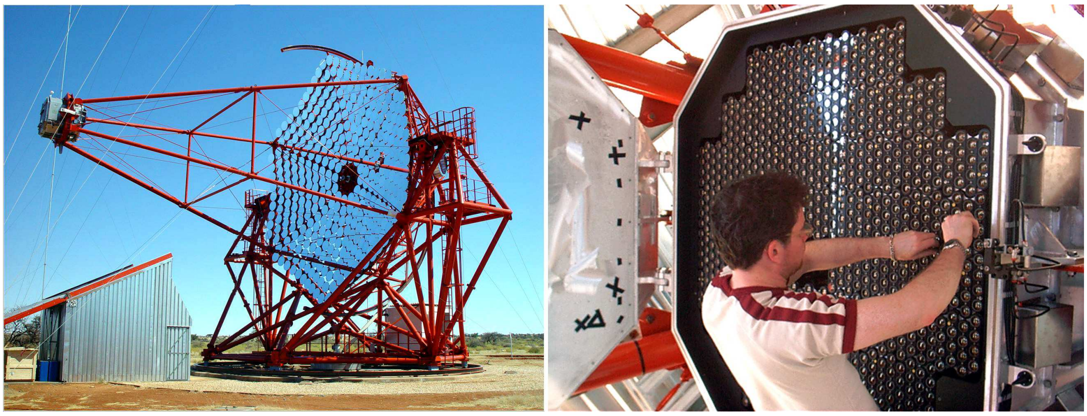

Figure 2.12: H.E.S.S. telescope and camera

The cameras of IACT telescopes are required to record images of the few-nanosecond long Čerenkov-light flashes of air showers. The H.E.S.S. cameras provide a large field of view of 5° (full opening angle), the fast electronics for the triggering, data conversion and readout is fully integrated in the 1.4 m diameter camera body. In Fig. 2.11 one can see all four cameras, each supported by four masts emerging from four corners of the hexagonal dish. A closer view of one of the cameras is shown in Fig. 2.12, on the right-hand side. It consists of 960 individual photo-multiplier (PMT) pixels subtending 0.16° each. Winston cone light concentrators are mounted in front of the pixels to focus light onto the active area of PMTs thereby minimising photon losses. They are hexagonal in shape and close the gaps between the circular pixels. The camera is modular in design, housing 60 drawers of 16 PMTs each. The trigger electronics divide the camera into 64 overlapping sectors with a programmable trigger requirement that a sector has a minimum number of pixels with a signal above a threshold in photo-electrons (p.e.), coincident in an effective ≈ 1.3 ns trigger window. Upon receiving a camera trigger, the signal stored in 128 ns deep analog memories from each PMT, sampled at 1 GHz, is integrated within 16 ns. Once a camera has formed a trigger, a signal is sent via optical fibre to a central station, the *central trigger system* (Funk et al. 2004), which allows for multiple telescope coincidence requirements. The central trigger reduces thereby random NSB as well as single telescope triggers by local muons already at the hardware level. This then allows for lowering of the camera trigger thresholds and thus lowering of the energy threshold of the system, which is one of the great advantages of a stereoscopic telescope system (as was already mentioned above).

2.3.2 Monte-Carlo simulations

The Monte-Carlo simulations used throughout this work are performed in two steps. First the complete development of the air shower in the atmosphere is simulated including the formation of Čerenkov light, then a second programme is run that simulates the response of the detector to these air showers. The air-shower simulation code is CORSIKA, **CO**smic **R**ay **SI**mulations for **KA**scade (Heck et al. 1998). An important aspect of shower simulations are the atmospheric transmission models used. The simulations used here have been compared with the real conditions in Namibia, in particular for two different sets of transmission tables calculated using MODTRAN (Bernlohr 2000). One is based on a rather conservative assumption of aerosol content (maritime haze, boundary layer starting at sea level), the other one corresponds to a clearer atmosphere (desert haze, boundary layer starting at 1800 m) and seems therefore more appropriate for the desert-like conditions at the H.E.S.S. site. This one is used in the simulations taken for this work.

The detector simulation used here is called `sim_hessarray` (Bernlöhr 2002). It simulates the response of an array of H.E.S.S. telescopes at a great level of detail. It includes the exact layout of the light reflectors and telescope structures such as camera masts which cast shadows onto the cameras itself. The measured optical point-spread function (PSF) as well as quantum efficiencies of PMTs and their signal pulse shapes are also included. Moreover, potential degradation of mirror reflectivity and therefore decrease of the optical efficiency of the telescopes can be taken into account.

Monte-Carlo Samples

A fixed sample of Monte-Carlo simulations will be used throughout this work. It consists of gamma-ray point-source simulations with a primary spectrum obeying a power law in energy of E^{-2}. The simulations are performed at 13 fixed zenith angles of observation of the source: 0°, 20°, 30°, 40°, 45°, 50°, 55°, 60°, 63°, 65°, 67°, 69°, and 70°. For each zenith angle, the source is simulated for six different values of the inclination angle between the source direction and the telescope pointing direction, commonly referred to as *offset angle*: 0°, 0.5°, 1°, 1.5°, 2°, 2.5° Hence 78 combinations of zenith and offset angle are simulated. At the beginning of this work, simulations were used that reached only up to 20 TeV in primary energy, causing an upper energy limit for energy reconstruction of real events well below this value. The simulated energy range was eventually increased and these simulations with increased statistics are since then in use. The energy range covered by simulations goes up to 100 TeV for zenith angles $\phi_{\mathrm{z}} < 60°$, to 200 TeV for $\phi_{\mathrm{z}} = 60°$, and to 400 TeV for larger values of ϕ_{z}. Moreover, only Monte-Carlo simulations with showers incident from the South will be used since RX J1713.7−3946 is a South source. This is important because of the influence of the Earth's magnetic field on the shower development in the atmosphere, as will be explained later on.

One important aspect of the detector simulation is the optical efficiency of the telescope system. Since the reflectivity of mirrors degrades with time, the simulated optical efficiency has to be matched to reality to try and cope for this aging effect. Simulations used here are matched to the system performance at the end of 2003, when the fourth telescope became operational. At that time, the first telescope was running already for $\approx$ 18 months. Its optical efficiency was therefore assumed to be worse by 8%. The other three telescopes were simulated with 100% optical efficiency.

2.3.3 Data taking

IACT Čerenkov telescopes are normally operated in data-taking mode in moon-less nights only, during *astronomical darkness*. The available observation time is sub-divided into data-taking periods of typically 28 min, which are called *data runs* or simply *runs*. During a run, the telescopes are targeted at and track a certain astronomical object or a given position in the sky. The data is then continuously stored to disk.

Different modes of operation will be discussed in Section 3.6 when the background modelling is explained.

3 Analysis

Before presenting and discussing the results obtained from the H.E.S.S. RX J1713.7−3946 data, a thorough discussion of the methodology of the analysis will be given in the following. The different stages are explained and documented in the order they are traversed during real data processing. These include the reconstruction of the shower geometry, Section 3.1, the calculation of shower parameters used for the application of cuts to suppress background events, Section 3.2 and 3.3, and the reconstruction of the primary energy, explained in Section 3.5. Special attention is devoted to analysis aspects particularly important for an extended source such as RX J1713.7−3946. These include the angular resolution (Section 3.4) and the background modelling over the entire field of view (Section 3.6), which is discussed separately for the generation of gamma-ray excess images as well as for the generation of gamma-ray spectra. Finally, in Section 3.7, the procedure that is applied to generate gamma-ray spectra is explained.

3.1 Event reconstruction

The first step in the data processing chain is a run selection which removes data which were not taken under ideal weather conditions or where the telescope system was not operating within specified requirements (e.g. no hardware failure, trigger rate stable, 95% of pixels per camera operational). For data runs passing the selection criteria, camera images are then calibrated as described in Aharonian et al. (2004a). The next step in the chain is a cleaning procedure which removes noisy pixels originating from PMT noise or NSB from camera images. The cleaning is achieved by applying a two-stage tail-cut procedure in which a pixel is kept in the image, if it has an intensity of more than 10 p.e. and a neighbouring pixel with more than 5 p.e.. In addition pixels with more than 5 p.e. are included in the image if they have a neighbour with more than 10 p.e.. An NSB cut is also applied to avoid pixels suffering from bright star light in the images. A pixel which passes the tail cuts, but whose intensity does not exceed 3σ of the pedestal RMS, is excluded from the analysis.

After the cleaning procedure, camera images are parametrised using a Hillas-type approach (Hillas 1985). This approach is motivated by the roughly elliptical shape of shower camera images, which is due to the much larger longitudinal than lateral extent of showers in the atmosphere (for a detailed description of the geometry of the mapping, the formation of shower images and calculation of image parameters see, e.g., Berge (2002)). Images are characterised by means of their first and second moments. The first moments of the two-dimensional intensity distribution have the mathematical form of a centre of gravity (Hillas parameter *COG*). The matrix of second moments can be interpreted as an ellipse around the COG. Diagonalisation of the matrix yields the major and minor axes of the ellipse, specified by the Hillas parameters *width* and *length*, as square root of the eigen-

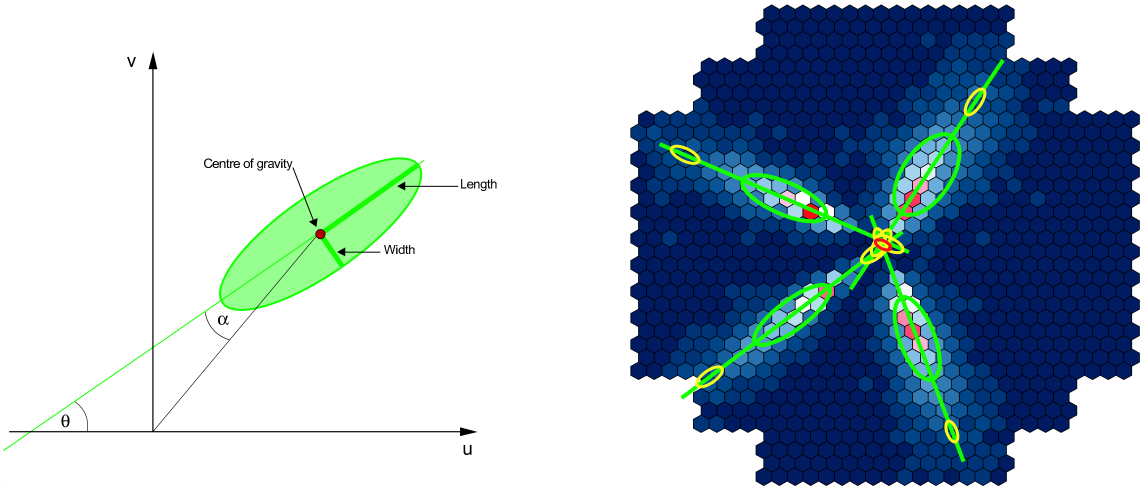

Figure 3.1: Left: Sketch of a Hillas ellipse. The parameters used for the event reconstruction are shown. **Right:** Illustration of the event reconstruction based on image parameters. Four camera images of a simulated 7 TeV gamma-ray shower, superimposed in a common camera plane are shown. The Hillas ellipses are overlaid on the intensity distributions. Estimated source regions of the advanced algorithm-3 type reconstruction method are drawn along the image axes as yellow ellipses on both sides of each image. The resulting optimum source direction is drawn as red error ellipse.

values. The angle of the principal-axis-transformation, ϑ, is the orientation angle of the ellipse. These five Hillas parameters are illustrated in Fig. 3.1. Furthermore the shower images are characterised by the image pixel amplitudes in p.e., the Hillas parameter *size*.

The image parameters contain crucial information about the shower. *Width* and *length* reflect the shower morphology and can therefore be used for gamma/hadron separation. The amount of light collected by the telescopes is connected to the energy of the primary particle, thus the *size* parameter can be used for energy reconstruction. Lastly, the COG and the image orientation ϑ are governed by the shower geometry, as is illustrated in Fig.2.7, Chapter 2. Parameters of the shower geometry like incident direction and shower impact position on the ground can be determined on the basis of these image parameters. The straightforward geometrical reconstruction technique is applicable as soon as more than one image of a shower is available.

For all pairs of telescopes, image axes are intersected in a common coordinate system. In case of N telescope images, the $N(N-1)/2$ intersection points are averaged, weighting each intersection point by the sine of the angle between the image axes, to take into account that images with large stereo angle provide the most precise determination of the shower direction. In addition, intersection points are weighted by a factor accounting for the relative intensity of images and for the ratio of *length* over *width*, since bright and elongated images provide well defined shower characterisations. The core location can be obtained in a similar way by intersecting image axes in an *array-wide* coordinate system, starting from the telescope locations. The technique is illustrated in Fig. 3.1 (right). An event display is shown of a 7 TeV gamma-ray shower, incident from a direction coincident with the telescope pointing direction. Hence, the source direction coincides with the camera centre.

It can be seen that the intersection points of image axes provide a reasonable estimate for the source direction. This method, referred to as *geometrical* method since it makes uses of image information only and calculates shower parameters in a simple analytical form, is the standard reconstruction technique used for publication of H.E.S.S. results. Most of the results obtained in this work are based on this (robust) technique.

The downside of this approach is that differences between the quality of images are not properly taken into account (the weighting factor that accounts for image sizes and *length* over *width* is not sufficient). One can improve the technique by determining errors on the image parameters and taking these into account when intersecting the image axes. In addition, image shape information can be used to obtain an estimate for the distance d between the image COG and the source location along the image axis. This approach corresponds to algorithm 3 of Hofmann et al. (1999), where a comprehensive study of different techniques for the reconstruction of VHE gamma-ray showers from stereoscopic Čerenkov images is presented. In this work, an algorithm-3 type technique is compared to the standard geometrical reconstruction technique. For this purpose, lookup tables generated from simulations are used to obtain an estimate for the source distance d, the error on the distance, the error on the ellipse orientation angle ϑ, and the error on the image location, the COG, in a direction perpendicular to the image axis. The estimates are based on image parameters, the tables for d are filled in $\ln(size)$ and *length* bins, for the error on the COG in $\ln(size)$ and *width* bins, and for the error on ϑ in $\ln(size)$ and *width/length* bins. When combined, these parameters constrain the image of the source to two elliptical regions on both sides of the image, reflecting the left-right degeneracy of the Hillas ellipse. As soon as more than one image of a shower is available, the error ellipses can in most cases be unambiguously combined to yield the shower direction and an error estimate. In Fig. 3.1 (right) the elliptical regions on both sides of each image are indicated. The final optimum shower direction very close to the camera centre is also drawn.

3.2 Shower shape parameters

Once the shower geometry is reconstructed, cuts are applied to suppress the vast number of cosmic-ray background events. As explained in Chapter 2, hadronic showers are much more irregular and on average broader and longer than electromagnetic showers. A common means to separate gamma-ray from hadron showers is to apply a cut on the image shape parameters *width* and *length* (Hillas 1985). Before doing that, one has to take the basic dependencies of these parameters into account. The shape of shower images depends on the impact distance. The opening angles under which the light-emitting region around the shower maximum is viewed change. Well within the light pool, the *width* becomes smaller as the shower moves away from the telescopes. The *length* increases at the same time because the longitudinal opening angle increases. In addition, with increasing primary energy the shower penetrates deeper into the atmosphere, more secondary particles are created. Consequently, more light is emitted during the shower formation and more photons are collected by the telescope reflectors. Images will have a larger *size* and be at the same time broader and longer. Moreover, the amount of light that reaches the telescopes depends on the zenith angle; with increasing zenith angle, the shower maximum

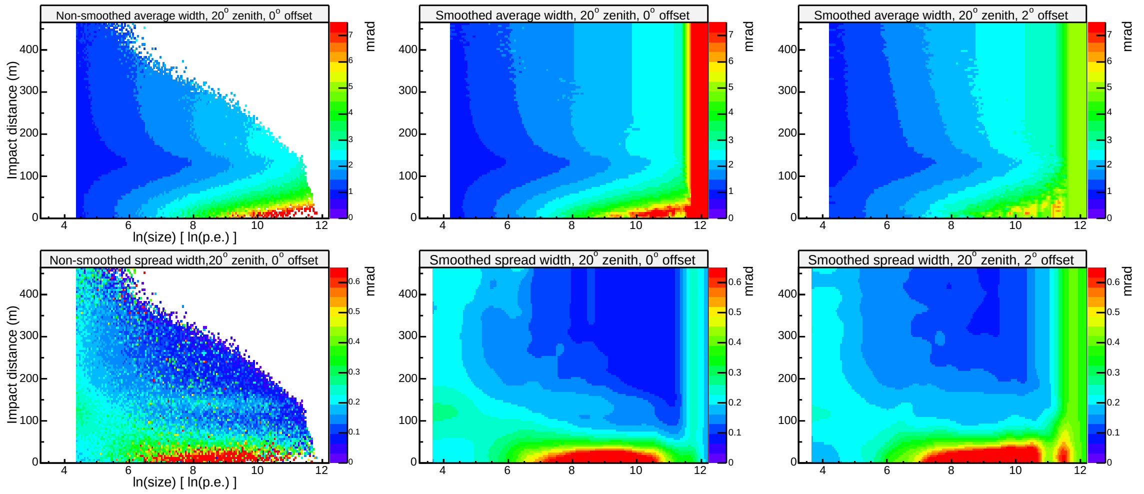

Figure 3.2: Shape parameter lookup tables generated from gamma-ray simulations of a point source, observed at 20° zenith, located on-axis and at 2° offset from the pointing direction . Shown are the mean (**top row**) and RMS values (**bottom row**) of the *width* as a function of reconstructed shower impact parameter (in metres) and natural logarithm of *size* (in $\ln(\mathrm{p.e.})$). A smoothing procedure has been applied to the tables in the **middle** and the **right-hand** column, as mentioned in the main text. The **left-hand** column shows the non-smoothed on-axis tables. The angular colour scale is in units of millirad. Note that a cut on the minimum image *size* at 80 p.e. has been applied when filling these tables. The sharp vertical edge in the tables around $4\ln(\mathrm{p.e.})$ is due to that cut, the exact position depends on the smoothing (larger smoothing values push the edge to the left).

is increasingly further away from the telescopes.

In order to apply cut values common for all offset and zenith angles, mean reduced scaled width (MRSW) and length (MRSL) parameters are computed for each event. These parameters are defined as the difference in units of standard deviation of the measured image *width* (*length*) from that which is expected from gamma-ray simulations for the corresponding image intensity, reconstructed impact parameter[1], zenith angle of the shower and its offset from the system pointing direction, averaged over all telescopes participating in the event:

$$MRSW = \frac{1}{N_{\mathrm{tel}}} \sum_{i \in N_{\mathrm{tel}}} \frac{width_i - \langle width \rangle_i}{\sigma_i}, \tag{3.1}$$

and similarly for MRSL. In Eq. (3.1), $\langle width \rangle_i$ and σ_i denote the mean simulated values of the image parameter (*width* or *length*) and its RMS spread, taken from lookup tables for the corresponding image *size* and impact parameter. By using a reduced scaled *width* and *length* for each telescope, one takes the basic dependencies of the image shape parameters into account, namely the dependency on the distance of the telescope to the shower axis and on the total intensity of the image. Moreover, typical fluctuations of image parameters determined from gamma-ray simulations are included. For each camera image, one obtains thereby a measure of how much its *width* (*length*) deviates from a typical gamma-

---

[1] Distance of the reconstructed shower impact point on ground to the telescope

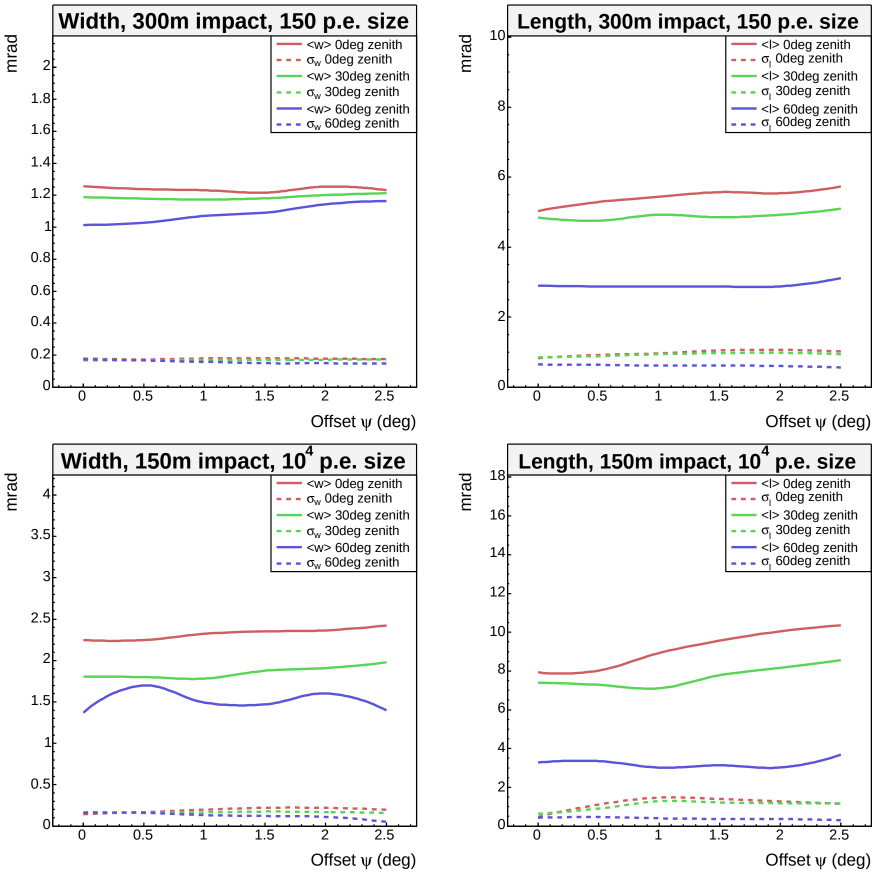

Figure 3.3: Plot illustrating the offset and zenith angle dependence of *width* and *length* for Monte-Carlo gamma rays. For two impact-parameter and *size* bins, the mean value and RMS spread of *width* and *length* from gamma-ray simulations are plotted as a function of offset angle, for three observation zenith angles. Note that all simulations are performed at six fixed offset angles, starting from $0°$ in steps of $0.5°$. Smooth lines are drawn connecting the six simulated values.

ray shower image, expressed in standard deviations. By averaging this number over all telescopes, statistical fluctuations are further reduced and shower information obtained under different viewing angles is combined. Discussed in Section 2.2 as one of the advantages of an array of IACT telescopes performing stereoscopic observations, it is now clear why it helps in terms of background rejection to view the shower under different angles from different sides. As said before hadronic showers are on average broader, but also less regular and symmetric than gamma-ray induced showers. By averaging over telescopes one increases the probability to reject a proton shower that looks like a gamma-ray shower from one side, but is broader from another side (in the case that different telescopes view the shower from different sides).

Representative lookup tables are shown in Fig. 3.2. The tables are generated from Monte-Carlo simulations, averaging over telescopes and events. On the left-hand side in the figure raw, very finely binned tables are shown the way they are generated from simulations. After that, a Gaussian smoothing procedure has been applied to these tables to reduce statistical fluctuations (see middle and right-hand column). The tables with the average *width* are smoothed with a Gaussian of $\sigma = 0.05\ \ln(p.e.)$ in x-direction and with $\sigma = 1.0$ m in y-direction[2]. For the RMS spread tables, fluctuations are larger, therefore larger smoothing values are applied here, $\sigma = 0.2\ \ln(p.e.)$ in x-, and $\sigma = 15$ m in y-direction. The same values are used for the smoothing of the tables containing the *length*. Furthermore, the lookup tables are extended continuously to large impact-parameter values. For that purpose, for a fixed x-bin, loops over the y-bins from small to large impact distances are performed. Where the bins are sparsely filled, the mean value of the last few filled bins (in y-direction) is taken and filled into the table up to the largest impact distances. Basic dependencies of the *width* can readily be seen in Fig. 3.2. The average *width* grows monotonically with increasing image amplitude, and with increasing impact distance, shower images get gradually smaller. Note how the Čerenkov shoulder, the edge of the Čerenkov light pool, is visible around 130 m impact distance (at the same distance as in Section 2.1.3, Fig. 2.6, where *size* was plotted versus impact distance). In the tables with the RMS spread there is one striking feature; the large spread of images with impact parameter close to 0 m. As can be seen from Fig. 2.8, in that case the shower hits the telescope dish or is at least very close to it. Accordingly, the images are almost circular, the image orientation is not well defined and therefore the major and minor axis of the Hillas ellipse, the *width* and *length*, are not well defined either.

The dependence of the mean value and spread of *width* and *length* on the shower zenith angle and the inclination angle ψ between shower axis and pointing direction is shown in Fig. 3.3. The average *width* and *length* increase moderately with offset angle due to the worsening of the optical PSF with increasing offset (Cornils et al. 2003). The zenith angle dependence is larger, especially for *length*. It can be seen that for fixed *size* and impact distance, images become more compact (*width* and *length* become smaller) with increasing zenith angle. As already mentioned, this is due to the zenith-angle dependence of the shower maximum (see Section 2.1.3): the maximum is viewed under increasingly larger distances from the telescopes with increasing zenith angles, therefore the viewing angles become smaller, and correspondingly the images.

A representative MRSW distribution obtained from simulations is shown in Fig. 3.4a which serves as consistency check. The distribution was created for simulations at 20° zenith and 1° offset angle, using lookup tables that were filled at fixed Monte-Carlo zenith and offset angles (including the 20°-zenith and 1°-offset simulation files). During the reanalysis, the reconstructed offset and zenith angle of the shower are taken to interpolate between the fixed Monte-Carlo offset and zenith angle bounds[3]. For the distribution in Fig. 3.4a the MRSW parameters are therefore determined for the same events that were used to fill the lookup tables (but the lookup values differ slightly due to the finite resolution of the reconstruction). There are slightly asymmetric, non-Gaussian tails visible in the distributions (much clearer in Fig. 3.4b where the y-axis is plotted logarithmically, although for a different distribution, explained below). Also shown in Fig. 3.4a is a reduced scaled width (RSW) distribution for one telescope (eq. (3.1), but without averaging over telescopes). The distribution looks very similar to the averaged one, except that it is broader. A fit of a Gaussian yields a width of $\sigma \approx 0.8$, as compared to $\sigma \approx 0.6$, the width

---

[2] The values of σ for the smoothing have been determined empirically.

[3] The interpolation is linear in the offset angle. For the zenith angle, the cosine of the zenith angle is interpolated linearly.

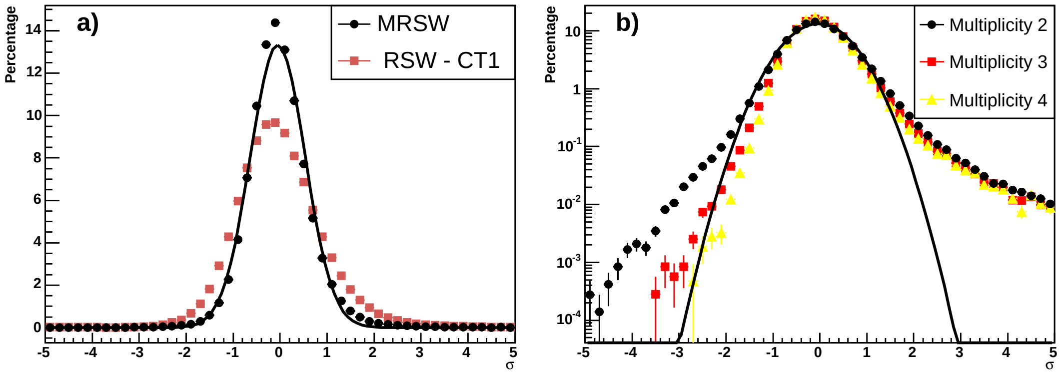

Figure 3.4: As consistency check of the lookup tables and of the interpolation, MRSW distributions are drawn. **a)** A MRSW parameter distribution from Monte-Carlo simulations of a point source, observed at $20°$ zenith angle, $1°$ off-set from the pointing direction is shown. The best-fit result of a Gaussian is drawn (thick black line). For comparison, an RSW distribution (distribution of reduced scaled *width* for one of the telescopes) is shown (red squares). **b)** MRSW distributions obtained from a sample of point-source simulations, $0.7°$ off-set from the pointing direction, observed at $10°$ zenith angle. The distributions have been produced using lookup tables at fixed values of $0°$ and $20°$ zenith angle, each for $0.5°$ and $1.0°$ offsets. The histograms show distributions for event multiplicities of two, three, and four telescopes, the best fit result of a Gaussian to the multiplicity-2 distribution is plotted as black line. Note that in the right-hand plot, the y-axis is plotted logarithmically to highlight the tails of the distributions.

of the averaged distribution. Ideally, if the variations of width and length for fixed image intensities, impact parameters, offset and zenith angle were purely Gaussian fluctuations, one would expect the RSW and reduced scaled length (RSL) distributions to be Gaussian, centred around 0 with a width of 1. Different effects are responsible for deviations from the ideal distribution. Firstly, and most importantly, shower fluctuations are not purely Gaussian, which might lead to asymmetric shaped distributions and long tails. Secondly, badly reconstructed showers lead to imprecise shower impact parameters, which in turn will produce outliers in the *width* or *length* distributions in a certain impact-parameter and *size* bin. Since the variation in each bin is taken as the RMS spread for simplicity (a fit of a Gaussian in each bin would require the storage of all the events of all bins in histograms), outliers will increase the RMS spread in that bin and therefore result in overestimated errors. This explains why the distributions are generally narrower than one would maybe expect. It is due to the fact that for the lookup, the RMS is used, but when quantifying the MRSW distribution, a Gaussian is fit. If one were to take the RMS of the distributions, they would be, as expected, 1. When comparing the telescope-wise RSW to the averaged MRSW distribution in Fig. 3.4a one notes that as expected statistical fluctuations are reduced, the curve becomes narrower because of the averaging. This is also seen in Fig. 3.4b where as a test of the interpolation mechanism, MRSW distributions are shown that have been produced for simulations at $0.7°$ offset and $10°$ zenith angle, using the four lookup tables generated with $0.5°$ and $1.0°$ offset angles, at zenith angles of $0°$ and $20°$. The distributions behave as expected, which demonstrates the validity of the interpolation scheme. Furthermore, the distributions for minimum event multiplicities of

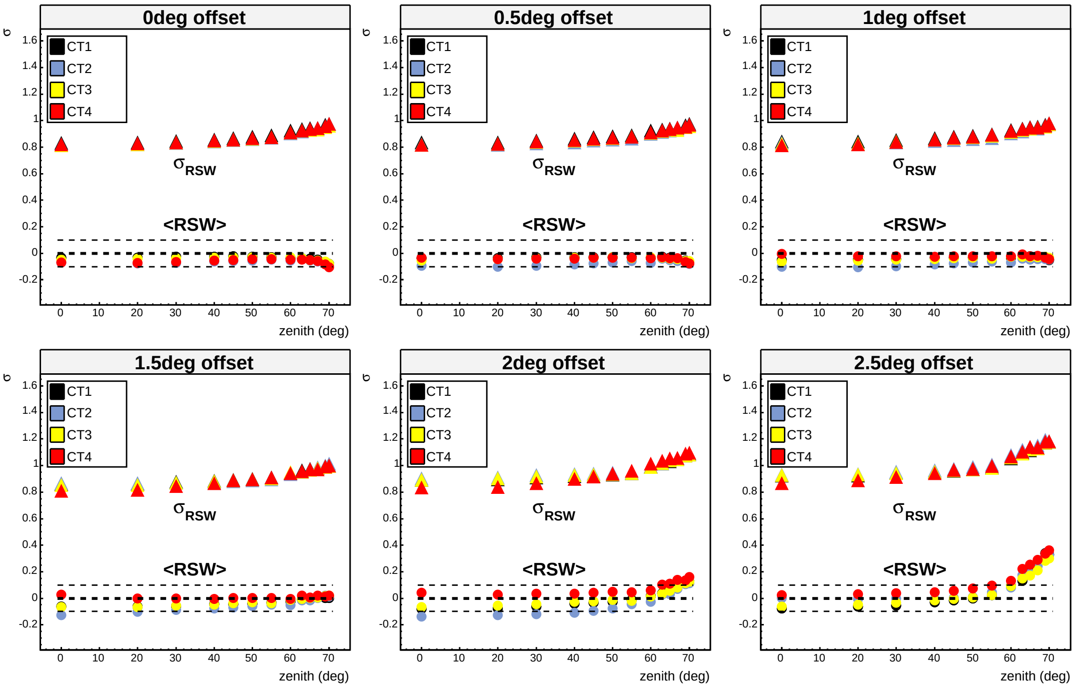

Figure 3.5: Shown are the telescope-wise mean and Gaussian σ values of the RSW distributions, for all zenith and offset angles the shape-parameter lookup tables are generated for. The values result from fits of Gaussian functions. The -10%, 0%, $+10\%$ levels are indicated by dashed lines. The values are sufficiently stable over the whole zenith and offset angle range.

2, 3, and 4 telescopes illustrate how the fluctuations are reduced. The shape of the curves remains more or less unchanged, but they become narrower. For example, the multiplicity-4 curve can be fit by a Gaussian of $\sigma \approx 0.47$, slightly larger than expected for the case of independent telescope images, where the width would be a factor of $1/\sqrt{N_{\text{tel}}} = 1/2$ smaller compared to telescope-wise distributions which typically have $\sigma \approx 0.8$ (Fig. 3.4a). The reason is that the telescope images are not independent of each other. Telescopes observe the same shower and therefore the image fluctuations are somewhat correlated.

The above mentioned features of MRSW and MRSL distributions – the slightly asymmetric shape and the small width – do not pose serious problems for the analysis, since the assumed RMS on *width* and *length* are not directly used, they are only required for the calculation of parameters to apply cuts on. Therefore, only stability over the offset and zenith angle range accessible to the experiment are important to assure stable cut efficiencies. This is demonstrated in Fig. 3.5, where mean value and width of the telescope-wise RSW distributions are shown, and in Fig. 3.6, where MRSW and MRSL distributions for events with multiplicity ≥ 2 are plotted. In both cases, the mean value is stable and well within 10% of zero, for all offset and zenith angles. The Gaussian σ, resulting from a fit of a Gaussian to the distributions, is stable for most zenith angles, only at large zenith angles of 60° and beyond does σ start to increase due to the fact that the distributions become more asymmetric. The impact of this large-zenith angle effect, if any, on the efficiency of the cut on MRSW and MRSL is shown later. The general notion that the MRSL distributions have larger σ than the MRSW distributions is probably due to a

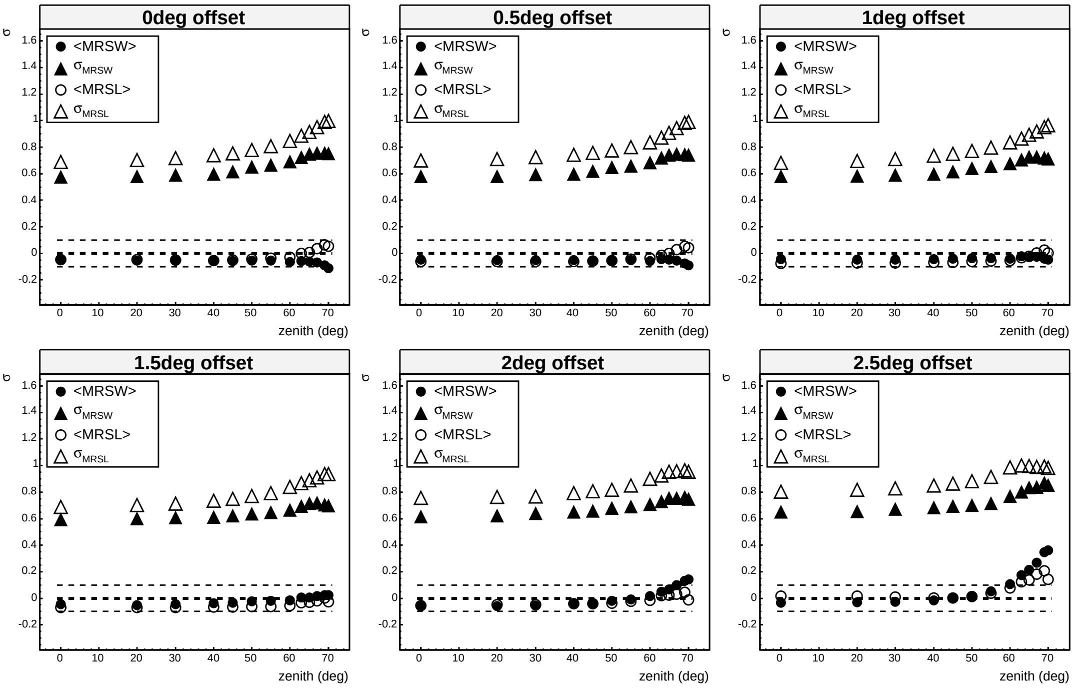

Figure 3.6: Mean and Gaussian σ values of MRSW and MRSL distributions for all zenith and offset angles. MRSW and MRSL are equally well behaved over the whole range. Note how the MRSL are systematically broader than the MRSW distributions.

stronger dependence on impact distance. The spread in the reconstructed core position induces therefore a larger spread in the MRSL than the MRSW distribution.

MRSW distributions from gamma-ray and proton simulations are compared to each other in Fig. 3.7. The differences are clearly visible; while the gamma-ray simulations are centred around zero and rather narrow, images from proton showers are on average much broader, the proton distribution extends to large positive values, and covers a broader range. Note that the comparison to data, also given in Fig. 3.7, shows good agreement with proton simulations. From the good separation of signal and background events, it is immediately clear that the MRSW parameter provides a good cut parameter to suppress background events. The same holds true for the MRSL parameter, although to a lesser extent; most of the rejection power is contained in MRSW. The data distributions are determined from the 2004 data of RX J1713.7−3946. They are determined by accumulating events in the region coinciding with the SNR and in a control region of the same size and shape in each data run (at the same distance from the pointing direction). The excess distribution is the difference of the signal and the normalised control region[4]. There is a 15% shift to negative values of the excess MRSW distribution, and the MRSL distribution has a tail to positive values, but note that also fluctuations become dominant there. There is in general an encouraging accordance of Monte-Carlo and data distributions.

---

[4] Normalised because the control region cannot be defined for every run.

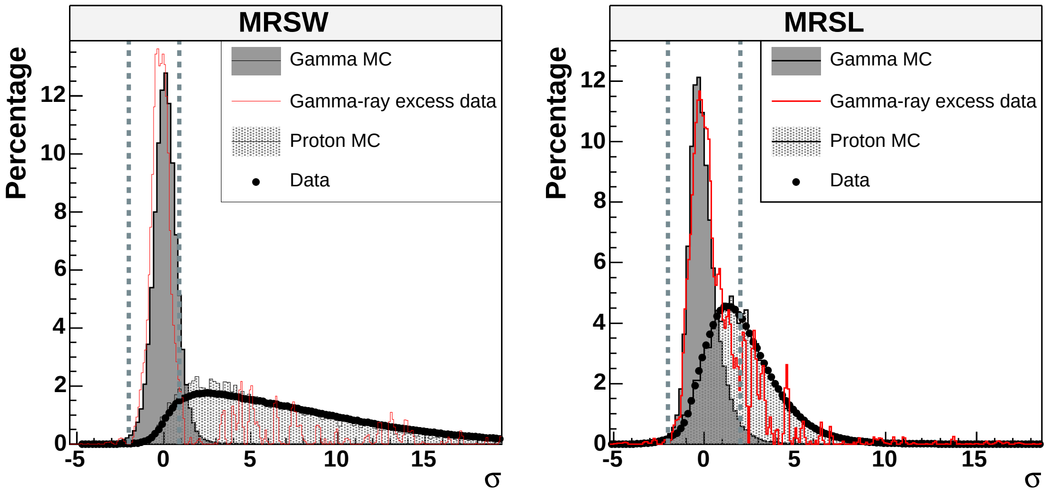

Figure 3.7: MRSW (**left**) and MRSL (**right**) distributions (adapted from Funk (2005)) generated from simulated Monte-Carlo (MC) gamma rays and protons, compared to data from empty-field observations and the gamma-ray excess distribution from the RX J1713.7−3946 data set. This data excess distribution has been renormalised to cover the same area as the MC distribution in the range $\sigma \in [-2, 1]$. No cuts on image parameters have been applied, only a cut selecting events with a minimum telescope multiplicity of two. The dashed vertical lines indicate the *std* cut values given in Table 3.1.

3.3 Analysis cuts

Optimum selection cuts depend on the gamma-ray source spectrum and the quantity one optimises for. The cuts used in the analysis presented here are optimised simultaneously to yield the maximum expected significance per hour of observation. Cuts are applied on MRSL and MRSW, and on the minimum image amplitude, the *size*. Furthermore, a cut on θ^2, the square of the angular difference between source and the reconstructed event direction, is applied and is equivalent to placing the data into a circular bin centred on the source position. Since the cosmic-ray background arrives isotropically, unlike the gamma-ray signal, this cut further suppresses the residual hadronic background, especially for point-like gamma-ray sources. The data used for optimisation consists of Monte-Carlo simulations of a gamma-ray point source at a zenith angle of 20°, offset from the pointing direction of the telescope system by 0.5°, and off-source data (i.e. data containing no gamma-ray signal[5]). The optimisation procedure was applied for two different assumed source spectra, once for a source with a flux of 10% of the Crab nebula and a Crab-like energy spectrum with photon index 2.6 (the resulting set of cut values will be referred to as configuration *std*[6]), and once for a source with a flux of 1% of the Crab and a photon index of 2.0 (the cut values will be referred to as configuration *hard*[7]). Table 3.1 lists

---

[5] With proton simulations one suffers from a lack of statistics due to the great rejection power of the image shape cuts. Moreover, for realistic simulations also Helium and heavier nuclei would have to be added.

[6] The set is called *"std"* because it is the H.E.S.S. standard cut configuration for the calculation of energy spectra

[7] The set is called *"hard"* because it applies tighter cuts on both *size* and MRSW compared to *std*, thereby reducing the efficiency of both cuts.

Configuration	MRSW Min	MRSW Max	MRSL Min	MRSL Max	θ^2 (deg.^{2})	*size* Min (p.e.)
std	-2.0	0.9	-2.0	2.0	0.0125 / 0.42	80
hard	-2.0	0.7	-2.0	2.0	0.01 / 0.42	200
$hard - 2tel$	-10.0	1.0	-1.8	2.0	0.01 / 0.42	300

Table 3.1: Optimised gamma-ray selection cuts, for three configurations, labeled *std*, *hard*, and *hard - 2tel*. The cut on θ^2 is split, the first value is the optimum point-source value, the second value is the one that will be used for the analysis of extended gamma-ray sources. For all three configurations a minimum of two camera images passing the cuts on *size* and on the distance of the image COG from the centre of the field of view (at 2°) are also required. These cuts define "gamma-ray like" events.

the resulting cut values. Note that another cut, not optimised but chosen a priori, is applied on the event multiplicity: a minimum number of two camera images has to pass the *size* cut and have their COG less than 2° away from the camera centre (the latter constraint, referred to as *nominal-distance* cut, is for minimising truncation effects close to the camera edge, which can be as close as 2.1°). In addition Table 3.1 lists another configuration, "hard - 2tel", which is a special configuration to be used later for the data of RX J1713.7−3946, recorded in 2003, when only two telescopes were operational.

Throughout the analysis presented here, the *std* configuration will be used for the determination of spectra. Its *size* cut at 80 p.e. results in a lower energy threshold compared to *hard*, in which a cut at 200 p.e. is applied. This increased *size* cut, however, makes the *hard* configuration well suited for morphology studies. It results in much better background suppression (as will be shown later) and in better reconstructed events and correspondingly superior angular resolution, because the camera images are better defined – at the expense of an increased energy threshold. Note that a tight θ^2 cut is only applicable for gamma-ray point sources. Since the studies presented here deal with an extended gamma-ray source, namely the SNR RX J1713.7−3946 with a roughly circular extension of $\approx 0.6°$ radius, the point-source value of the θ^2 cut will frequently be omitted in the following. Instead, a value of 0.65° is used to encompass the whole source region.

Figure 3.8 illustrates the different stages during measurement and analysis that cause a reduction of the initial number of simulated gamma rays. The curves are determined from gamma-ray simulations with a power-law source spectrum (photon index 2.0), at a zenith angle of 20° and an offset angle of 1°. The total number of simulated gamma rays that are fed into the detector simulation is shown in the upper panel, left-hand side, plotted as a function of simulated gamma-ray energy. Monte-Carlo showers are thrown within a circle of 1000 m radius around the centre of the telescope array. Note that the simulated source followed a *differential* power-law spectrum in energy with photon index 2, therefore the distribution of events versus energy, plotted in bins of logarithmically growing width (shown in Fig. 3.8), follows a power law with index −1. The simulated effect of the system trigger reduces the number of events dramatically and produces a steeply rising distribution at small energies ($E < 0.1$ TeV), which turns over just above 0.1 TeV. At this energy, the system is triggered by almost every shower impacting within ≈ 150 m radius,

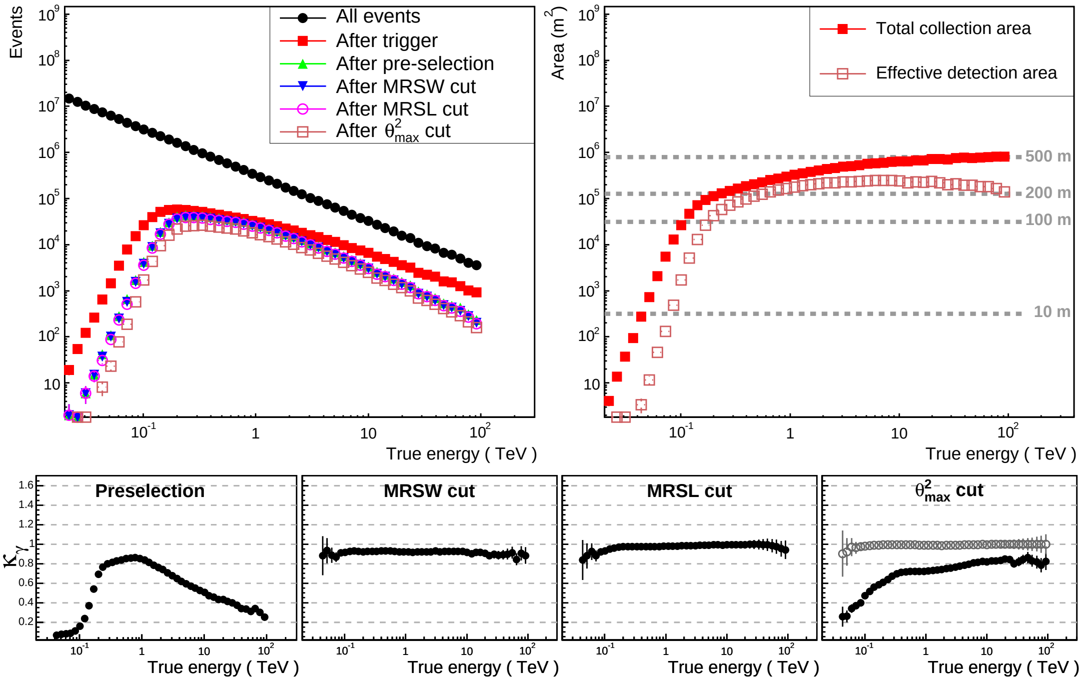

Figure 3.8: Various plots to characterise the energy dependence of the trigger efficiency and the efficiency of analysis-cuts, for the *std* configuration. **Upper panel:** Plotted on the left-hand side are simulated gamma-ray events at various stages of the analysis process, always as a function of the simulated gamma-ray energy. On the right-hand side, the total collection area is shown, given by the ratio of the number of events after to the number of events before trigger (both shown left), scaled by the simulated area, $A_{\mathrm{MC}} \approx 3.14 \times 10^6~\mathrm{m}^2$. The effective detection area is defined the same way as the collection area, but for events after cuts, instead of events after trigger. Indicated by dashed horizontal lines are the areas that correspond to circle radii of 10 m, 100 m, 200 m, and 500 m. **Lower panel:** The fraction of events passing the various cuts, κ_γ, is plotted as a function of energy. For the cut on θ^2, two distributions are shown, one for the point-source value (solid circles), and one for the extended-source value (open circles). Note that κ_γ is the ration of the number of events passing a certain cut to the number of events before that cut.

that is, within the plateau region of the Čerenkov light pool. This can be seen in the upper panel, right-hand side, where the total collection area, given by the fraction of incident events that trigger the array, multiplied by the thrown area, is shown (the collection area will be discussed in more detail further down). Once beyond the trigger threshold, the collection area is roughly equal to the area of the Čerenkov light pool on ground, $\approx 10^5~\mathrm{m}^2$. This can also be seen by means of the dashed grey lines which indicate the area of circles with radii of 10 m, 100 m, 200 m, and 500 m for reference. The gradual increase of the collection area with increasing energy is due to the increase in photon density within the light-pool on ground when the primary energy is rising: showers further away from the telescope system start to trigger the array. This is effect is clearly seen in Section 2.1.3, Fig. 2.6, where the mean image amplitude versus impact distance was plotted for two zenith angles and different energies. With increasing energy, the mean image amplitude is rising for fixed impact distance. Therefore the number of events at larger distances that trigger the array and is retained by the cuts increase, too (for orientation the two *size*-cut values in use here, 80 p.e. and 200 p.e., are drawn in Fig. 2.6).

In the first stage of the analysis, the pre-selection, cuts on image amplitude, nominal distance and event multiplicity are applied to the data. The distribution of all events that pass the pre-selection of the configuration *std* is also shown in Fig. 3.8, left-hand side. Compared to the all-events-after-trigger curve, there are two dominant effects apparent, more easily recognised in the plot of the cut efficiency κ_γ, bottom left plot, which is the fraction of all triggering events that pass the pre-selection. As can be seen, a large fraction of events is rejected at small energies, due to the cut on the minimum image *size*, which shifts the peak of the event distribution to larger energies. The second effect occurs gradually at large energies, notable beyond 1 TeV, where events are rejected because they fail the nominal distance cut: at these energies distant events produce images far away from the camera centre, which start to "see" the camera edge.

In the next analysis step, the application of image-shape cuts to reduce the hadronic background, almost all events are retained, as can be seen from the plot of the efficiency of the MRSW and MRSL cut, bottom panel of Fig. 3.8. The fraction of pre-selected events that pass the cut on MRSW is shown. Thus, almost all of the gamma-ray events, that pass the pre-selection, pass the gamma-ray shape cuts. Finally, the efficiency of the cut on θ^2 is also shown, for the point-source and the extended-source value. Only for a point-source, where this cut is of the order of the angular resolution of the system (see Section 3.4), a significant fraction of gamma rays is rejected, especially pronounced at small energies, where the angular resolution is worse.

Table 3.2 lists, for the same zenith and offset angle as above (20° and 1°, respectively), the total fraction of gamma-ray and cosmic-ray events retained by the two sets of cuts. The fraction of background events is determined from off-source data. To enable comparison with the gamma-ray values, off-source runs from a zenith-angle range around 20° have been selected. Background events were then accumulated within the θ^2 cut, at an offset of 0.7° from the pointing direction (typical offset of H.E.S.S. observations). Note how the fraction of background events, as opposed to the simulated gamma rays, is dramatically reduced by the θ^2 cut, especially in case of the point-source value, as a consequence of the uniform arrival directions of the background events. Figure 3.9 shows the cut efficiencies for gamma rays and cosmic rays for a range of zenith angles, again for both sets of cuts, at offset angles of 0.5° and 1.5°. In all four cases the cuts are quite stable over the full zenith-angle range. Only in case of the nominal point-source θ^2 cut a significant degradation beyond zenith angles of 40°–50° occurs. It is due to worsening of the angular resolution of the system (cf. Section 3.4). At very large zenith angles of 60° and beyond, the efficiency of the large θ^2 cut of 0.65° – applied for extended sources – also starts to become worse due to poor reconstruction. Comparing the two different offset angles to each other, a very similar zenith-angle dependence is seen, the major difference being overall $\approx$ 20% less events retained by the pre-selection for 1.5° offset, which is clearly due to the nominal distance cut. It is worth noting that in this case already $\approx$ 10% less events trigger the array. When comparing the two cut configurations, which differ mainly in the cut on the image *size*, to each other, one notes that the application of the 200 p.e. *size* cut of the configuration *hard* (bottom row of Fig. 3.9) reduces the efficiency by roughly a factor of two. Moreover, the zenith-angle dependence of the MRSW-cut efficiency is slightly larger, a gradual decrease is visible beyond 40°. This is due to the tighter cut on MRSW as

Configuration	$\epsilon_{\mathrm{Presel.}}$		ϵ_{MRSW}		ϵ_{MRSL}		ϵ_{θ^2}	
	γ	CR	γ	CR	γ	CR	γ	CR
	(%)		(%)		(%)		(%)	
std	62	35	58	4	56	3	38 / 56	0.01 / 0.3
hard	32	16	28	0.5	28	0.4	21 / 28	0.001 / 0.04

Table 3.2: Percentage of gamma-ray and background events retained by the different cuts, which are applied sequentially. A sample of gamma-ray simulations at 20° zenith angle and an offset of 1° was used. The data efficiencies were determined from off-source data, with zenith angles ranging from 15° to 25°, and a mean zenith angle of 22°. The values for the cut on θ^2 are again split, the first numbers given refer to the point-source value of $(0.11°)^2$, the second numbers to the extended-source value of $(0.65°)^2$. Note that ϵ, as opposed to κ_γ of Fig. 3.8, is the total fraction of events retained after the application of each cut.

listed in Table 3.1: at large zenith angles, the MRSW distributions widen, seen in Fig. 3.6. Therefore, a slightly larger fraction of gamma rays is rejected by the cut.

The percentage of background events retained by the cuts is also shown in Fig. 3.9. The numbers are determined from data containing no significant gamma-ray signal. For this purpose, OFF runs are grouped in zenith angle bins (bin edges are [0°, 15°, 25°, 35°, 45°, 55°, 58°][8]). After the pre-selection and the application of the shape cuts (MRSW and MRSL), events are integrated, as mentioned above, within a circular region at 0.7° offset, with a radius of the size of the θ^2 cut, to determine the efficiency of this angular cut. The background efficiency is already a factor of two smaller after pre-selection, mostly due to the cut on the event multiplicity. After that, the shape-parameter cuts reject most of the remaining background events.

A common means to quantify the rejection power of analysis cuts is the *quality factor Q* defined as:

$$Q = \frac{\kappa_\gamma}{\sqrt{\kappa_{\mathrm{CR}}}}, \qquad (3.2)$$

$$\text{with} \quad \kappa_i = \frac{\hat{N}_i}{N_i} \quad (i = \gamma \text{ or CR}).$$

κ_i is the cut efficiency, defined as the ratio of events after cuts, $\hat{N}_i$, to events before cuts, N_i. Figure 3.10 shows quality factors versus zenith angle calculated from the values shown in Fig. 3.9, for the gamma-ray simulations at 0.5° offset and the off-source data background sample taken at an offset of 0.7°. Q is a factor of 4–5 larger when applying the tight θ^2 cut, but in this case the background suppression suffers at zenith angle of 50° and beyond from the afore mentioned worsening of the angular resolution. Comparing *std* to *hard*, the increased *size* cut and the tighter MRSW cut of the latter helps for the background suppression at all zenith angles. This is very clearly visible in the case of the tight θ^2 cut, where the quality factor increases by almost a factor of two. In the other case of the loose θ^2 cut, the quality factor is still ≈ 40% larger.

---

[8] Above 58° there are no observations of empty sky fields in the whole H.E.S.S. data set.

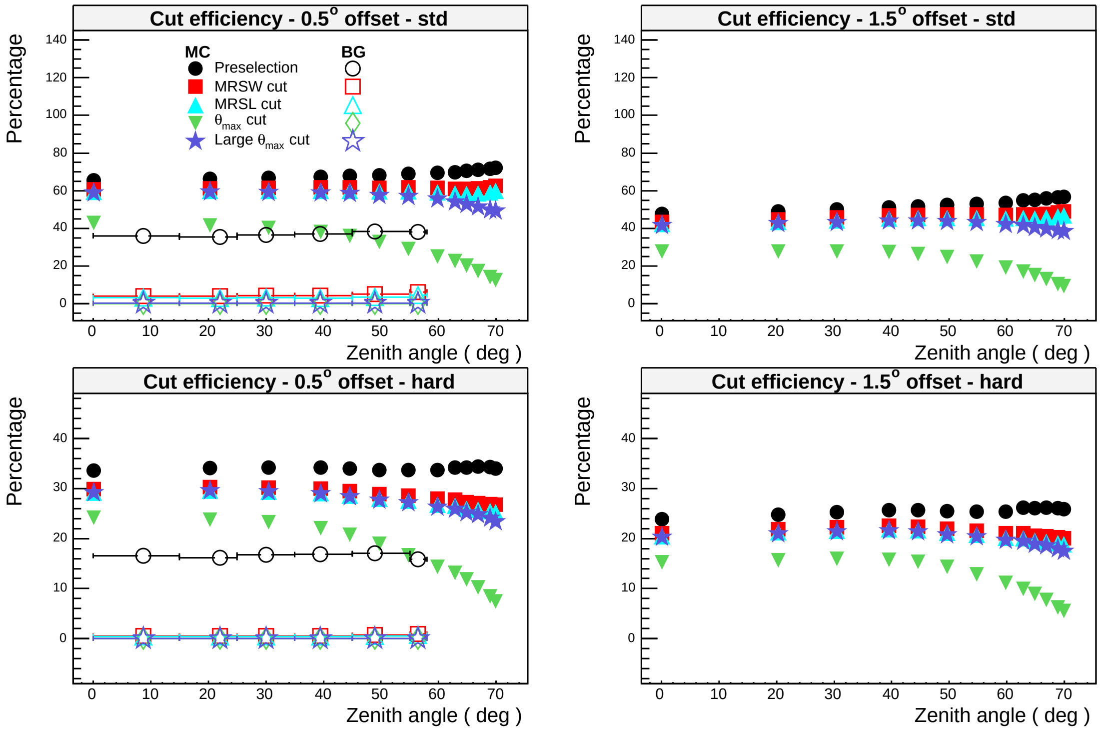

Figure 3.9: Plotted are the percentage of events retained by the different analysis cuts, as a function of zenith angle. Filled symbols always refer to gamma-ray simulations at fixed zenith angles, open symbols mark the background. These values are determined from off-source data, selected in zenith-angle bands that match simulated values. The points are always centred on the mean zenith angle of the data runs that are taken into account, the zenith-angle range is indicated by horizontal error bars. The two panels on the left-hand side are for 0.5° offset, these on the right-hand side for 1.5° offset. The upper row is for the configuration *std*, the lower for *hard*. Note the different scale, the pre-selection efficiency is a factor of two smaller after the application of the larger cut on *size*, as in *hard*.

3.4 Angular resolution

The angular resolution of H.E.S.S. depends upon observation conditions (for example the zenith angle), the analysis cuts applied, and the reconstruction algorithm. The resolution of H.E.S.S. can be quantified by means of the gamma-ray point-spread function (PSF), given by the squared angular distance (θ^2) between reconstructed and true direction of a Monte-Carlo gamma-ray point source, see Fig. 3.11a. The H.E.S.S. PSF is well described by the sum of two Gaussians. A narrow one describes the narrow central peak and a broad Gaussian accounts for the exponential tail which originates from badly reconstructed events. The commonly quoted figure for the angular resolution is the 68% gamma-ray containment radius R_{68}, the radius that encompasses 68% of the reconstructed gamma-ray directions from a simulated point source. The PSF shown in Fig. 3.11a is matched to the 2004 data set of RX J1713.7−3946 by combining simulated PSF distributions for different zenith and offset angles, weighting them suitably to match the zenith and offset angle distribution of the data set. A comparison of the θ^2 distribution from the PKS 2155−304 data

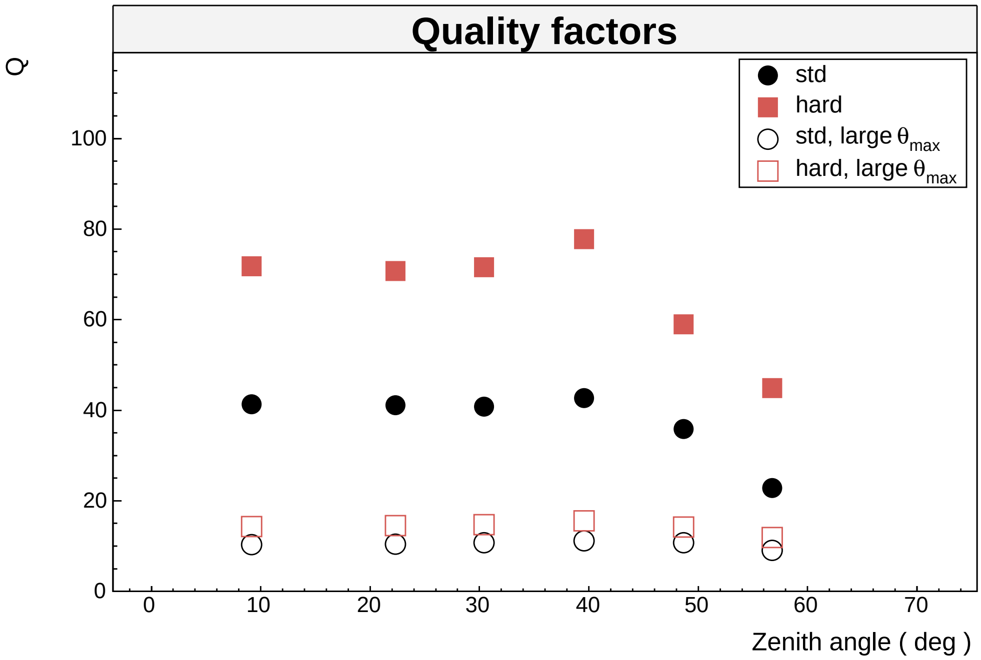

Figure 3.10: Quality factor (defined in the main text) as a function of zenith angle, for *std* and *hard*, for the tight point-source θ^2 cut and the large one for extended sources. The values for Q are determined using the background efficiencies plotted in Fig. 3.9, which are calculated for a range of zenith angles, and the gamma-ray efficiency of the zenith angle available from simulations which is closest to the mean zenith angle of the data runs used.

set, an extra-galactic gamma-ray source which is point-like for H.E.S.S., to the appropriate simulated PSF is shown in Fig. 3.11b. The agreement of the distribution demonstrates that the PSF is well understood and accurately characterised by simulations.

Dependence on zenith angle and source offset

For extended sources such as RX J1713.7−3946 (with a diameter of ≈ 1°) it is important that the PSF is well behaved and does not broaden significantly for any observation condition (for example, for all zenith angles of the observations) and for the full offset-angle range covered by the source. Figure 3.12 plots the zenith and offset angle dependence of R_{68} for different cut configurations. Comparing the *std* and *hard* cuts for the nominal cut on the event multiplicity of 2, one can clearly see how the resolution depends on the analysis cuts applied. The *hard* cuts yield superior results in all cases, R_{68} is about 25% smaller. As mentioned in Section 3.3 this is due to the increased *size* cut of 200 p.e. which selects better defined camera images than the lower cut at 80 p.e. in *std*. The zenith-angle dependence is small in both cases below 50°, the resolution worsens only slightly (by about 10%). At large zenith angles, however, mis-reconstruction effects become larger for the standard shower reconstruction algorithm that was applied here. Since the shower maxima are increasingly further away from the telescopes, images become more compact, *width* and *length* are smaller. Moreover, the Čerenkov light pool broadens. Typical impact

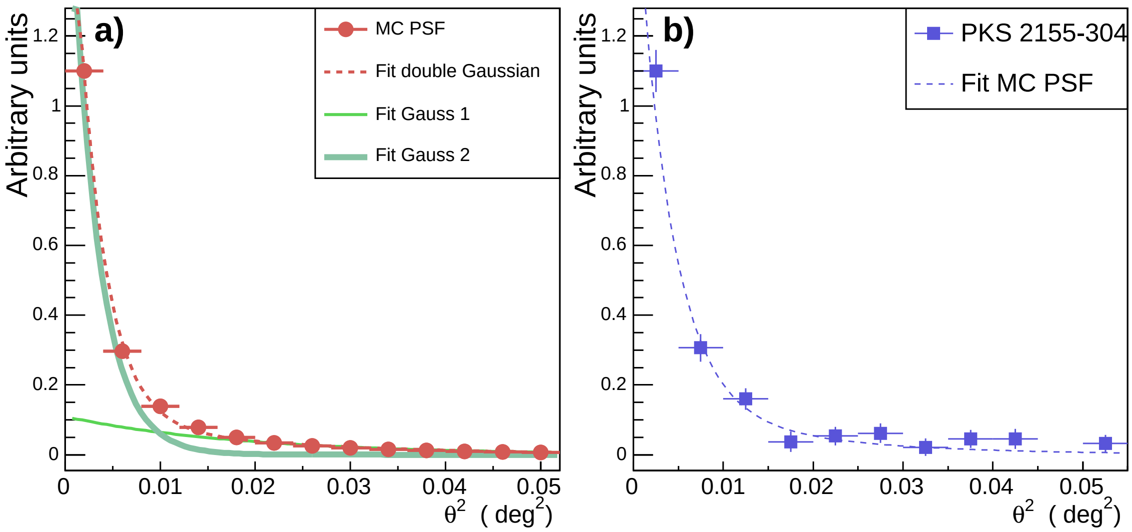

Figure 3.11: a) Gamma-ray point-spread function (PSF) obtained from simulations, matched to the 2004 data set of RX J1713.7−3946 by weighting simulated PSF histograms (for an assumed primary spectrum with $\Gamma = 2$) according to the zenith and offset angle distribution of the data. The mean zenith angle is $27°$, the mean offset angle $0.7°$. A cut on the image *size* of 200 p.e. (configuration *hard*) is applied. The θ^2 distribution (solid red circles) is plotted with the best fit of a double Gaussian (dashed red line). The two individual Gaussian resulting from the fit are also plotted. The narrow Gaussian has a width of $\sigma = 0.04°$, the broad one has $\sigma = 0.10°$. The angular resolution, given by the 68% containment radius obtained from the fit, is $0.075°$, $4.5'$. **b)** The reconstructed θ^2 distribution (solid blue squares) from the data set of PKS 2155−304 (Aharonian et al. 2005d) ($25°$ - $35°$ zenith angles), a point source for H.E.S.S., is shown. Also plotted for comparison is the fit to the simulated PSF, matched to the data set, for an assumed primary photon index of $\Gamma = 3.5$.

distances are therefore larger, images in the cameras become dimmer and smaller. Both of these effects increase the error on the image direction, the intersection point of image axes is only poorly defined. Correspondingly the angular resolution worsens, to $\approx 0.25°$ in the worst case for *std* cuts.

The offset dependence is generally weaker than the zenith-angle dependence, even at very large offsets the angular resolution is rather stable. This can also be seen in Fig. 3.13, left-hand side. For two zenith angles and both sets of cuts the angular resolution is plotted for the six different offset angles available from simulations. The PSF is rather stable, it degrades gradually with increasing offset, in fact there is almost no noticeable effect up to angles of $1.5°$. Eventually, at the maximum simulated offset angle of $2.5°$, the resolution is $\approx 0.03°$ worse than at $0°$ offset. Also indicated in the figure for orientation is the maximum offset angle of $1.35°$ under which parts of the SNR RX J1713.7−3946 were observed in the 2004 and 2005 observation campaign. It is clear that no significant variation of angular resolution occurs within this range. Figure 3.13, middle panel, illustrates the influence of the primary gamma-ray spectrum on the angular resolution. At offsets up to $1.5°$, harder spectra result in superior resolution. The reason for this can be seen in Fig. 3.13, right-hand side, where the energy dependence of R_{68} is shown. For moderate zenith and

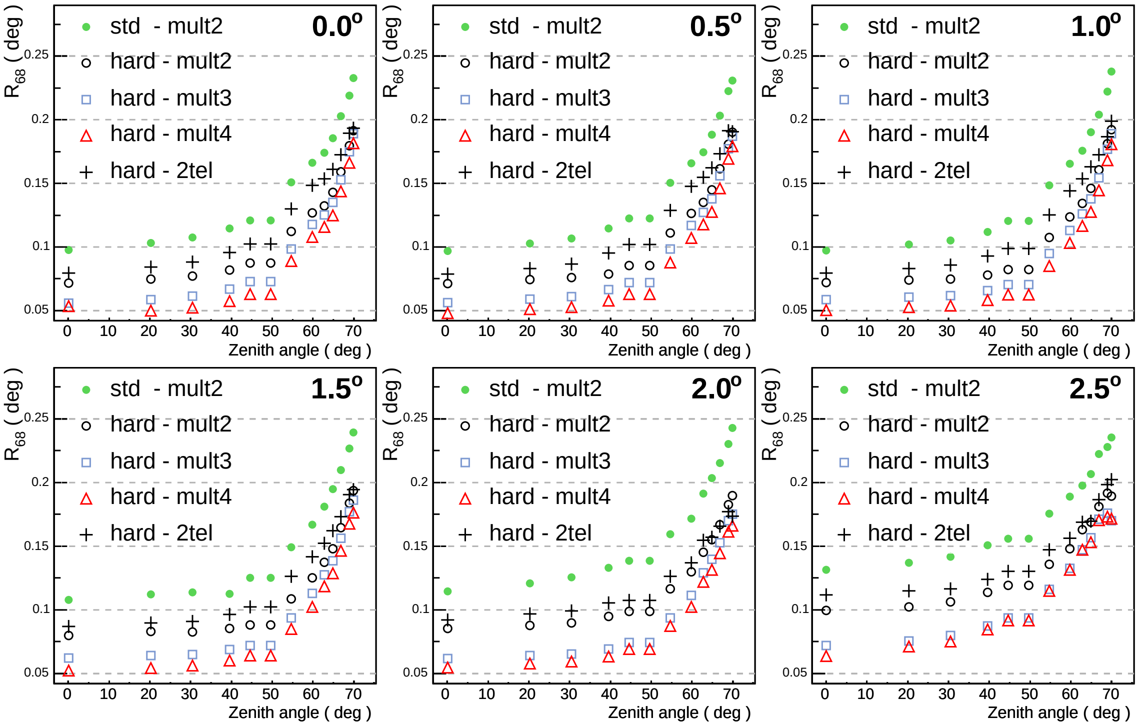

Figure 3.12: Zenith and offset angle dependence of the 68% containment radii of the gamma-ray PSF extracted from point-source simulations with a primary photon index of 2. The offset angle is given in the upper left-hand corner of each of the six plots. The values are plotted for five sets of cuts, *std* (solid green circles) with event-multiplicity 2, *hard* with event-multiplicity 2 (open black circles), with event-multiplicity 3 (open blue squares), and with event-multiplicity 4 (open red triangles). In addition, a two-telescope configuration with a *size* cut of 300 p.e. is shown (black circles) which is used later for the analysis of the 2003 RX J1713.7−3946 data set.

offset angles, the angular resolution is poor at small energies. Images have typically small *size*, therefore the image orientation is not well defined and hence the intersection point is poorly known. At larger energies, shower images contain on average more light (cf. Fig. 3.16, Section 3.5), and are therefore better defined resulting in superior resolution. For large zenith angles, the large-energy effect is noticeably weaker, the resolution improves only at very large energies due to the other effects mentioned above (small images, large core distances), which dominate the quality of the direction reconstruction. At large offsets the dependence on the primary spectrum becomes negligible (Fig. 3.13, middle), because there is almost no energy dependence (Fig. 3.13, right) of R_{68}

Dependence on cut configuration and optimum angular resolution

Referring again to Fig. 3.12, there are three more configurations shown to explore the dependence of the angular resolution on analysis cuts and system configuration in more detail. The configurations labelled “hard - mult3” and “hard - mult4” differ from the *hard* cuts by the event multiplicity (at least 3 and 4 telescopes per event, respectively).

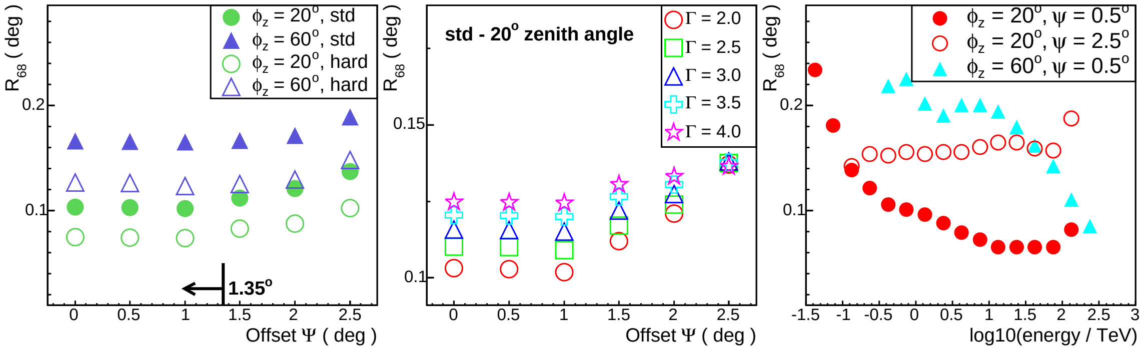

Figure 3.13: Plots to illustrate dependencies of the PSF on the offset angle are shown.**Left:** For an assumed simulated spectrum of photon index $\Gamma = 2.0$, R_{68} is plotted for one moderate and one large zenith angle, for both sets of cuts. The maximum offset of observations of RX J1713.7−3946, 1.35°, is indicated by an arrow. **Middle:** R_{68} versus offset angle for different primary input spectra. The PSF distributions for different photon indices have been generated from $\Gamma = 2$ simulations by weighting events based on their simulated energy. Note that the y-axis is zoomed compared to the other two plots. **Right:** R_{68} as a function of the logarithm of the energy. Plotted are two curves at a zenith angle of 20°, one for 0.5°, one for 2.5° offset, and one curve for 60° zenith angle, 0.5° offset.

“hard - 2tel” is a special configuration to be used later for the two-telescope data of RX J1713.7−3946 recorded during the construction and commissioning phase of H.E.S.S. in 2003 (see also Table 3.1). For this configuration, only two simulated telescopes are used corresponding to the two telescopes in full operational mode during 2003. Moreover, a cut on the *size* at 300 p.e. is applied. A drastic increase in angular resolution for the *hard - mult3* configuration is seen in the figure. At moderate zenith angles, for all offsets, the 68% containment radius is 20-25% smaller than for the nominal *hard* cuts. This is an effect of both the usage of more information for the reconstruction, one always uses at least three camera images, and of event selection. The requirement of at least three telescopes triggering on a Čerenkov shower effectively leads to on average smaller impact distances, preferentially showers move in reducing the error of the geometrical reconstruction – camera images are closer to the source location. The general zenith-angle dependence, however, is very similar, at large zenith angles of 55° and beyond the angular resolution worsens considerably. In comparison, the additional requirement of four camera images per event, as in *hard - mult4*, increases the angular resolution not as dramatically, there is an ≈ 10% effect apparent in Fig. 3.12. In case of *hard - 2tel* it can be seen that the angular resolution depends as expected on zenith and offset angle, it basically follows the behaviour of the *hard* cuts. The net effect of the larger cut on *size* and the smaller mean event multiplicity – in case of *hard - 2tel*, the multiplicity is exactly 2, for *hard* it is ≈ 2.5 for small zenith angles and exceeds 3 for large zenith angles – is that the resolution is 10%–15% worse.

For an extended gamma-ray source the angular resolution governs to which degree details of the morphology can be resolved. Hence, when seeking the optimum cut configuration one has to deal with two competing effects. One is purely related to the PSF. Only image structures that are separated by a certain fraction of the PSF can possibly be resolved.

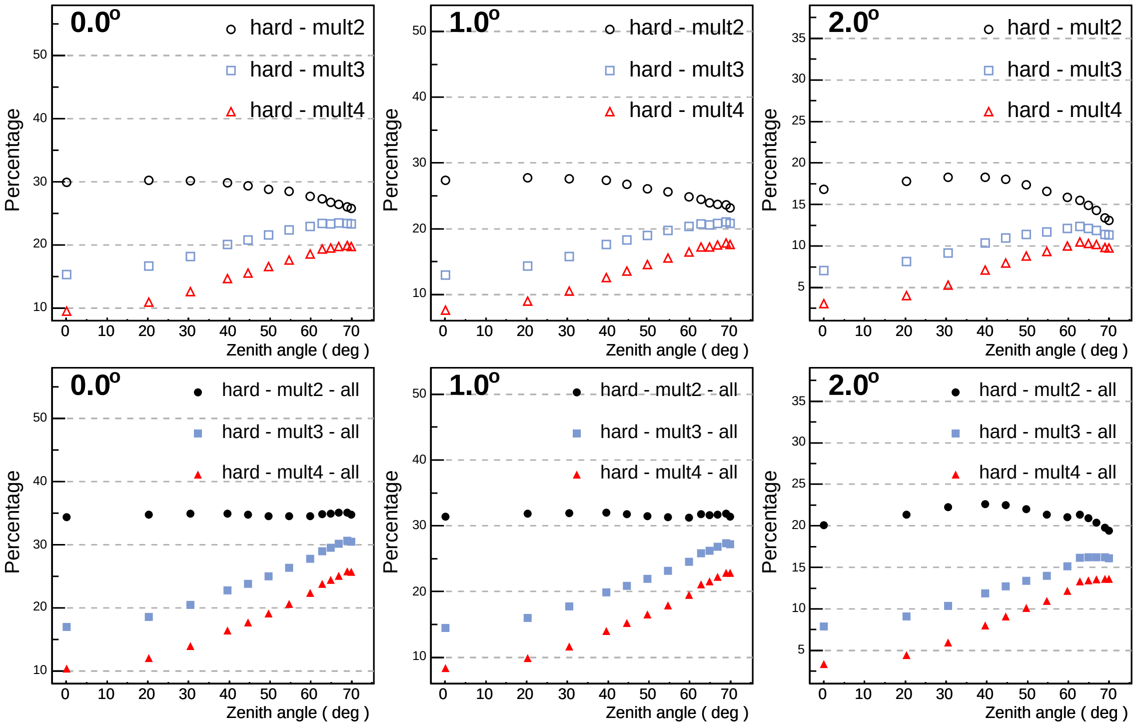

Figure 3.14: Cut efficiencies are shown for three simulated offset values for the three configurations with the best angular resolution (cf. Fig. 3.12: *hard* with multiplicity 2, 3, and 4). **Upper panel:** The fraction of events retained by the shape cuts is shown, plotted versus zenith angle. **Lower panel:** The fraction of events retained by the pre-selection is shown for comparison to disentangle effects of shape-cut efficiency (only included in the upper panel) from effects of event multiplicity. The mean event multiplicity increases with zenith angle, from ≈ 2.5 at zenith to more than 3 for very large zenith angles. Hence, the cut efficiency for *hard - mult3* and *hard - mult4* increases, too.

For this reason the 68% containment radius of the PSF is chosen as figure for angular resolution here. The other one is related to the available event statistics, the error on the measurement must be sufficiently small otherwise relative intensity differences between two adjacent sky positions are dominated by fluctuations. These two effects are competing in the sense that tightening cuts might result in increasingly better angular resolution, but it also leads to a reduction of events passing these cuts and remaining for analysis thereby increasing the fractional statistical error at each sky position. In Fig. 3.12 one can see that *hard - mult4* yields optimum angular resolution. Figure 3.14 shows the cut efficiencies of three configurations, the *hard* cuts with event multiplicity 2, 3, and 4, which are shown in Fig. 3.12, too. In the upper panel the fraction of events retained by all cuts up to the shape cuts is shown[9]. The increase in angular resolution for *hard - mult3* and *hard - mult4* goes along with a clear decrease of efficiency compared to *hard - mult2*, the nominal cut configuration for image generation. With increasing zenith angle the fraction of events

---

[9] This means that the number of events passing pre-selection and shape cuts, divided by the total number of events that triggered the array, are shown. This is the fraction of events that are available for further analysis of image morphology.

passing cuts increases, too. This is due to the increasing mean event multiplicity. For larger zenith angles, the radius of the light pool is larger, making it more likely that multiple telescopes are illuminated. For illustration the lower panel of Fig. 3.14 shows the fraction of events retained by the pre-selection, which (well beyond threshold) consists basically of the multiplicity cut. One can clearly see the increase of the efficiency with zenith angle for *hard - mult3* and *hard - mult4*. The pre-selection efficiency of *hard - mult2* remains basically unchanged because of the hardware-level multiplicity-2 trigger (plotted is in all cases the number of events after a certain analysis cut divided by the total number of events that triggered the telescope array). Note that the turnover of the efficiency in the upper panel for very large zenith angles beyond 60° is due to a worsening of the shape-cuts efficiency. At large zenith angles and more noticeably large offset angles, the MRSW and MRSL distributions of simulated gamma rays tend to be broader and more asymmetric (as shown in Fig. 3.6).

In summary, the best compromise is achieved with the configuration *hard - mult3*, which results in significantly better angular resolution compared to *hard - mult2*. The additional gain in resolution with *hard - mult4* is not so pronounced that it would balance the corresponding decrease in event statistics.

Comparison with the advanced reconstruction method

A possibility to overcome the drastic worsening of the angular resolution at large zenith angles is the inclusion of more image information for the shower reconstruction. The alternative reconstruction method discussed in Section 3.1 includes errors on image parameters and in addition an estimate of the distance between COG and the source image thereby accounting for poorly defined images which occur frequently during large-zenith angle observations. In Fig. 3.15 the angular resolution of this method (labelled “ALG3” since it is based on *algorithm 3* of Hofmann et al. (1999)) is explored in comparison to the standard geometrical reconstruction. Shown is a comparison of two configurations, *hard - mult2* and *hard - mult3*. Already for small zenith angles the inclusion of additional image information increases the resolution. For zenith angles beyond 50° a pronounced effect is apparent. There is a clear gain in resolution. The worsening proceeds smoothly with increasing zenith angle, for the geometrical as well as for the advanced shower-reconstruction method, but much less dramatic in case of the latter. Note that even at large zenith angles there is still room for improvements with the algorithm-3 type reconstruction. So far error estimates on the resulting reconstructed direction, readily available in this approach, are not used. They provide further means to select only well reconstructed events by applying a cut on the directional error. This possibility, however, is not pursued here.

3.5 Energy reconstruction

The primary energy of incident particles is reconstructed from shower images assuming that all particles are gamma rays. One makes use of the fact that for a certain type of primary particle, for a given zenith and offset angle, the density of Čerenkov light created in the air shower at a fixed distance to the shower axis is approximately proportional to the primary energy. As for the image shape parameters discussed above, the energy

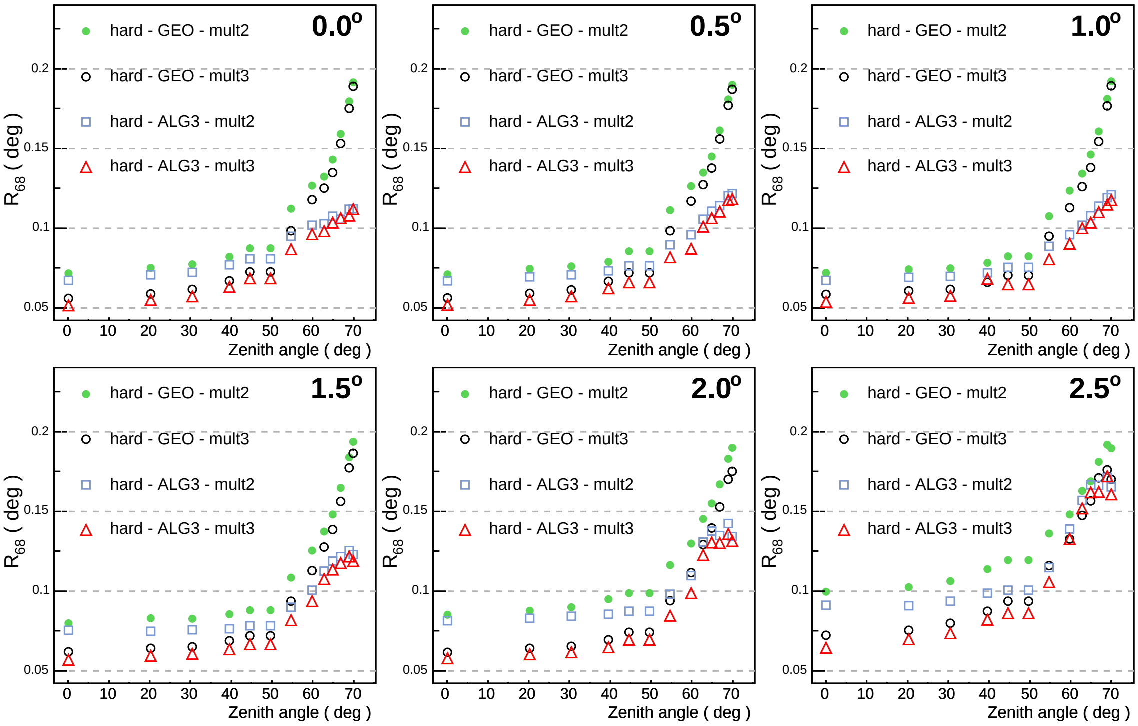

Figure 3.15: Similar to Fig. 3.12, but now comparing the standard geometrical to the advanced, algorithm-3 type reconstruction that takes error estimates of image parameters into account. Note that the angular resolution in both cases is generated using the same events passing shape cuts. The shower impact position on ground, used for the lookup of shape parameters, is reconstructed with the geometrical method only.

reconstruction utilises lookup tables generated from Monte-Carlo gamma-ray simulations. For fixed offset and zenith angles, event energies is averaged in bins of reconstructed image amplitude and simulated impact distance (distance between a telescope and the shower axis). Note that here the simulated impact parameter is used, as opposed to the lookup tables for *width* and *length*, which are filled using the reconstructed impact parameter. The reason for this difference is the much larger dependence of mean energy on impact distance. Therefore mis-reconstruction effects are much more crucial here and it proved more appropriate to use the true Monte-Carlo information when filling the lookup tables. The measurement effect – the finite resolution of the core reconstruction – is thereby separated from the lookup tables. Besides the average energy, also the RMS spread in each impact-parameter and *size* bin is stored in lookup tables to obtain an error estimate for this bin. Note that the tables are filled separately for each telescope. If there were no differences between simulated telescopes, only one table would be sufficient. However, as mentioned in Section 2.3.2, the simulated optical efficiencies of the telescopes are different accounting for the different times of installation of the telescopes on site and hence the degree of optical degradation.

During analysis, the energy reconstruction proceeds along the same lines as that for the image shape parameters. Given a reconstructed event–zenith angle and offset (reconstructed using all the telescopes that participated in the event), an energy estimate is obtained for

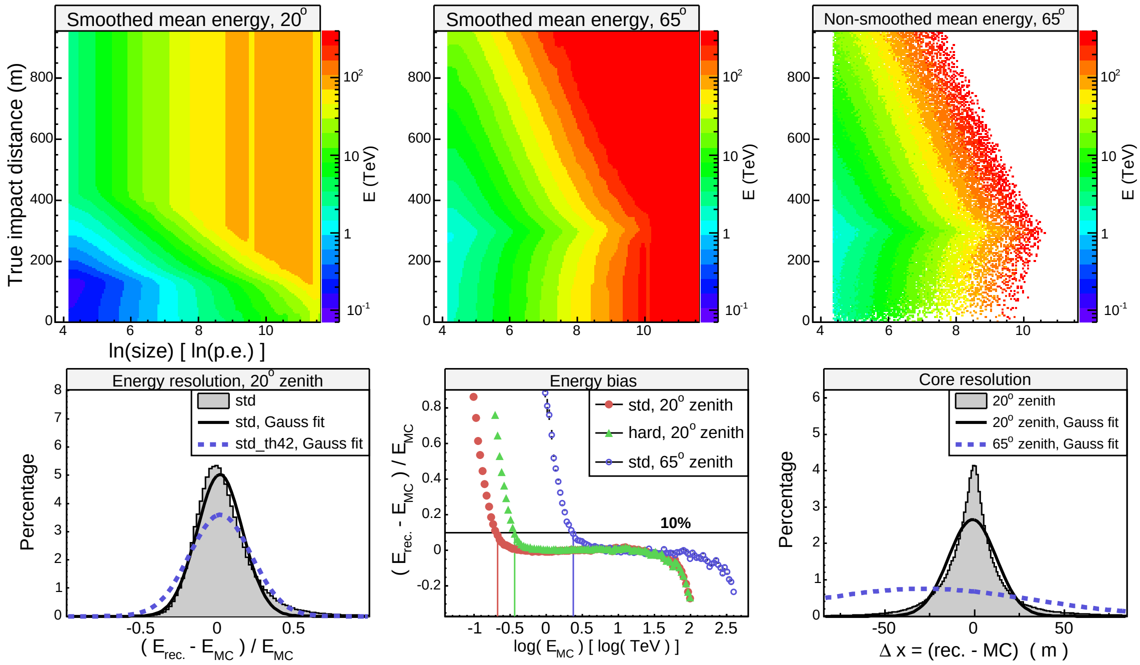

Figure 3.16: In the **upper row**, smoothed energy lookup tables are shown as they are used for the energy reconstruction (left and middle plot). They are generated from simulations at zenith angles of 20° and 65°, respectively, and an offset angle of 0.5°. The right-hand plot shows the non-smoothed 65° table. All three tables have the same colour scale in units of mean simulated gamma-ray energy in TeV. In the **bottom row**, the left-hand plot shows the relative error of the energy reconstruction, for a zenith angle of 20° and an offset of 0.5°. The dashed blue curve was obtained with the increased θ^2_{max} cut. The bottom middle plot shows the bias of the energy reconstruction. Two zenith angles are plotted for *std*, one for *hard*. The vertical lines indicate the energy values at which the energy bias falls below 10% (0.21 TeV, 0.37 TeV, and 2.37 TeV from left to right). The bottom right-hand plot shows the resolution of the reconstructed shower impact distance on ground for one telescope for *std* cuts. Plotted are the histogram and the best-fit Gaussian of 20° ($\sigma \approx 13$ m), and the best fit of 65° zenith angle ($\sigma \approx 60$ m).

each telescope: taking the reconstructed *size* and impact parameter, four energy values are obtained from the lookup tables of the closest simulated zenith and offset angles. The telescope energy is then obtained by interpolating the offset and the cosine of the zenith angle linearly between the four available bounds. The same procedure is followed for the error on the energy, σ_{E}. Subsequently, the energy estimates from all participating telescopes are averaged, weighted by $1/(\sigma_{\mathrm{E}})^2$, to yield the energy of the event. Note that the offset dependence of the energy reconstruction is much less pronounced since the only measured parameter involved when filling the lookup tables is the image *size*, which depends only very weakly on the offset. However, for consistency reasons, the same procedure is applied for the energy reconstruction as it is applied for the shape-parameter reconstruction. Therefore, the offset is also interpolated here.

Representative lookup tables are shown in Fig. 3.16, upper panel. The tables are filled from gamma-ray simulations for one telescope at 20° and 65° zenith angle, both at an offset of 0.5°. As for the shape parameters, the lookup tables are smoothed to reduce the effect of statistical fluctuations. In the x-direction, a Gaussian with $\sigma = 0.07\ \ln(p.e.)$ is used, in the y-direction $\sigma = 10$ m. Moreover, the extension procedure is applied up to the largest impact distances, too. The resulting lookup tables reveal features of the shower physics already discussed in Section 2.1. Within the Čerenkov light pool the density of Čerenkov photons is approximately constant for fixed primary energy and zenith angle. The table for 20° zenith angle (Fig. 3.16, top left) shows therefore almost no impact-parameter dependence of the energy within ≈ 150 m, only with increasing image *size* is there an increase in energy apparent. Once beyond the Čerenkov shoulder (at ≈ 130 m for 20° zenith angle), the impact-parameter dependence is much stronger, the mean energy rises steeply with increasing distance between the shower axis and the telescope for fixed image amplitude. The 65° zenith-angle table (Fig. 3.16, top middle) looks somewhat different, as expected from the zenith-angle dependence of the Čerenkov light-cone radius on ground, discussed in Section 2.1.3. The energies are on average much larger, showers further away still trigger the telescope system, and the Čerenkov light-pool radius is larger, close to 300 m (cf. Section 2.1.3, Fig. 2.6). Moreover, the Čerenkov shoulder is clearly visible, beyond it the energies do not rise as steeply as for moderate zenith angles.

The relative error in reconstructed energy $\Delta E/E \equiv (E_{\mathrm{rec.}} - E_{\mathrm{MC}})/E_{\mathrm{MC}}$ is plotted in Fig. 3.16, bottom left-hand side. The plot was produced processing the same simulations that were used for the filling of the lookup tables. The distribution is well centred around zero and slightly asymmetric in shape with a tail to positive values. There is reasonable agreement with a Gaussian, a fit (also plotted) yields a resolution of 15% for the configuration *std* (20° zenith angle, 0.5° offset). When applying the loose θ^2 cut of $(0.65°)^2$, as used for RX J1713.7−3946 in Chapter 4, badly reconstructed gamma-ray events are not rejected and the energy resolution correspondingly worsens, to 20% in this case. The best-fit Gaussian, also plotted in Fig. 3.16, is clearly broader.

Energy bias curves, that is, the mean fractional error of the energy reconstruction as a function of simulated energy, are shown in Fig. 3.16, bottom row (middle). At small energies there is an unavoidable positive bias, reconstructed energies are overestimated due to a selection effect: only small-energy showers that fluctuate upward remain in the analysis and are filled into the lookup tables, the others are rejected by the *size* cut (or do not even trigger the system)[10]. Correspondingly these small-energy showers end up in *size* bins in the tables that are dominated by showers of larger energies. Therefore, the reconstructed energy in that bin will always be larger resulting in a positive bias[11]. Far beyond threshold the bias becomes negligible. Also shown in Fig. 3.16 are vertical lines at energies where the bias falls below 10%. This criterion will be used for the threshold of spectral analyses presented later. Note how the application of a larger cut on *size*, as in the configuration *hard*, results in an increased energy threshold. The threshold is also increased in case of large zenith-angle observations, much more dramatically though. At large zenith angles the longer distance to the shower maximum leads automatically to a decrease of the photon density in the light pool on the one hand, on the other hand

---

[10] Even without any *size* cut there would be a selection effect due to the trigger threshold of the system

[11] Note that exactly the opposite happens at very large energies. Since the simulated energy range is restricted, only downward, no upward fluctuations appear when approaching the upper end of the energy range causing a negative bias.

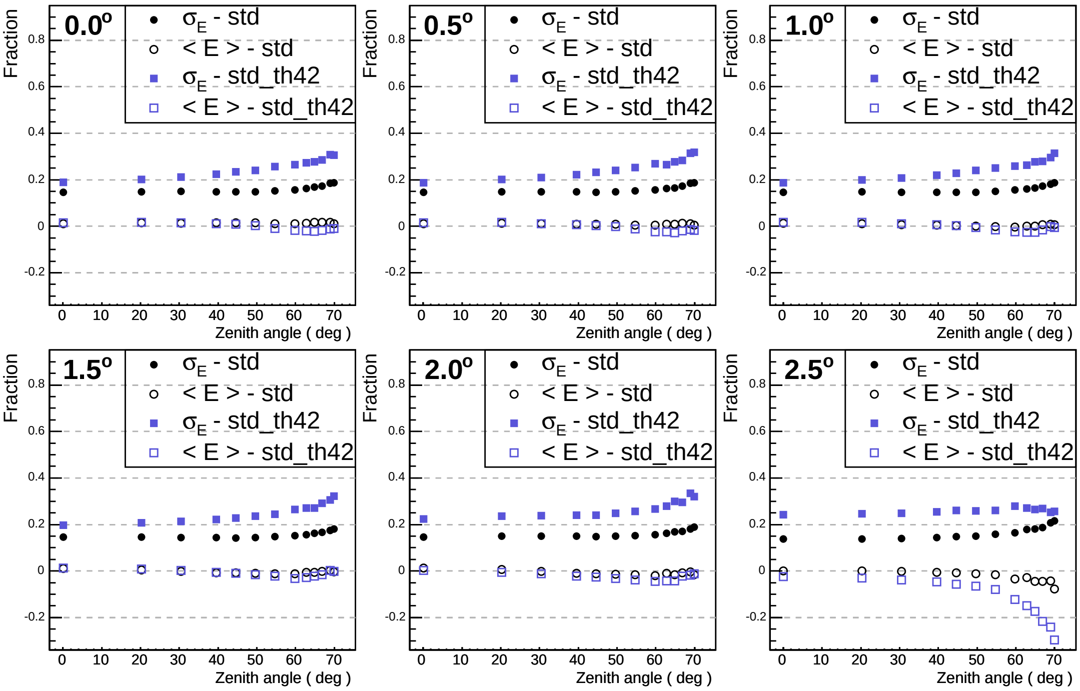

Figure 3.17: Energy resolution and mean bias are shown versus zenith angle for the six simulated offset angles. The plotted values are the mean value and width of a Gaussian fit to the distributions of relative reconstruction errors (as shown in Fig. 3.16, bottom left-hand plot). The extension "_th42" denotes the case of the larger θ^2 cut of 0.42 $(\mathrm{deg})^2$.

the showers are observed through a much greater atmospheric column depth. Čerenkov photons from such showers suffer more from scattering and absorption and have a larger and dimmer footprint on ground. As consequence, the effective energy threshold of the system is increased.

Also shown in Fig. 3.16, bottom right-hand side, is a plot of the deviation of the reconstructed from the simulated impact distance for one telescope. This distribution is important for the energy reconstruction because the impact distance is used for the lookup to determine the energy of an event. For a moderate zenith angle of 20°, *std* cuts, a resolution of 13 m (Gaussian σ) is achieved. The best-fit Gaussian at 65°, overlaid in the figure, is, compared to the moderate zenith angle, very broad and shifted towards negative values, the resolution is relatively poor, 65 m. However, the lookup table for this zenith angle plotted in the upper row reveals that the dependence of the primary energy on impact distance is less dramatic than at small zenith angles, since the light-pool radius is rather large. Larger errors on the reconstructed impact distance are thus tolerable, as can also be seen from the bias curve in the bottom-middle panel. Even at 65° zenith angle this curve is well behaved, for a large energy range the reconstructed is well compatible with the simulated energy.

The zenith-angle dependence of the energy reconstruction is shown in Fig. 3.17. For the configuration *std*, the energy resolution for most zenith angles is stable and close to 15%, only for very large zenith angles of 55° and beyond the resolution starts to approach 20%

due to the worsening of the core resolution at these large zenith angles. The average bias is always very close to 0. When applying the larger θ^2 cut, the energy resolution worsens slightly, at small zenith angles it is $\approx 20\%$, at very large zenith angles it exceeds 30%. This is again an effect of mis-reconstruction of the shower geometry.

3.6 Background modelling

One of the (if not *the*) major source of systematic errors for IACT telescopes is the subtraction of background from non-gamma-ray induced air showers. Only in the case of an incorrect background subtraction, apart from miscounting of statistical trial factors, may an apparently significant gamma-ray source appear from background fluctuations. As was described in detail in Section 3.3, the application of image shape cuts reduces dramatically the number of background events (by a factor of ≈ 100), but they cannot be removed completely. The remaining background stems mostly from hadronic cosmic-ray showers, at low energies up to a few hundred GeV cosmic-ray electrons contribute as well.

For single telescope instruments such as the Whipple observatory (Weekes et al. 1989) the classical approach to background subtraction was the *ON/OFF* observation mode: Observation runs centred on the targeted source (the *ON* runs) are interspersed with equal length observations of an empty sky field (the *OFF* runs) offset by 30 minutes in Right Ascension, at equal zenith angle. The OFF runs are obtained with a similar level of NSB over the field of view. The difference between the two runs is then a measure for the gamma-ray signal. The main disadvantage of this method is the need for spending half of the available observation time off-source. The *wobble* observation mode overcomes this downside by keeping the targeted source in the field of view at all times, positioning the centre of the source at alternating offset angles from the pointing direction of the telescope (system). If the offset angle is chosen such that the actual observation position of each run lies outside the assumed source region, a background estimate for this region can be derived from the opposite side of the field of view to the target source.

Before the advent of high-sensitivity instruments with wide fields of view like H.E.S.S., background subtraction was mainly pursued in a one-dimensional way. The significance of a gamma-ray signal from an a priori chosen source region was determined by estimating the background from a different region of sky with presumably the same background rate[12]. With the wide field of view of H.E.S.S., however, this approach is not satisfactory any more. It is desirable to model and subtract the background of the whole field of view to search for unknown gamma-ray sources, for example in survey-type observations (Aharonian et al. 2005b,e), and to study the morphology of extended gamma-ray sources such as RX J1713.7−3946.

Following this motivation, methods for two-dimensional background modelling have been developed for extraction of gamma-ray spectra and morphology from the RX J1713.7−3946 data set of H.E.S.S. and will be presented in the following.

---

[12] This is called a *one-dimensional approach* because the significance of a signal is tested only at one position in the sky.

3.6.1 Signal extraction

In order to extract the significance of a possible gamma-ray signal, the background of gamma-ray like events passing analysis cuts must be estimated. Given a number of counts N_{on} in a test region and N_{off} background counts, the gamma-ray excess N_{excess} is defined as $N_{\mathrm{excess}} = N_{\mathrm{on}} - \alpha\, N_{\mathrm{off}}$. The parameter α is the normalisation factor. It accounts for solid-angle, exposure-time, zenith-angle, and acceptance differences between the test region and the background control region[13]. It can generally be defined as:

$$\alpha = \frac{\int_{\mathrm{on}} \epsilon^{\gamma}_{\mathrm{on}}(\theta_x, \theta_y, \phi_{\mathrm{z}}, t)\, \mathrm{d}\theta_x\, \mathrm{d}\theta_y\, \mathrm{d}\phi_{\mathrm{z}}(t)}{\int_{\mathrm{off}} \epsilon^{\gamma}_{\mathrm{off}}(\theta_x, \theta_y, \phi_{\mathrm{z}}, t)\, \mathrm{d}\theta_x\, \mathrm{d}\theta_y\, \mathrm{d}\phi_{\mathrm{z}}(t)}\,. \tag{3.3}$$

$\epsilon^{\gamma}_{\mathrm{on,off}}$ is the system acceptance of gamma-ray like events. It depends on the position (θ_x, θ_y) in the field of view and on the zenith angle ϕ_{z} of observations. Additionally, different exposure times t for ON and OFF region have to be taken into account.

The statistical significance S of the gamma-ray excess is typically calculated following the prescription of Li & Ma (1983):

$$S = \sqrt{2}\left(N_{\mathrm{on}}\, \ln\left(\frac{(1+\alpha)N_{\mathrm{on}}}{\alpha(N_{\mathrm{on}} + N_{\mathrm{off}})}\right) + N_{\mathrm{off}}\, \ln\left(\frac{(1+\alpha)N_{\mathrm{off}}}{N_{\mathrm{on}} + N_{\mathrm{off}}}\right)\right)^{1/2}\,. \tag{3.4}$$

Any background model must provide N_{off} and α so that one can calculate a significance or find the gamma-ray excess morphology at any point in the sky. A choice of background regions such that $\alpha \ll 1$ results in general in higher statistical significance, but may also increase the systematic error. The principle difficulty in deriving a background estimate is to find the correct value of α.

3.6.2 H.E.S.S. cosmic-ray acceptance after gamma-ray cuts

The system acceptance is conventionally defined as the detector response to gamma-ray like events, that is, events passing all analysis cuts except for the θ^2 cut. For most background models some knowledge of the system acceptance is required to generate an excess sky map or calculate significances of arbitrary positions in the field of view (cf. eq. 3.3). In general the acceptance depends on the zenith angle of observations ϕ_{z} and on the azimuth ϑ_{az} (due to the influence of the Earth's magnetic field on the shower development in the atmosphere), on the primary energy, and on the position in the field of view. It is nevertheless in most cases a reasonable assumption that the acceptance is approximately radially symmetric (this notion will be reassessed later). The acceptance can be determined on a run-by-run basis from the data set to be analysed, facing the problem of possible gamma-ray contamination by a source, or be extracted from OFF runs, maybe encountering the problem that the data and OFF run acceptances are not equal. For the purpose of the analysis of the extended strong gamma-ray source RX J1713.7−3946, 220 live hours of H.E.S.S. observations without gamma-ray sources in the field of view are used to obtain

---

[13] The term "background control region" must be understood in a general sense. It can refer to a different region of sky within the same field of view, or to a region of sky in a different field of view. Moreover, background events could be accumulated in many different regions of sky, or stem from the same region, but from a different parameter-space region.

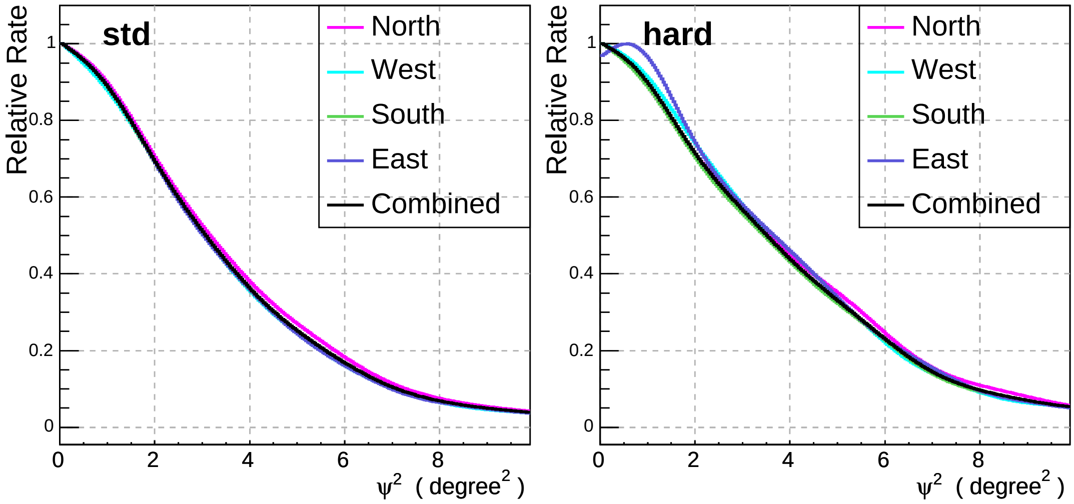

Figure 3.18: Illustration of the weak azimuth dependence of the system acceptance of H.E.S.S.. Shown are radial acceptance curves for *std* and *hard* cuts, split up into four azimuth ranges corresponding to north, south, east, and west. The curves are produced from OFF runs taken at zenith angles between 20° and 30°.

a model of the radial system acceptance. These reference observations are sub-divided into zenith-angle bands. Events passing gamma-ray cuts are then binned according to the squared angular distance between the reconstructed event direction and the system's pointing direction. Figure 3.18 shows a few of these curves obtained by smoothing the one-dimensional histograms. To explore the azimuth dependence of the system acceptance, runs taken at zenith angles from 20° to 30° are sub-divided into four azimuth bins corresponding to north, south, east, and west. It is apparent from the figure that for both sets of cuts used here, variations around the combined model curve are only marginal. In case of *hard* cuts the deviations appear to be somewhat larger, but within the available statistics there is no significant difference. Therefore, during further analysis, any azimuth dependence will be neglected, model curves used will always depend only on zenith angle.

Figure 3.19 shows the zenith-angle dependent variation of the shape of the radial system acceptance extracted from the OFF data set. The general characteristics of the system acceptance are rather independent of the exact cuts applied or the zenith angle of observations: it exhibits a shallow peak in the centre and drops off rapidly towards larger distances. 2° away from the system centre, the gamma-ray acceptance for moderate zenith angles has decreased to 20% - 50% of the peak value, depending on analysis cuts. This is an effect of geometry, the larger the inclination angle between shower axis and pointing direction, the smaller is the probability for the shower to be detected by at least two telescopes. Apart from that, there is a smooth variation with zenith angle apparent independent of the exact set of cuts applied. With increasing zenith angle, the system acceptance broadens, an increasing fraction of events with directions further away from the system pointing direction is detected. This is a direct consequence of the fact that with increasing zenith angle the average impact distance increases, i.e. showers further away from the telescope array can produce a trigger. When comparing the average curve for any given zenith-angle band to the radial acceptance in different fields of view, observed at the same altitude, the scatter is relatively small, less than 3% within 1° of the observation position and less than 10%

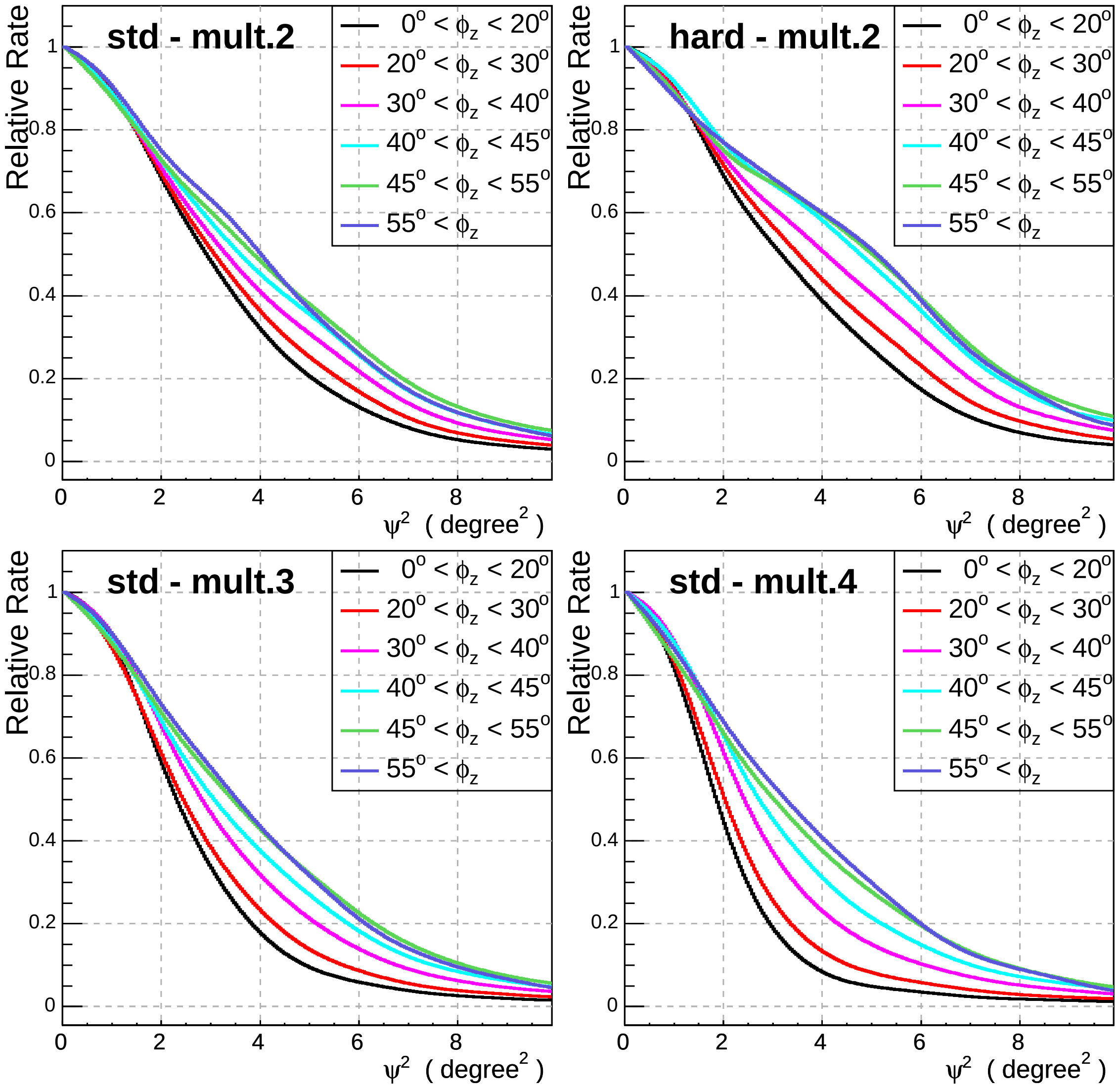

Figure 3.19: Plot to illustrate the variation of the radial system acceptance function with zenith angle, for different sets of cuts. The two standard cut configurations, *std* and *hard*, are shown in the upper panel. The lower panel shows acceptance functions for *std* cuts, increasing the cut on the event multiplicity to 3 (left) and 4 (right).

out to 3°. It is therefore well justifiable to use OFF data taken in different fields of view to determine the system acceptance.

A characteristic feature of the system acceptance, more pronounced at large zenith angles, is the presence of *steps*. These steps are an artefact of the linear offset interpolation applied to obtain the image-shape parameters MRSW and MRSL. They occur around the fixed offset values that are available from simulations and are due to not strictly linear dependence of the image parameters *width* and *length* (and their typical fluctuations) on the offset angle. There is thus a slight change of cut efficiency in transition regions from one offset-angle bound to the next. However, as long as this effect can be parametrised,

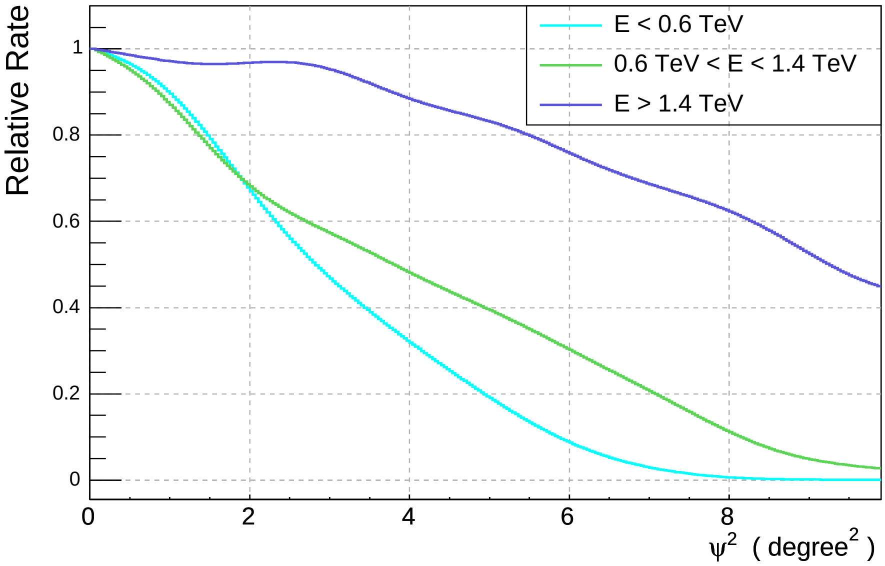

Figure 3.20: The energy dependence of the system acceptance is demonstrated. For the three different energy bands shown, the shape of the acceptance broadens dramatically with increasing energy.

that is, as long as the exact shape of the system acceptance is known, there will be no artifacts in the final background-subtracted sky maps.

The influence of analysis cuts is also apparent in Fig. 3.19. In the upper panel the *std* and *hard* cuts are compared. The application of a larger cut on the minimum *size* results in acceptance curves which exhibit generally a less pronounced peak, the decline towards large distances is less rapid, i.e. more events with larger distances to the system pointing direction are detected. The situation changes when applying a higher cut on event multiplicity, as is shown in the bottom panel of Fig. 3.19, where curves for a multiplicity of 3 and 4 telescopes are shown. In this case, the curves are more peaked towards small angular distances, which is again a phase-space effect caused by the geometry of the mapping process: the larger the required event multiplicity, the more are the shower impact points on ground concentrated to small distances to the array centre. Therefore, small offset angles with respect to the pointing direction are favoured.

The considerations so far were mainly governed by the need to model and subtract the background at any position in the field of view to extract the total significance of a possible signal. For the generation of gamma-ray energy spectra, the situation is more complicated. The energy dependence of the system acceptance is generally much stronger than the zenith angle dependence, greatly complicating the use of background models that require an acceptance correction for spectral analysis. Figure 3.20 illustrates the energy dependence for a zenith angle range from 0°to 20°. Curves are shown for three different energy bands, $E < 0.6$ TeV , 0.6 TeV $< E <$ 1.4 TeV, and 1.4 TeV $< E$ (used later on for the analysis of the morphology of RX J1713.7−3946). For relatively small energies the acceptance declines rapidly with increasing offset. For large energies the shape is completely different. Again due to increasingly larger shower impact distances with increasing energy, showers with large inclination angles start to trigger the array more often, the acceptance becomes

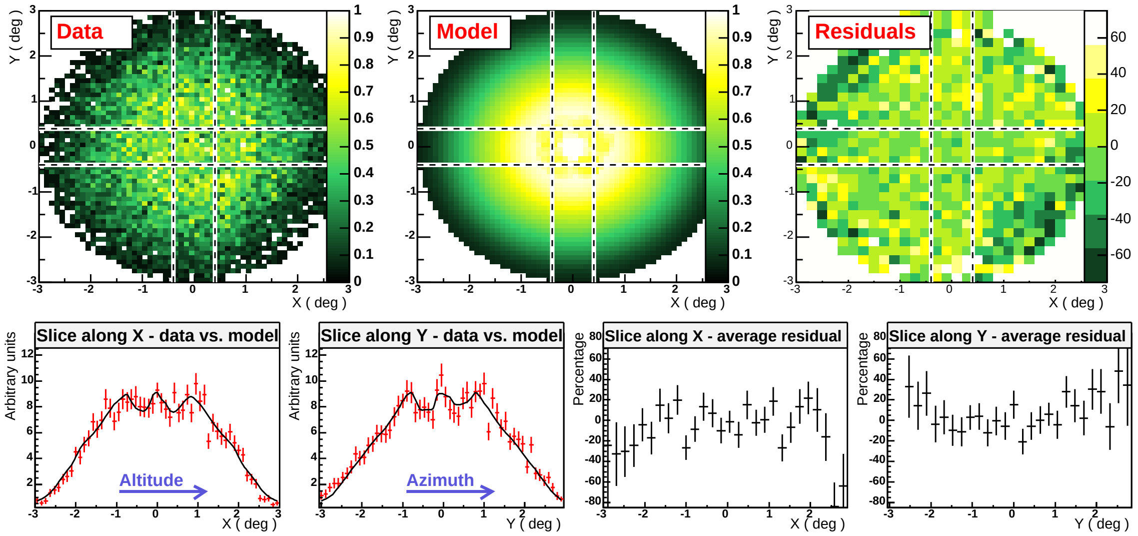

Figure 3.21: Plots of the system acceptance are shown extracted from observations of SN 1006, compared to the radially symmetric model acceptance determined from OFF runs. **Upper panel:** Plots labelled "Data" and "Model" are the (arbitrarily normalised) acceptances determined in the nominal system on a run-by-run basis, excluding the region around the presumed source centre, as explained in the main text. Positive x-direction corresponds to positive altitude, positive y-direction to positive azimuth. The values in the residuals plot are $100 \times (data_i - model_i)/model_i$ in each bin i (i.e. the deviations of the data from the model acceptance in percent). The parallel horizontal and vertical lines define bands (0.8° wide) used to produce slices for a one-dimensional comparison, shown in the **lower panel:** The two plots on the left show projections along x and y through data (red crosses) and model map (black lines) within the thick bands indicated in the upper panel. The shape of the distributions is governed by the exclusion of the source region during data taking. The two plots on the right-hand side show profiles along x and y in the residuals map. Bin contents are the average deviation of the data from the model acceptance in percent.

almost flat out to a distance of 2° to the system pointing direction for energies beyond 1.4 TeV.

Deviations from radial symmetry and gradients

In order to explore the ad hoc assumption that the system acceptance is radially symmetric, the accordance of such a symmetric model acceptance derived from OFF data with the gamma-ray acceptance of single data sets can be checked. For that purpose, reconstructed directions of gamma-ray like events of a given data set are plotted in a coordinate system centred on the system pointing direction in the "altitude-azimuth" (*alt-az*) system (the system is also referred to as *nominal system*). Accumulating events from different runs one obtains thereby a sample two-dimensional gamma-ray acceptance. This can be compared to a model acceptance which is derived by choosing, on a run-by-run basis, the one-dimensional radial acceptance discussed in the previous section for the corresponding

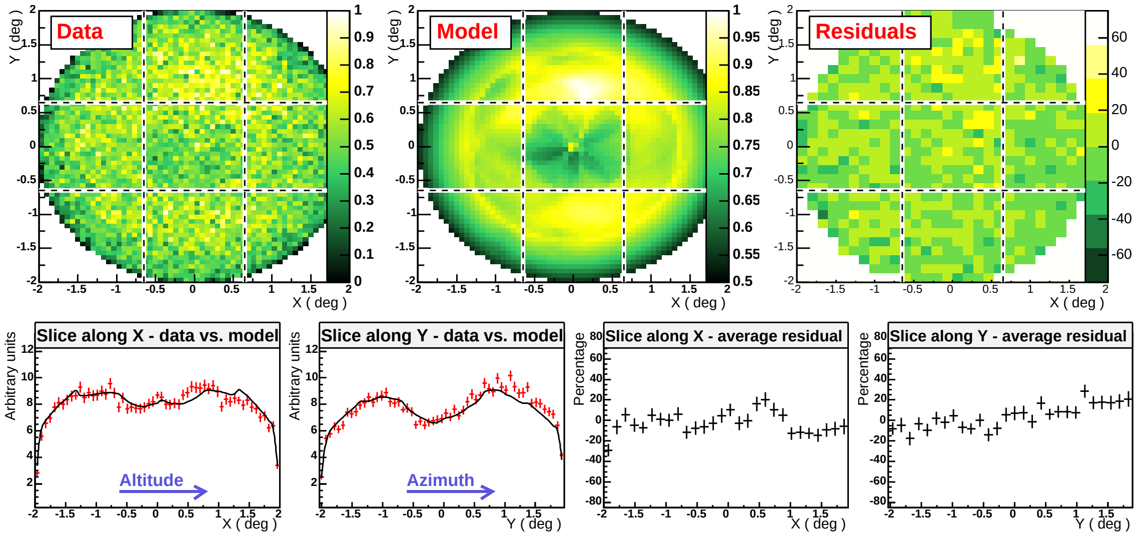

Figure 3.22: Plots shown correspond to Fig. 3.21, but are extracted from the 2004 RX J1713.7−3946 data set. Note that the source region that was excluded during analysis here is larger, $r_{\mathrm{ex}} = 0.65°$. Correspondingly, the projections and profiles shown in the lower panel have been taken from $1.3°$-thick bands, indicated by the white dashed lines in the upper panel.

zenith angle. The acceptance is then rotated in the nominal system and accumulated for all runs yielding an acceptance model which can be compared to the actual system acceptance from the data set. A slight complication arises from the possible presence of gamma-ray sources in the field of view, which, in case of a reasonably strong source, would spoil a model-data comparison. This problem is overcome by excluding the region covered by the targeted source from the data acceptance map and the acceptance model map. Since a fixed position in the sky rotates in the field of view in the nominal system, the source and therefore the region to be excluded will rotate around the centre of the field of view during the 28 minutes of a data run. To get a matching model curve, the source rotation is mimicked by producing a two-dimensional acceptance model every 100 seconds, excluding the region that is covered by the source at that moment. The resulting data and model acceptances can be seen in Fig. 3.21 for the data set of SN 1006, which exhibits no gamma-ray signal (Aharonian et al. 2005f), and Fig. 3.22, which shows the 2004 RX J1713.7−3946 data set.

For SN 1006, there is reasonable agreement between data and model acceptance, as can be seen from the two-dimensional plot of the residuals remaining after subtracting the two maps from each other. The match is, however, not perfect, there are deviations from radial symmetry. The data acceptance is squashed in the diagonal direction running from the bottom right to the top left corner, resembling an ellipsoidal form. Correspondingly, there is a region of average deficit in the residuals map in these two corners. This can also be seen from the $0.8°$-wide slices along x- and y-direction through the centre of the field of view, shown in the bottom panel of Fig. 3.21, although to a lesser extent. The average-residuals slices are generally compatible with zero (that is, agreement between data and model) within statistics. The RX J1713.7−3946 data set shown in Fig. 3.22 is much larger, it comprises 33 live hours, compared to 6.3 live hours for SN 1006. Statistical

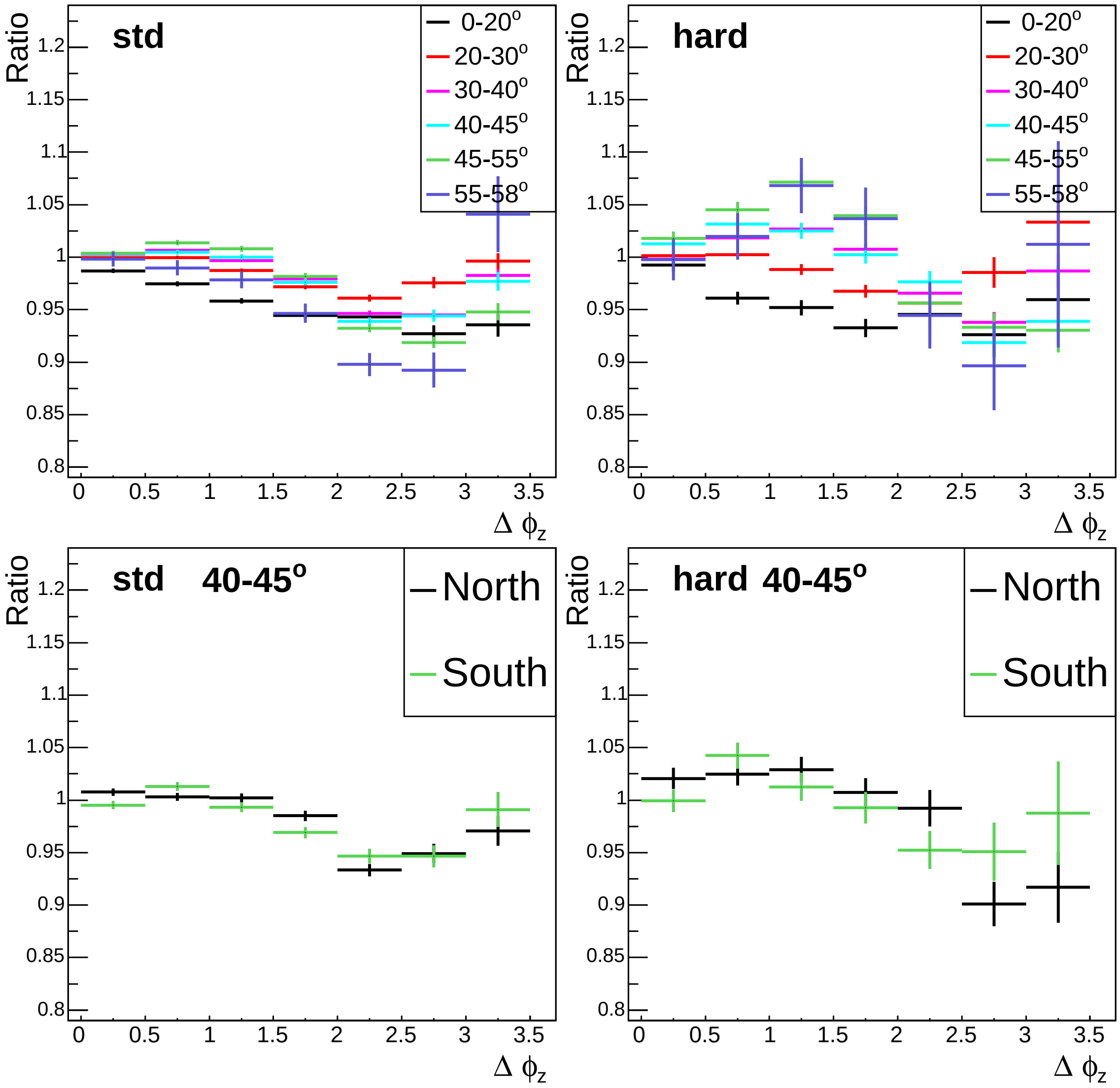

Figure 3.23: Zenith-angle dependent field-of-view gradient

fluctuations are now much smaller. Moreover, since the source is large, a larger region is excluded from the acceptance maps. The residuals here also scatter around zero with an overall good agreement between data and model acceptance. However, when taking slices through the field of view centre, the slice width corresponding to the source size, through data and model acceptance, deviations from radial symmetry do occur. In the worst cases they exceed the 20% level. In the azimuth direction there are indications for a linear gradient over the field of view.

The most intuitive cause of deviations from radial symmetry is probably a zenith-angle dependent linear gradient across the field of view. The larger the zenith angle of observation, the larger is the effective energy threshold of the system (cf. Section 3.5). Since the energy spectrum of the hadronic background after gamma-ray cuts is rather steep, the trigger rate and thus the event rate of the system decreases smoothly with increasing zenith angle (Funk et al. 2004). Hence, in the H.E.S.S. field of view of ≈ 5° there might be significant variations of the system acceptance along the zenith axis. Figure 3.23 explores deviations from radial symmetry along this axis. For this purpose, OFF runs are processed in zenith-angle bands, storing event distributions as a function of the zenith-angle difference between the pointing direction of the system and the event direction. From the resulting distributions (ranging from $\Delta\phi_{\mathrm{z}} = \pm 3.5°$) a ratio is created dividing the number of events on the positive $\Delta\phi_{\mathrm{z}}$-side by the number of events on the negative side to test for symmetry around the zenith angle of observation. Resulting distributions are shown in the upper panel of Fig. 3.23 for six zenith-angle bands. If there was no zenith-angle dependent effect the ratio would be 1 for the whole field of view. As can be seen, for most cases there seems to be a distortion of the system acceptance along the zenith axis, in the direction one would expect from the trigger-rate variation. Larger zenith angles have smaller event numbers. In case of *hard* the case is less clear, within the available statistics, especially for large zenith angles, higher order effects might be apparent which are not further investigated here. Remaining uncertainties are estimated to be on the level of 5%. In the lower panel of Fig. 3.23 OFF runs taken at 40°–45° zenith angle are split into North and South to search for effects of the Earth's magnetic field. Within statistics there is no effect apparent, the event-ratio distributions are in good agreement with each other.

3.6.3 Generation of gamma-ray excess images

For the generation of sky maps to study the gamma-ray morphology the background subtraction applied in the following will make use of the one-dimensional lookup curves of the radial system acceptance. The method is referred to here as the *field-of-view* method. Given an observation at a certain zenith angle, a model background is created by selecting the one-dimensional radial lookup from the zenith-angle band that matches the zenith angle of the observation. For each run a two-dimensional background map of the sky is then created by rotating the corresponding one-dimensional lookup around the actual observation position. Finally, having processed the whole data set in this way, an overall background map is created as the exposure-weighted sum of the individual maps. The entire field of view (excluding known regions of gamma-ray emission) is then used for normalisation. α approaches zero in this case, it is calculated as ratio of the number of events in the data map (excluding the possible gamma-ray signal) to the number of events in the background model map. Figure 3.24 a) shows two radial profiles, one from the acceptance model, one from the RX J1713.7−3946 data set, that are used for the calculation of α. The model profile is already scaled by α, the accordance of shape of the two profiles illustrates again that it is reasonable to parametrise the system acceptance of single data sets by means of OFF runs. The profiles are created during the generation of sky maps, data events are filled as a function of squared distance to the pointing centre. The maximum allowed distance to the centre is 2°, events further out are rejected for the creation of sky maps: Systematic uncertainties in modelling the system acceptance for such large angles might become large, and the angular resolution starts to degrade. Since RX J1713.7−3946 was observed at maximum at 1.35° offset (cf. Fig. 3.13), no signal events are lost. The deficit at small offset angles in Fig. 3.24 a) in both the data and the model profile are due to the exclusion of the region around RX J1713.7−3946, events reconstructed in that region are not considered for normalisation. The model profile is weighted to take this into account. Both histograms have the same area after the renormalisation. In addition, the average radial acceptance curve of the data set is plotted for

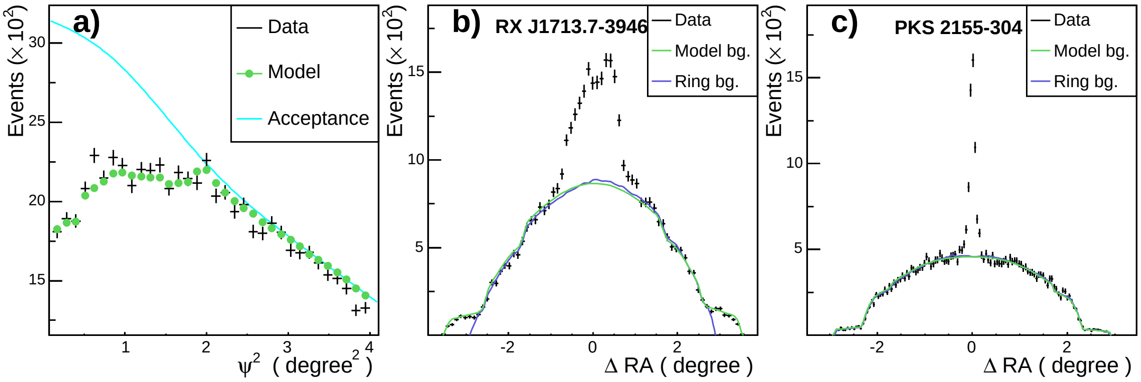

Figure 3.24: Illustration of the good match between data (black) and background model (green) for *hard* cuts. The model curves are scaled by α. **a)** Radial profiles from the RX J1713.7−3946 data set are shown. The strange shape with a deficit at small offsets angles arises from excluding the region around RX J1713.7−3946. At larger offsets beyond $(1.35°)^2$ the profiles agree very well with the average radial acceptance curve of the data set shown as turquoise solid line. **b)** and **c)** Comparison of the RX J1713.7−3946 data set to PKS 2155−304, an extra-galactic gamma-ray source which appears as a point source for H.E.S.S.. Shown are slices along Right Ascension (RA), through the centre of the sources and fully encompassing them. Two background models are plotted, the standard *field-of-view* method (green line, labelled "Model bg.") using the acceptance model, and the *ring*-background model. In b), the *ring*-background model stops at $\sim 3°$ to avoid the edge of the usable range of the field of view with the thick ring (see main text).

illustration. It is the exposure-weighted sum of the radial acceptance curves that are used for the individual runs. The acceptance curve and the model profile are almost identical beyond $(1.35°)^2$, since this distance is beyond the region covered by the SNR. Remaining differences in the range 2-3° are due to other, weaker sources close to RX J1713.7−3946 discovered in the H.E.S.S. Galactic plane survey (Aharonian et al. 2005e) which must be excluded for normalisation.

Figure 3.24 b) and c) illustrate the validity of this approach by means of two H.E.S.S. data sets, now *including* the gamma-ray sources. Shown are slices along Right Ascension through the centre of RX J1713.7−3946 and PKS 2155−304, a point-like extra-galactic gamma-ray source for which a high-statistics data set exists (Aharonian et al. 2005d). Overlaid in both cases are the normalised background models of the entire data sets. In both cases, at different regions in the sky, for an extended and a point-like gamma-ray source, there is clearly a good match between model and data in regions outside the gamma-ray sources. Referring again to Fig. 3.21 and Fig. 3.22 where deviations of the system acceptance from radial symmetry were encountered in the nominal system it becomes clear here that such effects are averaged out in the final gamma-ray count map on the sky. This is at least in part due to the wobble mode of observations.

Note that there are steps in the distributions in Fig. 3.24 b) and c), in the case of RX J1713.7−3946 at ±1.1° and ±2.1°. These are artefacts of the analysis. As mentioned above, the usable range in the field of view of every observation was restricted to a radius of 2° around the camera centre. Since the figure combines data from different

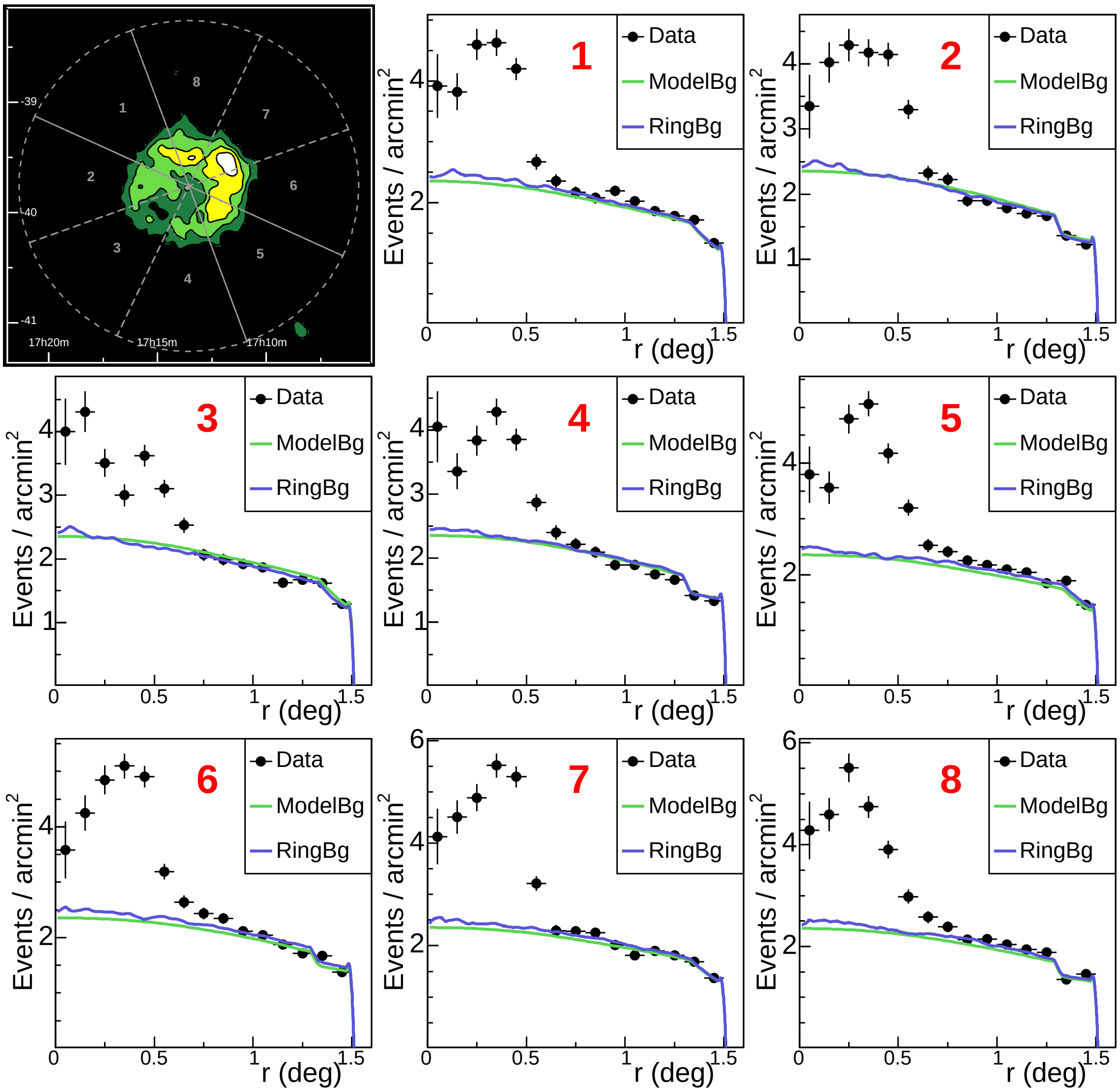

Figure 3.25: Data and background-model radial profiles are compared to each other in eight wedge-shaped regions for the 2004 RX J1713.7−3946 data set (for *hard* cuts). The eight regions are shown in the upper left-hand corner together with a gamma-ray excess image of RX J1713.7−3946. They extend beyond the remnant to demonstrate that the background models satisfactorily describe the actual background of this data set. Note that the two background models, shown for comparison (see also Hinton et al. (2005)), agree well.

pointings, in the case of RX J1713.7−3946 with wobble offsets in Right Ascension and Declination, steps occur.

Figure 3.25 provides a further demonstration that the *field-of-view*–background model describes the data very well. Shown are radial profiles, that is, the number of counts per unit solid angle as function of distance to the SNR centre for several azimuth bands (see top-left corner of Fig. 3.25[14]). The background counts are already normalised by α. Most

---

[14] Very similar regions will be used later to compare the H.E.S.S. data to ASCA X-ray data of the SNR.

of the structures seen in the two-dimensional excess image, which is also shown in the figure, are robust and significant. The model provides a satisfactory description of the background of this data set out to a distance of 1.5°.

The advantage of using a model of the system acceptance, as described above, is that it can readily be applied to extended sources which may cover a significant fraction of the field of view. All that is needed is the exclusion of regions that emit gamma rays for the calculation of the normalisation factor α. Other models which estimate the local gamma-ray background from different regions of the same field of view are not equally well suited. Moreover, the *field-of-view* method results in the highest possible statistical significance, there are no more statistical fluctuations in the background estimate. The downside is that this method is very sensitive to any deviations of the true system acceptance from the model applied.

Alternative methods

In general, a comparison of several background models with different systematics is necessary to establish the reality of a source and to cross-check significant features of the morphology of extended sources. The estimated statistical significance of a source and possibly its morphology are largely irrelevant if background systematics are not under control. For this purpose comparisons of the results obtained with the *field-of-view* method are performed with two alternative methods, one is the *ring*-background model (Funk 2005; Hinton et al. 2005), and the other one is the *weighting* method (Lemoine-Goumard 2005).

The *ring*-background model is robust in the face of linear gradients in arbitrary directions in the field of view. In this model a thick ring around all trial source positions (in celestial coordinates) is used to provide a background estimate for any point in the field of view. The normalisation parameter α is approximately the ratio of the solid angle of the ring to the trial source region, $\Omega_{\mathrm{on}}/\Omega_{\mathrm{off}}$, with a small correction factor to account for differences in the system acceptance in the two regions. Again, knowledge of the system acceptance is required to calculate α. For point sources α is not very sensitive to effects of relative acceptance since the differences for small angles are not very large. In this case the *ring* model is also robust against systematic effects from imprecise knowledge of the system acceptance. For large extended sources a complication arises. The inner radius of the ring has to exceed the radius of the source. Even then, unless the inner radius exceeds even the diameter of the source, certain regions towards the edge of the source will have larger values of α because ring passages that cross the source region on the other side of the source centre are excluded. If on the other hand a large ring is used with inner radius larger than the source diameter, α is constant and small inside the source region at the expense of increased relative acceptance corrections across a larger portion of the field of view thereby increasing systematic uncertainties. For point sources a typical mean ring radius is 0.5°, the inner and outer ring radii are then chosen such that $\alpha \approx 1/7$. For the case of RX J1713.7−3946 a mean ring radius of 0.8° was used as compromise following the considerations given above.

In general there are two possibilities to obtain a system acceptance function for a given data set. One can either determine a one-dimensional radial acceptance on a run-wise basis, excluding the region covered by the gamma-ray source and weighting events accordingly to account for the solid-angle deficit in certain bins. This method works only reliably if the gamma-ray source does not cover a substantial fraction of the field of view. For large extended sources such as RX J1713.7−3946 the system acceptance for the *ring*-background model is not determined on a run-wise basis but from the one-dimensional radial lookups that were already used for the *field-of-view* method. Comparisons of the resulting normalised background counts of the *ring* model to the standard method are shown in Fig. 3.24 and Fig. 3.25. The agreement between the two models is very good. Figure 3.24 shows that in projections along Right Ascension for both an extended and a point-like source differences are at maximum at the few-percent level. For the *ring* background α is larger than for the *field-of-view* background and therefore larger statistical fluctuations are apparent. For the point-like source PKS 2155−304 the standard mean ring radius of 0.5° was used. The fact that the *ring*-background curve for RX J1713.7−3946 does not extend as far as the *field-of-view*-background curve is due to the large ring radius that was used. For sky positions very close to the edge of the usable range of the field of view of every observation no background events are integrated since the ring would mostly run outside the usable range. In Fig. 3.25 one can see that in different regions of the SNR the agreement is at the same few-percent level, if not better. There is reasonable agreement also at large distances up to 1.5°, already way outside the SNR.

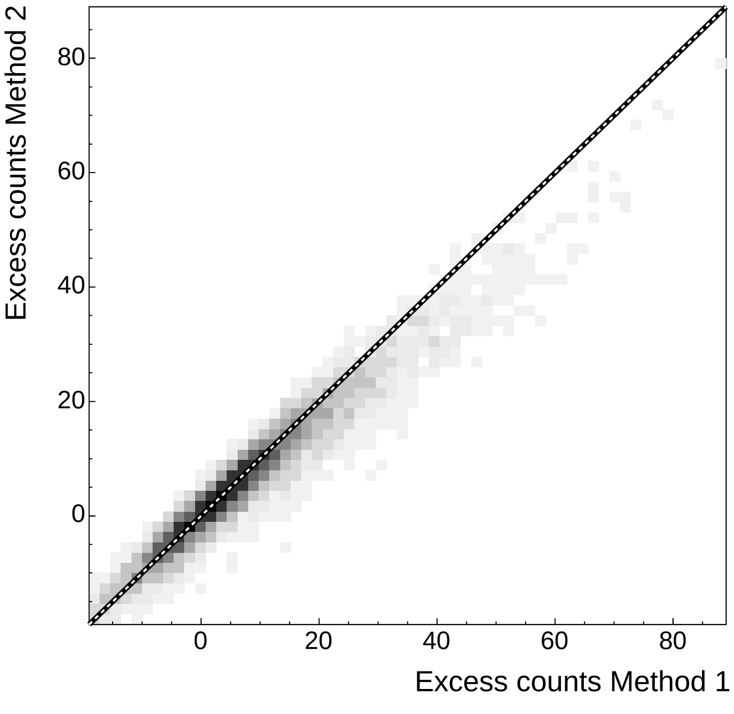

Figure 3.26: Correlation between the standard calibration, event reconstruction, and the *field-of-view* background-reduction method (*Method 1*) and an alternative, completely independent approach (*Method 2*, see main text for more details). The black and white dashed line runs through the origin with a slope of 1. A linear correlation is clearly visible, deviations from the line originate from the different cut efficiencies of the two methods.

The *weighting* method provides not only a cross-check of the background model, but also of the complete analysis chain. It is based on an independent calibration and analysis approach. Rather than using standard (Hillas) parameters for image parametrisation and reconstructing shower geometry based on these parameters, this approach is based on a 3-D model of Čerenkov photon emission during the shower development in the atmosphere assuming rotational symmetry, thereby predicting pixel amplitudes (Lemoine-Goumard & de Naurois 2005). For the background modelling, signal and background are estimated simultaneously from the same portion of the sky. Events with directions associated with a certain sky bin are assigned two weights, one for the assumption that it is a signal event, one that it is a background event. These weights are used to create two count maps, a signal and a background map. Subtraction of the two yields the gamma-ray excess (Lemoine-Goumard 2005). A comparison of the standard *field-of-view* model with the *weighting*–analysis method is shown in Fig. 3.26. The correlation of gamma-ray excess counts for the sky region around RX J1713.7−3946is plotted. A linear correlation is clearly apparent illustrating the reasonable agreement between the two independent methods.

3.6.4 Generation of gamma-ray spectra

The strong energy dependence of the gamma-ray system acceptance (cf. Fig. 3.20) complicates the background estimation for the generation of gamma-ray spectra. One cannot, as for the image generation, simply use a one-dimensional radial lookup (which is integrated over all energies) as a background estimate. Instead, the acceptance lookups would have to be generated in energy bins which in practice is difficult to handle. The *ring*-background method is also disfavoured because of the energy-dependent acceptance. OFF events have different distributions of offsets with respect to the pointing direction, trying to correct for energy-dependent offset differences of ON and OFF events would introduce additional sources of systematic errors. Instead, the preferred method, the *reflected-region* method, selects background events from the same field of view, from the same data run, by selecting N_{OFF} regions of the same size and form as the ON region, but displaced on a circle around the pointing direction of the system. The circle is chosen such that the OFF regions are at exactly the same offset as the ON region. As many OFF regions as possible are fit on the circle whilst avoiding the area close to the test position to prevent contamination of the background estimate by mis-reconstructed gamma rays. Therefore, a minimum distance between the ON and OFF regions of 0.1° is demanded. Furthermore, known gamma-ray sources in the field of view not associated with the test region are excluded from the OFF regions. This approach ensures that background events are taken at the same zenith and offset angles, no radial acceptance correction is required with this method and α is just $1/N_{\mathrm{OFF}}$. Moreover, more or less the same region of sky is used with a similar level of NSB noise. For an object of the size of RX J1713.7−3946 this approach results in one ON and OFF region, the latter being simply the reflection of the former at the system centre. This is illustrated in Fig. 3.27, where the OFF regions used for each observation position are drawn.

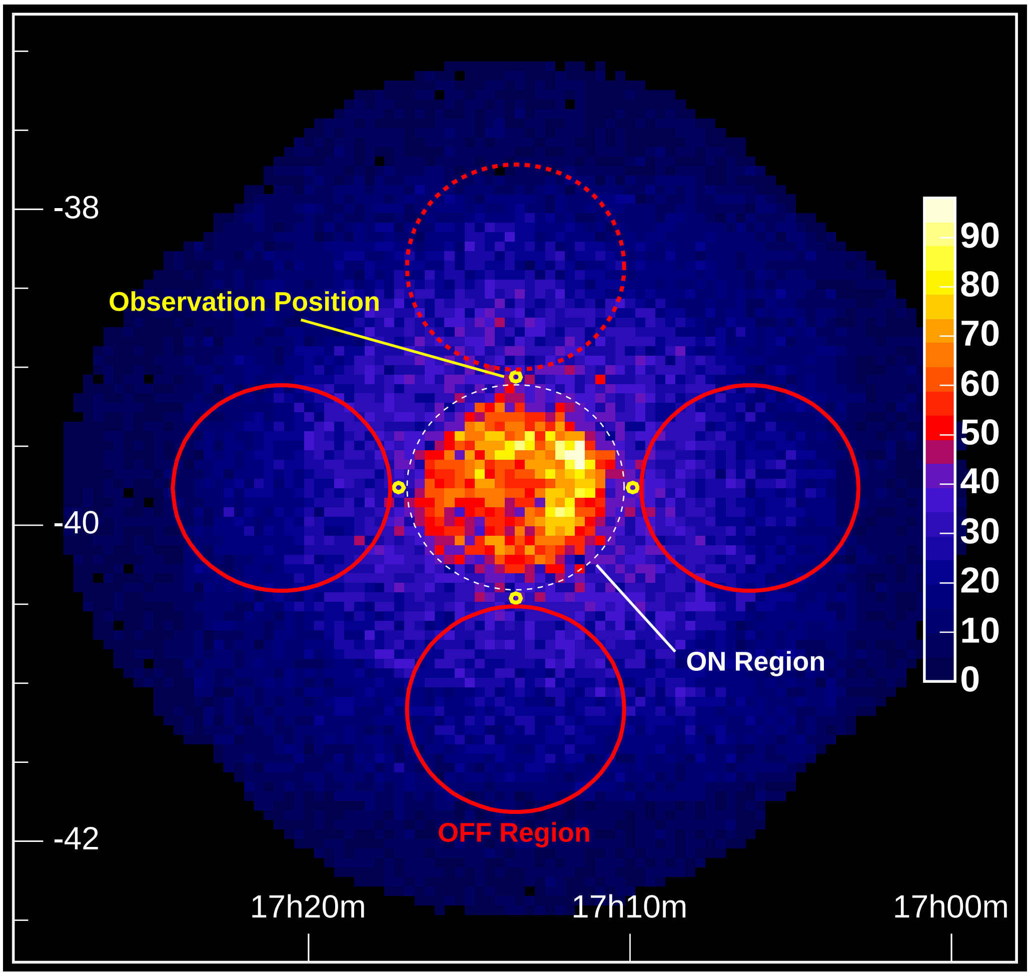

Figure 3.27: Count map of gamma-ray candidates for the region around RX J1713.7−3946. The *hard* cuts have been applied. The bins are uncorrelated and the background is not subtracted. The white dashed circle indicates the region used to extract the spectrum of the whole SNR (the *ON* region), the red circles indicate the OFF regions, the regions used for background estimation for the spectrum in each of the four wobble observation positions, which are marked as yellow circles. The dashed red circle to the north of the SNR indicates an OFF region that was not used in the spectral analysis because it contains a gamma-ray source discovered in the H.E.S.S. Galactic plane survey (Aharonian et al. 2005e).

3.7 Spectral analysis

After the geometrical selection of ON and OFF events (as explained in the previous section), a differential gamma-ray spectrum, can be calculated. It is conventionally defined as the measured number of gamma rays, N_γ, per unit area, time and energy, and can be determined as

$$F(E) = \frac{1}{\epsilon_{\mathrm{cuts}}(E)\,A(E)}\,\frac{d^2}{dE\,dt}\,N_\gamma = \frac{1}{\epsilon_{\mathrm{cuts}}(E)\,A(E)}\,\frac{d^2}{dE\,dt}\,N_\gamma\,, \qquad (3.5)$$

where $\frac{d}{dE\,dt}\,N_\gamma$ is the measured rate of gamma rays after event selection and background subtraction, $\epsilon_{\rm cuts}$ is the cut efficiency and $A(E)$ is the collection area which is defined as the energy-dependent area available for 100% efficient gamma-ray detection (already in Fig. 3.8). The cut efficiency and the collection area have to be derived from Monte-Carlo simulations and are usually determined in a combined manner. They are therefore not treated separately, their product yields the effective (detection) area $A_{\rm eff}(E) \equiv \epsilon_{\rm cuts}(E)\,A(E)$, which will be used from now on.

Effective Gamma-Ray Detection Area

The effective area $A_{\rm eff}$ of an instrument like H.E.S.S. depends on trigger conditions and analysis cuts. Well above the trigger threshold of the system, it is of the order of the area of the Cerenkov light pool on ground. $A_{\rm eff}$ is determined from Monte-Carlo simulations, in general it can be computed as:

$$A_{\rm eff}(E, \phi_{\rm z}, \psi, \vartheta_{\rm az}) = \frac{N_\gamma^{\rm sel}(E, \phi_{\rm z}, \psi, \vartheta_{\rm az})}{N_\gamma^{\rm MC}(E, \phi_{\rm z}, \psi, \vartheta_{\rm az})}\, A_{\rm MC}(E, \phi_{\rm z}, \psi, \vartheta_{\rm az})\,. \tag{3.6}$$

$N_\gamma^{\rm MC}$ is the total number of simulated gamma rays, $N_\gamma^{\rm sel}$ is the number of gamma rays that trigger the telescope system and pass all of the analysis cuts, and $A_{\rm MC}$ is the simulated area the gamma rays were “thrown” over. The basic dependencies of the effective area are also given in Eq. 3.6; it depends on the primary energy E, on the zenith angle $\phi_{\rm z}$ due to the zenith-angle dependence of the Čerenkov light-cone radius on the ground (cf. Section 2.1.3) and absorption effects of Čerenkov photons, on the offset angle ψ between source and telescope pointing direction due to the offset dependence of the gamma-ray detection efficiency (cf. Section 3.6.2), and on the azimuth angle $\vartheta_{\rm az}$ due to the impact of the Earth’s magnetic field on the shower development in the atmosphere.

A complication arises from the finite energy resolution of the system. True primary energies $E_{\rm true}$ are reconstructed at energies $E_{\rm reco}$ with a probability given by the probability or response function $P(E_{\rm true}, E_{\rm reco})$. Therefore, the measured gamma-ray rate is given by the convolution

$$\frac{d}{dE_{\rm reco}\,dt}\,N_\gamma(\phi_{\rm z}, \psi, \vartheta_{\rm az}) =$$

$$\int P(E_{\rm true}, E_{\rm reco}, \phi_{\rm z}, \psi, \vartheta_{\rm az})\, A_{\rm eff}(E_{\rm true}, \phi_{\rm z}, \psi, \vartheta_{\rm az})\, F(E_{\rm true})\, dE_{\rm true}\,. \tag{3.7}$$

Equation 3.7 can no longer be analytically inverted to yield the source flux $F(E_{\rm true})$ as in Eq. 3.5. There are three possibilities to overcome this complication. Firstly, one could deconvolve the response function of the instrument. Secondly, one could use a *forward-folding* method and fit Eq. 3.7 to the data: parameters like source flux and spectral index are obtained from a comparison of the reconstructed energy distribution to the expected distribution for a given spectral shape (Piron et al. 2001). Thirdly, the energy smearing can be absorbed into the effective areas by using a modified definition of $A_{\rm eff}$ such that Eq. 3.5 holds. In this case, one uses the reconstructed energy $E_{\rm reco}$ rather than $E_{\rm true}$ in Eq. 3.6 and weights incident events to obey a power-law spectrum (with a canonical spectral index of $\alpha = -2$ – see Section 2.3.2) thereby taking the bias of the energy reconstruction into

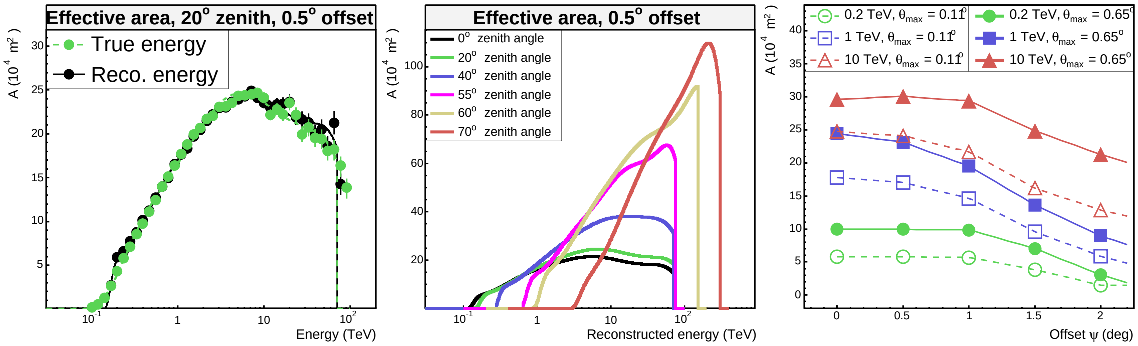

Figure 3.28: Some effective detection-area curves obtained with *std* cuts. The left-hand plot shows histograms filled using true simulated and reconstructed energy, along with fit functions as described in the main text. The plot in the middle shows (for a fixed offset angle of 0.5°) the evolution of the effective collection area with increasing zenith angle. Note that the sharp drop of the curves at high energies is due to the limited simulated energy range. On the right-hand side are effective-area values for a moderate zenith angle of 20° as a function of offset angle. Plotted are values at three representative energies of 0.2 TeV, 1 TeV, and 10 TeV. The markers are at the fixed offset values available from simulations, between two offsets the effective area is interpolated linearly. Filled symbols and solid lines are for the extended θ^2 cut value of $(0.65°)^2$, open symbols and dashed lines are for the point-source value.

account (which itself depends on energy (see Fig. 3.16)). Results shown throughout this work are based on this last approach, which has the slight disadvantage that effective areas depend on the input spectral index α. However, due to the good energy resolution of $\approx 15\%$ of H.E.S.S. this is a small effect and can be disregarded in most cases. As will be shown in Section 3.7.1, Monte-Carlo studies revealed that spectral indices ranging from -1.7 to -2.9 are reconstructed correctly with less than 0.05 systematic uncertainty.

All the histograms and lookups that will be presented in the following and that are used throughout the analysis are generated from the same point-source simulations at fixed offset and zenith angles. For that purpose Monte-Carlo events are binned in true and reconstructed energy and effective-area histograms are obtained according to Eq. 3.6. In a second step, the histograms are fitted by high-order polynomial functions which are then used in the analysis to overcome the problem of limited event statistics in the histograms which would lead to step-like, unphysical behaviour at the edges of energy bins. The true-energy histogram is fitted by a sixth-order polynomial, the reconstructed energy histogram, much more irregular in shape close to the threshold due to effects of the reconstruction bias, is fitted in double logarithmic representation (for stability reasons), by an empirically determined function, the sum of a seventh-order polynomial and an exponential:

$$\sum_{n=0}^{7} a_n \, (E_{\mathrm{reco}})^n \, + \, a_8 \, \exp(a_9 \, E_{\mathrm{reco}}) \, . \tag{3.8}$$

The energy dependence of typical collection and effective area curves was already shown in Fig. 3.8 as a function of E_{true}. Figure 3.28 shows some additional representative effective area curves and illustrates the basic dependencies. The first plot on the left-hand side compares the effective area for a zenith angle of 20° and an offset of 0.5° as a function of true and reconstructed energy. Since the bias of the energy reconstruction exceeds the energy resolution only at very small and very large energies (cf. Fig. 3.16 and Fig. 3.17), it is only at these energies that differences between the true and the reconstructed energy curves appear. As can also be seen, the fit functions describe the histograms reasonably well, they will be used from now on and not be discriminated from the histograms. The second plot in Fig. 3.28 illustrates the zenith angle dependence of the effective area. For moderate zenith angles the curves reveal similar features, they rise steeply, once beyond threshold, the curves flatten somewhat but keep rising (less dramatically) with increasing energy (as already mentioned in Section 3.3). Eventually the curves turn over and the area decreases again, the decrease of cut efficiency at high energies (cf. Fig. 3.8) starts to dominate. With increasing zenith angle, two effects are apparent. One is the increase of the energy threshold as discussed in Section 3.5. The second effect, again caused by the zenith-angle dependence of the Čerenkov light-cone radius, is that the effective area well beyond threshold for a fixed energy is much larger for large zenith angles. For example the 60° zenith-angle curve is about a factor of 4 above the 0° curve at 10 TeV, in good accordance with eq. (2.14), Section 2.1.3, from which one can approximate $A_{\mathrm{eff}} \propto R_{\mathrm{c}}^2 \propto (1/\cos\phi_z)^2$.

Note that simulated effective-area curves shown here are always generated using simulations with orientations to the South. This is important because of the Earth's magnetic field. During shower formation in the atmosphere, the paths of electrons and positrons are bent in diametrically opposite directions in the plane perpendicular to the B-field. For the H.E.S.S. site, the angle between the B-field direction and the shower axes is smaller pointing to the North than it is when pointing to the South. Therefore, due to the resulting larger angular spread of Čerenkov light when pointing South, the effective area is shifted to larger energies. Close to the trigger threshold this effect can be as large as 20%. Since RX J1713.7−3946 is located in the South, only these effective areas are shown and used in the analyses presented here.

The plot on the right-hand side of Fig. 3.28 illustrates the evolution of the effective area with the offset angle between source and pointing direction. For a zenith angle of 20° effective-area values for three different energies are shown, at 0.2 TeV (near the post-cuts trigger threshold, see below), 1 TeV, and 10 TeV. The markers at 0°, 0.5°, 1.0°, 1.5°, and 2° represent the offset values for which simulations are available. In between these values, effective-area values are interpolated, shown in the plot by straight lines. The two sets of curves refer to two different θ^2 cuts. The filled symbols and solid lines were obtained applying the *std* cuts with $\theta^2 = (0.65°)^2$, the cut appropriate for an extended source such as RX J1713.7−3946. The open symbols and the dashed lines were obtained using the tight point-source cut value of $\theta^2 = (0.11°)^2$. As expected and in accordance with Fig. 3.8, where the cut efficiencies versus energy were shown, the effective area is larger when integrating events in a larger region. Apart from that the curves are very similar, they increase with energy, are reasonably flat within the inner 1°, and decrease towards larger offset values.

Energy threshold

The trigger threshold (also simply referred to as the energy threshold) of an experiment like H.E.S.S. (after analysis cuts) is conventionally defined as the energy value at which the differential gamma-ray rate of a source reaches its maximum. It therefore depends on the source spectrum, on analysis cuts, the zenith angle of observation and (rather weakly) on the offset angle of the source. Sample differential-rate curves are shown in Fig. 3.29, left. The curves of the differential rate have been obtained from simulations, by convolving effective-area curves with an assumed input source spectrum $\propto E^{-2}$. Curves obtained from the application of *std* cuts are shown, with the extended θ^2 cut of $(0.65°)^2 = 0.42\ (°)^2$ and with the point-source cut of $(0.11°)^2 = 0.0125\ (°)^2$, for two different zenith and two different offset angles. It is apparent from the figure that with increasing offset, only the absolute rate changes, not the peak position, and hence the energy threshold is rather constant. The same holds true when applying an extended θ^2 cut. The absolute value of the maximum rate increases slightly, but the energy threshold remains unchanged. The zenith angle of observations on the other hand makes a dramatic difference, as is already seen in the effective areas (Fig. 3.28). For observations of a source on-axis, at zenith angles of 65°, the trigger threshold of the system exceeds 2 TeV. When increasing the minimum *size* cut as in the configuration *hard*, the energy threshold rises, too. This can also be seen in Fig. 3.29. The curve for the *hard* cuts for a zenith angle of 30° and an offset of 0° peaks at ≈ 450 GeV, compared to ≈ 200 GeV, the corresponding value for *std* cuts.

The evolution of the trigger threshold for *std* and *hard* cuts with zenith angle is shown in Fig. 3.29, right. For both sets of cuts, the threshold changes smoothly with zenith angle. Compared to the trigger threshold is the *safe analysis threshold*, a software threshold that is used during spectral analysis. There are two motivations for applying such a threshold, the first is to stay away from the steeply rising region of the effective area curve just below the trigger threshold, because this is the region that is most prone to systematic errors if the experiment's true collection area is not well enough described by the simulations used. The second is to avoid too great a bias in the reconstructed energy (cf. Section 3.5). To avoid systematic errors when the measured source spectrum differs significantly from the simulated E^{-2} spectrum, the safe spectral threshold is defined as the energy at which the energy bias falls below 10% (cf. Fig 3.16). Values of this analysis threshold are plotted in Fig. 3.29, for both sets of cuts. As one can see, the safe threshold is in most cases very close to the trigger threshold.

Differential Gamma-Ray Flux

Once the gamma-ray excess and effective collection area are known, a differential gamma-ray flux in units of (TeV^{-1} cm^{-2} s^{-1}) can be calculated. Firstly, ON and OFF events (N_{ON} and N_{OFF}) are binned logarithmically in energy and divided by the mean effective area and the exposure time in each bin. The energy-dependent effective area is determined for each data run. From the corresponding zenith (θ_{z}) and offset (ψ) angle range covered by the source, an average area is determined, multiplied by the live time[15] of the run and then added to the overall effective area of the full data set. Then, for each energy bin i, the bin entries are divided by the width (Δ_{i}) of that bin to obtain a differential flux

---

[15] Defined as the dead-time corrected observation time.

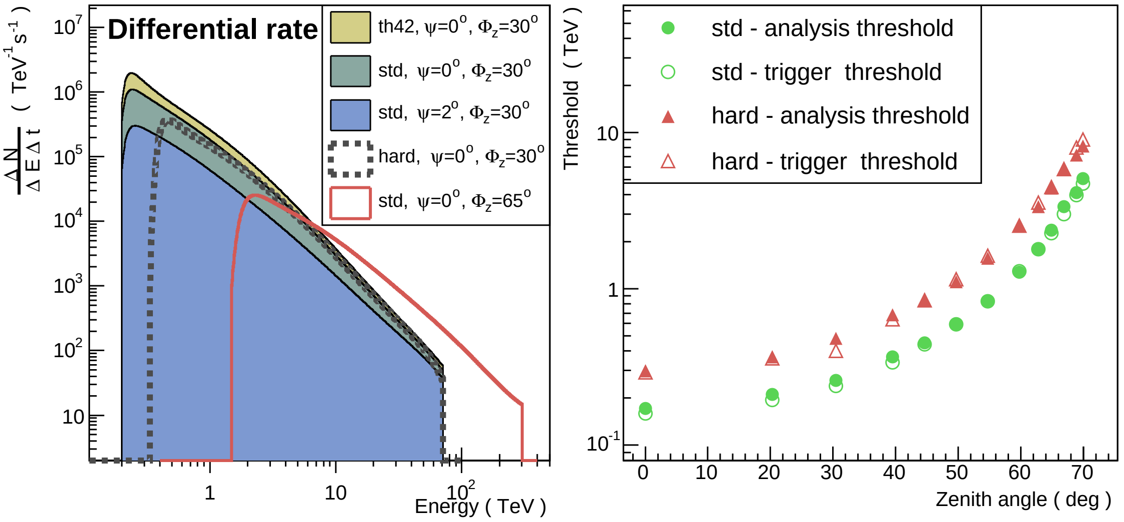

Figure 3.29: Left: Differential gamma-ray rate obtained from simulations by convolving effective-area curves with an E^{-2} spectrum. Curves shown are for *std* and *hard* cuts with different θ^2 cuts ("th42" means an extended θ^2 cut of $(0.65°)^2 = 0.42\ (°)^2$), for different zenith and offset angles. **Right:** Trigger threshold values are shown, given by the energy at which the differential rate reaches its maximum (post analysis cuts), as a function of zenith angle, for *std* and *hard* cuts, and a source offset of $0.5°$. The safe spectral threshold for comparison lies generally just above the trigger threshold for a fixed zenith angle as desired. Note that threshold values are determined from simulations pointing to the South. To the North, the energy thresholds are slightly lower since in that case Čerenkov images are not broadened by effects of the Earth's magnetic fields.

value. The differential flux results from subtracting the differential OFF- from the ON-flux histograms:

$$\left(\frac{\mathrm{d}N}{\mathrm{d}E}\right)_{\mathrm{i}} = \frac{N_{\mathrm{on,i}}}{\Delta_{\mathrm{i}}\,\Sigma_{\mathrm{runs}} T A_{\mathrm{i}}(\theta_{\mathrm{z}},\theta)} - \alpha_{\mathrm{i}} \frac{N_{\mathrm{OFF,i}}}{\Delta_{\mathrm{i}}\,\Sigma_{\mathrm{runs}} T A_{\mathrm{i}}(\theta_{\mathrm{z}},\theta)} \tag{3.9}$$

Figure 3.30 illustrates the different steps in the generation of spectra. On the left-hand side the raw ON and OFF events from the RX J1713.7−3946 2004 data set are plotted as a function of energy. These distributions are the starting point for the generation of a spectrum. They still contain the detector effects. The centre plot of Fig. 3.30 shows exposure-weighted effective-area curves for the ON and the OFF regions. The OFF events are assumed to have the same system acceptance, therefore the OFF effective area is the same as the ON one, except that it contains already the normalisation, a factor of $1/\alpha$ is multiplied to the OFF effective area of every data run. Dividing the raw energy distributions by the effective area–exposure curves, and taking the bin width into account, one obtains flux points. These are shown on the right-hand side of Fig. 3.30. Instead of a differential flux, an energy flux is drawn instead: flux points have been multiplied by E^2 to highlight prominent features. As can be seen, ON and OFF flux are both rather steep, power-law like distributions, and their slope changes or breaks at ≈ 600 GeV and becomes harder. When fitting a power law at small energies of 0.2–0.5 TeV, below the break, to ON and OFF data, the resulting spectral index is -3.4 and -3.6, respectively.

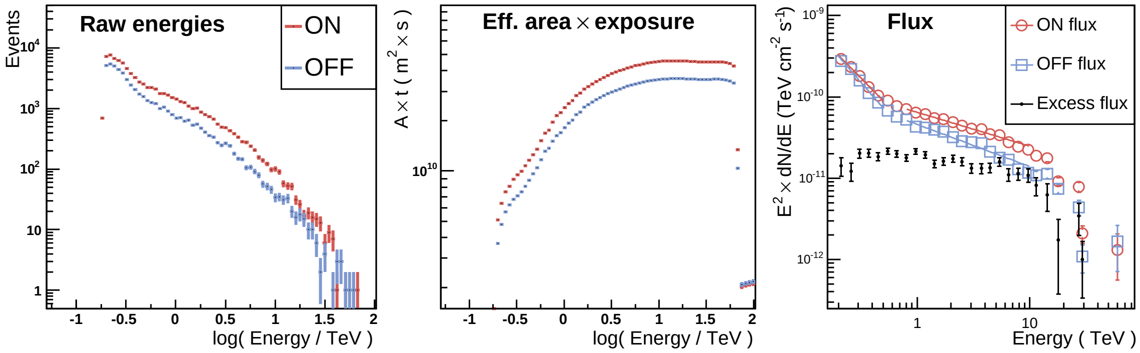

Figure 3.30: ON and OFF distributions from the 2004 RX J1713.7−3946 data set. The left-most plot shows raw event distributions plotted versus energy as they are used during analysis. The plot in the middle shows averaged effective-area curves adopted for this particular data set. The OFF effective area differs from the ON one only by a scaling factor of $1/\alpha$. The right-most plot shows the resulting ON and OFF flux points. Points have been multiplied by E^2 to visualise basic features. Also drawn are best fits of a power law in two energy ranges, 0.2–0.5 TeV and 0.8–10 TeV (see main text).

When fitting beyond the break, at energies of 0.8–10 TeV, the indices are -2.4 for ON and -2.5 for OFF data. The difference between ON and OFF flux is clearly due to the gamma-ray excess of RX J1713.7−3946. The subtraction of both fluxes yields the source or gamma-ray excess flux, also plotted in Fig. 3.30. Its energy-dependence is different, the source spectrum is harder. Its spectral index is close to -2, significantly different from the background spectrum. Further discussions of the spectral data of RX J1713.7−3946 will be given in Chapter 4 when the analysis results are discussed.

Initially the events and the exposure-weighted effective areas are stored in very fine logarithmic energy bins, 24 per decade. Having processed the whole data set, a suitable binning is chosen based on the total significance. A re-binning procedure is then applied which merges bins together. The finest binning is 12 bins per decade to assure that the bin width always exceeds the energy resolution of $\approx 15\%$. Figure 3.31 shows the gamma-ray spectrum of the 2004 RX J1713.7−3946 data set. Plotted are the initial spectrum in the very fine energy binning and the final spectrum resulting from the re-binning procedure. The re-binning proceeds such that an initial binning is a priori chosen. If the total significance exceeds 30 σ, 12 bins per decade are chosen, if it is beyond 12σ, 6 bins per decade, else 4 bins per decade are chosen. The required number of bins are then merged, ON and OFF events are added together, weighted effective areas are averaged. The flux value of each bin is then calculated by means of eq. (3.9). The corresponding energy value, the value at which the flux point will be positioned in the final spectrum, is determined as the gamma-ray excess–weighted average bin centre of all the energy bins that contributed events. As can be seen from Fig. 3.31, the binning is eventually adjusted again for high energies. For that purpose a significance of the gamma-ray excess in each energy bin is calculated. The number of ON and OFF counts is the number of events in a certain bin, the bin-wise normalisation factor α is obtained by dividing the ON effective area histogram by the OFF effective area, which, as explained above, is generated during the data processing as the exposure weighted sum of the run-wise effective area, multiplied by $1/\alpha_{\mathrm{run}}$. As soon

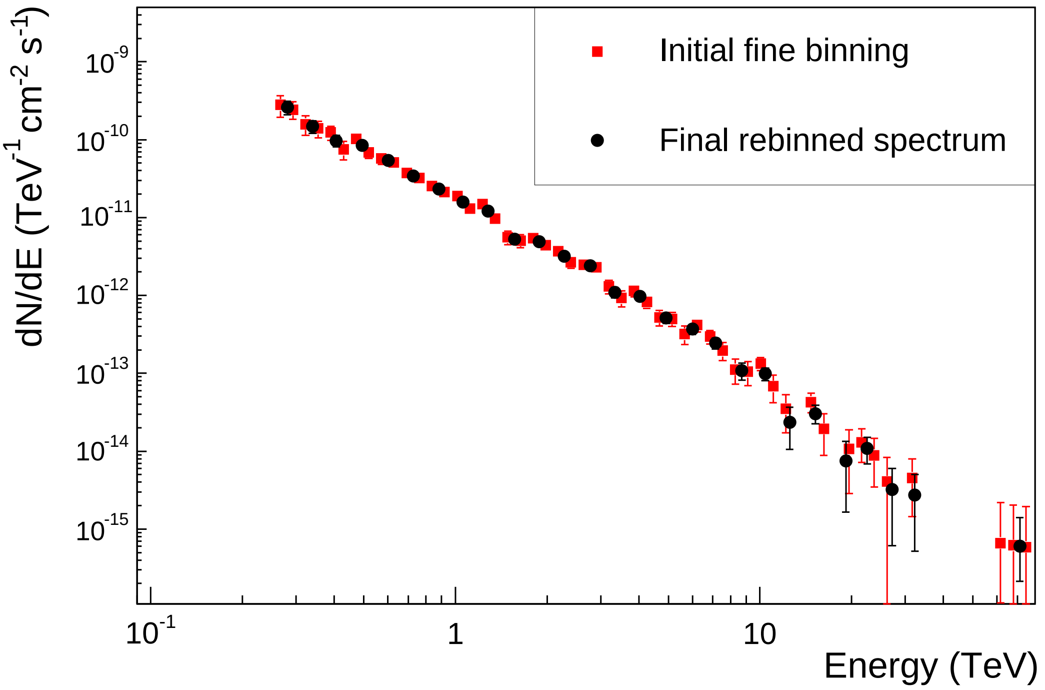

Figure 3.31: Plot to demonstrate the re-binning during spectrum generation. The red graph shows the initial, finely binned flux points, the black graph shows the resulting final spectrum. Note that in the finely binned version, only positive flux points are drawn (which is also the reason for the gap in the final spectrum at 40-50 TeV). Since for the rebinned version all points are merged to yield a flux value, the finely binned points have a tendency at high energies to exceed the coarsely binned points.

as the significance of a bin after merging is less than 2σ, the bin width is doubled. A point is finally accepted for inclusion in the final spectrum if it has a positive significance and if its fractional error is below 100%. Otherwise, the point is rejected from the spectrum and the procedure is halted, points at higher energies are not taken into account any more. In principle it is not necessary to exclude points of negative significance from the analysis. As long as there is at least one ON or OFF event, an upper limit could be calculated instead and this could also be included in fits of different spectral shapes to the data, but this variant is not pursued here.

The error bars on the gamma-ray flux points are calculated under the assumption that the fractional flux error is equal to the fractional error on the gamma-ray excess, which itself can be calculated applying Poisson statistics from the number of ON and OFF counts and from α in each energy bin. Any error on the effective detection area in a bin is not taken into account.

Alternative method

An alternative approach for the generation of spectra exists which differs only slightly to the procedure described above. Instead of determining average effective areas on a run-by-run basis, the effective area is taken into account on an event-by-event basis. Each ON and OFF event is weighted with the inverse of the effective area, taking the event zenith angle, offset, and energy. This approach is equally well suited in most cases. It will generally result in slightly larger statistical errors in bins with low event statistics, because the spread of the effective areas is added to the spread of the events.

Exploring systematic uncertainties

The key aspect in obtaining a reliable and precise estimate of the gamma-ray spectrum of a source is the control of systematic errors. Sources of systematic uncertainties include errors on the absolute energy scale, the background modelling, uncertainties in the energy-dependent cut efficiency, and the spectral analysis technique applied. For qualitative comparisons, in order to establish shape and characteristics of the energy spectrum of RX J1713.7−3946, different and independent analysis methods and background-modelling approaches are in the following compared to each other. Spectra are furthermore determined in sub-sets of the data – for small and large zenith angles – and applying different analysis cuts. Finally a quantitative estimate for the energy-dependent systematic error is derived by taking into account independent sources of uncertainties.

Figure 3.32 compares the spectrum obtained with the standard spectral analysis technique and the *reflected-region* background approach to two independent spectra. The middle set results from the event-by-event effective-area weighting. Moreover, an *ON/OFF*-type analysis is applied. The background is estimated from OFF runs and is therefore completely independent to the one from the standard method. These OFF runs are selected from the archive of contemporaneously taken empty-field data, already used for the acceptance lookups. One OFF run is assigned to each ON run[16], observed at as closely matching zenith angles as possible. ON or signal events are then integrated within a circle encompassing RX J1713.7−3946 in the ON runs, background regions in the OFF data are selected such that they have the same shape and distance to the pointing direction as the signal region. For the case of RX J1713.7−3946, exactly two background regions can be fit into each OFF-run field of view. In the figure the resulting spectrum is scaled by a factor of 10^{-2} for better visualisation. Moreover, the fit of a curved power law (a power law with energy-dependent photon index), which provides a reasonable description of the spectrum from the standard approach, is plotted on top of the *ON/OFF* spectrum (further details of the spectral shape and integral flux will be given in Chapter 4). There is apparently very good agreement between the two spectra. The other spectrum shown in the lower set of Fig. 3.32 is produced with the independent calibration and analysis scheme already mentioned in Section 3.6.3. An alternative spectral-analysis approach, the *forward-folding* method, was followed here which, as mentioned above, fits the true gamma-ray rate, Eq. 3.7, directly to the data assuming a certain spectral shape (Piron et al. 2001).

Further consistency checks related to possible systematic uncertainties in determining

---

[16] "ON run" denotes in this case the runs taken on-source in wobble-mode.

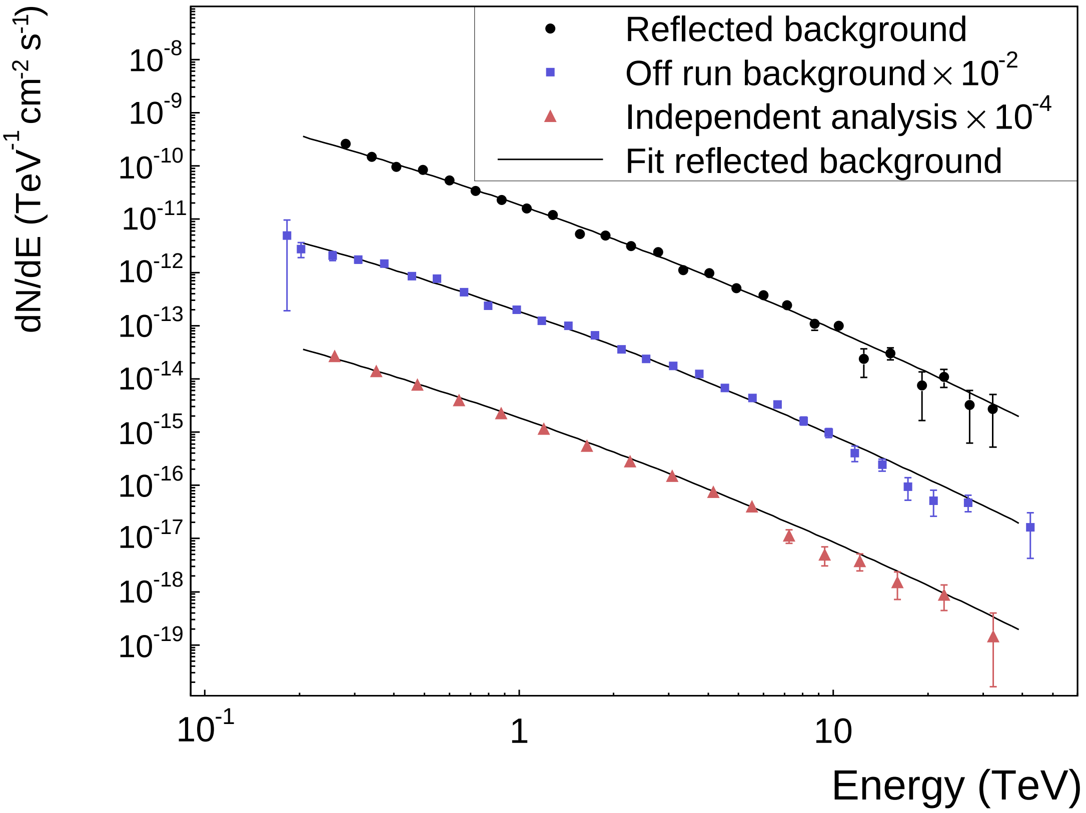

Figure 3.32: Shown are three spectra that were produced to explore the systematic uncertainties. The alternative spectra (blue squares and red triangles) were scaled by factors of 10^{-2} and 10^{-4}, respectively, for presentation reasons. **Upper set:** Standard analysis and standard background modelling applying the *reflected-region* method. **Middle set:** Alternative spectral analysis technique (event-wise effective-area weighting) with an independent background estimate taken from OFF runs. **Lower set:** Spectrum from an independent analysis chain. The background was determined similarly to the upper set. Plotted as black line on top of all three spectra to guide the eye is the best fit of a power law with energy dependent photon index to the spectrum shown in the upper set (fits to the data are discussed in detail in Chapter 4). The error bars on the spectral points denote $\pm 1\sigma$ statistical errors.

gamma-ray spectra include the analysis of the data in distinct data subsets like small and large zenith angles, different observation positions, and analysis applying different cuts on image intensity, telescope multiplicity or shape parameters. The alternative spectra, all from the 2004 data, are again compared to the *preferred* spectrum determined with the *reflected-region* method. Figure 3.33 shows this spectrum together with the best fit of a curved power law in the upper panel. The lower panel shows the ratio of the flux points to the fit values at the corresponding energy. The fit of a constant is well compatible with the data points, as expected from the notion that the curved power law provides a reasonable description of the data. The same distributions, flux ratios of spectral data points to the fit function from the *preferred* spectrum, are shown in Fig. 3.34, for four cases. The first case in the top-left corner results from completely omitting the shape cuts, which select gamma-

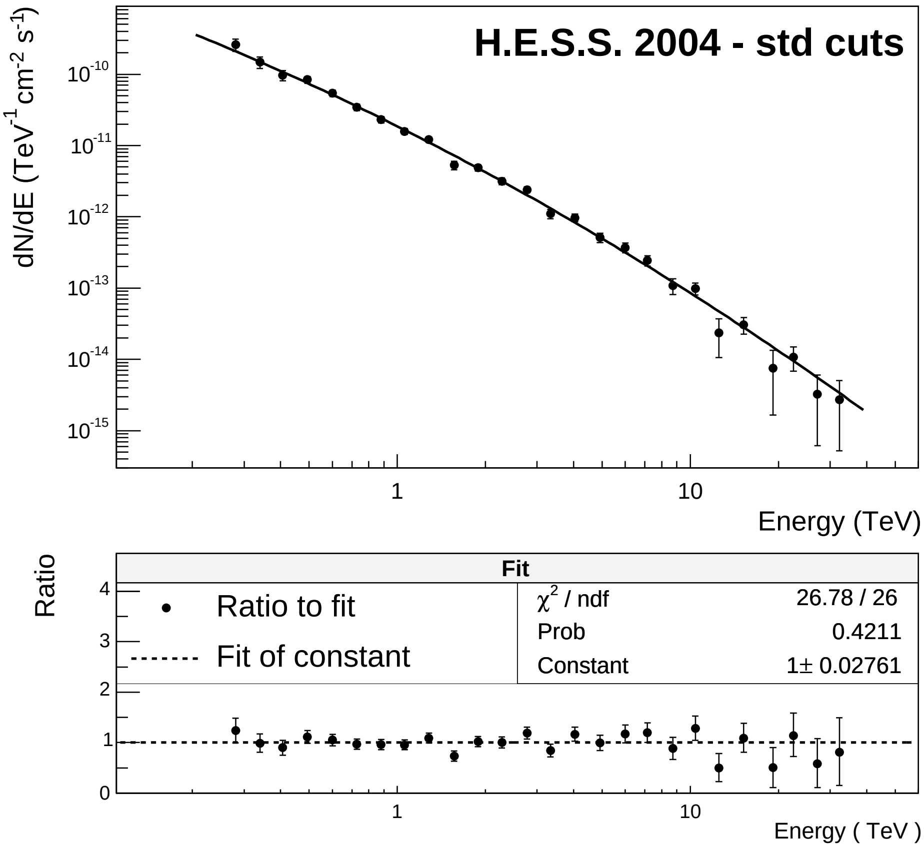

Figure 3.33: Show in the upper panel is the H.E.S.S. 2004 spectrum including the best fit of a curved power law which describes the data reasonably well. Plotted in the lower panel is the ratio of flux points to the fit value, including a fit of a constant (dashed line). Error bars correspond to the $\pm 1\sigma$ statistical errors of the flux points in the upper panel.

Spectrum	Obs. time (live hours)	ON	OFF	α	Excess	Significance (σ)
standard	30.5	103380	89851	1.0	13875	31.6
No shape cuts	30.5	1110399	832331	1.3	16310	10.2
$\phi_z < 30$	19.8	79703	70123	1.0	9873	25.6
$\phi_z > 30$	10.7	23677	19728	1.0	4002	19.2
$N_{\text{tel}} = 4$	30.5	18011	12646	1.0	5416	31.1

Table 3.3: Shown are for comparison the statistics of the spectra used for systematic comparisons (Fig. 3.33 and Fig. 3.34). Given are the live time of observations, the number of on-source and off-source events passing cuts, the normalisation α, the gamma-ray excess and the statistical significance of the excess.

ray like events (cf. Section 3.3). It is remarkable that even without applying gamma-ray cuts, the SNR stands out significantly from the cosmic-ray background. Table 3.3 shows results of the different spectral analyses discussed here, without the shape cuts the statistical significance is still 10σ. The spectrum is in complete agreement within the available

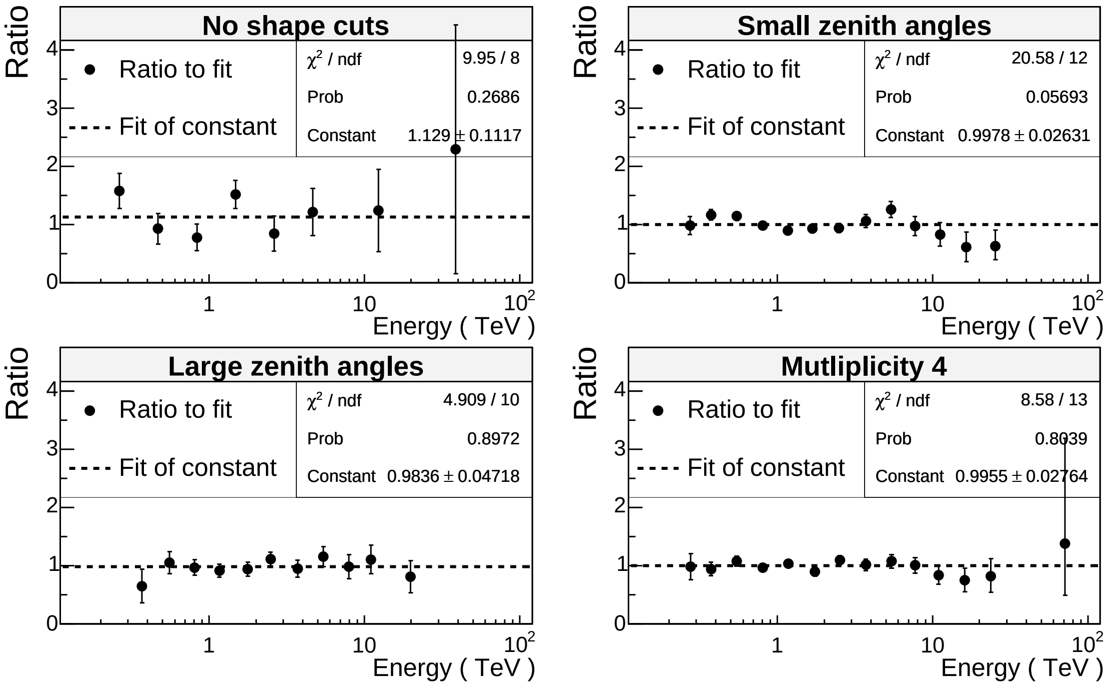

Figure 3.34: As systematic test, four spectra obtained from applying different analysis cuts and splitting-up the data in zenith-angle bands (small zenith angles: $\phi_z < 30°$, large zenith: $\phi_z > 30°$) are compared to a fit to the reference spectrum. Plotted is, analogue to Fig. 3.33, the ratio of flux points to fit values.

statistics, which is a strong confirmation of the standard spectrum, the energy-dependent efficiency of the shape cuts, which are the dominant cuts to suppress the hadronic background, is reasonably well understood and described by simulations (as it is factored into the effective detection areas). Splitting-up the data set in small and large zenith angles results in compatible spectra, too, although for small zenith angles the χ^2/ndf of 20.6/12 is rather large indicative of a slightly different spectral shape. This effect is, however, well within the systematic uncertainty estimated below. The final spectrum for comparison was generated applying a cut on the event multiplicity at four telescopes, shown in the bottom right-hand corner of Fig. 3.34. There is satisfactory agreement.

In order to obtain a quantitative estimate for the systematic error on each flux point, independent sources of systematic errors (at least as independent as possible) must be identified. Comparisons of data in different subsets or with different analysis cuts, as shown above, are a good measure for consistency but not suited to determine an estimate for the systematic error since for each flux point, the statistical error changes from one spectrum to the next, too. It is therefore desired to vary contributions of sources of uncertainties whilst keeping the event statistics unchanged. If one obtains thereby a sample of spectra (on the order of five or more to apply Gaussian statistics) one can from the spread of each flux point around the mean value determine the systematic uncertainty of this point and then eventually the uncertainty of spectral parameters like integral flux or spectral index which result from a fit of a certain spectral shape to the flux points. There are at least two methods to do this, one is, under the assumption of a certain spectral shape, to establish a covariance matrix of systematic errors from the shift of each flux point for all spectra of the sample. Fitting the flux points including the full covariance matrix, once with the statistical and systematic, once only with the statistical uncertainties, results in two covariance matrices of the fit parameters. The difference of the two are the systematic errors of the fit parameters. However, since the spectral shape is a priori not known, this approach is forgone here. Instead, a systematic error band is determined from the error on each flux point. Having this band then at hand one can easily see the uncertainty of the spectrum when plotting the band on top of the data points. Every fitted spectral shape basically has to run through this band.

Sources of systematic uncertainties include

1. The background estimation.
2. the atmospheric transmission models used in simulations and light-collection efficiencies of the telescopes which both affect the absolute energy scale of the experiment.
3. The spectral determination technique, e.g., event-by-event versus average effective area.
4. The fit to the effective area histograms determined from simulations.
5. The binning chosen for the final spectrum.

The dominant effects are clearly 1.-3., if one varies 4. and 5., that is, uses the actual effective-area histogram obtained from simulations instead of the fit values, or choses different binnings, and compares the resulting spectra to each other, differences are at the sub-percent level and are therefore negligible. The uncertainty in the energy scale is a global uncertainty which might cause a shift of the whole spectrum to lower or larger energies. The uncertainty in the light-collection efficiency of the telescopes is estimated from the system response to Čerenkov light from single muons passing close to a telescope which have a predictable Čerenkov light yield (Bolz 2004). It is on the level of $\approx 15\%$. The uncertainty in the atmospheric transmission models is estimated from the difference in the predicted system trigger rate using two different transmission models, one suited for a maritime, one for a desert atmosphere (see also Section 2.3.2). It has been found to be $\approx 10\%$ (Funk et al. 2004) resulting in a combined error on the energy scale of $\approx 20\%$. The remaining energy-dependent contributions are 1. and 3.. For the background modelling, an uncertainty on α of $\Delta\alpha = 1\%$ was derived from the RX J1713.7−3946 data set by comparing the standard analysis to the *ON/OFF* analysis, which employs and independent background model. It is noteworthy that the 1% variation found in the total number of background counts is compatible with being due to a statistical variation and thus must be regarded as an upper limit. Taking this systematic uncertainty and the two spectral analysis techniques, an energy dependent systematic error is obtained by analysing the data set six times – scaling α by $(1. + [-1, 0, +1] \times \Delta\alpha)$ and applying both analysis techniques. The RMS of the resulting six flux points in each energy bin was taken as the systematic uncertainty. Figure 3.35 shows the resulting error band plotted on top of the spectrum. It is centred on the best-fit value of the curved power law and represents the systematic error due to background uncertainties and the spectral determination technique only. The energy scale is an energy independent uncertainty; its scale (20%) is indicated in the figure with a blue arrow at one representative position (at 11 TeV). If the energy scale

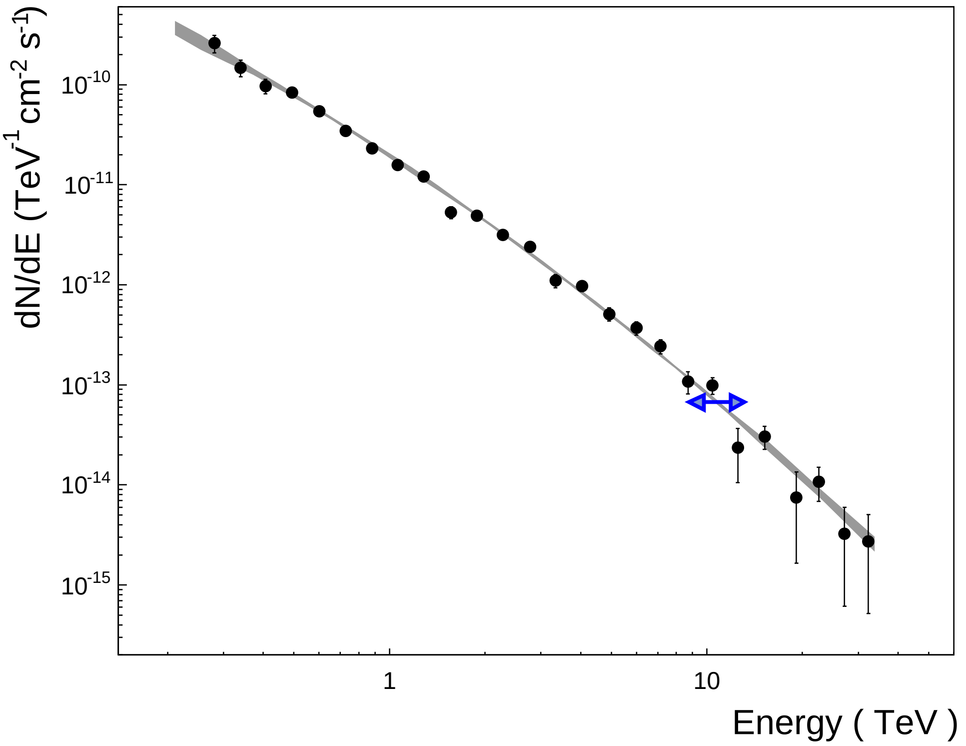

Figure 3.35: Shown is the H.E.S.S. 2004 spectrum of RX J1713.7−3946. The shaded grey band marks the systematic uncertainty stemming from the uncertainty in the background estimation and from the spectral reconstruction technique. The blue arrow indicates the 20% uncertainty on the energy scale, which is a global, not an energy-dependent uncertainty and might shift the whole curve.

changes by 20%, the whole curve would be shifted. It is worth noting that the systematic uncertainty on the background has a considerable impact on the first few flux points because of the smaller signal-to-noise ratio (as compared to points at higher energies). For the spectrum shown here the systematic uncertainty is $\approx 18\%$ for the two lowest-energy points; it decreases rapidly with increasing energy being well below 10% at 350 GeV.

When fitting a power law with index Γ to the spectrum, the systematic error on the integral flux obtained from the fit function is now conservatively estimated to be 25%, on the fit index it is $\Delta\Gamma = 0.1$.

3.7.1 Simulation Studies of the Spectral Reconstruction

For the purpose of testing the whole analysis chain that is run to produce a spectrum, involving the background determination and subtraction, the determination (that is, the Monte-Carlo generation with an E^{-2} input spectrum) and usage (that is, the interpolation of offset and zenith angle) of the effective detection area as well as technical aspects like for example the (re-)binning of the events based on the reconstructed energy and the exact energy value flux points are positioned at, Monte-Carlo simulations of known spectral index and absolute flux can be used. Gamma-ray events from a simulated point source are injected into real data runs of an empty sky field without gamma-ray source. It is then checked if spectral index and flux normalisation are correctly reconstructed.

The merging of simulated and data events works as follows: the simulations are performed for a gamma-ray source at a fixed zenith angle and offset from the system pointing direction. The source is also positioned at a fixed azimuth angle in the telescope-array coordinate system. The telescopes are not tracking but point to a fixed position. Since during real data taking the telescopes do track a fixed position in sky, thereby covering a range of zenith and azimuth angles, simulation and data run to be merged are selected such that the simulated zenith angle is contained in the angular range of the data. When the simulated events are then inserted into the data at the very time the telescopes pass the corresponding zenith angle in the data run, their direction, when transformed into an equatorial or Galactic coordinate system, will end up in the field of view of the telescope system, at the simulated offset from the pointing direction. After that, in order to realise a certain gamma-ray flux $F(E)$ obeying a power law $F(E) = F_{1\mathrm{TeV}} \cdot E^{-\Gamma}$ ($F_{1\mathrm{TeV}}$ is the flux normalisation at 1 TeV, Γ the photon index), a selection is applied to simulated events that triggered the telescope array. Only a suitable fraction $p(E)$ of events is allowed to pass, depending on the event energy E:

$$p(E) = \frac{F_{1\mathrm{TeV}}}{F^{\mathrm{MC}}_{1\mathrm{TeV}}} \cdot \frac{(1\mathrm{TeV}/E_{\mathrm{min}})^{-\Gamma}}{(1\mathrm{TeV}/E_{\mathrm{min}})^{-\Gamma_{\mathrm{MC}}}} \cdot \frac{(E/E_{\mathrm{min}})^{-\Gamma}}{(E/E_{\mathrm{min}})^{-\Gamma_{\mathrm{MC}}}} \equiv p \cdot \frac{(E/E_{\mathrm{min}})^{-\Gamma}}{(E/E_{\mathrm{min}})^{-\Gamma_{\mathrm{MC}}}}\,, \tag{3.10}$$

$$F^{\mathrm{MC}} = \int_{E_{\mathrm{min}}}^{E_{\mathrm{max}}} F^{\mathrm{MC}}_{1\mathrm{TeV}} \cdot E^{-\Gamma_{\mathrm{MC}}}\, dE = \frac{N_{\mathrm{MC}}}{A_{\mathrm{MC}} \cdot t_{\mathrm{obs.time}}}\,. \tag{3.11}$$

All energies are in units of TeV, E_{min} and E_{max} are the minimum and maximum simulated energies, Γ_{MC} the simulated photon index. N_{MC} is the total number of simulated gamma rays, before any trigger decision, thrown over the area A_{MC}. $t_{\mathrm{obs.time}}$ is the live time of the data run which determines the maximum possible integral gamma-ray flux F^{MC} (eq. (3.11), right hand side). The Monte-Carlo flux normalisation $F^{\mathrm{MC}}_{1\mathrm{TeV}}$, needed for the calculation of $p(E)$ in eq. (3.10), is easily deduced from eq. (3.11). The selection decision is drawn for each event by means of random numbers p_r (normally distributed between 0 and 1), letting an event pass if $p_r < p(E)$. In practice, one can of course only reduce the number of available simulated gamma rays, therefore $p \leq 1$. Nevertheless, depending on the choice of $F_{1\mathrm{TeV}}$ and Γ, one might still encounter values of p greater than 1. In that case, p is set to 1, effectively only the energy-dependent weighting of events is applied to achieve a spectral index of Γ, the expected flux normalisation is smaller than $F_{1\mathrm{TeV}}$.

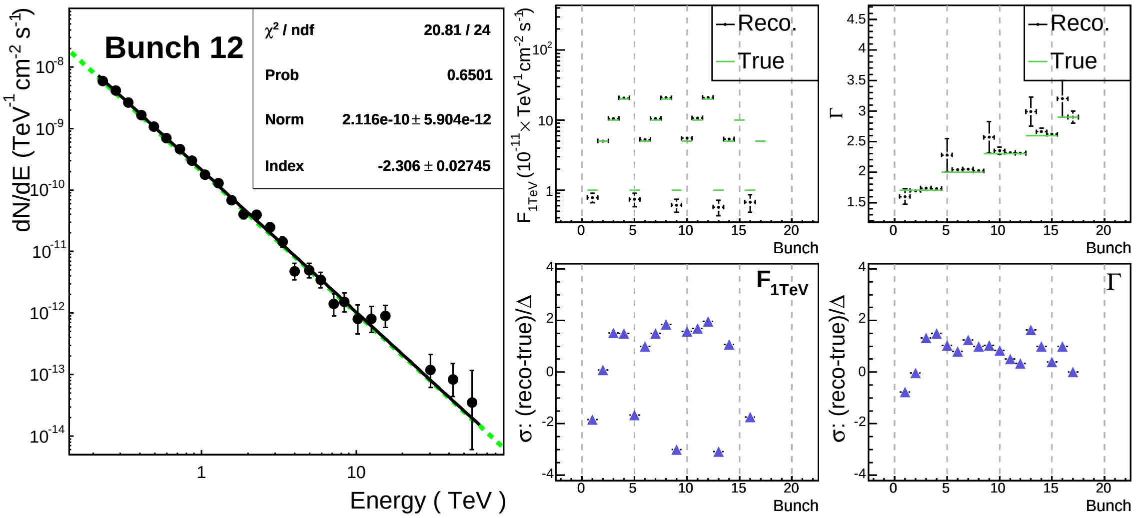

Figure 3.36: Illustrated are the test of the spectral reconstruction with simulations. The simulated source is a point source, observed at 17° zenith angle and an offset of 1.0°. The spectrum on the left-hand side is a representative spectrum obtained from bunch number 12 (cf. Table 3.4). The true Monte-Carlo spectrum with an index of $\Gamma = 2.3$ and $F_{1\mathrm{TeV}} = 20 \times 10^{-11}\ \mathrm{cm}^{-2}\mathrm{s}^{-1}$ is indicated by a dashed green line. The plots on the right-hand side compare for all bunches true and reconstructed values, the reconstructed ones resulting from a power-law fit to the data. The upper row shows the absolute values including the statistical error, the lower row shows the corresponding deviation from the true value in units of standard deviation σ. Note that for bunches 15 and 17, the number of gamma rays required to account for the demanded flux and index values exceeded the number of available simulated gamma rays. In this case, only the energy-dependent weighting is applied to test the reconstruction of the spectral index, $F_{1\mathrm{TeV}}$ is not plotted.

Figure 3.36 shows results from the spectral reconstruction after injecting simulated gamma rays from a point source, at 17° zenith angle and an offset to the pointing centre of 1.0°, into one OFF run, which exactly matches the zenith angle of observations. 20 combinations of simulated and then reconstructed flux and spectral index are shown in the figure. A point-source analysis is applied using the *std* cuts with $\theta^2 = (0.11^\circ)^2$. The different combinations are labeled by a "bunch" number for identification, the exact values of each bunch are given in Table 3.4. As can be seen, true simulated spectra are very accurately reconstructed with the standard analysis chain. Photon indices ranging from 1.7 to 2.9 for sources of different strength can be precisely determined. This justifies the procedure of simulating gamma rays with an E^{-2} input spectrum and using the effective areas as function of reconstructed energy to determine source spectra of arbitrary indices. Note that from Fig. 3.36 it seems like there is an indication for a bias towards steeper spectra, that is, larger indices. Also the flux seems to have a tendency to be reconstructed too large, although both effects are well within the statistical error of the reconstruction.

Bunch	$F_{1\mathrm{TeV}}$		Γ	
	reco.	true	reco.	true
1	0.8 ± 0.1	1	1.60 ± 0.13	1.7
2	5.0 ± 0.3	5	1.70 ± 0.04	1.7
3	10.6 ± 0.4	10	1.74 ± 0.03	1.7
4	20.8 ± 0.5	20	1.73 ± 0.02	1.7
5	0.7 ± 0.2	1	2.28 ± 0.27	2.0
6	5.3 ± 0.3	5	2.04 ± 0.05	2.0
7	10.6 ± 0.4	10	2.05 ± 0.04	2.0
8	21.0 ± 0.5	20	2.02 ± 0.02	2.0
9	0.6 ± 0.1	1	2.57 ± 0.26	2.3
10	5.5 ± 0.3	5	2.35 ± 0.06	2.3
11	10.7 ± 0.4	10	2.32 ± 0.04	2.3
12	21.2 ± 0.6	20	2.31 ± 0.03	2.3
13	0.6 ± 0.1	1	2.99 ± 0.24	2.6
14	5.3 ± 0.3	5	2.66 ± 0.06	2.6
15	-	10	2.62 ± 0.05	2.6
16	0.7 ± 0.2	1	3.2 ± 0.3	2.9
17	-	5	2.9 ± 0.1	2.9

Table 3.4: Given are the true simulated and the reconstructed flux and photon-index values for each bunch number as plotted in Fig. 3.36. The reconstructed flux is only listed when appropriate, when the probability p, Eq. (3.10), is less than 1. This is not the case for bunches 15 and 17. The flux normalisation at 1 TeV, $F_{1\mathrm{TeV}}$, is given in units of $10^{-11}\ \mathrm{cm}^{-2}\mathrm{s}^{-1}$.

Demonstration of systematic mis-reconstruction

The injection of simulated gamma-ray events into data files and the processing of these files with the standard analysis chain provides a good possibility to study systematic effects of the spectral reconstruction. One can artificially alter input parameters that are assumed to have an impact on the reconstructed spectra and study the outcome, compare it to the known simulated spectrum. Figure 3.37 shows the spectrum for bunch 12, which is already shown in Fig. 3.36, resulting from a mismatch between the θ^2 cut applied for the generation of the effective areas and the one used during analysis. For that purpose the size of the ON region, defined by the position of the simulated source in the sky and the θ^2 cut, was increased by 25% and a spectrum was generated. As one can see, this has the effect of steepening the spectrum, the photon index changes from 2.31 to 2.36, by $\approx 2\sigma$, and, more dramatically, the flux normalisation at 1 TeV is now $\approx 6\sigma$ off. These effects demonstrate the expected behaviour, due to the larger integration area when processing the data as compared to the generation of the effective areas, more gamma rays are reconstructed within the source region and the flux increases. The steepening is also expected, it is due to the energy dependence of the PSF. At small energies the PSF has long tails of mis-reconstructed events, increasing the angular cut around the source position slightly also increases the number of gamma rays after cuts significantly. For increasingly larger energies, as can also be seen from the figure, the increased θ^2 cut makes almost no difference any more, the cut efficiency of the nominal θ^2 cut is already close to 1 (cf. Fig. 3.8).

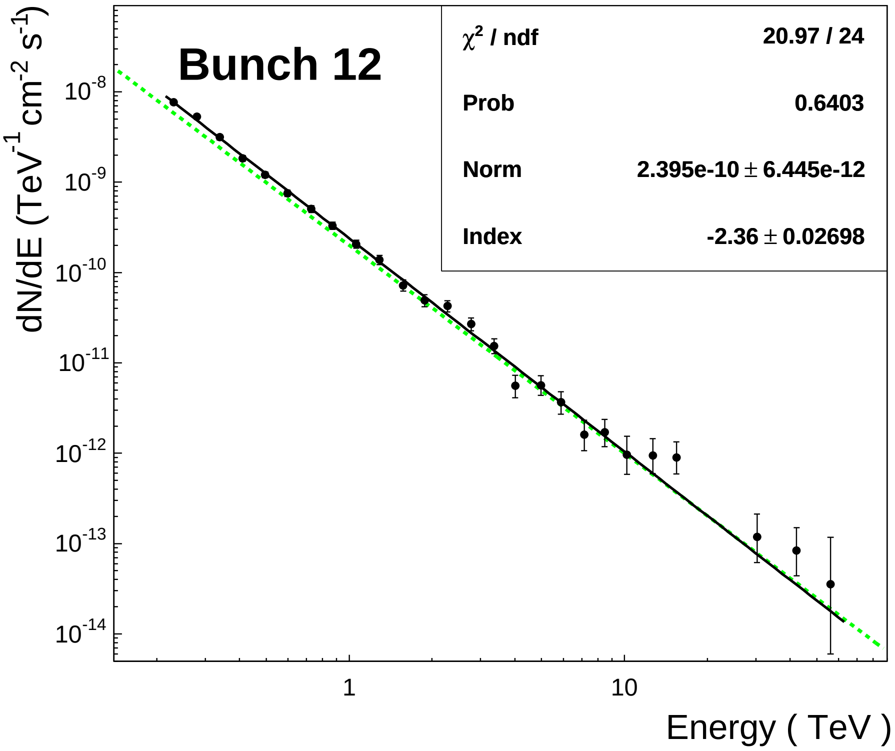

Figure 3.37: Plot to illustrate the effect of a non-understood gamma-ray efficiency on the spectrum. Shown is the spectrum of bunch 12, cf. Fig. 3.36, generated using point-source effective areas, but with an artificially increased θ^2 cut (see main text for details). The true simulated spectrum is drawn as green dashed line. One can clearly see that the reconstructed spectrum does not reproduce the simulated one.

4 RX J1713.7−3946 in VHE gamma rays

Having introduced all of the necessary tools to perform detailed analyses of extended gamma-ray sources, the analysis results of the H.E.S.S. data of RX J1713.7−3946 recorded in 2003, 2004, and 2005 will be presented in the following. The analysis of the 2003 data (published in Aharonian et al. (2004b)) was only the beginning of a phase of development of tools for the analysis of extended gamma-ray sources. Most of the software tools presented in chapter 3 were developed during the analysis of the 2004 RX J1713.7−3946 data set (Aharonian et al. 2005a). Moreover, with better data in 2004 came slightly different conclusions about the possible generation mechanisms of VHE gamma rays from RX J1713.7−3946. Instead of starting in the middle and presenting at first the analysis of the 2004 data, which is by far more detailed than the analyses of the data of the other two years, a chronological approach is followed here. First, the initial analysis of the 2003 data will be presented, accompanied by a short description of the analysis technique applied by the time of writing of the first publication (if it differs from the standard methods presented so far). After that, the results, still only from 2003, will be compared to the ones obtained by applying the latest analysis tools. This first section will conclude with a discussion and interpretation of the H.E.S.S. results as permitted by the first data set, not taking into account arguments and conclusions made in Aharonian et al. (2005a), from the second RX J1713.7−3946 data set. These will only be presented at the end of Section 4.2, after the detailed discussion of the main analysis work of this thesis, the analysis of the 2004 data set which demonstrates the full power of H.E.S.S. by means of resolved high-statistics gamma-ray morphology plots, spatially resolved spectral studies, and comparisons with multi-wavelength data. Hopefully, this order enables the reader to follow the development of the interpretation of the gamma-ray signal in a realistic way. At the end of this chapter a comparison and combination will be shown of the H.E.S.S. data taken on RX J1713.7−3946 over three years including the 2005 data set, whose analysis is still ongoing by the time of this writing. Therefore, parts of the results shown in Section 4.3 must be considered (and will be marked) as preliminary.

4.1 2003 data set

The first H.E.S.S. observations of RX J1713.7−3946 were performed between May and August 2003 during two phases of the construction and commissioning of the telescope system. During the first phase, two telescopes were operated independently with stereoscopic event selection done offline using GPS time stamps to identify coincident events. During the second phase, also using two telescopes, coincident events were selected in hardware using an array level trigger (Funk et al. 2004). The observations were performed in Declination wobble mode (see Section 3.6 for a discussion of observation modes) around the northwest shell of the SNR, namely around a position very close to the brightest spot in

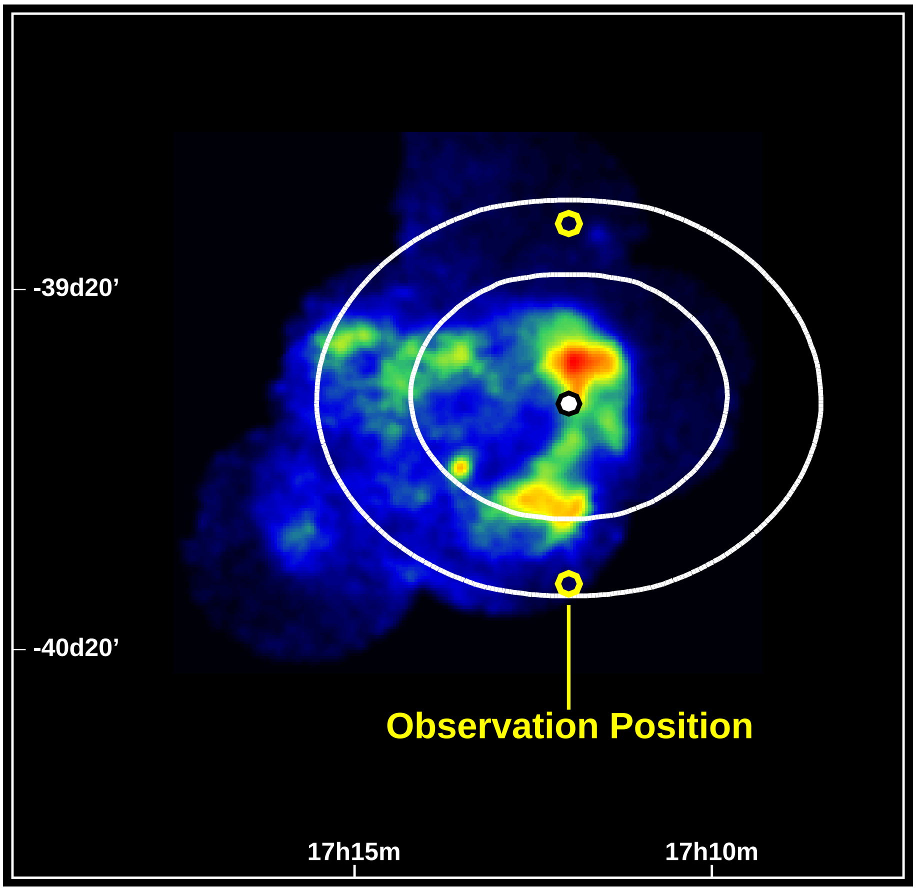

Figure 4.1: X-ray image of RX J1713.7−3946 (colour scale, 1-3 keV, from Uchiyama et al. (2002)). Note how the edges of the fields of view of ASCA appear in the image. The superimposed thick white contours indicate the 94% and 98% levels of the exposure weighted combined detection efficiency of H.E.S.S.for the 2003 data set. The target position in the western shell is indicated by a black-on-white circle, the two observation positions, with an offset of $\pm 0.5°$, are indicated as yellow circles. Here and in the following images, unless otherwise stated, an equatorial coordinate system will be used. The x-coordinate is Right Ascension, the y-coordinate is Declination.

hard X-rays (Koyama et al. 1997; Slane et al. 1999) which is coincident with the source position reported by the CANGAROO-II collaboration (Muraishi et al. 2000; Enomoto et al. 2002). The target position was at $\alpha_{\mathrm{J2000}} = 17\mathrm{h}12\mathrm{m}0\mathrm{s}$, $\delta_{\mathrm{J2000}} = -39°39'0''$, the wobble offset in Declination was $\pm 0.5°$. For background estimation purposes each pair of on-source observation runs was interspersed by one off-source observation run where the system was pointed to an empty field 30 minutes offset in Right Ascension from RX J1713.7−3946. The resulting effective exposure distribution, given by the product of the combined gamma-ray detection efficiency and the exposure time, is illustrated in Fig. 4.1. Shown is the ASCA X-ray measurement (Uchiyama et al. 2002) of RX J1713.7−3946 with superimposed white thick contour lines which indicate the 94% and 98% levels of the effective H.E.S.S. exposure. Also drawn in the figure are the two observation positions and the target position.

The total on-source observation time amounts to 26 hours, after run selection rejecting

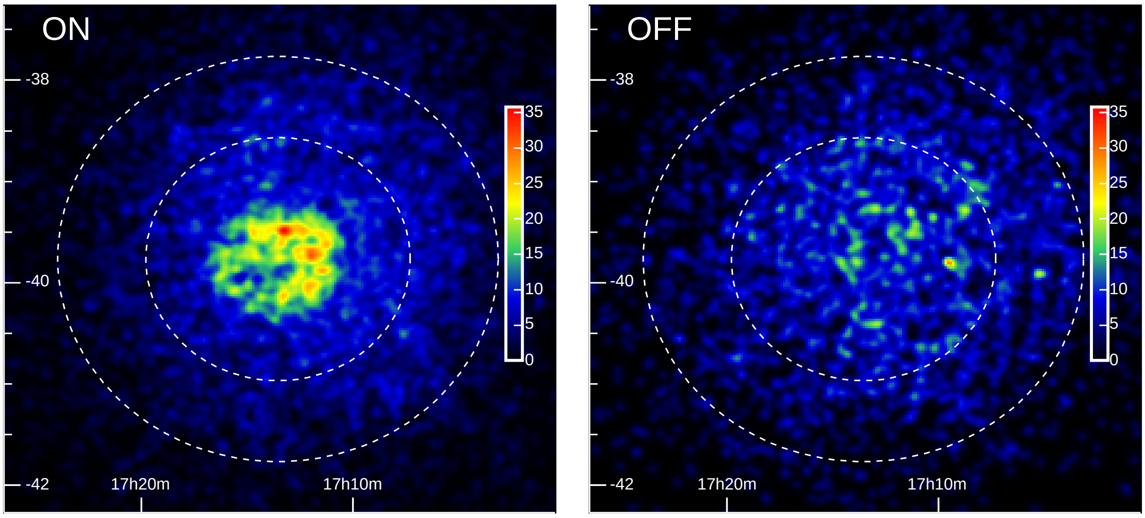

Figure 4.2: Full 2003 H.E.S.S. data set. The left hand side shows the Gaussian smoothed (2′) gamma-ray count map from all data taken on the RX J1713.7−3946 region in 2003. For comparison, the right hand side shows the OFF data taken during the same observation campaign, smoothed with the same Gaussian, and readily scaled for comparison. For both images the linear colour scale is in units of counts per smoothing radius. The dashed circles indicate the sky regions that were used for normalisation. Note that the OFF data were taken with an offset of $\pm 30\,\mathrm{min}$ in Right Ascension. For illustration purpose, the sky positions of the OFF events were transformed; the offset of $\pm 30\,\mathrm{min}$ was reverted.

data taken under bad weather conditions and dead time correction a data set of 18.1 live hours on source (divided up equally into wobble observations with positive and negative offset) is used in this analysis. The off-source observations amount to 8.3 live hours (slightly less than the expected one third of the whole data set due to rejected OFF runs which are affected by bad weather). At the trigger level (for the observation altitude angles of 60° to 75°), the energy thresholds for the two hardware configurations during observations (mentioned above) are 250 GeV (without the array level trigger) and 150 GeV (with the array level trigger). In the analysis presented here, the configuration *hard - 2tel* is used (see Table 3.1). A hard cut in the minimum size of camera images of 300 p.e. is used to select only well reconstructed showers. This primarily serves to drastically reduce the number of background cosmic-ray events, but it also homogenises these data taken with two different hardware configurations and it improves the angular resolution. Thus, systematic errors are greatly reduced at the expense of a higher energy threshold of $\sim$ 800 GeV for the combined data set.

4.1.1 Gamma-ray morphology

Figure 4.2 shows count maps centred on RX J1713.7−3946. The on-source data set is shown on the left hand side, for comparison the off-source data set taken with an offset of $\pm 30\,\mathrm{min}$ in Right Ascension from the target position (which is drawn in Fig. 4.1), is plotted on the right hand side. Note that for the sky map generation, the reconstructed directions of the OFF data were transformed into the sky field around the nominal position

Wobble offset $\Delta\delta_{\mathrm{J2000}}$	Live time (hours)	ON	OFF	α	Excess	Significance (σ)
+0.5°	9.05	1160	402	1.33	626.8	14.2
−0.5°	9.04	1285	471	1.29	678.9	14.7

Table 4.1: Given are event statistics of the original analysis of the 2003 data set. A cut on the minimum image size at 300 p.e. was applied. Numbers are obtained by accumulating events in the sky region covered by RX J1713.7−3946. Background counts are obtained from contemporaneously taken OFF data.

of RX J1713.7−3946, that is, the pointing offset of 30 min was reverted. Moreover, the OFF data were renormalised to account for the different live time and event rate due to sky brightness differences between the ON and OFF data set. The normalisation factor was determined as the ON-to-OFF ratio of events falling into a ring-shaped region, indicated by dashed circles in Fig. 4.2.

An extended region of gamma-ray excess in the centre of the field of view is clearly visible in the figure, spatially coincident with the position and extension of the SNR RX J1713.7−3946 as given in Green's catalog (Green 2004). The fact that the source is apparent without background subtraction or correction of the falloff of the gamma-ray detection efficiency towards the edges of the field of view demonstrates that the structures seen are not artefacts of the analysis, but real and visible in the raw post-cuts data. The SNR stands out clearly from the residual charged cosmic-ray background with a significance of 20 standard deviations when integrating ON events in a circle of 0.6° radius around the SNR centre (α_{J2000} = 17h13m33.6s, $\delta_{\mathrm{J2000}} = -39^\circ45'36''$), and OFF events in a sky region with the same size and shape. A complication arises for the determination of a significance for the whole SNR region from the observation strategy for RX J1713.7−3946 in 2003. Firstly, the wobble offset is too small to apply the *reflected-region* method, the SNR extends beyond the centre of the field of view. Secondly, the SNR centre was observed under different offsets with respect to the pointing direction of the system since the data were taken in (Declination) wobble mode around the west shell of the SNR (cf. Fig. 4.1). To account for the resulting acceptance differences between the data set taken with a positive and a negative wobble offset, these data were analysed separately with the full set of OFF data runs, respectively. For the integration of background events a sky region with similar system acceptance was chosen in both cases, located at the same offset to the pointing direction as the SNR. This procedure results for the hard cuts mentioned above in 2445 ON events, 873 OFF events, a normalisation factor $\alpha = 1.3$, and correspondingly $\approx$ 1300 gamma-ray excess events. The event statistics are listed separately for the two wobble positions in Table 4.1.

Figure 4.3 shows again a wide field of view count map, without background subtracted, centred on RX J1713.7−3946, as published in Aharonian et al. (2004b). Indicated are integration regions to be used for flux estimates from the northern, western, south-eastern, and interior part (given later, Section 4.1.2). An overall shell structure is clearly visible and coincides closely with that seen in X-rays, as can be seen from Fig. 4.4, where the gamma-ray count map is shown with superimposed contours of X-ray surface brightness. The X-ray measurement is again the ASCA data, 1−3 keV (Uchiyama et al. 2002). A direct spatial correlation between VHE gamma-ray and X-ray peaks is not apparent in Fig. 4.4.

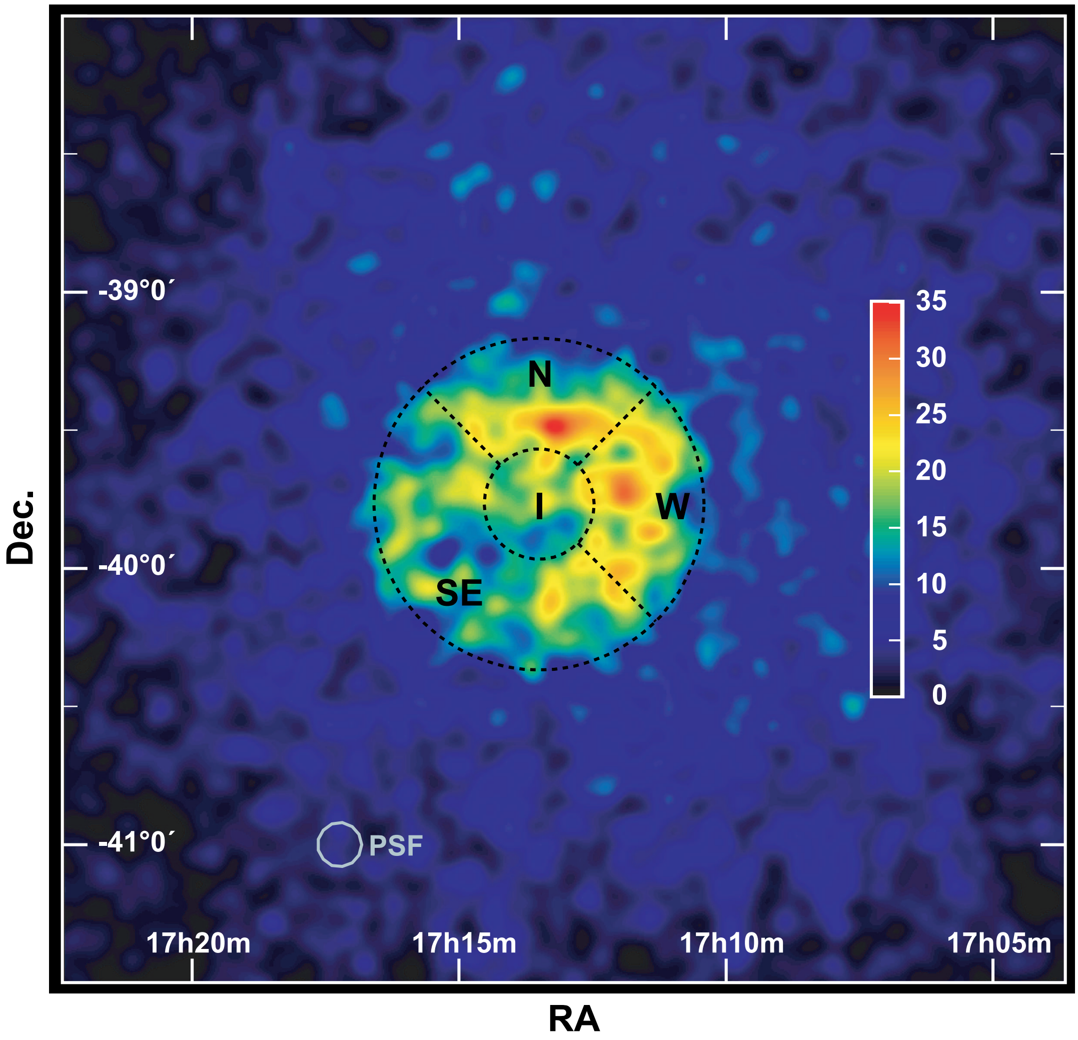

Figure 4.3: Wide field of view ($3.5° \times 3.5°$) gamma-ray count map around the SNR RX J1713.7−3946 (Aharonian et al. 2004b). Integration regions for gamma-ray flux estimates from the northern, western, south-eastern, and interior region are shown (dashed lines). The 68% containment radius of the gamma-ray PSF (cf. Section 3.4) for this particular data set is indicated in the bottom left-hand corner. Any structure smaller than that circle should not be considered as real since it is beyond the angular resolution of the instrument. The map itself is smoothed with a Gaussian of standard deviation $2'$, matched to the PSF. The linear colour scale is in units of counts per smoothing radius.

However, one should note that the statistical error of the H.E.S.S. 2003 data set is large (on the order of six counts for peak values of 36 counts in the gamma-ray image assuming Poisson statistics) and therefore detailed correlation studies have to await the analysis of the follow-up H.E.S.S. observations of this source (Section 4.2). The conclusion that on larger scales the northwest part of the shell of RX J1713.7−3946 exhibits an enhanced gamma-ray emission compared to the rest of the SNR remains nevertheless valid, and this resembles very much the picture seen in X-rays.

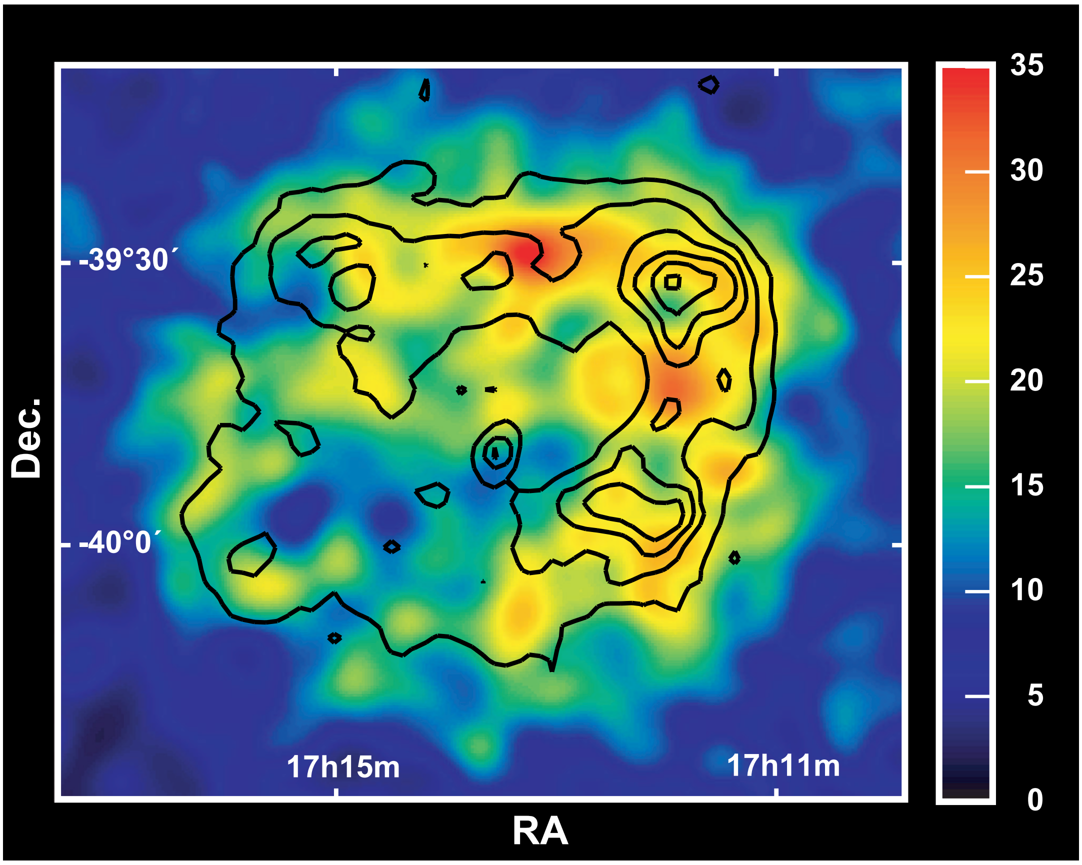

Figure 4.4: Gamma-ray image of the SNR RX J1713.7−3946 obtained with H.E.S.S.. The image is smoothed with a Gaussian as in Fig. 4.3, having the same scale in units of counts. The superimposed (linearly spaced) contours show the X-ray surface brightness as seen by ASCA in the 1-3 keV range for comparison (Uchiyama et al. 2002).

Comparison with the latest analysis

Initially, for the generation of a gamma-ray excess image, a procedure similar to the one described in Section 3.6.3 was applied, except that at the time of the first analysis only the OFF data taken as part of the RX J1713.7−3946 observation campaign could be used for the generation of the one-dimensional acceptance curve. In the early commissioning phase of H.E.S.S. in 2003 there were no appropriate OFF data sets with good zenith angle match available. Moreover, no offset interpolation was applied for the shape parameter calculation (cf. Section 3.2). Since *width* and *length* do depend moderately on the offset angle, this has the effect that MRSW and MRSL distributions are shifted with increasing offset angle towards positive values. Since the shape cuts are applied on these distributions (cf. Section 3.3), the cut efficiency is decreased in this case for both ON and OFF events.

The gamma-ray excess map produced with the "old" analysis is shown in Fig. 4.5, on the left-hand side. It looks very similar to the raw count map shown for example in Fig. 4.2. Also here, the SNR stands out very significantly. The right-hand side shows the re-analysis of the data set using the latest analysis chain. The one-dimensional lookups are taken

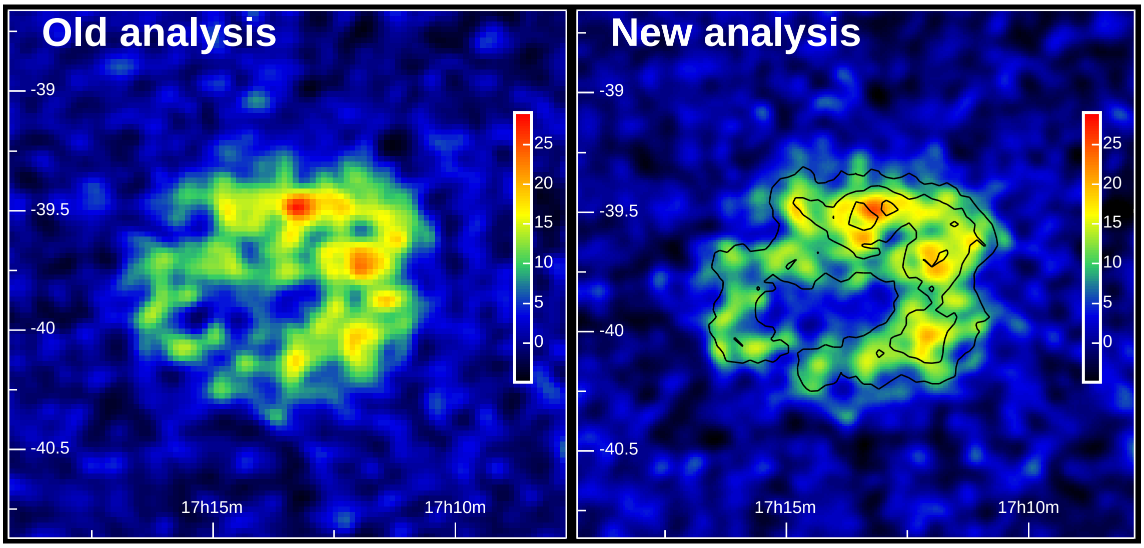

Figure 4.5: Gamma-ray excess images from the H.E.S.S. 2003 data set. Compared to each other are the initial analysis, published in November 2004 (Aharonian et al. 2004b), and the latest analysis developed for the 2004 data set with much deeper exposure. There is a very good agreement apparent. Significance contours are superimposed on the right-hand side with levels at 5, 7.5, and 10 σ. The significance of each point has been calculated assuming a point source at that position, integrating events within a circle of 0.1° radius.

from the complete set of H.E.S.S. empty-field observations collected during three years of running, and the shape parameters are interpolated linearly in offset. The resulting image nicely confirms the initial analysis, there is very good agreement apparent. Drawn additionally in Fig. 4.5 (right) are black contours of significance (5, 7.5, and 10 σ) to illustrate the significance of different features. The significance of the signal at each sky position is calculated integrating events within 0.1°. As can be seen, almost the entire shell exceeds 5σ, only a small portion in the southeast falls below this level. The entire bright northwest shell exceeds 7.5σ confirming once more the notion of enhanced gamma-ray emission from this part.

4.1.2 Gamma-ray energy spectrum

For the generation of an energy spectrum the data are processed as described above, the two subsets of data taken with different wobble offsets are processed separately, each with the complete set of RX J1713.7−3946 OFF runs. ON events are integrated within a radius of 0.6° around the SNR centre, OFF events are taken from a region of the same size, shape, and position with respect to the pointing direction of the OFF runs. The normalisation factor is determined from the observed rate in both ON and OFF runs in a ring well outside the inner region of the field, as shown in Fig. 4.2. A differential gamma-ray flux is then derived by applying an event-wise effective-area weight based on the offset and zenith angle of the event (see Section 3.7). The effective area is determined from gamma-ray point-source simulations covering primary energies up to 20 TeV. The two separately determined gamma-ray fluxes of the two subsets of data are then combined to yield the final spectrum

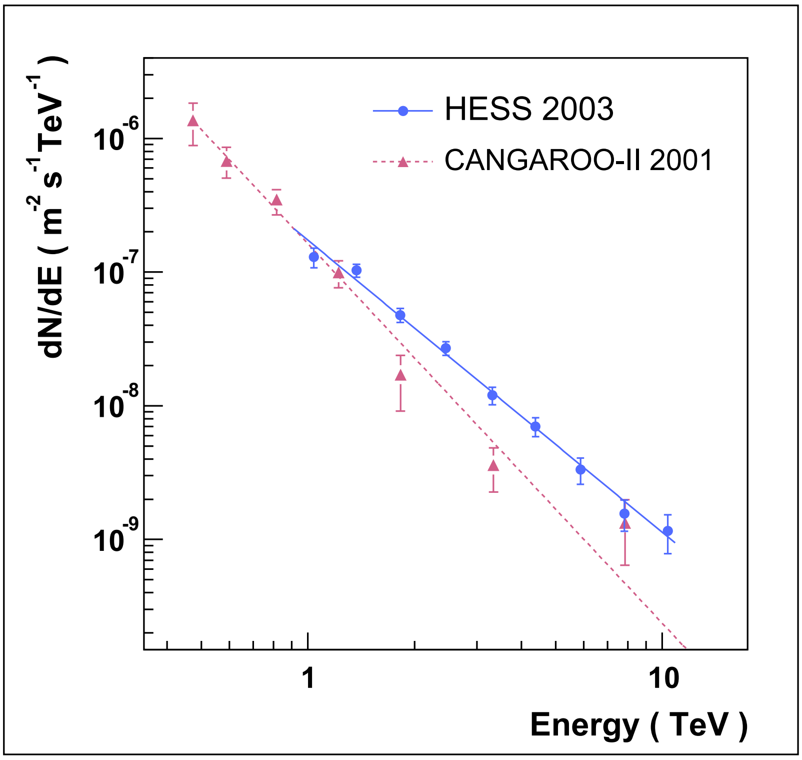

Figure 4.6: 2003 gamma-ray energy spectrum of RX J1713.7−3946. These data (indicated as solid circles) can be described by a power law, the best fit result is drawn as blue solid line. The spectral data points reported by the CANGAROO-II collaboration (Enomoto et al. 2002) for the northwestern part of the remnant are shown for comparison as red triangles, and the best fit result as a dashed red line. Error bars denote $\pm 1\sigma$ statistical errors.

Bin energy (TeV)	Flux (cm^{-2}s^{-1})	Bin range (TeV)
1.0	$(1.30 \pm 0.22) \times 10^{-11}$	0.89 – 1.19
1.4	$(1.03 \pm 0.11) \times 10^{-11}$	1.19 – 1.58
1.8	$(4.78 \pm 0.57) \times 10^{-12}$	1.58 – 2.11
2.5	$(2.70 \pm 0.31) \times 10^{-12}$	2.11 – 2.82
3.3	$(1.20 \pm 0.18) \times 10^{-12}$	2.82 – 3.76
4.4	$(7.01 \pm 1.12) \times 10^{-13}$	3.76 – 5.01
5.9	$(3.32 \pm 0.74) \times 10^{-13}$	5.01 – 6.68
7.8	$(1.56 \pm 0.41) \times 10^{-13}$	6.68 – 8.91
10.4	$(1.16 \pm 0.38) \times 10^{-13}$	8.91 – 11.89

Table 4.2: Flux values of the initial analysis of the 2003 data (shown in Fig. 4.6).

of the whole SNR. The exact flux values are listed in Table 4.2, the points are plotted in Fig. 4.6. The spectrum appears rather hard, the data are well described by a power law, $\mathrm{dN/dE} \propto \mathrm{E}^{-\Gamma}$, the best fit result is $\Gamma = 2.19 \pm 0.09\,(\mathrm{statistical}) \pm 0.15\,(\mathrm{systematic})$ with $\chi^2 = 5.9$ with 7 degrees of freedom. The integral flux of the whole SNR above 1 TeV is $(1.46 \pm 0.17\,(\mathrm{statistical}) \pm 0.37\,(\mathrm{systematic})) \times 10^{-11}$ photons cm^{-2} s^{-1} which corresponds to ≈ 70% of the Crab nebula flux as measured by H.E.S.S.. The integral energy flux between 1 TeV and 10 TeV is estimated to be 5.3×10^{-11} erg cm^{-2} s^{-1}, which is an order of magnitude smaller than the non-thermal X-ray flux. There is no evidence for a cutoff in the data, but if one nevertheless fits a power law with exponential cutoff, $\mathrm{dN/dE} \propto \mathrm{E}^{-\Gamma_c} \mathrm{e}^{-\mathrm{E}/\mathrm{E_c}}$, the minimum acceptable value of $\mathrm{E_c}$ is 4 TeV with a very hard photon index of $\Gamma_c = 1.5$. For comparison, the photon index reported by the CANGAROO-II collaboration for the northwest part of the SNR is $\Gamma = 2.84 \pm 0.15 \pm 0.20$ (Enomoto et al. 2002). The difference between the two measurements amounts to 3.7σ including just the statistical errors and 2.13σ including both statistical and systematic errors. They are thus in marginal statistical agreement. However, if one takes further into account that the CANGAROO-II measurement covered only a part of the SNR, there would be even less agreement if one was to scale down the CANGAROO-II flux points accordingly.

Although only at the edge of being possible due to limited statistics, attempts to perform a spatially resolved spectral analysis have also been performed. The integrated fluxes above 1 TeV from the regions indicated in Fig. 4.3 are: $(3.0 \pm 0.6) \times 10^{-12}$ cm^{-2} s^{-1} from the northern (N) rim, $(4.1 \pm 0.8) \times 10^{-12}$ cm^{-2} s^{-1} from the western (W) rim, $(5.9 \pm 1.0) \times 10^{-12}$ cm^{-2} s^{-1} from the southeastern (SE) rim, and $(1.7 \pm 0.6) \times 10^{-12}$ cm^{-2} s^{-1} from the interior (I). The mean gamma-ray brightnesses per unit solid angle from these regions (that is, the flux values normalised to the area covered) are in the ratio $1 : 1.4 : 1 : 1.2$ ($N : W : SE : I$). These values might contradict the visual impression that the northwestern shell of the SNR is brighter than the rest. However, one should keep in mind that the statistics of the data sample are limited. Moreover, the different areas were chosen for geometric reasons. Dim regions are included in the seemingly brighter northern and western area. More detailed spatially resolved flux studies will be presented below by means of the 2004 data set (Section 4.2).

Comparison with the latest analysis

Figure 4.7 shows two spectra, one stems from the initial analysis and is already plotted in Fig. 4.6. Compared to that the latest analysis extends to much larger energies, a direct consequence of the application of offset interpolation for shape parameters, and, more importantly, the usage of simulations extending up to 100 TeV, not only 20 TeV as for the old analysis. Apart from that the spectra are in very good agreement in the range from 1 to 10 TeV. The event statistics of the re-analysis of the 2003 data set are listed in Table 4.3. For comparison also the values from the initial analysis are listed. For that purpose the numbers given in Table 4.1 separately for the two wobble subsets are combined. The significance quoted for the old analysis is the quadratic sum of the individual significance which is therefore slightly overestimated because in the old-style analysis, the one set of 21 OFF runs that was taken contemporaneously in 2003 was used twice for both subsets of ON runs. For the re-analysis, a procedure which was already followed for the *ON/OFF* analysis of the 2004 data to obtain a cross-check of the spectrum, see Section 3.6.4, was applied[1]: one OFF run is selected for each ON run, observed at as closely matching zenith angles as possible, to supply a background estimate. The OFF runs are selected from the large sample of empty-field observations obtained with H.E.S.S. during the first three years of running, all of them are taken in the nominal system configuration with four telescopes.

---

[1] Note again that an *ON/OFF*-type analysis has to be applied because of the wobble offset of observations of 0.5° of the 2003 data set, which does not allow the usage of the *reflected-region*-type analysis.

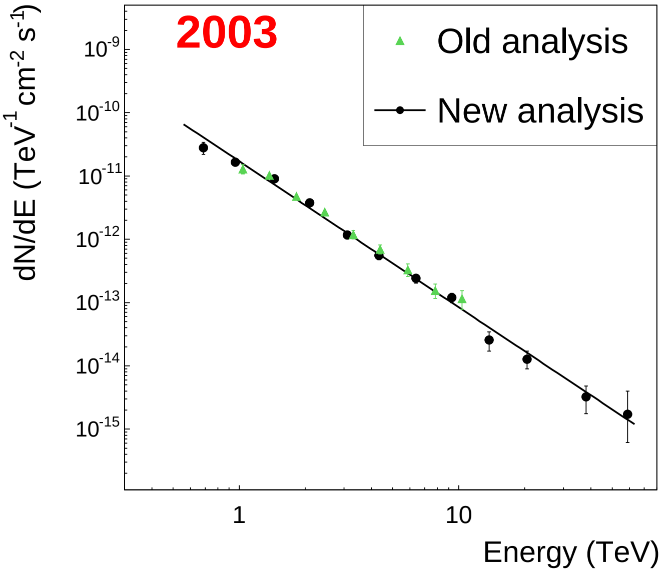

Figure 4.7: The spectrum published in Aharonian et al. (2004b) is shown (green triangles) and compared to the spectrum from the same data set but determined after re-analysis (black circles). The best fit of a power law (black line) to the spectrum of the re-analysis yields $dN/dE = (1.78 \pm 0.10) \times 10^{-11}$ cm^{-2} s^{-1} $\cdot$ $E^{-2.29\pm0.04}$ with a $\chi^2/\mathrm{dof} = 25.15/10$.

Analysis	ON	OFF	α	Excess	Significance
new	3194	1764	1.0	1432	20.5
old	2445	873	≈ 1.3	1306	≈ 20

Table 4.3: Event statistics of the re-analysis of the 2003 data set. The configuration *hard - 2tel* (see Table 3.1) is applied with a cut on the minimum image size at 300 p.e.. For comparison, also the combined values from the old analysis, given in Table 4.1, are shown.

To mimic the system configuration of 2003, of the ON data, where only two telescopes were operational, only these two telescopes are actually used in the analysis of the OFF runs.

4.1.3 Conclusions

The first H.E.S.S. measurement of the SNR RX J1713.7−3946 presented above is unique in different regards. Experimentally it is a significant step forward and marks the dawn of a new astronomical imaging technique operating at photon energies some 12 decades higher than those of visible light. The image shown in Fig. 4.3 is the first ever resolved gamma-ray image in VHE gamma rays. It is the first case where the identification of an active, that is accelerating, celestial gamma-ray source (as opposed to a passive cloud or density enhancement, merely penetrated by energetic particles which are accelerated elsewhere) can be based, not just on a positional coincidence, but on the image morphology. Only with the sensitivity achieved and the wide field of view realised by experiments like

E (TeV)	ON	OFF	α	σ	Flux ($\mathrm{cm^{-2}s^{-1}}$)	Range (TeV)
0.69	516	372	1.0	4.7	$(2.8 \pm 0.6) \times 10^{-11}$	0.54 – 0.80
0.96	495	271	1.0	8.2	$(1.6 \pm 0.2) \times 10^{-11}$	0.80 – 1.17
1.44	445	176	1.0	11.2	$(9.1 \pm 0.8) \times 10^{-12}$	1.17 – 1.71
2.1	320	94	1.0	11.5	$(3.8 \pm 0.3) \times 10^{-12}$	1.71 – 2.51
3.1	204	80	1.0	7.6	$(1.2 \pm 0.2) \times 10^{-12}$	2.51 – 3.68
4.3	155	54	1.0	7.2	$(5.5 \pm 0.8) \times 10^{-13}$	3.68 – 5.40
6.4	103	31	1.0	6.5	$(2.4 \pm 0.4) \times 10^{-13}$	5.40 – 7.90
9.3	74	18	1.0	6.1	$(1.2 \pm 0.2) \times 10^{-13}$	7.90 – 11.59
13.7	28	10	1.0	3.0	$(2.6 \pm 0.9) \times 10^{-14}$	11.59 – 16.99
20.5	15	2	1.0	3.4	$(1.3 \pm 0.4) \times 10^{-14}$	16.99 – 24.89
38.1	19	8	1.0	2.2	$(3.2 \pm 1.6) \times 10^{-15}$	24.89 – 53.46
58.9	2	0	1.0	1.7	$(1.7 \pm 2.3) \times 10^{-15}$	53.46 – 64.71

Table 4.4: Flux values of the re-analysis of the 2003 data as shown in Fig. 4.7. The columns are energy, ON counts, OFF counts, normalisation α, significance in standard devations σ, the gamma-ray flux, and the bin range in TeV.

H.E.S.S. it is now possible to image extended objects such as RX J1713.7−3946 in VHE gamma rays.

The second major step forward, maybe towards a solution of the longstanding puzzle of the origin of Galactic cosmic rays, is the unequivocal proof for acceleration of particles to multi-TeV energies in the shell of an SNR. Although the shell morphology seen in X-rays and the remarkable power-law spectrum without detectable line emission are already most plausibly explained by non-thermal processes, the synchrotron radiation of 100-TeV electrons (Koyama et al. 1995; Ellison et al. 2001; Uchiyama et al. 2003), alternative explanations are not absolutely ruled out (Laming 1998): it was suggested that electrons can be heated at the shock wave to very high temperatures thereby emitting thermal Bremsstrahlung and producing power-law spectra. Line emissions could at the same time be suppressed in the ASCA bandpass of ≈ 1-10 keV if the ejecta plasma would purely consist of carbon. The detection of VHE emission correlated with the shell of the SNR provides now unambiguous proof. The extension of the gamma-ray spectrum shown in Fig.4.6 to energies of 10 TeV implies for the parent particle population energies of 100 TeV and beyond, whether they are of hadronic or leptonic nature. These high energies are consistent with ideas of particle acceleration in young SNR shocks.

The question if the VHE gamma rays contain a component due to accelerated protons interacting with the ambient gas is a difficult one. The contribution of this component should be significantly enhanced when the supernova shell overtakes nearby dense molecular clouds (Aharonian et al. 1994), as seems to be the case for this object. The CO data (Fukui et al. 2003; Moriguchi et al. 2005) suggest that a cloud is indeed interacting with the northwestern part of the SNR, where a striking spatial coincidence between the CO density peaks and the regions of peak X-ray emission is seen. The X-ray data (Cassam-Chenaï et al. 2004b) also indicate significant absorption column densities in the western part of the remnant, at values about twice those to the east. These findings fit qualitatively with the gamma-ray image presented here, where VHE emission is seen from the whole SNR shell with enhanced flux values from the northwestern side.

Given the recent estimates of the distance to the source of 1 kpc (Fukui et al. 2003; Cassam-Chenaï et al. 2004a), if a significant part of the TeV flux were to be formed by interactions of cosmic-ray nuclei with gas atoms in the cloud with density n exceeding 100 cm^{-3}, the energetics implied by the gamma-ray flux and spectrum would be a few times $10^{49}\ n^{-1}$ erg between 10 and 100 TeV. This is consistent with the picture of an SNR origin of Galactic cosmic rays involving about 10% conversion efficiency of the mechanical energy of the explosion into non-thermal particles. This assumes an E^{-2} production power law in the SNR from several GeV to about one PeV[2]. Moreover, the gamma-ray morphology is qualitatively what one would expect from particles accelerated at the shock, interacting and radiating in the compressed post-shock region. The extension of the energy spectrum up to energies of 10 TeV and beyond requires an efficient accelerator boosting particles up to energies of 100 TeV and beyond. The source RX J1713.7−3946 is located in a complex environment, it seems to interact with molecular clouds of different densities and the VHE emission might emerge from various processes. Without doubt there can be a contribution from energetic electrons though the inverse Compton process, especially from low-density regions of the SNR. At the elevated densities likely to exist in the northwest rim, π^0-decays following proton-proton interactions, but also non-thermal Bremsstrahlung of electrons, could make significant contributions. Although disentangling the relative contributions of the various processes is difficult, it might be possible through spatially resolved multi-wavelength studies, the first attempts of which will be presented below using the data of the complete H.E.S.S. array.

4.2 2004 data set

The H.E.S.S. observations of RX J1713.7−3946 in 2004 were conducted with the complete four-telescope array between April and July 2004. The observations were mostly performed in wobble mode around the SNR centre. As opposed to 2003, where observations were taken with a wobble offset of 0.5°, in Declination only, around the northwest shell of the SNR, in 2004 a pointing strategy with a wobble offset of ±0.7° in Declination and Right Ascension around the SNR centre was applied to cover the whole remnant more uniformly and to enable usage of the *reflected-region* background model for spectral analysis. Towards the end of the observation campaign, pure on-source pointings in which the centre of the SNR was coincident with the system centre were additionally performed. In each of the five pointings RX J1713.7−3946, roughly 1° in diameter, was fully contained in the $\approx 5°$ field of view of the system. The resulting effective exposure distribution (the product of the detection efficiency and the exposure) is illustrated in Fig. 4.8, analogue to Fig. 4.1 for the 2003 data. The five observation positions are also drawn. The ASCA X-ray measurement (Uchiyama et al. 2002), this time the 1-5 keV band, is shown as colour scale with superimposed white, almost circular contours indicating the 94% and 98% levels of the effective exposure. The observation strategy for this data set combined with the detector efficiency results in a very flat plateau in the region of the SNR; from the centre to the boundaries the relative gamma-ray detection efficiency decreases by only about 5%, which is a great advantage compared to ASCA, for example. Not only is the SNR fully contained in all of the five pointing positions, but one can also disregard for most purposes

---

[2] Further details about the calculation of the involved energetics will be given below in Section 4.2.5 for the 2004 data.

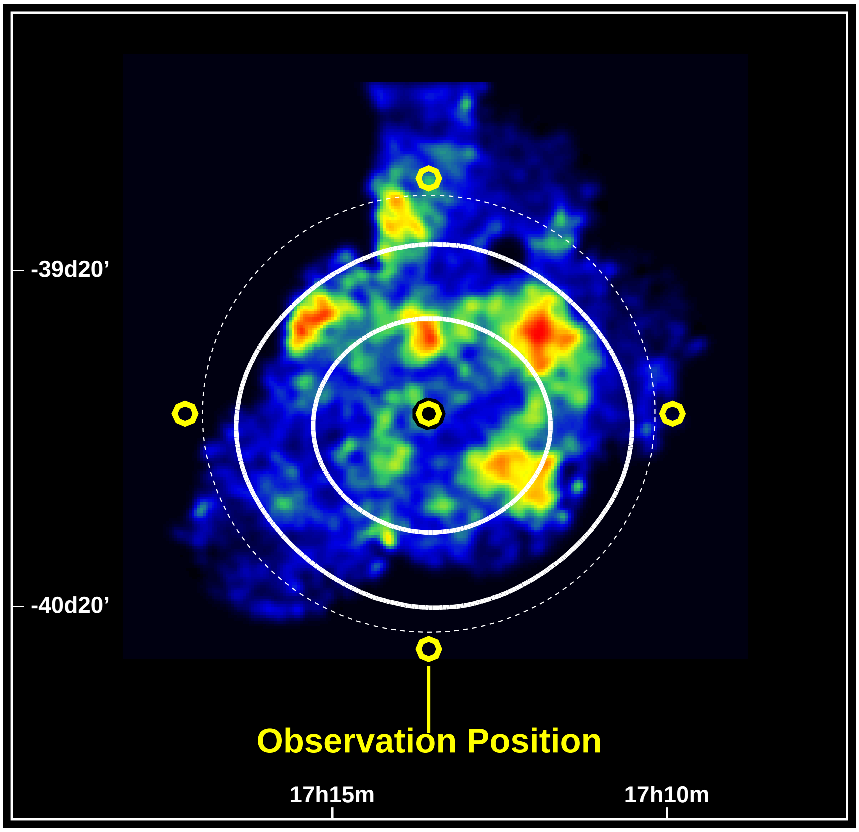

Figure 4.8: X-ray image of RX J1713.7−3946 (colour scale, 5-10 keV, from Uchiyama et al. (2002)). The superimposed thick white contours indicate the 94% and 98% levels of the detection-efficiency weighted H.E.S.S. exposure, analogue to Fig. 4.1. The five observation positions are indicated by yellow circles, the target position, the centre of the SNR, is indicated by a black solid circle. The dashed line denotes the region that is used for spectral analysis of the whole SNR. Note how the relative gamma-ray detection efficiency between the centre region and the edges of the SNR differs only by ≈ 5%.

the modest change in relative detection efficiency from one region of the SNR to another.

The 2004 data comprise a total exposure time of 40 hours. Rejecting data taken under bad weather conditions, 33 hours of live observation time remain for the analysis. The zenith angle of observations ranged from 16° to 56° with a mean of 26°; about 68% of the data were taken at small zenith angles between 16° to 26°. The energy threshold (defined by the peak gamma-ray detection rate for a given source spectrum after all gamma-ray selection cuts, see Section 3.6.4) of the system increases with zenith angle. For the observations presented here, assuming a spectrum appropriate for RX J1713.7−3946, the threshold was ≈ 180 GeV at 16°, ≈ 340 GeV at 40°, and ≈ 840 GeV at 56°.

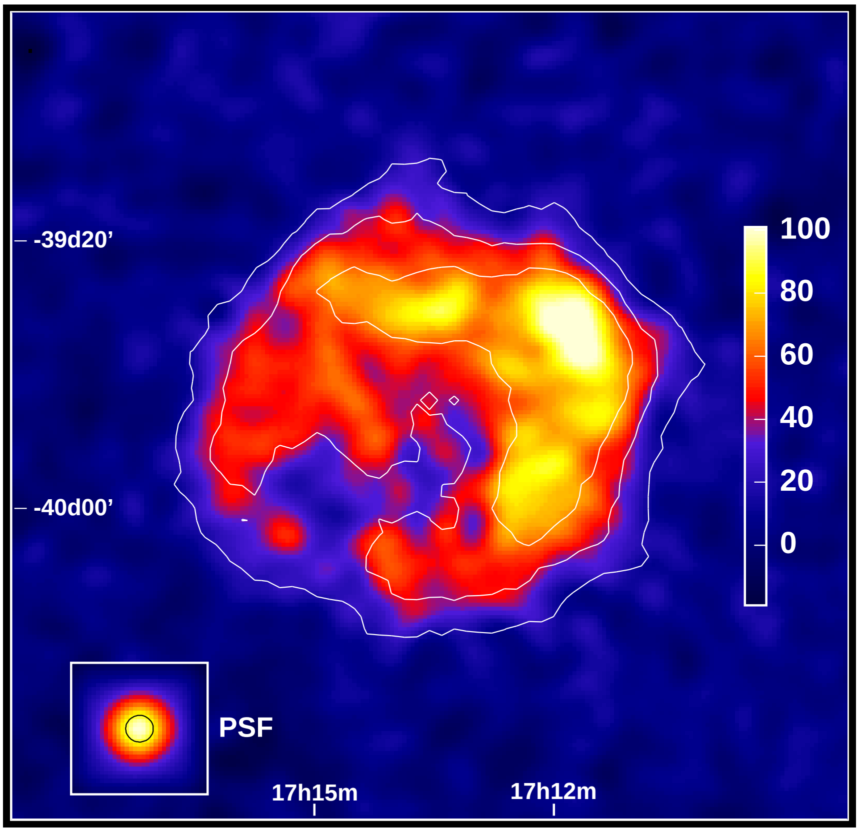

Figure 4.9: Gamma-ray image of RX J1713.7−3946. The linear colour scale is in units of excess counts per smoothing radius. The white contour lines indicate the significance of the different features, the levels are linearly spaced and correspond to 5, 10, and 15σ, respectively. The significance of each point has been calculated assuming a point source at that position, integrating events within a circle of 0.1° radius. In the lower left hand corner a simulated point source is shown as it would appear in this particular data set (taking the point spread function and the smoothing into account) along with a black circle of $2'$ radius denoting the σ of the Gaussian the image is smoothed with.

4.2.1 Morphology

Figure 4.9 shows a $2^\circ \times 2^\circ$ field of view around RX J1713.7−3946. The *hard* cuts are applied resulting in an angular resolution of $\approx 0.08^\circ$ (see Section 3.4, Fig. 3.11). The corresponding energy range is $\approx$ 300 GeV to $\approx$ 40 TeV. The overall gamma-ray appearance resembles a shell morphology with bright emission regions in the western and northwestern part where the SNR is believed to impact molecular clouds (Fukui et al. 2003; Moriguchi et al. 2005). It is worth noting that there is a possible gamma-ray void in the central-southeastern region. The event statistics for both sets of cuts are listed in Table 4.5. The cumulative significance for the whole SNR is about 40σ with the *hard* cuts, which corresponds to an excess of $\approx$ 7300 events from the region of RX J1713.7−3946. Drawn as white lines in Fig. 4.9 are in addition the contours of significance of the gamma-ray signal (levels correspond to 5, 10, and 15σ). The significance has been calculated considering events

Configuration	ON	OFF	α	Excess	Significance (σ)	Live time (hrs)
std	115141	75829	1.3	15370	30.8	30.5
hard	17932	7725	1.4	7277	39.4	33.0

Table 4.5: Event statistics of the 2004 data set are given, for the *std* cuts used for the spectral analysis and the *hard* cuts used for investigations for the morphology. Note that the live time difference between the two configurations comes from the fact that pure on-source runs were not used for the spectral analysis.

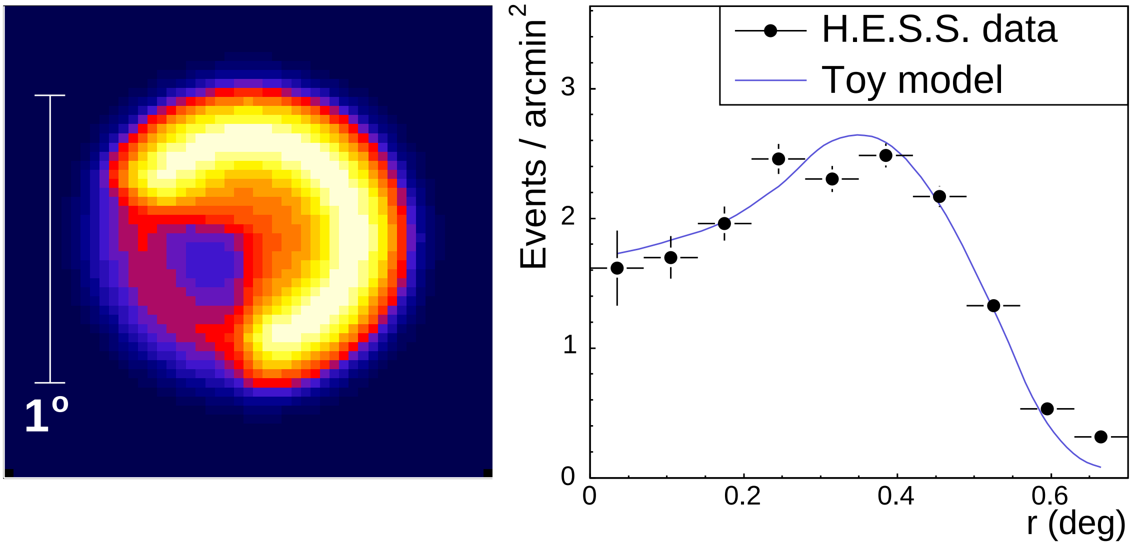

Figure 4.10: Shown is a simple geometrical model for the emission from a thick sphere matched to the dimensions and relative fluxes of RX J1713.7−3946. **Left:** Two-dimensional projection of a thick and spherical radiating shell, 1° in diameter, smoothed with the H.E.S.S. point spread function. **Right:** Radial profile from the geometrical model compared to the H.E.S.S. data profile of RX J1713.7−3946. The centre coordinates used for the data plot are $\alpha_{\mathrm{J2000}} = 17\mathrm{h}13\mathrm{m}33.6\mathrm{s}$, $\delta_{\mathrm{J2000}} = -39°45'36''$. The geometrical model profile has been scaled to the same area as the data profile.

that fall within an angle of 0.1° of each trial source position. Thus, the contours quantify the significance for each point as if there was a point source at that position. The brightest parts of the SNR exceed 20σ. Except for the void structure, where the significance just exceeds 5σ, most of the remaining emission regions are well above 10σ.

From the gamma-ray image presented here it is clear that the emission regions cannot be distributed homogeneously in the *sphere* RX J1713.7−3946. The image is neither rotational symmetric nor does it exhibit a shallow peak towards the centre. Instead, a shell seems to be apparent in the northern, and western to southwestern part. Apart from that, there is more or less uniform emission found in the rest of the SNR with a slight flux increase towards the southeastern boundary. This resembles very much the image one would expect from a thick spherical shell radiating gamma rays with enhanced emission on one side, as is illustrated in Fig. 4.10 where a geometrical model of a thick radiating sphere

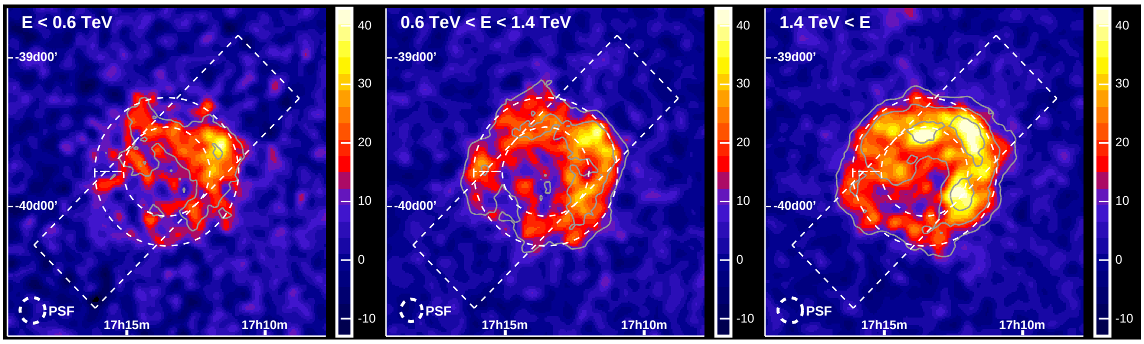

Figure 4.11: Morphology of RX J1713.7−3946 as it appears at different energies. Shown from left to right are gamma-ray excess images with energies of $E < 0.6$ TeV, $0.6\ \mathrm{TeV} < E < 1.4$ TeV, and $1.4\ \mathrm{TeV} < E$. The *hard* cuts are applied. Drawn additionally as grey lines are contours of significance, linearly spaced at 5, 10, 15σ (as in Fig. 4.9). The resolution of each data subset is indicated in the bottom left-hand corner. The dashed box (dimensions $2^\circ \times 0.6^\circ$) and ring ($r_1 = 0.3^\circ$, $r_2 = 0.5^\circ$) are used for obtaining the one-dimensional distributions in Fig. 4.12. For all three images the linear colour scale is in units of excess counts per smoothing radius of $2'$.

is presented. Shown on the left-hand side of the figure is the two-dimensional projection of a thick and spherical radiating shell, 1° in diameter, smoothed with the H.E.S.S. point spread function. Adapted empirically to match the radial shape of the H.E.S.S. data set, the dimensions of the geometrical sphere are 5.5 pc for the inner and 10 pc for the outer boundary if one adopts a distance of 1 kpc to the source, the presumed distance to RX J1713.7−3946. The emissivity in the northern, western, and southwestern part is a factor of two higher than in the southeast and east. The right-hand side of Fig. 4.10 compares radial profiles from the H.E.S.S. data and the geometrical model to each other. The good match in shape between the data and the toy-model profile lends support to the assumption that indeed it is the shell of RX J1713.7−3946 which radiates gamma rays.

Energy dependent morphology

For the investigation of spatial variation of spectral shape, two approaches can be taken. One is the determination and comparison of energy spectra in different regions of the SNR. Results of this approach will be presented in Section 4.2.3. The other possibility is the search for an energy dependence of the gamma-ray morphology. Any difference found in spectral shape between two regions must inevitably appear in the morphology when splitting a data set up into distinct energy bands, given sufficient event statistics. To look for this, the data are split up in different energy bands and then processed separately in each band. Because of the energy dependence of the system acceptance, one-dimensional radial acceptance models for the background subtraction have to be generated for each energy band (see Section 3.6.2, Fig. 3.20). Resulting gamma-ray excess maps are shown in Fig. 4.11. The distinct energy bands are $E < 0.6$ TeV, $0.6\ \mathrm{TeV} < E < 1.4$ TeV, and $1.4\ \mathrm{TeV} < E$ (left to right in the figure). In all three cases the *hard* cuts are applied. The energy bands were chosen such that each band represents about a third of the full data

Data set	$\langle\phi_{\rm z}\rangle$	$\langle\psi\rangle$	R_{68}	ON	OFF	α	Sign. (σ)
All energies	27°	0.73°	0.075°	17932	7725	1.4	39.4
$E < 0.6$ TeV	20°	0.76°	0.080°	7993	4523	1.3	15.1
0.6 TeV $< E <$ 1.4 TeV	27°	0.73°	0.070°	4846	1816	1.4	25.4
1.4 TeV $< E$	37°	0.7°	0.081°	5093	1386	1.5	30.7

Table 4.6: Listed are the 68% containment radii resulting from the application of *hard* cuts, together with the mean zenith and offset angle ant the event statistics of events falling into the region of RX J1713.7−3946. Numbers are given for the whole data set, and for different subsets, split up in the energy bands that are shown in Fig. 4.11.

set (taking all events in the field of view after cuts). All images are also smoothed with a Gaussian of 2′, the same smoothing as in Fig. 4.9 for consistency, due to reduced event statistics the images are slightly under-smoothed here. The colour scale in all three cases is set to the same minimum and maximum value to make the images readily comparable to each other. However, before comparing images resulting from different subsets of data to each other, one has to account for possibly different angular resolutions and different signal-to-noise ratios[3]. Otherwise pronounced differences in both of these quantities might mimic different morphological features which are not real. For the determination of the angular resolution of a data set, one has to take the basic dependencies of the PSF into account (cf. Section 3.4): these are the exact analysis cuts and the distribution of zenith and offset angles of the data. The angular resolution, taken as the 68% containment radius of the PSF, is determined from the set of simulations at fixed zenith and offset angles, processed with the *hard* cuts, averaging the simulated PSF histograms based on the zenith and offset angle event distribution of the actual data set (weighting the simulated histograms appropriately). The resulting PSF histogram for the whole 2004 RX J1713.7−3946 data set for *hard* cuts is shown in Section 3.4, Fig. 3.11. Table 4.6 lists the angular resolutions, the mean zenith and offset angle and the event statistics of the whole data set and for the different energy bands. In Fig. 4.11, the resolution of each band is indicated in the lower left hand corner of the images. As can be seen from the table, differences in the angular resolutions of the data sets are small, at maximum for the medium energies the difference is on the order of 10%, a mismatch which can be neglected. Thus, the images are readily comparable to each other. Note that with increasing energy the mean zenith angle of events increases, too. Therefore, the increased angular resolution of high energy events is somewhat compensated by this zenith-angle effect, for all energies the angular resolution is similar.

From the superimposed contours of significance in Fig. 4.11 (which are, as in Fig. 4.9, point-source significances), and from the total significance of the gamma-ray signal integrated over the whole remnant (given in Table 4.6), one can see that the signal-to-noise ratio changes drastically. The significance of the signal in the low-energy image is evidently smaller than in the two high-energy images. The shell-like morphology of the SNR is blurred by fluctuations. Correspondingly, the significance contours indicate that only the bright northwestern half is significant in this energy band. In contrast, the whole remnant sticks out significantly in the two high-energy bands. Most of the northwestern parts exceed

---

[3] This would equally be true when comparing images resulting from different sets of cuts to each other.

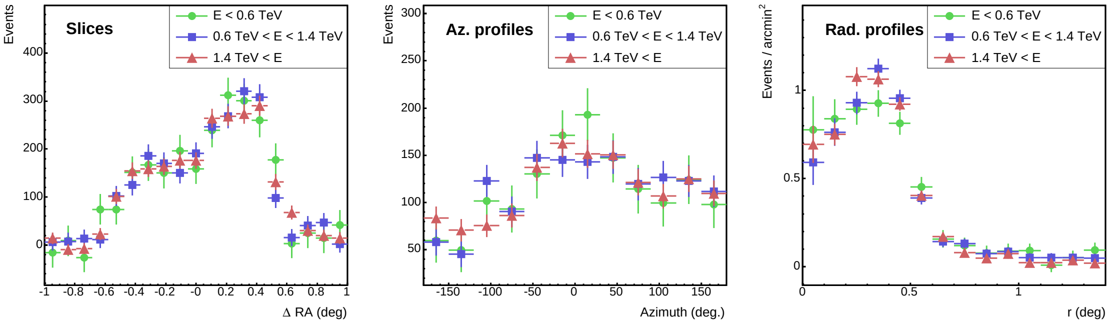

Figure 4.12: Shown are one-dimensional distributions of the three energy bands. **Left:** Slices taken within a rotated box running through the SNR region, see main text for details. Plotted are events versus angular distance to the centre. **Middle:** Azimuth profiles integrated in a thick ring covering the shell of RX J1713.7−3946. The azimuthal angle of the events is calculated with respect to the SNR centre ($\alpha_{\mathrm{J2000}} = 17\mathrm{h}13\mathrm{m}33.6\mathrm{s}$, $\delta_{\mathrm{J2000}} = -39^\circ 45' 36''$). **Right:** Radial profiles around the centre of the SNR. All distributions are generated from the raw, non-smoothed and acceptance-corrected gamma-ray excess images. All distributions are scaled to the area of the high-energy band to account for the signal-to-noise differences.

10σ, the brightest spots even exceed 15σ for energies beyond 1.4 TeV. From these two-dimensional excess images it remains difficult to decide if there are changes of morphology with increasing energy. The remnant does seem to emit gamma rays more uniformly with increasing energy, but the significance of certain features is not apparent from the figure. A proper treatment of the changing signal-to-noise ratio can be achieved by means of one-dimensional distributions where one can take the errors on the measurement into account. Figure 4.12 shows three types of one-dimensional excess distributions of the SNR region, always comparing the three energy bands to each other. In all three cases, the distributions are obtained from the raw, non-smoothed excess maps. The errors in each two-dimensional bin – basically $\sqrt{N_{\mathrm{ON}}}$ since the background is estimated from the one-dimensional radial lookups which are assumed to have infinite statistic – are propagated into the one-dimensional distributions. The left-hand plot of the figure shows slices in a $2^\circ \times 0.6^\circ$ rotated box, indicated as dashed line in Fig. 4.11. For each event contained in this box, the angular distance between the event and the SNR centre, projected onto the axis running through the centre with the same orientation as the box (45° from horizon, anti-clockwise), is plotted. The small- and medium-energy histograms are scaled to the same area as the high-energy histogram, scaling factors are 1.6 and 1.4, respectively. In the plot, the northwest shell sticks out clearly at distances of +0.2-0.4° from the SNR centre in all three energy bands. There are no significant differences apparent.

The middle plot of Fig. 4.12 shows "azimuth profiles" of the SNR shell. Plotted are events that fall into an 0.2°-wide ring covering the shell of RX J1713.7−3946, see Fig. 4.11 where the ring is indicated with dashed lines. Events are binned according to their azimuthal angle with respect to the SNR centre. 0° corresponds to the west part of the shell, 90° is north or upward in the figure, −90° is south or downward. Scaling factors for the small- and medium-energy histograms are 1.6 and 1.3, respectively. Also here the west shell appears as brightest region in all energy bands, there are no significant variations with

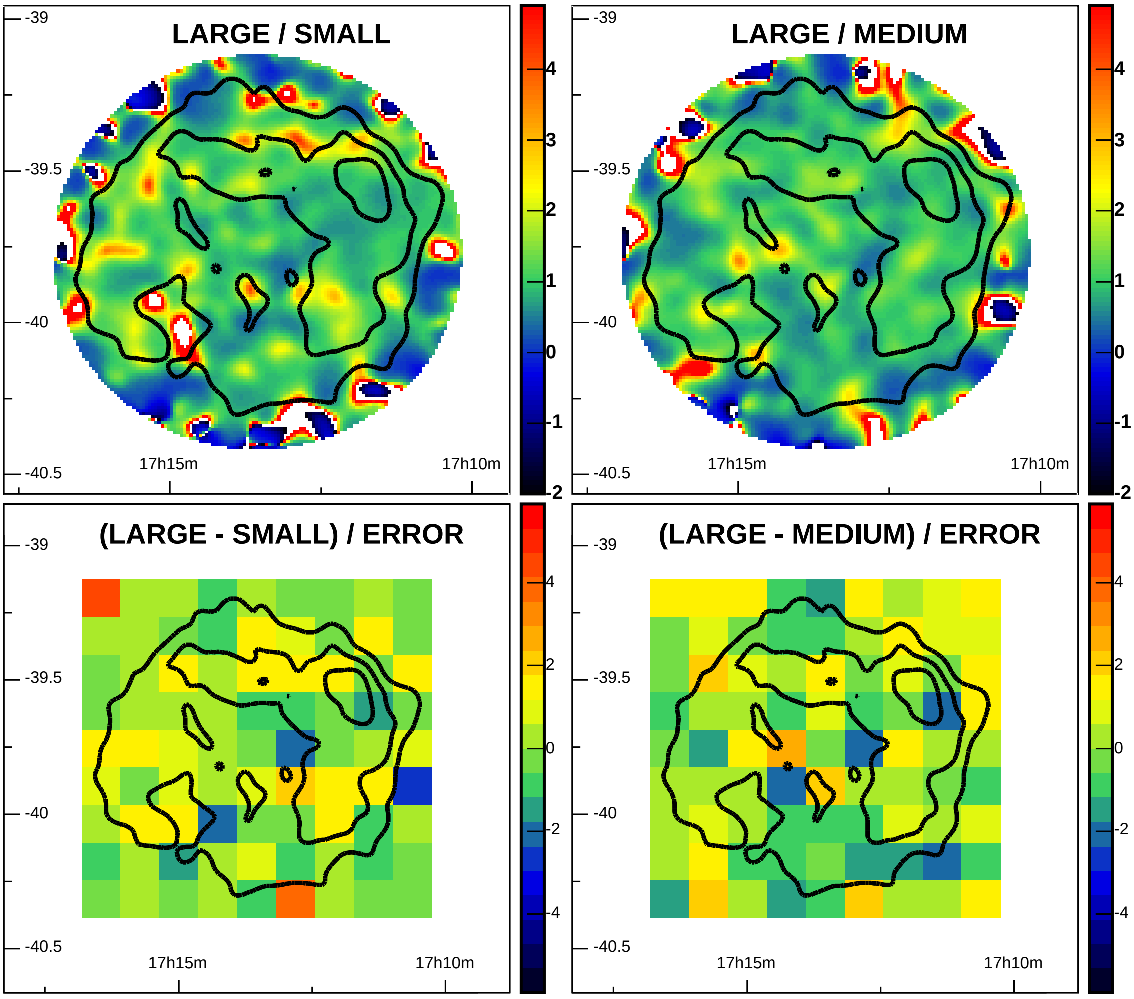

Figure 4.13: Shown are two-dimensional maps comparing the three energy bands to each other. Overlaid on all four images are gamma-ray excess contours from the combined data set for orientation. In the top row, maps of hardness ratio are drawn. These are the ratio of the smoothed acceptance-corrected high-energy image, $E > 1.4$ TeV, to the smoothed medium- (0.6 TeV $< E < 1.4$ TeV, right-hand side) and the small-energy image ($E < 0.6$ TeV, left-hand side). The bottom row shows the corresponding maps of residuals, defined as the difference of excess counts per bin, divided by the combined error. For these maps, non-smoothed acceptance-corrected images are used, with coarse binning. Note that for all four maps, the lower-energy images are re-normalised to account for signal-to-noise differences.

energy. The final plot on the right-hand side of Fig. 4.12 shows radial profiles of the SNR region analogue to Fig. 4.10, where the profile of the combined data set is shown. For the radial profiles the scaling factors are 1.5 and 1.3 for the small- and medium-energy histograms, respectively. In all three energy bands the bright shell sticks out clearly at 0.4° distance from the centre, and the bands are well compatible with each other.

Other possibilities for testing the compatibility of subsets of data exist, in a somewhat two-dimensional fashion. Essays of these are shown in Fig. 4.13. Plotted in the top row are maps of *hardness ratio*, that is, the ratio of the smoothed $E > 1.4$ TeV to the $E < 0.6$ TeV image on the left-hand side, and the ratio to the medium-energy image on the right-hand side. The bottom row shows *residuals maps*, produced from coarse, non-smoothed and acceptance-corrected excess images of RX J1713.7−3946 in the different energy bands. The maps show the difference of excess counts per bin, divided by the quadratic sum of the errors on the excess counts. Hence, the maps are the residuals between energy bands in units of standard deviation.

Also from the representations of Fig. 4.13 there is no clear difference of morphology in distinct energy bands apparent. While there are localised regions with indications for somewhat larger deviations between energy bands, these are within statistical uncertainties of the measurement, and there is no general trend for regions with different spectral shapes apparent. Further studies of the spectral shape in different regions of the SNR will be undertaken in Section 4.2.3.

4.2.2 Spectral analysis of the whole SNR

The energy spectrum of the whole SNR is determined by integrating events within 0.65° radius around the centre of the SNR, $\alpha_{\mathrm{J2000}} = 17\mathrm{h}13\mathrm{m}33.6\mathrm{s}$, $\delta_{\mathrm{J2000}} = -39°45'36''$, as indicated by a dashed circle in Fig. 4.8. The *reflected-region* technique is applied for the background modeling (see Section 3.6.4): OFF events are selected from a reflected region in the same field of view. To ensure optimum match in the offset distributions of ON and OFF events, runs taken directly on the source, where no appropriate OFF region can be selected in the same field of view, are discarded from the spectral analysis. Accordingly, the total live time reduces slightly to 30.5 hours. The *std* cuts adopting a *size* cut of 80 p.e. are applied for the spectral analysis. The resulting event statistics are given in Table 4.5, the cumulative significance of the SNR region amounts to $\approx 31\sigma$. Note that the normalisation factor, $\alpha = 1.3$, is noticeably larger than 1 because one of the OFF regions, the one north to RX J1713.7−3946 (cf. Fig. 3.27, where ON and OFF regions, together with the different observation positions are drawn), covers a gamma-ray source discovered in the H.E.S.S. Galactic plane survey (Aharonian et al. 2005e), HESS J1713−381. The OFF region of all runs taken with a wobble offset of +0.7° is therefore excluded from the analysis of the 2004 data set, implying $\alpha > 1$.

The resulting spectrum of the whole SNR is shown in Fig. 4.14, complete numbers for all flux points (including for each energy bin ON and OFF events, the normalisation α, and the flux values with statistical and systematic errors) are listed in Table 4.8. The data is in excellent agreement with the previous measurement in 2003, which covered the energy range from 1 TeV to 10 TeV. The latest data span more than two orders of magnitude in energy, from 190 GeV to 40 TeV. The best fit of a power law with energy dependent photon index is plotted (the exact formula is given below). It describes the data reasonably well. Table 4.7 summarises fits of different spectral shapes to the data. Four spectral shapes are fit to the data:

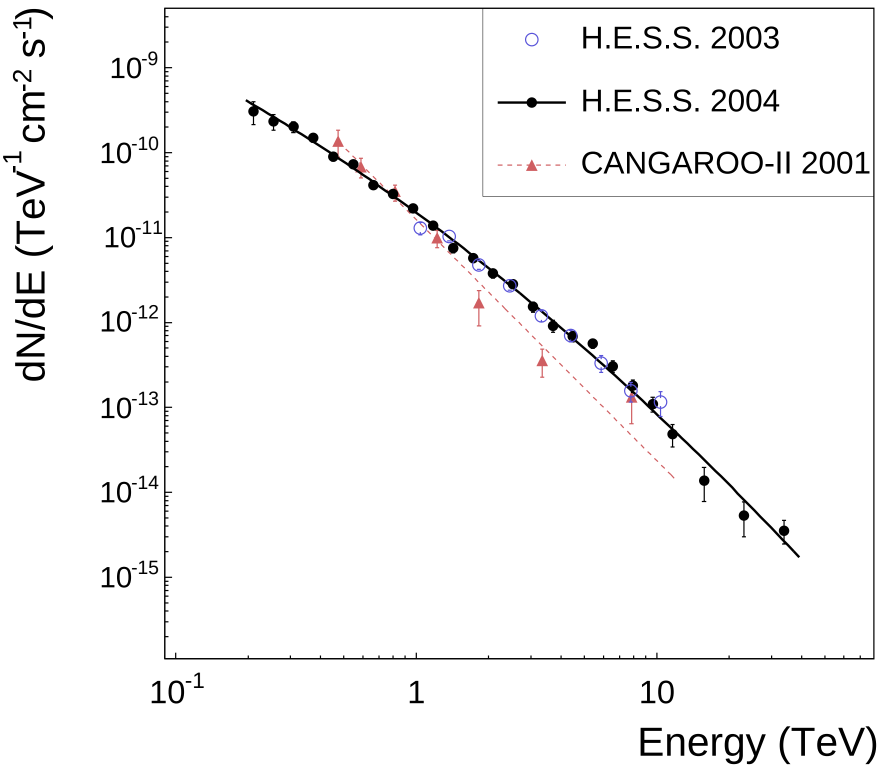

Figure 4.14: Differential gamma-ray energy spectrum of RX J1713.7−3946, for the whole region of the SNR (solid black circles). The best fit of a power law with energy dependent photon index is plotted as black line. For comparison the H.E.S.S. 2003 data points from Fig. 4.6 are also shown (blue open circles). Note the vast increase in energy coverage due to the increased sensitivity of the complete telescope array. The spectrum ranges now from 190 GeV to 40 TeV, spanning more than two decades in energy. The data points reported by the CANGAROO-II collaboration (Enomoto et al. 2002) for the northwestern part of the remnant are also shown as red triangles, the corresponding best fit result as dashed red line. Error bars are $\pm 1\sigma$ statistical errors.

$I_0 \left(\frac{E}{1\ \mathrm{TeV}}\right)^{-\Gamma}$	Simple power law with photon index Γ.
$I_0 \left(\frac{E}{1\ \mathrm{TeV}}\right)^{-\Gamma} \exp\left(-\frac{E}{E_\mathrm{c}}\right)$	Power law with exponential cutoff E_c.
$I_0 \left(\frac{E}{1\ \mathrm{TeV}}\right)^{-\Gamma+\beta\ \log\frac{E}{1\ \mathrm{TeV}}}$	Power law with exponent depending logarithmically on energy.
$I_0 \left(\frac{E}{E_\mathrm{B}}\right)^{-\Gamma_1} \left(1+\left(\frac{E}{E_\mathrm{B}}\right)^{1/S}\right)^{S\,(\Gamma_2-\Gamma_1)}$	Broken power law with transition from Γ_1 to Γ_2 at break energy E_B; S: sharpness of transition.

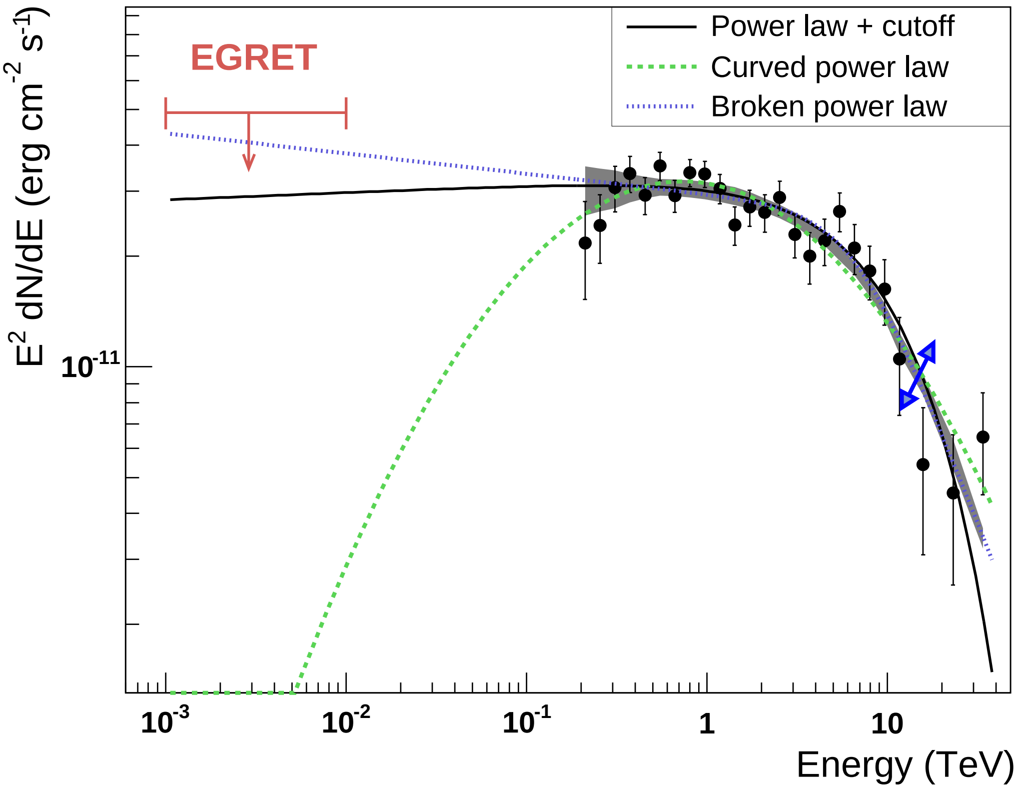

Figure 4.15: H.E.S.S. energy spectrum of RX J1713.7−3946. Plotted are the H.E.S.S. points with their $\pm 1\sigma$ statistical errors in an energy flux diagram. The three curves (specified in Table 4.7) are the best fit results of a power law with an exponential cutoff, a power law with energy dependent photon index, and a broken power law, extrapolated to 1 GeV to enable comparisons with the EGRET upper limit in the range of 1–10 GeV. The shaded grey band represents the systematic uncertainty on the measurement, originating from the uncertainty on the background estimation. The blue arrow indicates the 20% systematic uncertainty on the energy scale, which might shift the whole curve in the given direction.

In all cases, I_0 is the differential flux normalisation, the energies E are normalised at 1 TeV and photon indices are specified with Γ. The pure power law does not provide a reasonable description of the data, the three alternative shapes describe the data significantly better. Amongst the alternative spectral shapes, none is significantly favoured over the others. At the highest energies, above 10 TeV, there is still a significant gamma-ray flux in excess of 6σ, the significance of all flux points is listed in Table 4.8. It should be noted, though, that in order to draw strong conclusions about the high-energy shape of the spectrum, more data with better statistics at the high-energy end of the spectrum are needed.

The spectrum reported by the CANGAROO-II collaboration (Enomoto et al. 2002) for the northwest part of the SNR is also shown in Fig. 4.14. From a power-law fit to the data they quoted a photon index $\Gamma = 2.84 \pm 0.15\,(\text{statistical}) \pm 0.20\,(\text{systematic})$ and a differential flux normalisation at 1 TeV $I_0 = (1.63 \pm 0.15 \pm 0.32) \times 10^{-11}\,\text{cm}^{-2}\,\text{s}^{-1}\,\text{TeV}^{-1}$. The difference between the two spectra is somewhat larger than the quoted errors of the measurements. However, the CANGAROO-II spectrum is only for a part of the remnant.

I_0	Fit Parameters			χ^2 (d.o.f.)	$I(> 1$ TeV)
17.1 ± 0.5	$\Gamma = 2.26 \pm 0.02$			85.6 (23)	13.5 ± 0.4
20.4 ± 0.8	$\Gamma = 1.98 \pm 0.05$	$E_{\mathrm{c}} = 12 \pm 2$		27.4 (22)	15.5 ± 1.1
19.7 ± 0.6	$\Gamma = 2.08 \pm 0.04$	$\beta = -0.30 \pm 0.04$		25.5 (22)	15.6 ± 0.7
$0.4^{+0.6}_{-0.2}$	$\Gamma_1 = 2.06 \pm 0.05$	$\Gamma_2 = 3.3 \pm 0.5$	$E_{\mathrm{B}} = 6.7 \pm 2.7$	26.2 (21)	15.4 ± 0.8

Table 4.7: Fit results for different spectral models. The differential flux normalisation I_0 and the integral flux above 1 TeV ($I(> 1\ \mathrm{TeV})$) are given in units of $10^{-12}\,\mathrm{cm}^{-2}\,\mathrm{s}^{-1}\,\mathrm{TeV}^{-1}$ and $10^{-12}\,\mathrm{cm}^{-2}\,\mathrm{s}^{-1}$, respectively. The power-law fit is clearly an inappropriate description of the data, a power law with an exponential cutoff (row 2), a power law with an energy dependent photon index (row 3), and a broken power law (row 4; in the formula, the parameter $S = 0.4$ describes the sharpness of the transition from Γ_1 to Γ_2 and it is fixed in the fit) are equally likely descriptions of the H.E.S.S. data. Note that when fitting a broken power law to the data, some of the fit parameters are highly correlated.

Moreover the CANGAROO-II collaboration has recently revised their systematic errors upwards. For example, the Galactic Centre photon index, which was initially given as 4.6 ± 0.5 (Tsuchiya et al. 2004), was recently quoted as $4.6^{+5.0}_{-1.2}$ (Katagiri et al. 2005).

Figure 4.15 illustrates the three spectral shapes that were found to describe the data reasonably well. The three curves are extrapolated to 1 GeV to compare them with the EGRET upper limit on the energy flux of 4.9×10^{-11} erg cm^{-2} s^{-1}, ranging from 1 GeV to 10 GeV, centred at 2.9 GeV. The limit was determined at the H.E.S.S. position of RX J1713.7−3946 by modelling and subtracting the known EGRET source 3EG 1714−3857 (Hartman et al. 1999), assuming that 3EG 1714−3857 is not linked to the gamma-ray emission of RX J1713.7−3946. Since the H.E.S.S. location is in close vicinity of 3EG 1714−3857 (actually it is overlapping), this procedure could only be carried out successfully above 1 GeV (see also Section 4.2.5 for a comment on the EGRET upper limit). The systematic error band for the H.E.S.S. data was obtained as described in Section 3.6.4. It is centred on the mean value of the three fit curves and represents the systematic error due to background uncertainties and the spectral analysis technique only. The energy scale is an energy independent uncertainty; its scale and the direction the curve is shifted to are marked with a blue arrow at one representative position (at 15 TeV). It is worth noting that the systematic uncertainty on the background has a considerable impact on the first few flux points because of the smaller signal-to-noise ratio (as compared to points at higher energies). For the spectrum shown here the systematic uncertainty is $\approx 18\%$ for the two lowest-energy points; it decreases rapidly with increasing energy being well below 10% at 350 GeV (see also Table 4.8).

4.2.3 Spatially resolved spectral analysis

The results of the spatially resolved spectral analysis are shown in Fig. 4.16. It shows the distribution of photon indices over the SNR resulting from a power-law fit. The spectra

#	E (TeV)	ON	OFF	α	σ	Flux ($\mathrm{cm}^{-2}\mathrm{s}^{-1}$)	Δ_{sys} (%)	Range (TeV)
1	0.21	15336	10846	1.35	3.4	$(3.06 \pm 0.91) \times 10^{-10}$	19	0.19 – 0.23
2	0.25	13583	9772	1.30	4.8	$(2.33 \pm 0.49) \times 10^{-10}$	18	0.23 – 0.28
3	0.31	10599	7161	1.33	7.1	$(2.02 \pm 0.29) \times 10^{-10}$	7	0.28 – 0.34
4	0.37	7691	4965	1.32	8.8	$(1.50 \pm 0.17) \times 10^{-10}$	7	0.34 – 0.41
5	0.45	5594	3553	1.31	8.6	$(8.95 \pm 1.03) \times 10^{-11}$	5	0.41 – 0.50
6	0.55	4994	2964	1.30	11.1	$(7.33 \pm 0.65) \times 10^{-11}$	4	0.50 – 0.60
7	0.66	4226	2581	1.28	9.9	$(4.16 \pm 0.42) \times 10^{-11}$	3	0.60 – 0.73
8	0.80	3967	2222	1.31	11.7	$(3.28 \pm 0.28) \times 10^{-11}$	2	0.73 – 0.88
9	0.97	3218	1704	1.32	12.0	$(2.22 \pm 0.18) \times 10^{-11}$	8	0.88 – 1.06
10	1.18	2926	1615	1.31	10.7	$(1.38 \pm 0.13) \times 10^{-11}$	1	1.06 – 1.29
11	1.42	2456	1438	1.30	8.3	$(7.50 \pm 0.89) \times 10^{-12}$	5	1.29 – 1.56
12	1.72	2313	1332	1.29	8.8	$(5.72 \pm 0.65) \times 10^{-12}$	2	1.56 – 1.89
13	2.09	1835	1028	1.29	8.5	$(3.78 \pm 0.44) \times 10^{-12}$	3	1.89 – 2.28
14	2.52	1451	744	1.29	9.4	$(2.83 \pm 0.30) \times 10^{-12}$	6	2.28 – 2.77
15	3.06	1135	616	1.29	7.3	$(1.53 \pm 0.21) \times 10^{-12}$	2	2.77 – 3.35
16	3.70	885	487	1.29	6.2	$(9.13 \pm 1.45) \times 10^{-13}$	5	3.35 – 4.05
17	4.48	678	337	1.29	6.9	$(6.86 \pm 0.99) \times 10^{-13}$	2	4.05 – 4.91
18	5.42	540	225	1.28	8.2	$(5.63 \pm 0.68) \times 10^{-13}$	7	4.91 – 5.94
19	6.56	396	177	1.28	6.3	$(3.06 \pm 0.47) \times 10^{-13}$	1	5.94 – 7.19
20	7.95	252	101	1.28	5.9	$(1.81 \pm 0.30) \times 10^{-13}$	6	7.19 – 8.70
21	9.62	197	83	1.28	4.9	$(1.10 \pm 0.22) \times 10^{-13}$	1	8.70 – 10.53
22	11.64	116	53	1.28	3.3	$(4.84 \pm 1.43) \times 10^{-14}$	10	10.53 – 12.75
23	15.72	124	69	1.28	2.3	$(1.37 \pm 0.59) \times 10^{-14}$	7	12.75 – 18.69
24	23.04	44	19	1.27	2.3	$(5.35 \pm 0.23) \times 10^{-15}$	9	18.69 – 27.39
25	33.76	25	5	1.27	3.2	$(3.53 \pm 0.11) \times 10^{-15}$	6	27.39 – 40.14
26	49.48	21	17	1.27	-0.09	$(-8.1 \pm 0.0) \times 10^{-17}$	-	40.14 – 58.82
27	72.51	3	1	1.25	0.8	$(4.79 \pm 6.33) \times 10^{-16}$	-	58.82 – 86.20

Table 4.8: Energies and flux values of the 2004 gamma-ray spectrum of RX J1713.7−3946, as shown in Fig. 4.14, are listed here. The columns are flux-point number (#), energy, ON counts, OFF counts, normalisation α, significance in standard devations σ, the gamma-ray flux, the systematic uncertainty as determined in Section 3.6.4, and the bin range in TeV. Note that the last two points, # 26 and # 27, are not included in the spectrum in Fig. 4.14. Only points exceeding 2σ are shown in the figure.

are determined in rectangular regions, denoted 1–14, each $0.26^\circ \times 0.26^\circ$ in dimension. The fit range is limited to 8 TeV to account for (and avoid when fitting) the deviation from a power law seen in the spectrum of the whole remnant. Table 4.9 summarises the fit results. There is a significant flux variation over the SNR. From the brightest region in the northwest to a relatively dim one in the central part, the flux varies by more than a factor of two. There is no significant difference in spectral shape apparent, the photon indices agree with each other within statistical and systematic errors. The distribution of photon indices has a mean value of 2.09 with a root-mean-square of 0.07. This is well compatible with the spectrum of the whole SNR when the fit range is also restricted to

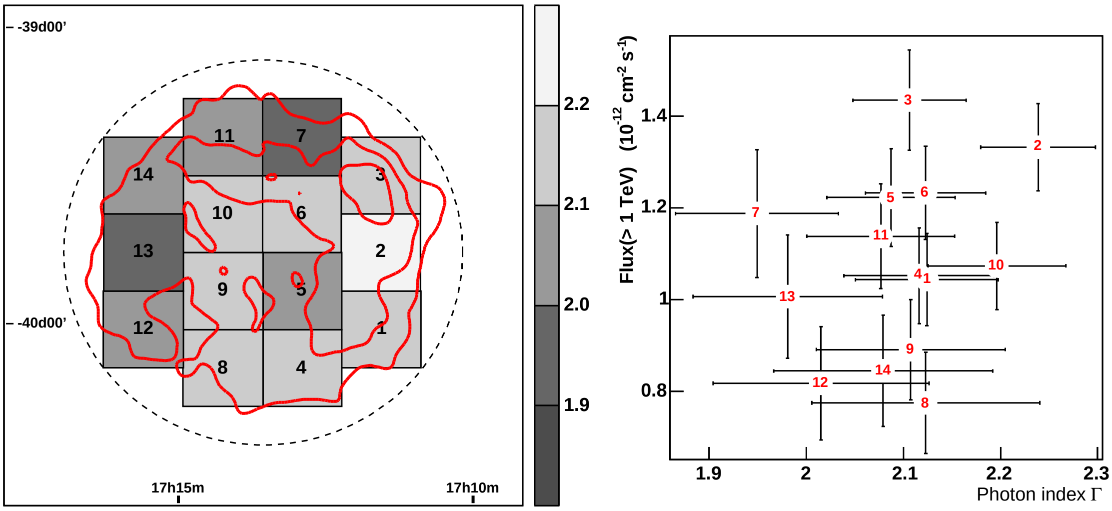

Figure 4.16: The image illustrates the results of the spatially resolved spectral analysis. **Left part:** Shown in red are gamma-ray excess contours from Fig. 4.9, linearly spaced at 30, 60, and 90 counts. Superimposed are the 14 boxes (each $0.26° \times 0.26°$ in dimension) for which spectra are obtained independently. The dashed line is the $0.65°$ radius circle that was used to integrate events to produce a spectrum of the whole SNR. The photon index obtained from a power-law fit in each region is colour coded in bins of 0.1. The ranges of the fits to the spectra have been restricted to a maximum of 8 TeV (see Table 4.9). **Right part:** Plotted is the integral flux above 1 TeV against the photon index, for the 14 regions the SNR is sub-divided in. The error bars are $\pm 1\sigma$ statistical errors. Note that systematic errors of 25% on the flux and 0.1 on the photon index are to be assigned to each data point additionally.

maximum 8 TeV for consistency (first row in Table 4.9). If one adds up the integral fluxes above 1 TeV of the individual regions, a flux of $15.1 \times 10^{-12}\,\mathrm{cm}^{-2}\,\mathrm{s}^{-1}$ is obtained, 5% less than the flux of the whole SNR (with the restriction of the fit range). This is in excellent agreement with expectations; the boxes as they are plotted in Fig. 4.16 cover the region of RX J1713.7−3946 with significant gamma-ray excess almost completely.

As can be seen from Fig. 4.16, right part, there is no correlation of the gamma-ray flux and the photon index visible in the data. This, together with the absence of any change in the spectral shape, is a remarkable difference between the gamma-ray and X-ray data (cf. Section 4.2.4). The spectral variation in X-rays was found to be much larger (Cassam-Chenaï et al. 2004a).

4.2.4 Comparisons with other wavelengths

VHE gamma rays versus X-rays

As was already mentioned, when comparing the H.E.S.S. image of RX J1713.7−3946 to the X-ray data, e.g. Fig. 4.4, or Fig. 4.9 compared to Fig. 4.8, there are striking similarities. The overall morphology appears to be very similar, there exists emission throughout the

Region	Γ	χ^2 (d.o.f.)	$I(>1$ TeV) ($10^{-12}\,\mathrm{cm}^{-2}\,\mathrm{s}^{-1}$)	Excess (σ)
All	2.12 ± 0.03	24.5 (18)	15.9 ± 0.6	30.8
1	2.12 ± 0.07	34.7 (18)	1.05 ± 0.13	12.9
2	2.24 ± 0.06	26.0 (17)	1.34 ± 0.10	17.2
3	2.11 ± 0.06	30.2 (18)	1.45 ± 0.13	16.7
4	2.10 ± 0.08	15.7 (18)	1.06 ± 0.12	11.5
5	2.09 ± 0.07	12.6 (18)	1.22 ± 0.11	13.3
6	2.13 ± 0.06	35.7 (17)	1.23 ± 0.12	14.1
7	1.95 ± 0.08	9.4 (16)	1.19 ± 0.12	10.9
8	2.11 ± 0.12	13.8 (14)	0.78 ± 0.11	8.0
9	2.11 ± 0.10	12.5 (16)	0.89 ± 0.11	8.7
10	2.19 ± 0.07	24.8 (17)	1.09 ± 0.10	14.1
11	2.08 ± 0.08	11.6 (15)	1.13 ± 0.11	11.8
12	2.01 ± 0.11	8.4 (16)	0.81 ± 0.12	8.2
13	1.98 ± 0.10	10.7 (15)	1.00 ± 0.14	9.8
14	2.08 ± 0.11	9.9 (15)	0.84 ± 0.12	9.4

Table 4.9: Fit results for distinct regions of the SNR. Given are for each region the photon index resulting from a power-law fit, the best-fit χ^2 and the number of degrees of freedom (d.o.f.), the integral flux above 1 TeV and the significance of the excess events in units of standard deviation (σ). The background for each region was determined from the same field of view, as described in Section 3.6.4, for each region separately, and hence the background estimates for different regions are not independent. The first row is the fit result of the whole SNR for comparison. For the whole table, the upper fit range was restricted to 8 TeV to avoid biases due to the deviation from a power law at high energies.

whole SNR, and the brightest spots in both images are distributed on the shell, especially to the west. For a detailed comparison of X-ray to VHE gamma-ray counts one must account for the slightly better angular resolution of ASCA compared to H.E.S.S.. Similar to H.E.S.S., the ASCA PSF consists of two parts: a narrow Gaussian core with $\sigma \approx 0.5'$, and a broad exponential tail (Uchiyama 2005, priv. comm.). The *half-power diameter*, that is, the diameter that encloses half of the photons from a point source, is $3'$. In order to compare H.E.S.S. to ASCA images, the following procedure is applied: the ASCA PSF that corresponds to the available X-ray data, the 1-5 keV and the 5-10 keV band[4], is compared to the H.E.S.S. PSF of the 2004 data set (see Fig. 3.11). Step-wise Gaussian smoothing is applied to the ASCA PSF to degrade the resolution until optimum match with the H.E.S.S. PSF is achieved. This optimised value of σ_{smooth} is then used to smear the ASCA images, thereby degrading their resolution beyond the PSF and enabling comparisons with the H.E.S.S. images.

Figure 4.17 shows the point-spread functions of ASCA on the left-hand side. It is obtained from a two-dimensional simulated point-source image, which is already smoothed with a Gaussian of $0.75'$ to match the available X-ray data; the data as published in Uchiyama et al. (2002) is smoothed slightly to reduce fluctuations. The 68% containment radius of

---

[4] The ASCA PSF depends only weakly on energy; this effect is neglected here.

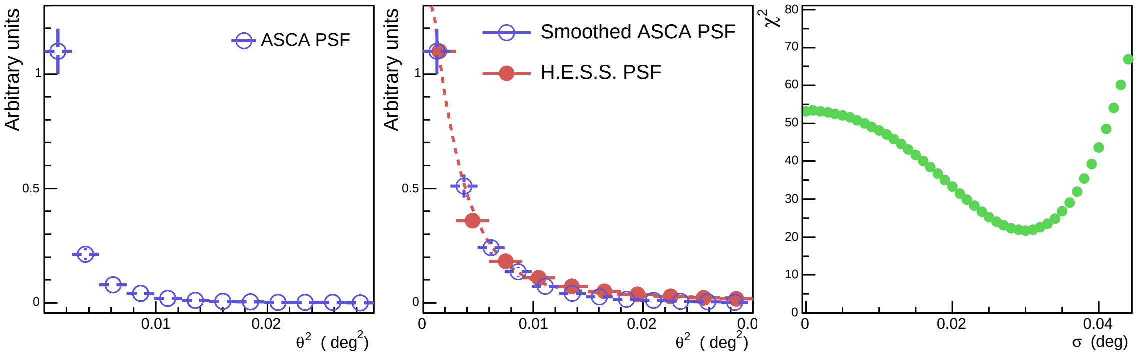

Figure 4.17: Shown are ASCA and H.E.S.S. point-spread functions and the results of the adaption of the two instrumental resolutions. **Left:** ASCA PSF, smoothed with a Gaussian of $0.75'$ to match the available X-ray data. **Middle:** H.E.S.S. PSF of the 2004 data set (for *hard* cuts), with a fit of a double Gaussian (dashed line). The degraded ASCA PSF (open circles) is smoothed by $0.03°$. **Right:** Distribution of χ^2 versus smoothing radius σ. The χ^2 results from a fit of the function describing the H.E.S.S. PSF to the smoothed ASCA PSF, leaving just one normalisation parameter free.

the one-dimensional ASCA PSF, as plotted in the figure, resulting from a fit of a double Gaussian, is $2.6'$, $\approx 0.043°$, about a factor of 1.7 smaller than the H.E.S.S.value. To obtain the optimum value of the smoothing radius σ, the two-dimensional point-source profile of ASCA is smoothed in steps of $0.001°$. For each step, a one-dimensional θ^2 histogram is generated and fit by a double Gaussian, which itself results from a fit to the H.E.S.S. PSF. Only one global normalisation factor is left as free parameter in the fit to the ASCA histogram to preserve the shape of the function. Resulting values of χ^2 of the fit versus the smoothing radius σ are plotted in Fig. 4.17 on the right-hand side. The distribution is well behaved as is to be expected from the notion that both instruments have similarly shaped point-spread functions. The well-defined minimum χ^2 around $0.03°$ defines the optimum solution, when degrading the ASCA images by smearing them with a Gaussian of $0.03°$, an almost perfect match of the point-spread functions of the two instruments is achieved, as can be seen from the middle plot in Fig. 4.17. The H.E.S.S. PSF has slightly larger tails, but apart from that the two distributions agree nicely. Note again that this smearing by $0.03°$, $1.8'$, is to be understood as additional smearing on top of the $0.75'$ the X-ray images are already smoothed with.

Figure 4.18 illustrates the effect of smearing the ASCA image additionally. Plotted on the left-hand side is the original 1-5 keV image from Uchiyama et al. (2002). It is worth noting that two X-ray sources are subtracted and not shown in the image for the purpose of comparison with VHE gamma rays. One is the bright (soft-spectrum) X-ray source 1WGA J1713.4-3949, the central point source, which was argued to be the compact relic of the supernova progenitor (Cassam-Chenaï et al. 2004a). The other one, situated to the north of the SNR and apparent e.g. in Fig. 4.8, is called AX J1714.1-3912 (Uchiyama et al. 2002). It is a flat-spectrum X-ray source not associated with the SNR but with a molecular-cloud complex at 6 kpc distance. The centre plot is the ASCA image after smoothing. It resembles already very much the H.E.S.S. picture, shown on the right, with X-ray contours overlaid. Both images are corrected for acceptance and exposure and can

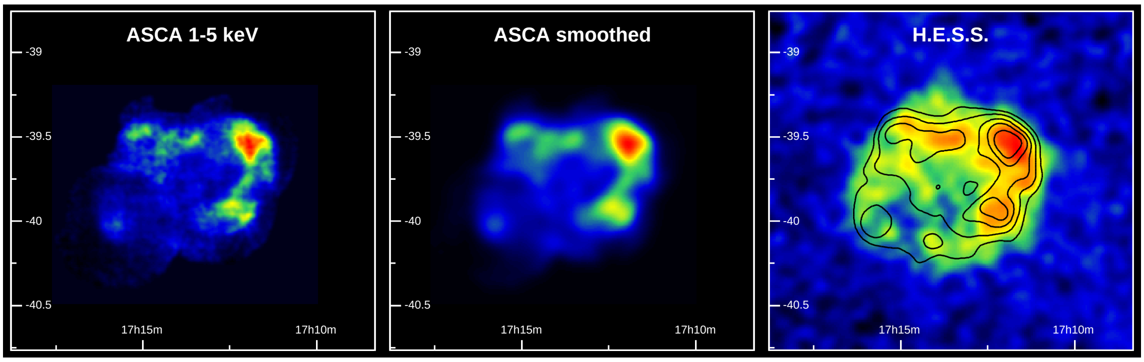

Figure 4.18: Shown are the ASCA X-ray image before (**left**) and after (**middle**) smoothing by $1.8'$. After smoothing, the image is directly comparable to the H.E.S.S. *hard* cuts image, shown on the **right**. Overlaid on the H.E.S.S. image are additionally contours (black lines) of the X-ray image plotted in the middle. Both images are corrected for acceptance and exposure.

therefore be readily compared.

The degraded ASCA and the H.E.S.S. data are compared to each other in eight wedge-shaped regions as they are drawn in Fig. 4.19. Note that in the ASCA image, most of the regions (faint solid lines) do not reach as far as in the H.E.S.S. image (faint dashed lines), accounting for the limited field of view of ASCA, whose coverage did not always extend to the boundaries of the SNR. Therefore, the radial profiles are only taken up to distances which are still well contained in the field of view to avoid edge effects and leave room for the smoothing. In each wedge, radial profiles are determined, from the H.E.S.S. data and from both X-ray energy bands, 1-5 keV and 5-10 keV. To account for the differences in the absolute count level, the X-ray images are scaled by a normalisation factor, which has been calculated as the ratio of TeV counts, integrated in a rectangle encompassing the SNR (and within the ASCA field of view), to keV counts, integrated in the same rectangle. The result is shown in Fig. 4.20 for all eight wedges. There is a very good general agreement between the keV and TeV data sets. The most pronounced differences appear in regions 3 & 4, where the TeV flux drops almost to zero at $\approx 0.35°$ and $\approx 0.15°$, respectively, and region 7, where a pronounced peak appears in the 1-5 keV X-ray data, which repeats neither in the 5-10 keV X-ray nor the TeV data. For a quantitative statement on the compatibility of the two data sets, however, one would have to model and subtract the contribution from Galactic diffuse X-ray emission in the ASCA image, which amounts to $\approx 10\%$ in the X-ray bright parts of the SNR, but might increase to $\approx 30\%$ in the faint parts in the east (Uchiyama 2005, priv. comm.).

The interesting question of the boundaries of the SNR and if they are the same in X-rays and gamma rays can unfortunately not be addressed with the ASCA data set due to limited sky coverage.

The XMM X-ray spectra of different regions of the SNR revealed significant variations of the photon index ($1.8 \leq \Gamma \leq 2.6$), spectra were found to be generally steep in the faint central regions and flatter at the shock locations, with indications again for steepening at locations where the shock impacts molecular clouds (Cassam-Chenaï et al. 2004a). In contrast, the H.E.S.S. spectra remain unchanged for different SNR regions (Section 4.2.3).

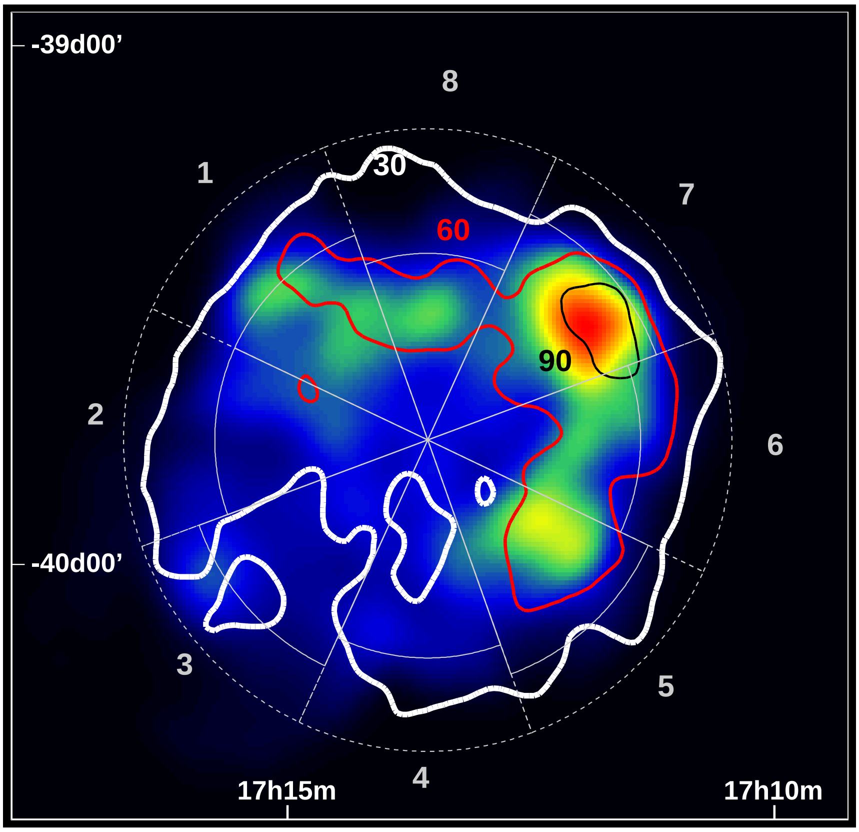

Figure 4.19: Smeared ASCA X-ray (1-5 keV band) image of RX J1713.7−3946, overlaid with contours of the smoothed, acceptance-corrected H.E.S.S. gamma-ray image. The coloured contour levels are labelled and linearly spaced at 30, 60, and 90 counts. Drawn as grey thin lines are eight wedge-shaped regions for which the radial profiles are compared to each other in Fig. 4.20. Solid lines are region used for ASCA, dashed lines regions used for H.E.S.S..

For a direct comparison of the spectra, in order to explore if there is nevertheless a correlation apparent, spectra from XMM data are generated within the 14 boxes used for H.E.S.S.(see Fig. 4.16). *Preliminary* results (Uchiyama 2005, priv. comm.) are given in Table 4.10. The X-ray spectra are fit by an absorbed power law with absorbing column density N_{H} and photon index Γ. Spectra cannot be determined for regions 4, 8, 13, and 14 because these boxes are not completely covered in the XMM observations. As can be seen now more quantitatively, variations of spectral shape seen in X-rays are pronounced and significant (the statistical error on the XMM indices is estimated as ≈ 0.05), whereas for H.E.S.S. within statistics the spectral shapes are found to be compatible in these boxes. A correlation plot is shown in Fig. 4.21, photon indices of H.E.S.S. are plotted versus those of XMM. As is apparent from the figure, within the current statistical error of the H.E.S.S. data there is no correlation.

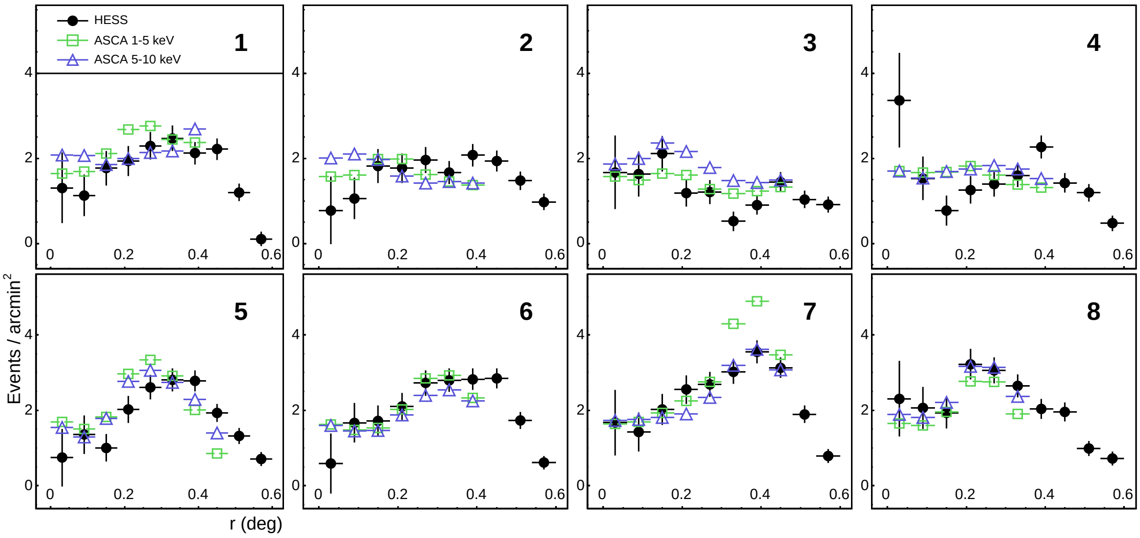

Figure 4.20: Radial profiles for the eight regions marked in Fig. 4.19. Plotted are H.E.S.S. excess counts per unit solid angle (solid circles) as a function of distance r in degrees to the centre of the SNR, compared to soft (1-5 keV) and hard (5-10 keV) X-ray data. All data were corrected for relative acceptance.

Region	N_H (10^{22} cm^{-2})	Γ
1	0.92	2.52
2	0.72	2.62
3	0.81	2.30
4	-	-
5	0.70	2.35
6	0.56	2.62
7	0.73	2.44
8	-	-
9	0.62	2.23
10	.0.47	2.40
11	.0.61	2.10
12	0.53	2.06
13	-	-
14	-	-

Table 4.10: Preliminary fit results obtained from XMM spectra (Uchiyama 2005, priv. comm.) which are determined in the 14 boxes used for the spatially resolved spectral analysis of the H.E.S.S. data. An absorbed power law with absorbing column N_H and photon index Γ is fit to the data in regions where XMM had complete coverage. Systematic errors on the indices are still under investigation.

CO and radio observations

CO data at 2.6 mm wavelength of RX J1713.7−3946 and its surroundings were taken with the 4-m, mm and sub-mm telescope NANTEN in 2003 (Fukui et al. 2003). Based on positional coincidences of CO and X-ray peaks and (in velocity space) shifted CO peaks,

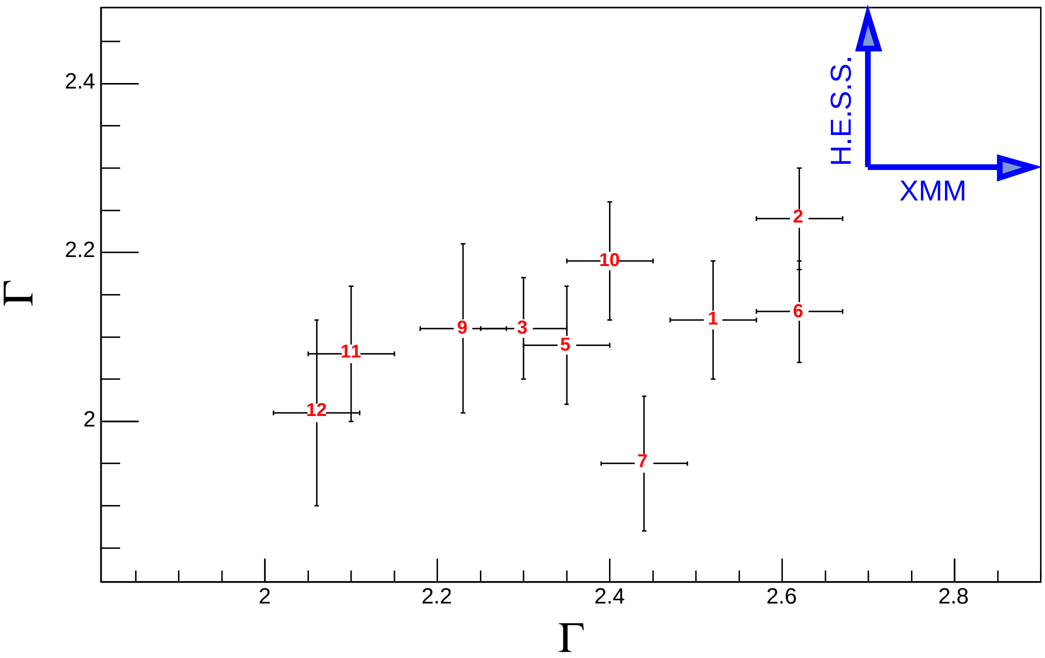

Figure 4.21: For 10 of the regions drawn in Fig. 4.16 the photon index resulting from a fit to XMM spectra in these regions is plotted versus the index from the H.E.S.S. data set. Note the aspect ratio, variations seen in the H.E.S.S. data are on smaller scales than those seen in the XMM data. There is no correlation apparent.

Fukui et al. (2003) concluded that the SNR blast wave is interacting with molecular clouds situated on its western side at a distance of ≈ 1 kpc. Further possible support for that scenario was recently published in Moriguchi et al. (2005), where high gas excitations are reported for this part, which could arise from heating of the molecular gas by the shock wave. The CO intensity distribution in the corresponding velocity interval is shown in Fig. 4.22, together with H.E.S.S. gamma-ray excess contours. One notes that in the central and southeastern part of the SNR the CO emission becomes very faint or is completely absent. Apart from that, there are local CO maxima that coincide with TeV-bright parts on the western side of the SNR. The azimuth profile plotted on the right-hand side of Fig. 4.22 is generated with respect to the SNR centre, events are integrated in a 0.2°-wide ring covering the shell of RX J1713.7−3946. Looking at the figure, 0° azimuth is to the left, −90° downward. The resulting profile illustrates a global agreement between the two measurements, regions with low gamma-ray flux reveal also low CO intensity, but there is no exact proportionality for the shell region. Taking the peak values, one notes that they are shifted with respect to each other and that the gamma-ray flux varies by a factor of about three, whereas the CO intensity drops by roughly a factor of 100 in the central-southeastern part.

Figure 4.23 shows a comparison of the 1.4 GHz radio image obtained with ATCA (Lazendic et al. 2004) and the H.E.S.S. gamma-ray excess contours. The SNR is a very weak radio emitter, in fact from the figure it is not even clear if the radio emission is associated with the remnant at all. Nevertheless, there are two faint arc-like structures of emission in the west part of RX J1713.7−3946, almost perpendicular to each other, one of them directly coincident with the brightest TeV emission region. Apart from that, there is no

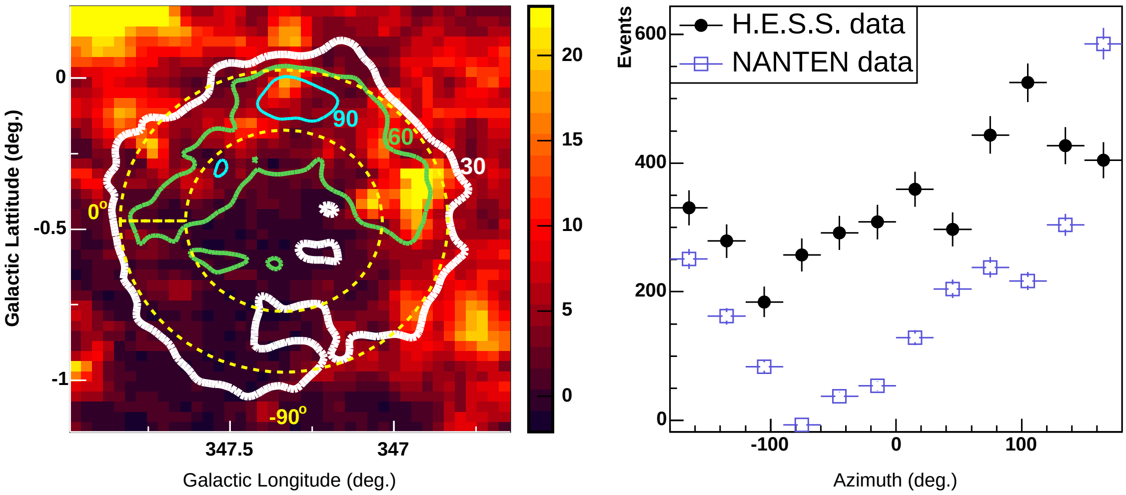

Figure 4.22: Left panel: Shown are the intensity distribution of CO $(J = 1 - 0)$ emission (Fukui et al. 2003) (linear colour scale in units of $\mathrm{K\ km\ s^{-1}}$, truncated at a value of 23 to highlight important features), derived by integrating the CO spectra in the velocity range from $-11\ \mathrm{km\ s^{-1}}$ to $-3\ \mathrm{km\ s^{-1}}$ (which corresponds to $0.4\ \mathrm{kpc}$ to $1.5\ \mathrm{kpc}$ in space). Overlaid are coloured contours of the H.E.S.S. gamma-ray excess image. The levels are labelled and linearly spaced at 30, 60, and 90 counts. Note that the image is shown in Galactic coordinates. **Right panel:** Azimuth profile plot, integrated in a $0.2°$-wide ring covering the shell of RX J1713.7−3946 (dashed yellow circle in the left-hand panel; directions corresponding to $0°$ and $-90°$ azimuth angle are indicated). Plotted are the H.E.S.S. gamma-ray and the NANTEN data set.

notable resemblance between the two wavelength regimes. Spectral analysis of the X-ray- and TeV-bright northwestern part of the SNR shell yields a spectral index of 0.50 ± 0.40, derived from two flux values taken at 1.4 GHz and 2.5 GHz. This measurement is used further down when comparing the H.E.S.S. spectral data to broadband models.

H.E.S.S. versus ASCA and NANTEN

One more comparison of H.E.S.S. data to X-rays and CO line emissions is undertaken in Fig. 4.24. Three thick boxes are overlaid on the SNR region and projections within these boxes onto the axis of Right Ascension are generated. The resulting one-dimensional distributions are shown in the bottom part of the figure. The basic resemblance of the H.E.S.S. and the ASCA data is seen also here, differences appear in *slice 1* at the position of the peak emission in X-rays, in accordance with Fig. 4.20. The X-ray peak is more pronounced with respect to adjacent regions than the VHE gamma-ray emission. Further differences between the ASCA and H.E.S.S. data are indicated in *slice 3*, however, here the complication of the limited field of view of ASCA makes detailed comparisons again difficult. The general agreement is nevertheless convincing and a real effect. In comparison, in the NANTEN data the basic effect is a drastic increase in CO line emission towards the North and West, dense molecular clouds are measured there. While this is in qualitative concordance with the X-ray and VHE gamma-ray data, where the bright emission regions

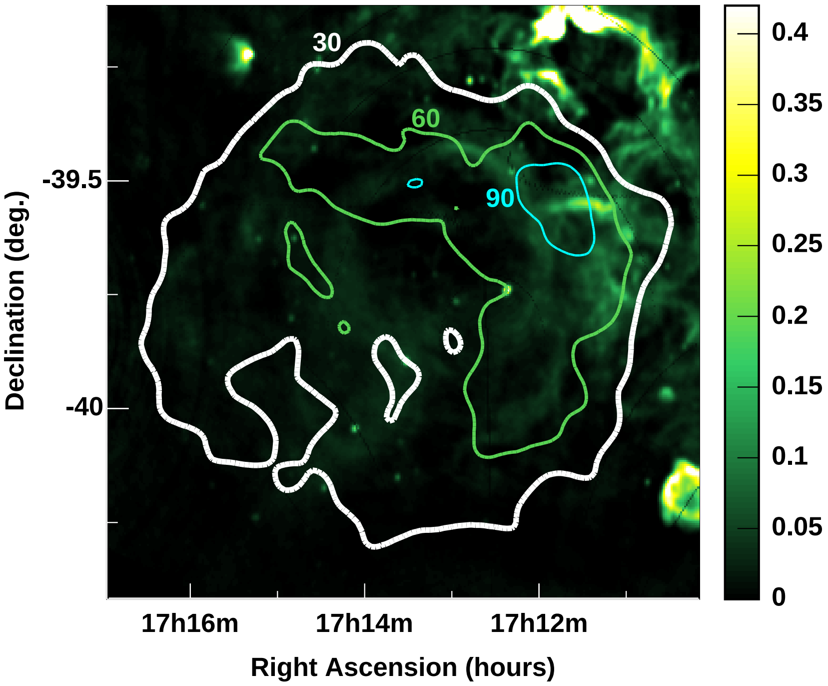

Figure 4.23: 1.4 GHz ATCA radio image (Lazendic et al. 2004, courtesy of P. Slane). The linear colour scale is in units of Jy beam^{-1}. Overlaid are coloured contour lines of the H.E.S.S. gamma-ray excess image.

are located to the North and West part, too, there is no sign for direct proportionality between the CO and the other two measurements.

4.2.5 Possible emission processes

One of the key issues in the interpretation of the observed gamma-ray emission is the identification of the particle population responsible for the generation of the gamma rays. The close correlation between X-rays and gamma rays might indicate an electronic origin; models of supernova remnants as Galactic cosmic-ray sources, on the other hand, suggest that primarily a hadronic component from pion decays exists. To identify the different contributions, the wide-band electromagnetic spectra from radio to multi-TeV gamma-rays must be compared to model calculations.

In the literature, different schemes are employed to model broadband emission from SNRs. Phenomenologically oriented models (Mastichiadis & de Jager 1996; Aharonian & Atoyan 1999) start by ad hoc assuming particle acceleration spectra - usually as power laws with a cutoff - to derive particle spectra taking into account energy losses and then calculate the electromagnetic spectrum with additional assumptions concerning the local magnetic field, the radiation fields which serve as target for the IC process, and the gas density. Spectral parameters are either taken from acceleration models, resulting in a spectral index around 2, or determined from data. More sophisticated gamma-ray models account for the non-linear effects arising from the interaction of the accelerated particles with the shocked

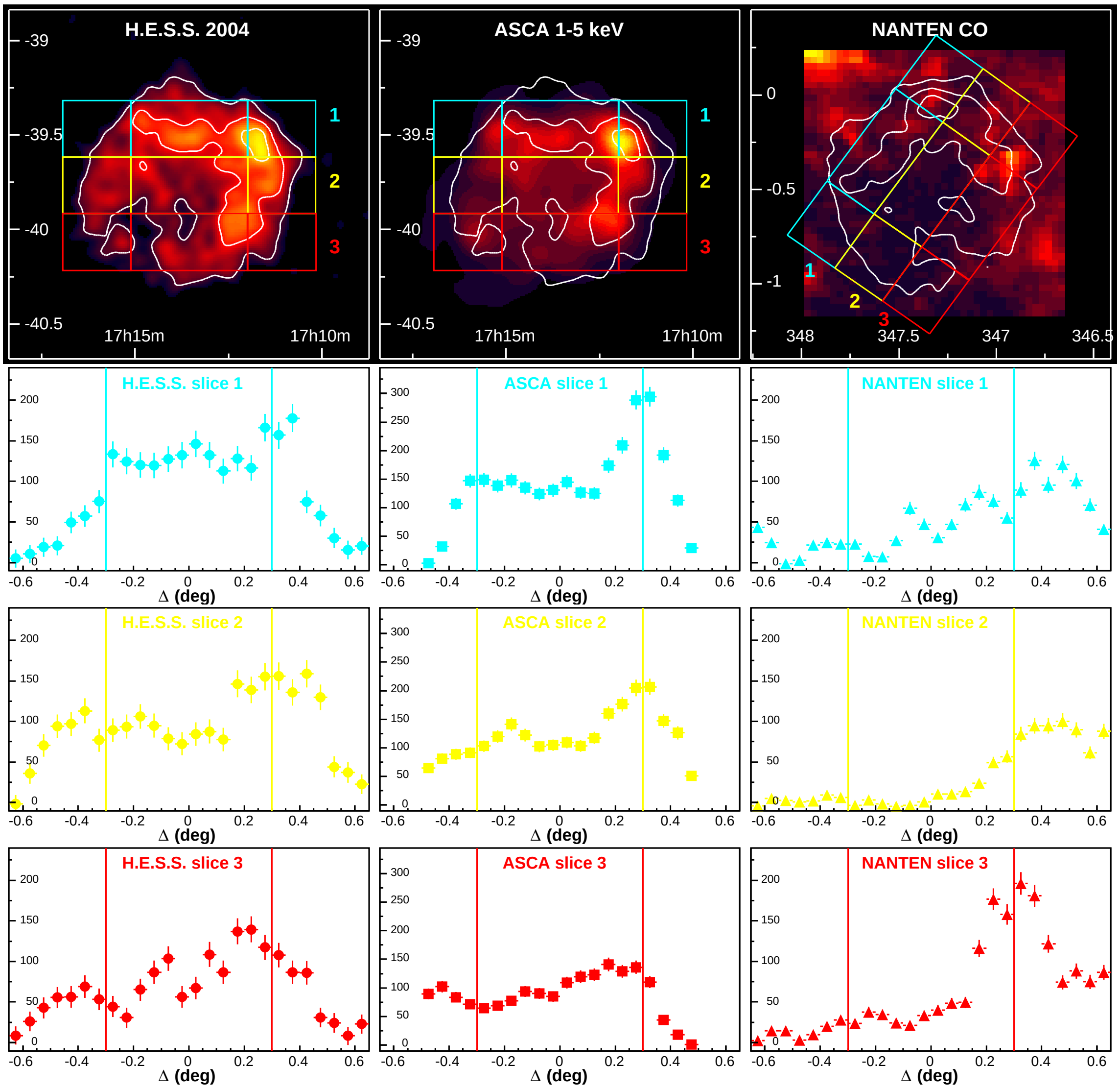

Figure 4.24: A comparison of the H.E.S.S. gamma-ray image to the ASCA 1–5 keV X-ray image and the NANTEN CO data of the region of RX J1713.7−3946 is shown. **Upper row:** Shown from left to right are the smoothed H.E.S.S. excess image, the 1–5 keV ASCA image, smoothed with the optimum Gaussian of $\sigma = 0.03°$, and the NANTEN CO data. Both the H.E.S.S. and the ASCA image are plotted in equatorial coordinates (RA/Dec), the CO data is (conventionally) plotted in Galactic coordinates. Overlaid on all three images for orientation are white H.E.S.S. excess contours at the level of 30, 60, and 90 counts. Additionally, three boxes are drawn, $0.3° \times 1.3°$ in dimensions, labelled "1", "2", "3". They are used to produce slices shown in the **three bottom rows** to enable better comparison between the images. The slices are the integrated counts within the boxes, projected onto the RA-axis, which is plotted in units of degrees with respect to the SNR centre coordinate, $\alpha_{\mathrm{J2000}} = 17\mathrm{h}13\mathrm{m}33\mathrm{s}$. The vertical lines drawn in both the images and the slices at $\pm 0.3°$ are for orientation to link positions in the images to the slices.

supernova shell, which result in deviations from pure power laws, with spectra flattening at higher energies (Berezhko & Völk 1997; Baring et al. 1999).

The original discovery paper of VHE gamma-ray emission from RX J1713.7−3946 (Muraishi et al. 2000) claimed electrons as the likely source particle population. However, it soon became evident that a consistent modelling of the spectra is hard to achieve in simple one-zone models. Apart from the choice of the electron spectrum, the only free parameter is the magnetic field strength, which controls the spacing of the synchrotron and IC peaks in the SED together with their relative intensities and – one should add – the amount of radiative cooling of the accelerated component. Enomoto et al. (2002) noted that for modest magnetic fields – B equal to a few μG – the measured intensity ratios are reproduced but the gamma-ray spectra are much too hard. Using higher fields, one can match the gamma-ray spectra at the expense of dramatically increased X-ray yields. While the H.E.S.S. data differ from the CANGAROO-II data both in terms of the region covered and the exact values for flux and index, this conclusion for the electronic scenario remains basically valid. The agreement can be improved by introducing an additional parameter to decouple the X-ray intensity and the spectral shape, namely the magnetic field filling factor which allows the X-ray flux to be tuned without change of the spectra. With very small filling factors of 0.001 (Pannuti et al. 2003) to 0.01 (Lazendic et al. 2004), difficult to justify physically, the X-ray and the CANGAROO-II gamma-ray spectra can be described for magnetic fields around 10 μG to 15 μG in the emitting region. This latter approach is not followed here.

The validity of electronic models could be judged more easily if the magnetic field values in the remnant were known. For typical shock compression ratios around 4 and pre-shock interstellar fields of a few μG, fields of 10 μG to 15 μG are at the lower limit of the expected range; mechanisms of dynamical field amplification in non-linear shocks (Lucek & Bell 2000; Bell & Lucek 2001; Bell 2004) will generally result in higher fields. The narrow filaments visible in many high-resolution X-ray images of SNRs (see, e.g., Bamba et al. 2005) have been pointed out to provide means to probe magnetic fields (Vink & Laming 2003; Berezhko et al. 2003): only relatively high fields can result in sufficiently rapid cooling of electrons to make such filamentary features possible and visible. On the basis of the structures seen in Chandra images in the northwest of RX J1713.7−3946 (Uchiyama et al. 2003), Völk et al. (2005) have argued that fields between 58 μG and a few 100 μG might be possible, depending on the detailed assumptions about the remnant's morphology[5]. Such high fields – likely to be present throughout the remnant – would rule out a leptonic origin of VHE gamma rays right away.

On the basis of the difficulty of accommodating broadband spectra in a single-zone electronic model, Enomoto et al. (2002) proposed RX J1713.7−3946 as the first well-identified proton accelerator. This interpretation was criticised by Butt et al. (2002) and Reimer & Pohl (2002) since the CANGAROO-II spectra, extrapolated to lower energies, would violate the flux level of the nearby EGRET source 3EG 1714−3857 (Hartman et al. 1999), which, if not associated with RX J1713.7−3946, must then be considered as upper limit on the GeV emission. However, the EGRET limit can be circumvented by reducing the amount of low-energy protons compared to the E^{-2} spectrum. This can be achieved by

---

[5] Note that in Hiraga et al. (2005), Fig. 2, a radial profile from the XMM image is shown. It reveals another very thin filament-like structure in the west of RX J1713.7−3946 which is a sign of high magnetic field values.

the ad hoc assumption of a spectral break, or – for the CANGAROO-II data – by assuming a flatter overall spectrum with a photon index smaller than 2.

Instead of detailed modelling, the approach presented in the following is a rather phenomenological one which serves mainly to illustrate that spectra and energetics can be reproduced with plausible input parameters.

Electronic scenario

In Fig. 4.25 the synchrotron and IC emission from relativistic electrons are modelled[6] within the framework of a one-zone model in which the electron acceleration and gamma-ray emission take place in the same region. It is assumed that the primary electrons follow a power law with index $\alpha = 2$ and with an exponential cutoff E_0,

$$Q(E) = Q_0 E^{-\alpha} \exp(-E/E_0)\,, \tag{4.1}$$

and that they are produced continuously over a fixed time interval T inside a region with given homogeneous distributions of magnetic field strength B and ambient gas density n. The energy distribution of the electrons is then calculated taking into account energy losses due to IC and synchrotron emission, Bremsstrahlung and ionisation as well as losses due to Bohm diffusion. The broadband energy distribution of the source is calculated for an age of $T = 1000$ years, an average gas density of $n = 1$ cm^{-3}, and a distance to the source of $D = 1$ kpc. For the IC emission, canonical interstellar values for the seed photon densities were considered: $W_{\mathrm{CMB}} = 0.25$ eV cm^{-3} for the cosmic microwave background (CMB), $W_{\mathrm{SL}} = 0.5$ eV cm^{-3} for optical star light and $W_{\mathrm{IR}} = 0.05$ eV cm^{-3} for infrared background light. The absolute electron production rate, Q_0, is determined from the constraint of matching the observed X-ray flux level. Figure 4.25 shows the resulting model curves, together with measurements in various wavelength regimes, for three different average magnetic field values. From the absolute levels it is evident that a magnetic field around 10 μG is required in order to explain both the X-ray and gamma-ray flux levels. Both the absolute levels and the spacing of the peaks are approximately described by Eq. 1.1 & 1.2 (Section 1.1). One notes that such a model with the above mentioned parameters does not provide a reasonable description of the H.E.S.S. data. The IC peak appears too narrow to reproduce the flat TeV emission. The detailed inclusion of non-linear acceleration effects should not change the situation very much. They are expected to steepen the synchrotron SED above the radio range. Synchrotron cooling of the accelerated electrons then tends to produce a flat-topped synchrotron and accordingly IC maximum. It is, however, a long way to flatten the IC spectrum so extensively at low energies as to achieve agreement with the H.E.S.S. spectrum.

Obviously, the model presented here is simplified and serves basically to underline the main arguments. Nevertheless, the conclusion that a power-law production spectrum fails to simultaneously account for the radio, X-ray and gamma-ray data appears to be a generic and stable feature. Additional parameters are required to decouple either the TeV and X-ray/radio fluxes - such as a $filling factor$ - or the X-ray and radio spectra - such as

---

[6] The model calculations for the electronic scenario presented in the following are not part of this work but have been undertaken by F. Aharonian and are included in the H.E.S.S. publication of the 2004 RX J1713.7−3946 data (Aharonian et al. 2005a).

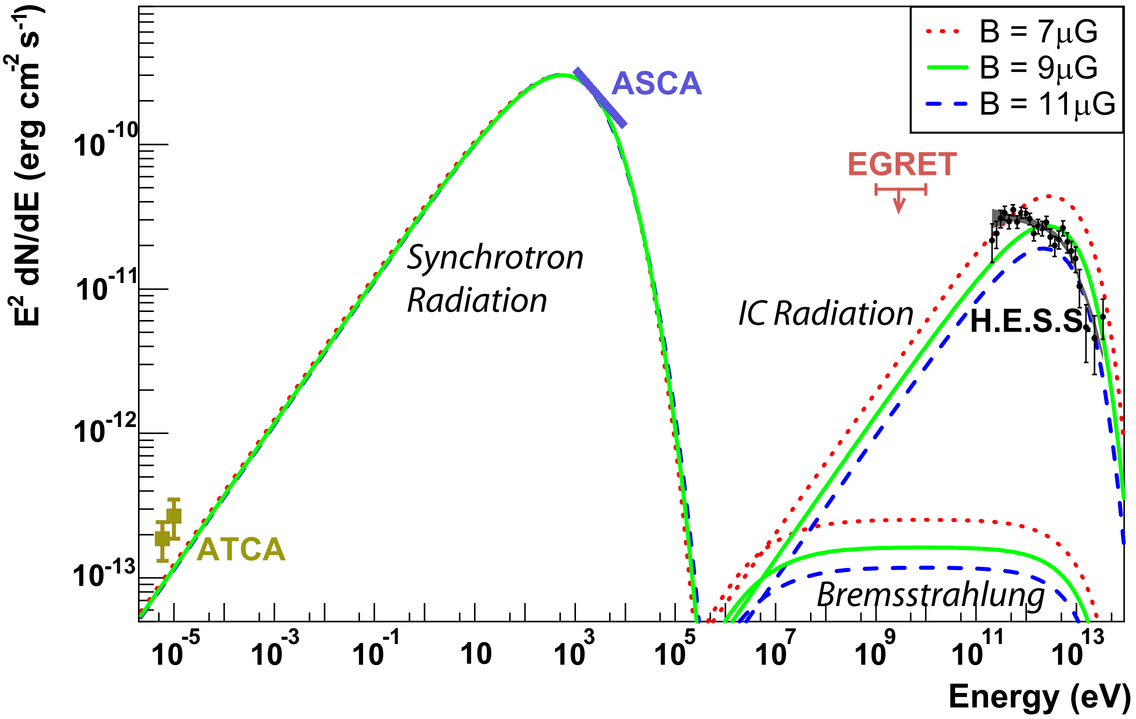

Figure 4.25: Broadband SED of RX J1713.7−3946. The ATCA radio data and ASCA X-ray data (Hiraga 2005, priv. comm.) for the whole SNR are indicated, along with the H.E.S.S. measurement and the EGRET upper limit. Note that the radio flux was determined in Lazendic et al. (2004) for the northwest part of the shell only and was scaled up by a factor of two here to account for the whole SNR. The model curves are kindly supplied by F. Aharonian. The synchrotron and IC spectra were modelled assuming a source distance of 1 kpc, an age T of 1000 years, a density n of $1\ \mathrm{cm}^{-3}$, and a production rate of relativistic electrons by the acceleration mechanism in the form of a power law of index $\alpha = 2$ and an exponential cutoff of $E_0 = 100\ \mathrm{TeV}$. Shown are three curves for three values of the mean magnetic field: $7\ \mu\mathrm{G}$, $9\ \mu\mathrm{G}$, and $11\ \mu\mathrm{G}$, to demonstrate the required range of the B field strength for this scenario. The electron luminosity is adopted such that the observed X-ray flux level is well matched. For the three magnetic field values the luminosity L_e is $L_\mathrm{e} = 1.77 \times 10^{37}\ \mathrm{erg\ s^{-1}}$ $(7\ \mu\mathrm{G})$, $L_\mathrm{e} = 1.14 \times 10^{37}\ \mathrm{erg\ s^{-1}}$ $(9\ \mu\mathrm{G})$, and $L_\mathrm{e} = 0.81 \times 10^{37}\ \mathrm{erg\ s^{-1}}$ $(11\ \mu\mathrm{G})$.

an ad-hoc spectral break, which for the given source age and magnetic field can not be justified as an effect of radiative cooling.

Hadronic scenario

Assuming alternatively that nuclear cosmic-ray particles, accelerated at the SNR shock, dominantly produce VHE gamma rays, theoretically the most plausible differential energy spectrum of accelerated nuclei is a concave $E^{-\Gamma(E)}$-type spectrum, due to nonlinear back coupling, with a cutoff at gamma-ray energy E_c, where Γ is decreasing towards higher energies (just below the TeV energy range) to a value between 1.5 and 2, before the spectrum is

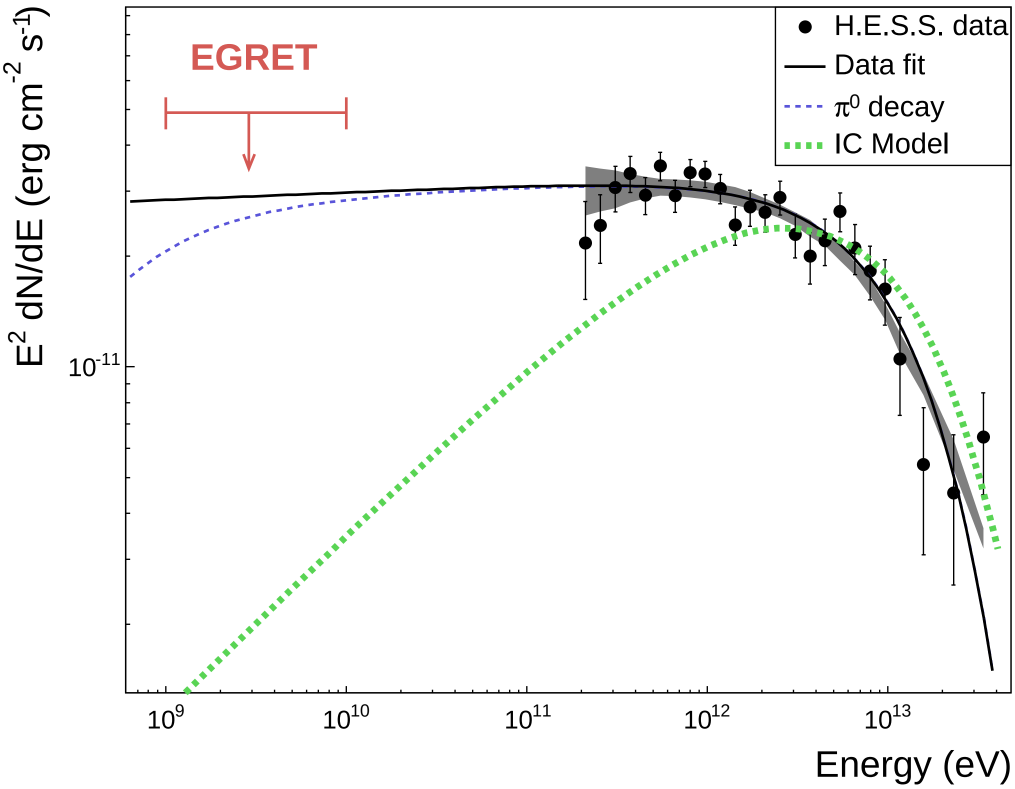

Figure 4.26: H.E.S.S. data points plotted in an energy flux diagram. They shaded grey band is the systematic error band for this measurement (see Section 3.6.4 & Fig. 4.15). The black curve is the best fit of a power law with exponential cutoff to the data, extrapolated to lower energies. The dashed blue curves is the same function, but it takes the π^0 kinematics into account. The EGRET upper limit from 1 GeV to 10 GeV is plotted as red arrow. For comparison an IC model curve is overlaid (thick green dashed line). It is similar to the model curves of Fig. 4.25, but for a slightly different magnetic field value of 10 μG and an exponential cutoff E_0 at 40 TeV.

steepening again in the cutoff region. In the test-particle approximation one expects $\Gamma \simeq 2$. The H.E.S.S. spectrum is indeed compatible with such a scenario. Figure 4.26 shows a νF_ν representation of the H.E.S.S. data, together with the best-fit curve of a power law with an exponential cutoff (see Table 4.7), extrapolated to small energies. Compared to that a curve is plotted which takes the kinematics of the production process of gamma rays, $pp \rightarrow \pi^0 \rightarrow \gamma\gamma$, into account (see Section 1.1, Eq. 1.3, 1.4 & 1.5). The power law spectrum continues to smaller energies with an index of ≈ 2, as expected in the test-particle limit, until the suppression of gamma rays due to π^0-decay kinematics is encountered and the curve is turning down. Note that already the extrapolation of the H.E.S.S. spectrum is well below the EGRET upper limit from the position of RX J1713.7−3946 (see Section 4.2.2). Taking into account non-linear effects would harden the gamma-ray spectrum even more. For illustration also an IC model curve is drawn in Fig. 4.26. It is for an electron injection spectrum with $\alpha = 2$ and exponential cutoff $E_0 = 40$ TeV, and a magnetic field strength of 10 μG. The parameters are chosen such that the model curve (i.e. the synchrotron flux) provides a reasonable description of the X-ray data, as shown in Fig 4.25. It can clearly be seen that the IC model curve is not appropriate to match the H.E.S.S. data.

One should mention at this point that on the theory side other mechanisms to suppress contributions from low-energy (E around 10 GeV) protons have been considered (Malkov et al. 2005). When the particles upstream of the shock hit a dense target with a spatial gradient, such as a dense molecular cloud, the gamma-ray emission of low-energy protons might also be suppressed due to the energy dependence of the diffusion length. In a more general context, such mechanisms - an accelerator of finite lifetime interacting with a target at a distance where diffusion time scales are comparable to the source lifetime - have been studied by Aharonian & Atoyan (1996). Such arguments, however, need to be reassessed when the exact location of the clouds with respect to the shock front is known.

To calculate the energetics in a hadronic scenario, the mean target gas density available for gamma-ray production in the region of RX J1713.7−3946 is a key question. The CO image shown in Fig. 4.22, left-hand side, reveals a hole in the CO emission and accordingly in the molecular hydrogen distribution in the central and eastern part of the SNR. In contrast, the TeV emission fills the whole region of the SNR (see Fig. 4.9). As is shown on the right-hand side of Fig. 4.22, there is no exact correlation between VHE gamma rays and CO intensity. From this one can conclude that in all likelihood cosmic rays do not penetrate the clouds uniformly. The bulk of the VHE gamma rays is not linked to the molecular clouds but must be due to interactions with a different target. Indeed, the rather good spherical shape of the remnant together with the fact that the X-ray and gamma-ray emission only varies by a factor of two to four across the remnant lends further support to the scenario that the SNR is running into a more or less uniform and probably low-density environment. Although it seems to be beginning to interact with the dense clouds to the west, the ones that are seen by NANTEN, VHE gamma rays are dominantly produced in cosmic-ray interactions with rather uniform ambient gas. One possible scenario is that the SNR is the result of a core-collapse supernova explosion that occurred into a wind bubble of a massive progenitor star. An SNR shock expanding into the bubble, with an ambient density much lower than that suggested by an average molecular cloud scenario, could explain the relative uniformity of the gamma-ray emission, compared to the large density variations in the clouds which likely surround the remnant (for a theoretical treatment of such configurations, see Berezhko & Völk (2000)).

The local target density is a crucial parameter in this scenario. With the NANTEN measurement of the void in the central part of the SNR one might constrain the local density in that region. The sensitivity of the final NANTEN data set as quoted in Fukui et al. (2003) corresponds to a molecular column density of 8.3×10^{19} cm^{-2} assuming the conventional conversion relation from CO intensity to H_2 column density (0.4 K km s^{-1}). Taking the diameter of the SNR as ≈ 20 pc for 1 kpc distance, one can deduce an upper limit on the molecular hydrogen column density of ≈ 2.6 cm^{-3} in parts of the SNR without detectable CO emission. The other existing constraint was inferred in Cassam-Chenaï et al. (2004a) from XMM data, based on the lack of thermal X-ray emission. By fitting the spectra with an absorbed power-law model and adding a thermal component, an upper limit on the mean gas temperature and, important here, the mean hydrogen number density of the ambient pre-shock medium of 0.02 cm^{-3} was obtained. One should note, though, that this value is likely to be too low – if the shocks are strongly modified by the accelerated particles, the shock heating is substantially reduced and the data would be consistent with higher densities.

Assuming for now a mean target gas density of $n \approx 1$ cm^{-3}, uniformly spread throughout the remnant, in accordance with the NANTEN, but not the XMM limit, one can calculate the proton energetics implied by the gamma-ray flux measured from 0.2 to 40 TeV. The total energy in accelerated protons from about 2–400 TeV, required to provide the observed flux, can be estimated as $W_p^{\rm tot}(2\text{–}400~\text{TeV}) \approx t_{pp\to\pi^0} \times L_\gamma(0.2\text{–}40~\text{TeV})$, where $t_{pp\to\pi^0} \approx 4.5 \times 10^{15} (n/1~\text{cm}^{-3})^{-1}$ s is the characteristic cooling time of protons through the π^0 production channel, $L_\gamma(0.2\text{–}40~\text{TeV}) = 4\pi d^2 w_\gamma(0.2\text{–}40~\text{TeV})$ is the luminosity of the source in gamma rays between 0.2 and 40 TeV, and $w_\gamma(0.2\text{–}40~\text{TeV})$ is the gamma-ray energy flux for the corresponding energy range. Assuming then that the proton spectrum with spectral index $\alpha \approx \Gamma$ continues down to 1 GeV, the total energy in protons can be estimated and compared to the total assumed mechanical explosion energy of the supernova of 10^{51} erg. These calculations reveal very similar values for the three spectral shapes given in Fig. 4.26 in the gamma-ray energy range between 0.2 and 40 TeV: for the gamma-ray energy flux one obtains $w_\gamma(0.2\text{–}40~\text{TeV}) \approx 10^{-10}$ erg cm^{-2} s^{-1}, the gamma-ray luminosity is $L_\gamma(0.2\text{–}40~\text{TeV}) \approx 10^{34} \left(\frac{d}{1000~\text{pc}}\right)^2$ erg s^{-1}, and the corresponding energy content of protons is $W_p^{\rm tot}(2\text{–}400~\text{TeV}) \approx 6 \times 10^{49} \left(\frac{d}{1000~\text{pc}}\right)^2 \left(\frac{n}{1~\text{cm}^{-3}}\right)^{-1}$ erg. The resulting total energy in protons, after extrapolating the proton spectrum to 1 GeV and using $E_{51} \equiv 10^{51} \left(\frac{d}{1000~\text{pc}}\right)^2 \left(\frac{n}{1~\text{cm}^{-3}}\right)^{-1}$ erg, is then $W_p^{\rm tot} \approx 0.19 \times E_{51}$ for a power law with exponential cutoff, $W_p^{\rm tot} \approx 0.08 \times E_{51}$ for a power law with energy dependent index, and $W_p^{\rm tot} \approx 0.26 \times E_{51}$ for a broken power law. These numbers are consistent with the notion of an SNR origin of Galactic cosmic rays involving the canonical ≈ 10% conversion efficiency of the total supernova explosion energy. The H.E.S.S. gamma-ray flux level is close to what was predicted in Drury et al. (1994) from nearby young SNRs for ambient densities of $n \approx 1$ cm^{-3}. One should keep in mind though that the order of magnitude uncertainties in the measurements of the distance to the source d and of the local gas density n feed directly into these estimates.

Discussion and conclusions

The models and ideas presented in this section were aiming at exploring the possibilities available in explaining the observed VHE emission in purely electronic and purely hadronic scenarios. It is found that in the hadronic scenario, assuming gamma rays to stem from π^0 decays, the extrapolation of the H.E.S.S. spectrum to lower gamma-ray energies leads to a picture that is consistent with the low-energy EGRET data. Furthermore, the spectral shape is well compatible with cosmic-ray acceleration theory. The energy requirements implied by the gamma-ray flux are in agreement with expectations from cosmic-ray acceleration in shell-type SNRs in our Galaxy, if one assumes a local target gas density of $n \approx 1$ cm^{-3} and takes the currently preferred distance estimate of 1 kpc. Unfortunately both of these parameters are not very well measured. The distance estimate, which factors quadratically into the energetics calculation, has uncertainties in the order of at least 30%. For the local target density there exist only upper limits, since from comparisons with CO data it turns out that gamma rays are most likely not exclusively linked to the dense molecular clouds surrounding the SNR. These clouds, however, obscure the measurement of the actual local target material available for gamma-ray production. Only towards the interior and the southeast of the SNR, where there is a hole in the molecular column density, is there hope to actually measure and constrain the density. Existing estimates in these regions are the NANTEN upper limit of 2.6 cm^{-3}, which does not cause any problem with the assumption made above, and the XMM upper limit of 0.02 cm^{-3} which, if correct, would seriously challenge the idea of a hadronic scenario of gamma-ray production at least for this object.

In the electronic scenario, on the other hand, the data are not easily reproduced taking only IC emission into account. The very low magnetic field of $\approx 10\ \mu$G, fixed by the ratio of synchrotron to IC flux, exceeds typical interstellar values only slightly and is difficult to reconcile with the paradigm of the diffusive shock acceleration of cosmic rays at supernova shock waves which predicts strong field amplifications in the region of the shock (Lucek & Bell 2000; Bell & Lucek 2001; Bell 2004). In the case of RX J1713.7−3946 it was indeed considered possible by Völk et al. (2005) that the magnetic field strength at the SNR shock front significantly exceeds typical interstellar values.

Complete understanding of gamma-ray emission processes can only be achieved by taking a broadband approach and using all the available measurements in the different wavelength regimes. In Section 4.2.4 the TeV data set was compared to X-ray, radio and CO emission measurements of the region surrounding RX J1713.7−3946. While there is no obvious resemblance with the radio image, it turns out that there is a striking spatial correlation between the ASCA X-ray and the H.E.S.S. gamma-ray data. Most of the emission regions seem to exhibit exactly the same morphology in both wavelength regimes. At first sight this supports the idea that X-rays and gamma rays are produced by the same particle population, namely electrons. Assuming a constant magnetic field throughout the remnant (not the most likely configuration), the intensity (and spectrum) of both synchrotron and IC radiation trace the density (and the spectrum) of electrons, giving rise to the observed correlation. If the VHE gamma rays were due to non-thermal Bremsstrahlung of electrons, which is correlated with gas density, the observed correlation could be due to a magnetic field and gas density correlation. However, as can be seen from Fig. 4.25, Bremsstrahlung dominates over IC radiation only for very large values of $n_H > 100$ cm^{-3}, which are not compatible with the CO measurements from the centre of the SNR, as mentioned above. But even given such a high density it is questionable if density, field strength and electron spectra can be fine-tuned such that the experimental results are approximately reproduced. Another difficulty for an electronic interpretation arises from the observation by Cassam-Chenaï et al. (2004a) that the X-ray spectra are steeper in the presumed shock front in the west, where the blast wave probably impacts the molecular cloud, than in the southeast, where the front propagates into a low density medium. It is very difficult to explain why the spectral shape in X-rays, but not in gamma rays, changes significantly in distinct regions of the shock, if they stem from the same particle population. If on the other hand gamma rays originate dominantly from nucleonic cosmic rays, a spatial correlation between X-rays and gamma rays is not automatically ensured either. There are two possible scenarios. The correlation could point to a common acceleration process accelerating both electrons and protons – indeed expected in the theory of diffusive shock acceleration – such that the spatial distributions are to first order the same and only differ because of the different loss processes. The second alternative is a correlated enhancement of magnetic field and local gas density.

Another possibility of course is that the VHE gamma rays are a roughly equal mixture of two components, produced by both electrons and protons. However, this scenario seems

Year	Target position		Wobble offsets		Live time	Total live time
	α_{J2000}	δ_{J2000}	$\Delta\alpha_{\mathrm{J2000}}$	$\Delta\delta_{\mathrm{J2000}}$	(hours)	(hours)
2003	17h12m00s	$-39°39'00''$	0°	+0.5°	9.1	18.1
			0°	−0.5°	9.0	
2004	17h13m33s	$-39°45'44''$	0°	+0.7°	9.0	36.4
			0°	−0.7°	8.8	
			+0.7°	0°	7.3	
			−0.7°	0°	8.3	
			0°	0°	3.1	
2005	17h13m33s	$-39°45'44''$	0°	+0.7°	9.0	40.0
			0°	−0.7°	9.4	
			+0.7°	0°	8.7	
			−0.7°	0°	9.4	
			0°	0°	3.5[7]	

Table 4.11: Summary of H.E.S.S. observations of RX J1713.7−3946 conducted during three years.

unlikely since the energy-independent gamma-ray morphology and the absence of variations in spectral shape would again require fine-tuning of parameters like the magnetic field B and the ambient density n.

To conclude, the straightforward and simplest approaches in both scenarios lead to problems and one has difficulties in finding unequivocal evidence for either of them when using all the available broadband data. Nevertheless, the shape of the gamma-ray spectrum favours a hadronic scenario.

4.3 2005 data set and comparisons with 2003 and 2004

The 2005 observation campaign, conducted from beginning of September to beginning of November, was aiming at increasing event statistics at the highest energies of the gamma-ray spectrum. Observations were preferentially taken at large zenith angles to make use of the drastically increased effective collection area (see Section 3.7, Fig. 3.28) at high energies. RX J1713.7−3946 was observed in wobble mode with an offset of 0.7° in Declination and Right Ascension, as in 2004. After run selection and dead-time correction, 40 hours of live time remain for the analysis. A summary of the observations conducted during three years with H.E.S.S. is given in Table 4.11. Figure 4.27a shows the zenith-angle distribution of events reconstructed in the region covered by the SNR, from the 2004 data compared to 2005. A pronounced difference is apparent, in 2004 the bulk of the data were taken at small zenith angles, the mean value is 26°. In 2005 observations were performed down to 70°, the mean zenith angle is 51°. When combining the data of 2004 and 2005 the mean zenith angle amounts to 36°.

From the effective collection area for large zenith angles, shown in Fig. 3.28, it is a priori not assured that one can gain sensitivity at high energies because the effective area reflects only the signal part, as they are determined from gamma-ray simulations. If for example the

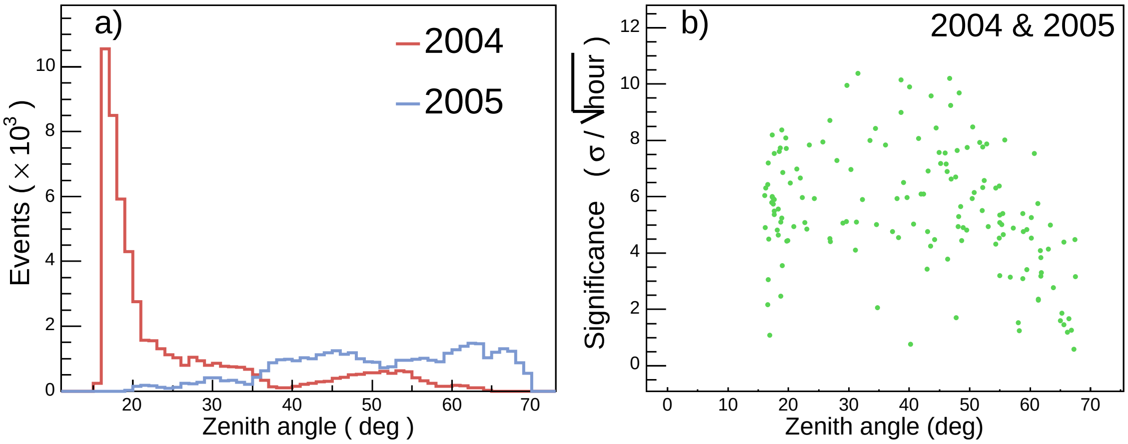

Figure 4.27: a) The zenith-angle distribution of events associated with the region of RX J1713.7−3946 is shown for the 2004 (red line) and the 2005 (blue line) data. **b)** The significance of the run-wise signal of RX J1713.7−3946 (in units of the square root of the observation time) is plotted versus the mean zenith angle of the run, determined from all events whose directions coincide with the SNR region. The numbers are determined from the nominal configuration for spectra, i.e. applying the geometrical reconstruction method and the *std* cuts.

background suppression worsens considerably at large zenith angles, the gain in detection area might be cancelled by this effect. In order to explore the sensitivity of the system at the zenith angles covered in 2004 and 2005, in Fig. 4.27b the significance of the gamma-ray excess of RX J1713.7−3946 for each observation run is plotted versus the mean event–zenith angle of the run. The numbers are determined using the nominal spectral analysis, with the *std* cuts and the geometrical reconstruction. A tendency is apparent at zenith angles larger than 50°, the run-wise significance drops from an average of $\approx 6\sigma/\sqrt{\mathrm{hour}}$ to $\approx 3\sigma/\sqrt{\mathrm{hour}}$ beyond 60°. There is, however, still a significant gamma-ray signal even at these very large zenith angles. One effect that causes a decline of sensitivity is the worsening of the angular resolution – once the 68% containment radius of the PSF reaches a noticeable fraction of the SNR radius, mis-reconstruction effects at the edges of the SNR lead to a leakage of signal events. Another effect is the worsening of the gamma/hadron separation. As mentioned before, at large zenith angles, due to the broadening of the Čerenkov light pool, events that trigger the system are on average further away, camera images become smaller and the background suppression, which is mainly based on image shape parameters, worsens correspondingly. Hadron and gamma-ray images look increasingly similar.

4.3.1 Morphology

The gamma-ray morphology as obtained from the different data of three years is seen in Fig. 4.28. For the 2003 data, the image of the re-analysis is shown (cf. Section 4.1.1), obtained with the two-telescope configuration *hard - 2tel* (see Section 3.4). The other two images of 2004 and 2005 are obtained with the *hard* cuts and the geometrical reconstruction. For the 2005 image, only observations at zenith angles smaller than 60° are taken into account (reducing the available live observation time by ≈ 10 hours), since there exist

Year	Configuration	$\langle\phi_\mathrm{z}\rangle$	$\langle\psi\rangle$	R_{68}	ON	OFF	α	Sign. (σ)	Live time (hrs)
2003	*hard - 2tel*	24°	0.64°	0.083°	3194	1764	1.0	20.5	18.1
2004	*hard*	27°	0.73°	0.075°	17932	7725	1.4	39.4	33.0
2005	*hard*	44°	0.73°	0.082°	10277	5124	1.3	33.2	29.7

Table 4.12: Summarised are the event statistics (of the whole SNR) and corresponding angular resolutions for the years 2003, 2004, and 2005. The configuration used for 2003, *hard - 2tel*, is adopted to match the system configuration of 2003, see Section 3.4 and Section 4.1. The nominal configuration *hard* is used for the other cases. All numbers listed here are obtained with the standard geometrical direction reconstruction.

no H.E.S.S. empty-field observations at larger zenith angles to create system-acceptance lookups, needed for the image generation. This is not a major disadvantage, in fact it would be very reasonable to exclude these observations even if there were acceptance lookups available, since at these large zenith angles the broadening of the PSF for the geometrical reconstruction might deteriorate the angular resolution of the resulting image already.

The images of Fig. 4.28 are readily comparable, they are corrected for system acceptance, which is different for the different data because of the zenith-angle dependence of the acceptance and the intermediate system configuration of 2003. Moreover, very similar angular resolutions are achieved for all years, see Table 4.12, where relevant parameters are listed. From the visual impression the three images shown in the figure are very similar. Within statistics, good agreement is achieved, as can be seen from the one-dimensional distributions shown in Fig. 4.29, which – as mentioned before when comparing distinct energy bands for the 2004 data – have the advantage that statistical errors on the measurement can be taken into account for the comparison. The three distributions shown in the figure are analogue to Fig. 4.12, from left to right they show a slice along a thick box (shown in Fig. 4.28), an azimuthal profile of the shell region, and a radial profile, generate from the non-smoothed, acceptance-corrected excess images. There is no sign of disagreement or variability, the H.E.S.S. data of three years are well compatible with each other.

The combined H.E.S.S. image is shown in Fig. 4.30. Data of 2004 and 2005 were used for this smoothed, acceptance-corrected gamma-ray excess map. In order to obtain optimum angular resolution, the configuration *hard - ALG3 - mult3* as discussed in Section 3.4 (see also Fig. 3.15) is used for analysis. In addition to the *size* cut of 200 p.e. of the *hard* cuts, a cut on the minimum event multiplicity at 3 telescopes, and the advanced, *algorithm-3* type reconstruction method are applied. The image corresponds to 62.3 hours of live observation time. With the *reflected-region* method, 12689 ON events from the region associated with the SNR are accumulated, and 4980 OFF events (normalisation $\alpha = 1.22$). Hence, 6595 gamma-ray excess events are measured with a significance of 46σ. The angular resolution for this data set is 0.06° (3.6′). For comparison, a resolution of 0.066° is achieved with similar events statistics with the configuration *hard - GEO - mult3*, with the geometrical reconstruction and a multiplicity-3 cut. With the nominal *hard* configuration (geometrical reconstruction and multiplicity-2 cut), the resolution is 0.077° (with 28081 ON, 15421 OFF events, $\alpha = 1.08$, and a significance of 53 σ).

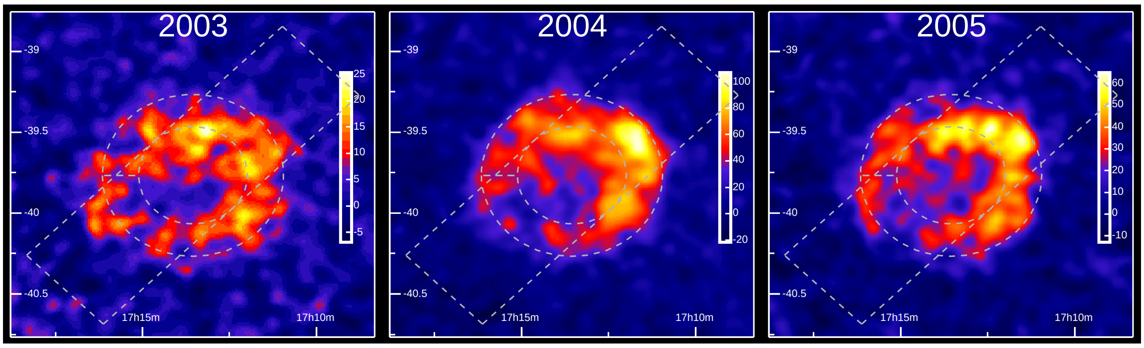

Figure 4.28: H.E.S.S. gamma-ray excess images from the region around RX J1713.7−3946 are shown for each year separately for comparison. From left to right, images are generated from data of 2003 (configuration *hard - 2tel*, see Section 3.4 and Section 4.1), 2004 and 2005 (both configuration *hard*). The images are corrected for the decline of the system acceptance with increasing distance to the SNR centre. The dashed gray box and ring are analogue to Fig. 4.11. They are used to generate the one-dimensional distributions shown in Fig. 4.29. All three images are smoothed with a Gaussian of $2'$, the linear colour scale is in units of excess counts per smoothing radius.

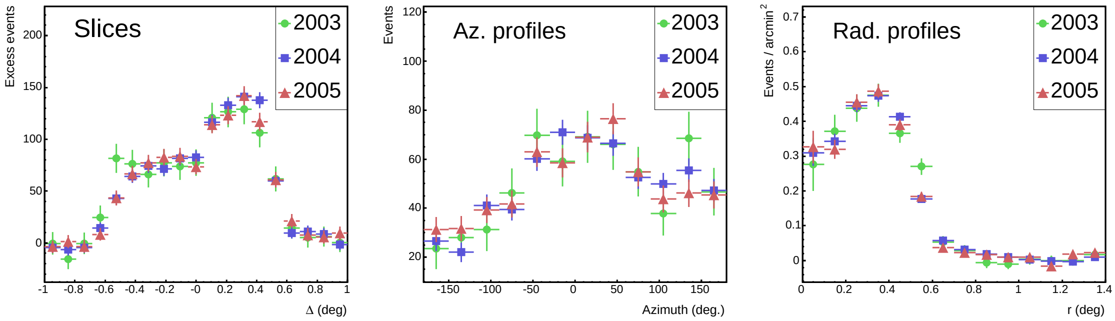

Figure 4.29: One-dimensional distributions for the data of three years are shown, analogue to Fig. 4.12. **Left:** Slices taken within the box drawn in Fig. 4.28 **Middle:** Azimuthal profiles integrated in the shell region of RX J1713.7−3946. **Right:** Radial profiles around the SNR centre. All distributions are scaled to the area of the 2003 histogram to account for differences in the event statistics.

The image in Fig. 4.30 confirms nicely the published measurements (Aharonian et al. 2004b, 2005a), with 20% better angular resolution (10% due to the multiplicity-3 cut, 10% due to the advanced reconstruction method) and increased statistics. The shell of RX J1713.7−3946, somewhat thick and asymmetric, sticks out clearly and is almost closed. The brightest parts are located in the north and west of the SNR. There are three more sources of VHE gamma rays (Aharonian et al. 2005e) beyond the boundaries of RX J1713.7−3946. Apart from that the background is clearly under very good control. It is flat, without noticeable gradients or other variations, and confirms that the correction for the non-uniform system acceptance works as expected.

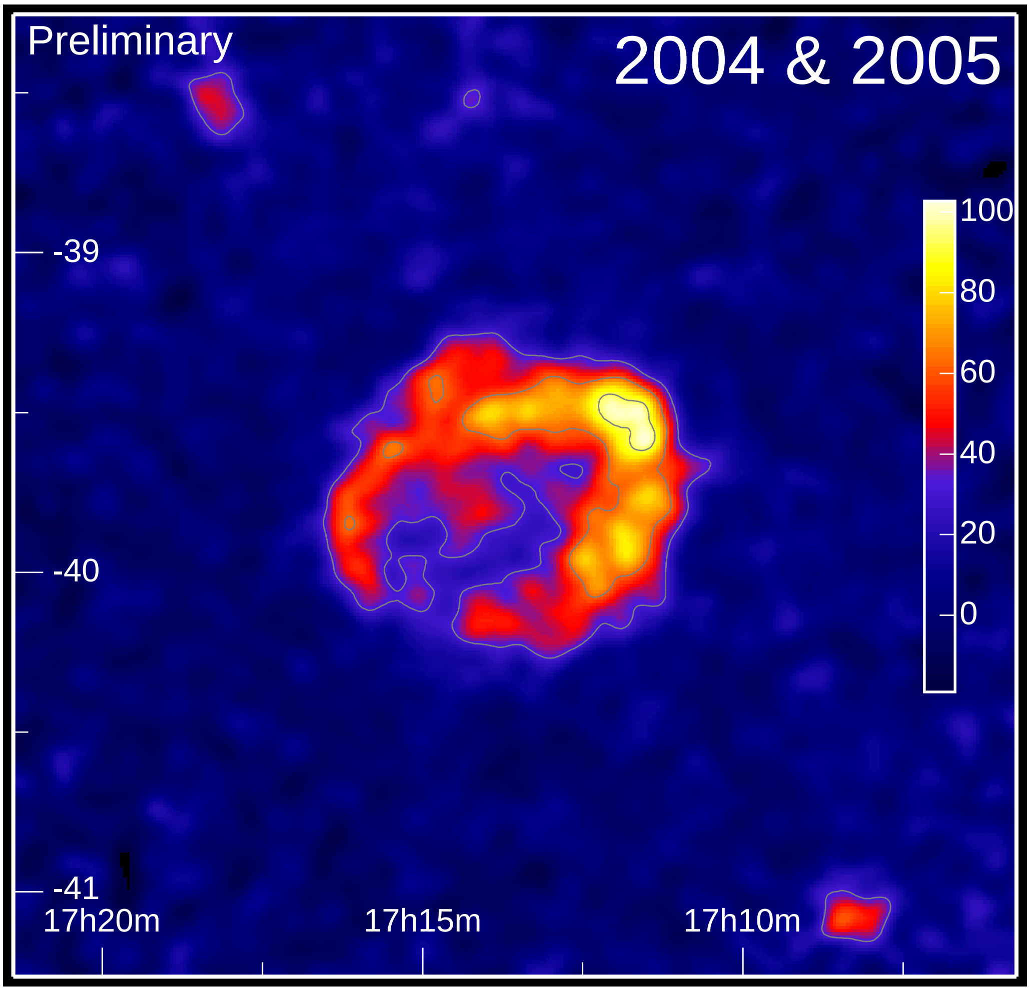

Figure 4.30: Combined H.E.S.S. image of 2004 and 2005. Shown is an acceptance-corrected excess map, smoothed with a Gaussian of $2'$. For comparison, the PSF radius for this data set is $3.6'$. The linear colour scale is in units of excess counts per smoothing radius. The light-grey contours are excess levels at 30%, 60%, and 90% of the maximum excess value. There are three more gamma-ray sources in the field of view (Aharonian et al. 2005e), which are not associated with RX J1713.7−3946.

4.3.2 Spectrum

The spectra determined from the data of 2003, 2004, and 2005 separately are compared to each other in Fig. 4.31. Similar to Fig. 3.34, where as systematic test different spectra are compared, Fig. 4.31 shows the ratio of the flux points of the 2003 and the 2005 spectrum to the best-fit spectral shape of the 2004 data. From the spectral shapes given in Table 4.7 that are in reasonable agreement with the data, the (curved) power law with the energy-dependent exponent is used for this purpose. Note that for the 2003 data the spectrum from the re-analysis is used, event statistics for the three spectra are given in Table 4.13. The 2005 data covers, as mentioned before (see Fig. 4.27), a large range of zenith angles, it especially extends to very low observation altitudes where the dependence of the effective collection area on zenith angle is more pronounced (see Fig. 3.28). In this case it is of

Year	Configuration	ON	OFF	α	Significance (σ)	Live time (hrs)
2003	*hard - 2tel*	3194	1764	1.0	20.5	18.1
2004	*std*	115141	75829	1.3	30.8	30.5
2005	*std*	70643	59836	1.0	30.3	36.8

Table 4.13: Comparison of event statistics from the SNR region used for the generation of the spectra for the three years separately. For 2003, the numbers of the re-analysis are given; the corresponding spectrum is plotted in Fig. 4.7, the numbers are also listed in Table 4.3. For 2004, numbers correspond to the spectrum shown in Fig. 4.14 and are also listed in Table 4.5. Note that $\alpha = 1$ for the 2005 analysis, see main text for explanation.

especial importance that ON and OFF events used to determine the gamma-ray excess flux have a well-matched zenith-angle distribution. For the 2005 data the OFF region to the North of RX J1713.7−3946, usable for all $\Delta\delta_{\mathrm{J2000}} = +0.7°$ runs, is *not* excluded. Initially, for the 2004 analysis, this OFF region was discarded. This is illustrated in Fig. 3.27, where the OFF regions used for the 2004 analysis and the observation positions as well as the ON region are overlaid on the event map of 2004. The OFF region to the North of RX J1713.7−3946 covers one of the gamma-ray sources discovered in the H.E.S.S. Galactic plane survey, HESS J1713−381(Aharonian et al. 2005e), whose gamma-ray signal can also be seen in Fig. 4.30. The flux level of HESS J1713−381 is, however, well below the level of RX J1713.7−3946, the integral flux above 200 GeV is $(4.2 \pm 1.5) \times 10^{-12}$ cm^{-2} s^{-1} (Aharonian et al. 2005e), whereas the integral flux of RX J1713.7−3946 above this energy is $(1.05 \pm 0.03) \times 10^{-10}$ cm^{-2} s^{-1}[8]. Hence, with roughly one quarter of the data taken at the North–observation position, the resulting contamination is at the 1% level. Keeping additionally in mind that the spectral shape of HESS J1713−381 is very similar ($\Gamma = 2.27 \pm 0.48$), it can safely be neglected since it is well within the systematic uncertainties of the flux determination (see Section 3.6.4). Hence, for the analysis of the 2005 data, and for consistency also for the combined spectral analysis shown later, all four OFF regions located symmetrically around the SNR region are used to assure that the normalisation factor α is close to 1.

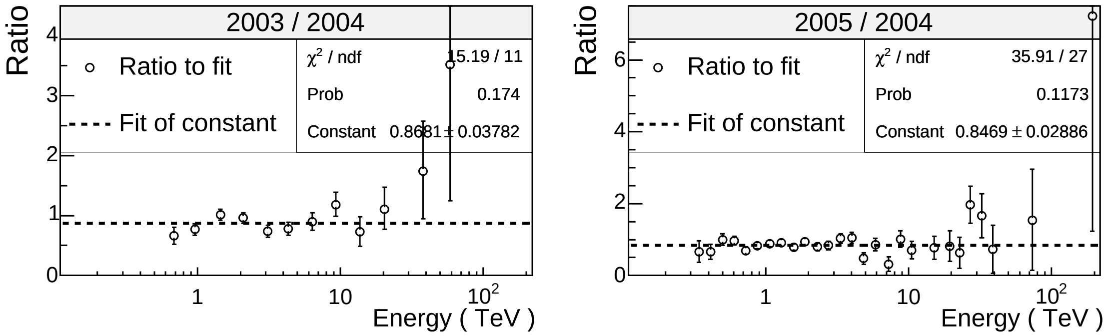

Figure 4.31: Comparison of the flux points of the 2003 (**left**) and the 2005 (**right**) spectrum to a fit to the reference spectrum of 2004. The fit of a constant is drawn as dashed line. The error bars correspond to the $\pm 1\sigma$ statistical errors of the flux points.

---

[8] Determined from a power-law fit to the data.

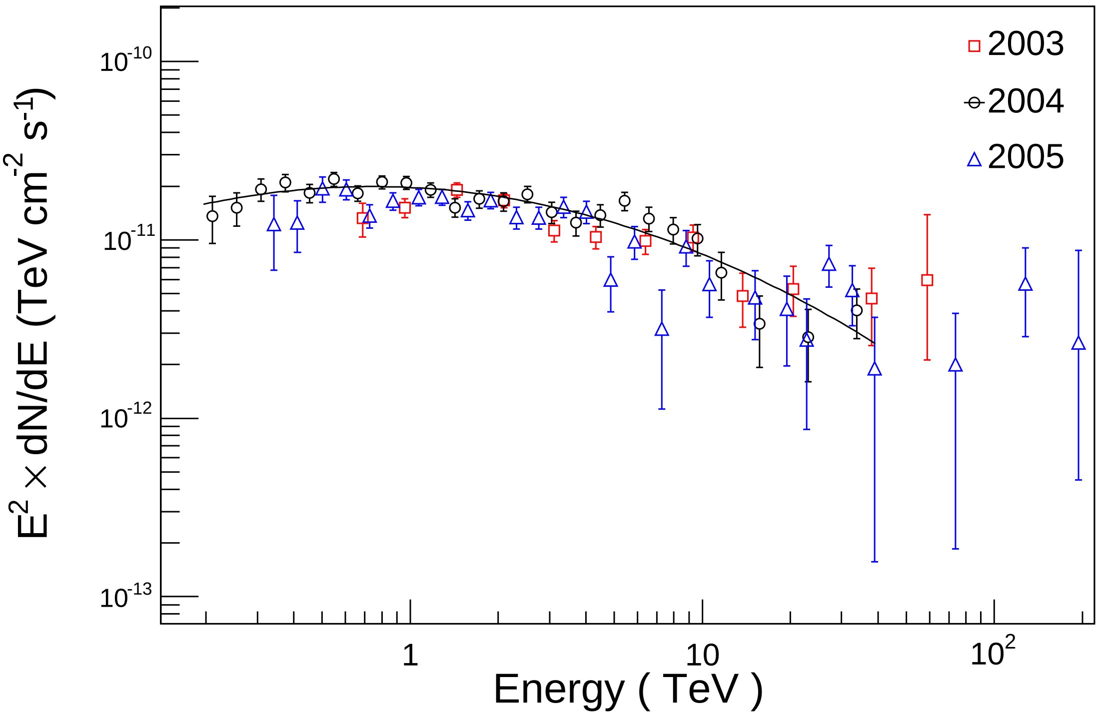

Figure 4.32: The H.E.S.S. spectra from 2003, 2004, and 2005 are plotted in an energy flux representation – the flux points have been multiplied by E^2. The black line is the best fit of a curved power law from the 2004 data as given in Table 4.7.

The comparison in Fig. 4.31 reveals reasonable agreement of the 2003 and 2005 spectra with the reference fit of 2004. The spectral shape remains unchanged over three years, the distributions are flat and a fit of a constant yields satisfactory χ^2/dof in both cases. The absolute flux level is well within the systematic uncertainty on the absolute energy scale of 20%, for the 2003 data more convincingly than for the 2005 data. To some extent this is conceivable since no attempt to correct for aging effects of the telescope system which result inevitably in a deterioration of the optical efficiency are undertaken here. As mentioned in Section 2.3.2, the Monte-Carlo simulations used in this work are somewhat matched to the end of 2003 when full operations of the telescopes system started. An evident explanation for the slight deviation of the mean ratio in Fig. 4.31 (right) from 1 (at the 4σ level) is hence the aging of the optics of the telescopes by 2005 which are not taken into account in simulations. In principal one can account for aging processes relative to what is simulated by means of the predictable Čerenkov light yield of muons passing close to the telescopes (Bolz 2004). This approach is not pursued here.

A comparison of the three raw spectra to each other is shown in Fig. 4.32. The flux points are multiplied by E^2 to yield the energy flux in this figure. In comparison, both the 2003 and 2005 data points are slightly below the 2004 points, more pronounced so for the 2005 data. The measured spectral shape is in good agreement. The best fit function of the 2004 data describes the shape of the 2003 and 2005 data reasonably well.

The combined data are shown in Fig. 4.33. No correction of efficiency losses is applied,

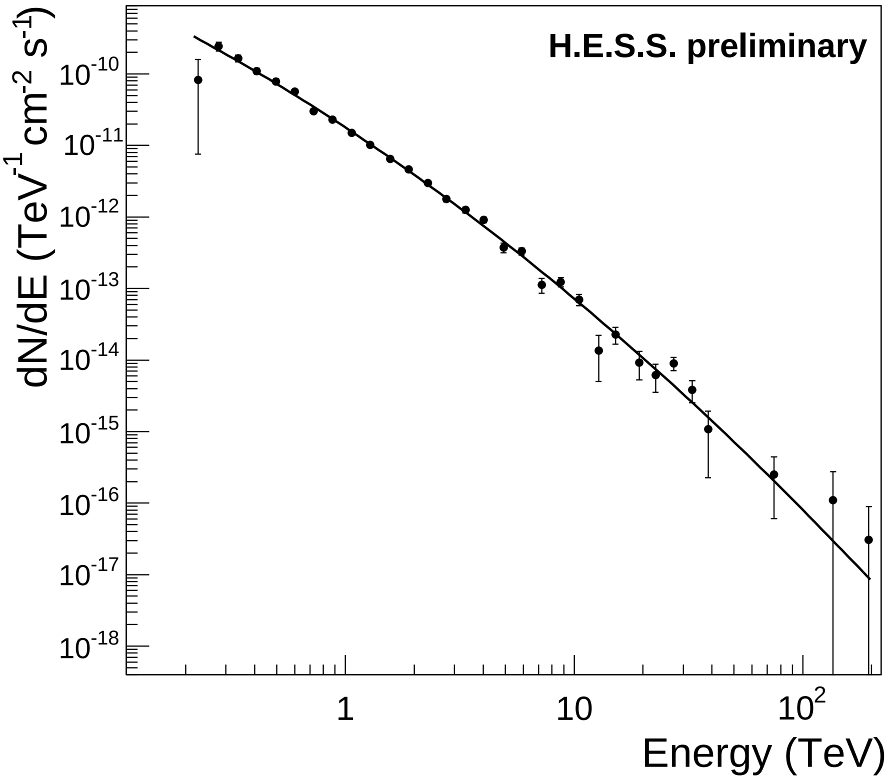

Figure 4.33: Combined H.E.S.S. gamma-ray spectrum of RX J1713.7−3946 generated from data of 2003, 2004, and 2005. Error bars are $\pm 1\sigma$ statistical errors. These data might be described by a curved power law (cf. Section 4.2.2), $dN/dE = I_0 \, E^{-\Gamma+\beta \log E}$, the best fit result (black line) gives $I_0 = (17.8 \pm 0.4) \times 10^{-11}$ cm^{-2} s^{-1} TeV^{-1}, $\Gamma = 2.11 \pm 0.03$, and $\beta = -0.28 \pm 0.04$ with $\chi^2/\mathrm{dof} = 49.6/28$. The fit results are in very good agreement with the numbers of the 2004 spectrum given in Table 4.7. Note that one negative flux point at ~ 55 TeV is excluded from the fit given here introducing a slight bias.

hence a *preliminary* combined spectrum is shown[9]. The spectrum is generated for the SNR region, processing the entire data together, applying for the 2003 observations the configuration *hard - 2tel* including appropriate effective collection area curves. The 2004 and 2005 data are processed with the nominal configuration for the generation of spectra, the *std* cuts. The resulting spectrum extends over *three* orders of magnitude, from 0.2 TeV to 200 TeV. A listing of all the flux points including all relevant information is given in Table 4.14. The event statistics at the highest energies improved clearly thanks to the observation strategy. The gamma-ray flux above 10 TeV, which is at the level of 6σ in the 2004 data alone (see Section 4.2.2), is in the combined data 8.6σ. Above 20 TeV, there is a significant gamma-ray signal of 6.2σ, and even above 30 TeV there are still 3.9σ. The spectral shape of the combined data is by the time of this writing still under investigation, in particular the issue of the decrease of optical efficiency needs to be resolved.

---

[9] Keeping in mind that the absolute flux level, not the spectral shape, might still change when applying an aging correction.

#	E (TeV)	ON	OFF	α	σ	Flux (cm^{-2}s^{-1})	Range (TeV)
1	0.23	5494	5394	1.0	1.1	$(8.28 \pm 7.53) \times 10^{-11}$	0.21 – 0.25
2	0.28	10021	9058	1.0	7.3	$(2.43 \pm 0.34) \times 10^{-10}$	0.25 – 0.31
3	0.34	8279	7217	1.0	8.8	$(1.65 \pm 0.19) \times 10^{-10}$	0.31 – 0.37
4	0.41	6744	5642	1.0	10.1	$(1.09 \pm 0.11) \times 10^{-10}$	0.37 – 0.45
5	0.50	5986	4739	1.0	12.3	$(7.87 \pm 0.64) \times 10^{-11}$	0.45 – 0.54
6	0.60	5733	4217	1.0	15.3	$(5.66 \pm 0.37) \times 10^{-11}$	0.54 – 0.66
7	0.73	5493	4196	1.0	13.4	$(3.02 \pm 0.23) \times 10^{-11}$	0.66 – 0.80
8	0.88	5228	3740	1.0	15.9	$(2.30 \pm 0.14) \times 10^{-11}$	0.80 – 0.97
9	1.06	5089	3654	1.0	15.6	$(1.50 \pm 0.10) \times 10^{-11}$	0.97 – 1.17
10	1.28	4971	3560	1.0	15.5	$(1.02 \pm 0.07) \times 10^{-11}$	1.17 – 1.42
11	1.57	4282	3041	1.0	14.8	$(6.48 \pm 0.44) \times 10^{-12}$	1.42 – 1.71
12	1.89	4137	2880	1.0	15.2	$(4.62 \pm 0.30) \times 10^{-12}$	1.71 – 2.08
13	2.30	4403	3249	1.0	13.4	$(2.98 \pm 0.22) \times 10^{-12}$	2.08 – 2.51
14	2.76	3781	2861	1.0	11.5	$(1.78 \pm 0.16) \times 10^{-12}$	2.51 – 3.04
15	3.35	3784	2911	1.0	10.9	$(1.25 \pm 0.12) \times 10^{-12}$	3.04 – 3.68
16	4.02	3474	2625	1.0	11.0	$(9.15 \pm 0.83) \times 10^{-13}$	3.68 – 4.46
17	4.91	2671	2221	1.0	6.6	$(3.74 \pm 0.57) \times 10^{-13}$	4.46 – 5.40
18	5.90	2179	1667	1.0	8.4	$(3.31 \pm 0.40) \times 10^{-13}$	5.40 – 6.53
19	7.22	1485	1266	1.0	4.3	$(1.12 \pm 0.26) \times 10^{-13}$	6.53 – 7.91
20	8.74	1201	896	1.0	6.8	$(1.23 \pm 0.18) \times 10^{-13}$	7.91 – 9.57
21	10.50	866	650	1.0	5.6	$(6.99 \pm 1.25) \times 10^{-14}$	9.57 – 11.59
22	12.80	579	528	1.0	1.6	$(1.36 \pm 0.85) \times 10^{-14}$	11.59 – 14.03
23	15.17	478	370	1.0	3.8	$(2.27 \pm 0.61) \times 10^{-14}$	14.03 – 16.99
24	19.26	306	252	1.0	2.3	$(9.25 \pm 3.99) \times 10^{-15}$	16.99 – 20.56
25	22.70	203	159	1.0	2.3	$(6.14 \pm 2.63) \times 10^{-15}$	20.56 – 24.89
26	27.24	180	101	1.0	4.8	$(8.96 \pm 1.91) \times 10^{-15}$	24.89 – 30.13
27	32.85	118	77	1.0	3.0	$(3.82 \pm 1.30) \times 10^{-15}$	30.13 – 36.48
28	38.56	70	56	1.0	1.3	$(1.08 \pm 0.86) \times 10^{-15}$	36.48 – 44.16
29	54.44	59	61	1.0	-0.2	$(-5.20 \pm 0.00) \times 10^{-17}$	44.16 – 64.71
30	74.81	28	19	1.0	1.3	$(2.49 \pm 1.92) \times 10^{-16}$	64.71 – 94.84
31	135.68	11	8	1.0	0.7	$(1.10 \pm 1.66) \times 10^{-16}$	94.84 – 138.98
32	194.28	2	1	1.0	0.6	$(3.04 \pm 5.94) \times 10^{-17}$	138.98 – 203.67
33	251.07	2	3	1.0	-0.5	$(-2.82 \pm 0.00) \times 10^{-17}$	203.67 – 298.47

Table 4.14: Flux points including relevant event statistics are listed for the spectrum of the combined H.E.S.S. data set, shown in Fig. 4.33. Note that in the figure, only points with positive flux values are shown.

Conclusion

An in-depth analysis of H.E.S.S. data of the shell-type SNR RX J1713.7−3946, an extended source of VHE gamma rays, is presented in this work. Special attention is devoted to tools developed and used for the analysis of a source that is significantly extended beyond the angular resolution of the experiment. It is shown that detector properties like the PSF and the collection area are well understood and sufficiently stable for any observation condition and over the whole field of view. One of the major complications of the analysis of extended gamma-ray sources is the background modelling. Different approaches are presented for the generation of gamma-ray excess images as well as for the generation of spectra. Comparisons of different and independent methods proved that systematic uncertainties are well under control.

Analysis results of data recorded in three consecutive years with H.E.S.S. are presented in Chapter 4. The H.E.S.S. measurement of RX J1713.7−3946 in 2003 presented the first confirmed detection of a shell-type SNR in VHE gamma rays and demonstrated – with an only partially complete array – the ability of H.E.S.S. to map extended objects. The first ever resolved image in VHE gamma rays marked a major improvement for the field of gamma-ray astronomy, which has now reached the stage of an imaging astronomical observation technique. The 2004 and 2005 data confirmed the previous measurement with greatly improved statistics which enabled detailed spatially resolved analyses. With RX J0852.0–4622 there are now two shell-type SNRs which exhibit largely extended VHE gamma-ray emission.

From the 2004 data, morphological and spectral properties of the whole SNR region are derived. Significant gamma-ray emission is detected throughout the entire remnant, with an increased flux from the northern and western part resembling a shell structure. The gamma-ray spectrum is measured over a large energy range. Indications for a deviation from a pure power law are found. The data are reasonably well described by a power law with an exponential cutoff and a power law with exponent depending logarithmically on energy, as well as a broken power law. The spatially resolved spectral analysis revealed no significant variation of the spectral shape over the SNR. The flux, on the other hand, varies by more than a factor of two. The northern and western part of the shell, where the SNR is believed to impact molecular clouds, are significantly brighter than the remaining parts. The 2005 data are aiming at extending the spectrum to higher energies to constrain the spectral shape. The preliminary analysis of the combined data yields a gamma-ray spectrum extending over three decades. Further analysis is underway by the time of this writing.

Multi-wavelength comparisons revealed a striking similarity between the X-ray and the VHE gamma-ray image. In contrast, variations in spectral shape seen with XMM are not found to be correlated with the H.E.S.S. data. A comparison with the NANTEN measurement of CO line emission, which traces molecular hydrogen, revealed no direct proportionality. If there is any link between the two measurements then only in the general sense that the regions of brightest gamma-ray emission are located on the northern and western side of the shell, where dense molecular clouds are believed to be interacting with the shock front.

RX J1713.7−3946 is discussed in terms of the available data from all wavelength bands including the H.E.S.S. gamma-ray signal. Two scenarios are addressed, one where gamma rays originate from electrons and one where they originate from protons. In both cases the large uncertainties on crucial parameters like the magnetic field strength and the effective ambient density, which are not directly accessible to measurements, hamper decisive conclusions. Nevertheless, the proton scenario seems to be favoured because of the shape of the gamma-ray spectrum, and, although to a lesser extent because experimentally less clear, because of large magnetic field values in the SNR region, which, if confirmed, would rule out an electronic origin. From the theory side, the remaining challenge is the connection of the different particle species, VHE electrons and nuclei, in a consistent broadband model of RX J1713.7−3946. Experimentally, with the current gamma-ray data set, more precise measurements of the surrounding molecular clouds are clearly needed in order to link emission regions of VHE gamma rays to regions of known density. H.E.S.S. itself can only marginally improve on the experimental data by trying to extend the low and high-energy limits. Significant improvement in the near future will rather be made with H.E.S.S. II and in particular GLAST which can constrain the energy range from 100 GeV down to a few GeV (in the case of GLAST), thereby providing a powerful test of the hypothesis of a hadronic origin of the gamma rays from RX J1713.7−3946. In addition, with better measurements of the ambient magnetic field in various regions of the SNR could one, if the field is confirmed to be high throughout the entire remnant, safely rule out an electronic origin.

In summary, the H.E.S.S. measurement of RX J1713.7−3946 provides the long-expected detection of VHE gamma rays from the shell of a supernova remnant, proving indisputable the existence of high-energy particles. It presents a significant step forward towards a solution of the Galactic cosmic-ray problem. While unequivocal proof for a *hadronic* origin of the VHE gamma rays is still missing, certainty about the question if shell-type SNRs can account for cosmic rays in the Galaxy up to energies of 10^{15} eV will most likely by reached gradually, with the detection of various such objects in VHE gamma rays, in conjunction with data of other wavelength regimes.

Bibliography

Aharonian, F., Akhperjanian, A., Barrio, J., et al. 2001, A&A, 370, 112

Aharonian, F. A. 2004, Very High Energy Cosmic Gamma Radiation : A Crucial Window on the Extreme Universe (River Edge, NJ: World Scientific Publishing, 2004)

Aharonian, F. A. & Atoyan, A. M. 1996, A&A, 309, 917

Aharonian, F. A. & Atoyan, A. M. 1999, A&A, 351, 330

Aharonian, F. A. & Atoyan, A. M. 2000, A&A, 362, 937

Aharonian, F. A., Drury, L. O., & Voelk, H. J. 1994, A&A, 285, 645

Aharonian et al. *(H.E.S.S. Collaboration)* 2004a, APh, 22, 109

Aharonian et al. *(H.E.S.S. Collaboration)* 2004b, Nature, 432, 75

Aharonian et al. *(H.E.S.S. Collaboration)* 2005a, Accepted for publication in A&A; astro-ph/0511678

Aharonian et al. *(H.E.S.S. Collaboration)* 2005b, Science, 307, 1938

Aharonian et al. *(H.E.S.S. Collaboration)* 2005c, A&A, 437, L7

Aharonian et al. *(H.E.S.S. Collaboration)* 2005d, A&A, 430, 865

Aharonian et al. *(H.E.S.S. Collaboration)* 2005e, Accepted for publication in ApJ; astro-ph/0510397

Aharonian et al. *(H.E.S.S. Collaboration)* 2005f, A & A, 437, 135

Aschenbach, B. 1998, Nature, 396, 141

Atkins, R., Benbow, W., Berley, D., et al. 2004, ApJ, 608, 680

Bamba, A., Yamazaki, R., Yoshida, T., Terasawa, T., & Koyama, K. 2005, ApJ, 621, 793

Baring, M. G., Ellison, D. C., Reynolds, S. P., Grenier, I. A., & Goret, P. 1999, ApJ, 513, 311

Bell, A. R. 2004, MNRAS, 353, 550

Bell, A. R. & Lucek, S. G. 2001, MNRAS, 321, 433

Berezhko, E. G., Ksenofontov, L. T., & Völk, H. J. 2003, A&A, 412, L11

Berezhko, E. G. & Völk, H. J. 1997, APh, 7, 183

Berezhko, E. G. & Völk, H. J. 2000, A&A, 357, 283

Berge, D. 2002, Master's thesis, Humboldt-Universität zu Berlin, http://www-eep.physik.hu-berlin.de/hess/public/diplom_david_berge.pdf

Bernlohr, K. 2000, Astroparticle Physics, 12, 255

Bernlöhr, K. 2000, Monte Carlo images of air showers, `http://www.mpi-hd.mpg.de/hfm/~bernlohr/HESS/`

Bernlöhr, K. 2002, CORSIKA and sim_hessarray – Simulation of the Imaging Atmospheric Cerenkov Technique for the H.E.S.S. Experiment, H.E.S.S. internal note 02/04 (unpublished)

Bethe, H. 1953, Phys. Rev., 89, 1256

Blandford, R. & Eichler, D. 1987, Phys. Rep., 154, 1

Bolz, O. 2004, PhD thesis, Ruprecht-Karls Universität, Heidelberg

Butt, Y. M., Torres, D. F., Romero, G. E., Dame, T. M., & Combi, J. A. 2002, Nature, 418, 499

Cassam-Chenaï, G., Decourchelle, A., Ballet, J., et al. 2004a, A&A, 427, 199

Cassam-Chenaï, G., Decourchelle, A., Ballet, J., et al. 2004b, A&A, 427, 199

Cornils, R., Gillessen, S., Jung, I., et al. 2003, APh, 20, 129

Daum, A., Hermann, G., Hess, M., et al. 1997, Astroparticle Physics, 8, 1

Davies, J. & Cotton, E. 1957, Journal of Solar Energy Sci. and Eng.

Drury, L. O., Aharonian, F. A., & Voelk, H. J. 1994, A&A, 287, 959

Ellison, D. C., Slane, P., & Gaensler, B. M. 2001, ApJ, 563, 191

Enomoto, R., Tanimori, T., Naito, T., et al. 2002, Nature, 416, 823

Fukui, Y., Moriguchi, Y., Tamura, K., et al. 2003, PASJ, 55, L61

Funk, S. 2005, PhD thesis, Ruprecht-Karls Universität, Heidelberg

Funk, S., Hermann, G., Hinton, J., et al. 2004, Astroparticle Physics, 22, 285

Gaisser, T. 1990, Cosmic Rays and Particle Physics (Cambridge University Press)

Ginzburg, V. L. & Syrovatskii, S. I. 1964, The Origin of Cosmic Rays (The Origin of Cosmic Rays, New York: Macmillan, 1964)

Green, D. A. 2004, Bulletin of the Astronomical Society of India, 32, 335

Hartman, R. C., Bertsch, D. L., Bloom, S. D., et al. 1999, ApJS, 123, 79

Heck, D., Knapp, J., Capdevielle, J., Schatz, G., & Thouw, T. 1998, CORSIKA: A Monte Carlo Code to Simulate Extensive Air Showers, Tech. rep., Forschungszentrum Karlsruhe, Wissenschaftliche Berichte, FZKA 6019

Heitler, W. 1954, Quantum Theory of Radiation, 3rd edn. (Dover Press)

Hess, V. 1912, Physikalische Zeitschrift, 13, 1084

Hillas, A. M. 1985, in Proc. 19th ICRC, 445–448

Hinton, J., Berge, D., & Funk, S. 2005, in Conference Proceedings "Towards a Network of Atmospheric Cherenkov Detectors VII", Palaiseau, France

Hinton, J. A. 2004, New Astronomy Review, 48, 331

Hiraga, J. S. 2005, private communication

Hiraga, J. S., Uchiyama, Y., Takahashi, T., & Aharonian, F. A. 2005, A&A, 431, 953

Hofmann, W., Jung, I., Konopelko, A., et al. 1999, Astroparticle Physics, 12, 135

Jones, F. C. & Ellison, D. C. 1991, Space Sci. Rev., 58, 259

Katagiri, H., Enomoto, R., Ksenofontov, L. T., et al. 2005, ApJ, 619, L163

Koyama, K., Kinugasa, K., Matsuzaki, K., et al. 1997, PASJ, 49, L7

Koyama, K., Petre, R., Gotthelf, E. V., et al. 1995, Nature, 378, 255

Kubo, H., Asahara, A., Bicknell, G. V., et al. 2004, New Astronomy Review, 48, 323

Kyle, T. 1991, Atmospheric Transmission and Scattering (Pergamon Press, Oxford)

Laming, J. M. 1998, ApJ, 499, 309

Lazendic, J. S., Slane, P. O., Gaensler, B. M., et al. 2004, ApJ, 602, 271

Lemoine-Goumard, M. 2005, in Conference Proceedings "Towards a Network of Atmospheric Cherenkov Detectors VII", Palaiseau, France

Lemoine-Goumard, M. & de Naurois, M. 2005, in AIP Conf. Proc. 745: High Energy Gamma-Ray Astronomy, 703–708

Li, T.-P. & Ma, Y.-Q. 1983, Astrophysical Journal, 272, 317

Lorenz, E. 2004, New Astronomy Review, 48, 339

Lucek, S. G. & Bell, A. R. 2000, MNRAS, 314, 65

Malkov, M. A., Diamond, P. H., & Sagdeev, R. Z. 2005, ApJ, 624, L37

Malkov, M. A. & O'C Drury, L. 2001, Reports of Progress in Physics, 64, 429

Mastichiadis, A. & de Jager, O. C. 1996, A&A, 311, L5

Moriguchi, Y., Tamura, K., Tawara, Y., et al. 2005, ApJ, 631, 947

Muraishi, H., Tanimori, T., Yanagita, S., et al. 2000, A&A, 354, L57

Pannuti, T. G., Allen, G. E., Houck, J. C., & Sturner, S. J. 2003, ApJ, 593, 377

Pfeffermann, E. & Aschenbach, B. 1996, in Roentgenstrahlung from the Universe, 267–268

Piron, F., Djannati-Atai, A., Punch, M., et al. 2001, A & A, 374, 895

Reimer, O. & Pohl, M. 2002, A&A, 390, L43

Shen, Y. 500, Sung Shu, 25

Slane, P., Gaensler, B. M., Dame, T. M., et al. 1999, ApJ, 525, 357

Slane, P., Hughes, J. P., Edgar, R. J., et al. 2001, ApJ, 548, 814

Tanimori, T., Hayami, Y., Kamei, S., et al. 1998, ApJ, 497, L25+

Tsuchiya, K., Enomoto, R., Ksenofontov, L. T., et al. 2004, ApJ, 606, L115

Uchiyama, Y. 2005, private communication

Uchiyama, Y., Aharonian, F. A., & Takahashi, T. 2003, A&A, 400, 567

Uchiyama, Y., Takahashi, T., & Aharonian, F. A. 2002, PASJ, 54, L73

Ulrich, M. 1996, PhD thesis, Ruprecht-Karls-Universität, Heidelberg

Vink, J. & Laming, J. M. 2003, ApJ, 584, 758

Völk, H. J., Berezhko, E. G., & Ksenofontov, L. T. 2005, A&A, 433, 229

Wang, Z. R., Qu, Q.-Y., & Chen, Y. 1997, A&A, 318, L59

Weekes, T. C., Badran, H., Biller, S. D., et al. 2002, Astroparticle Physics, 17, 221

Weekes, T. C., Cawley, M. F., Fegan, D. J., et al. 1989, Astrophysical Journal, 342, 379

Wiedner, C. 1998, Site aspects of the H.E.S.S. project: astronomical and visibility conditions, H.E.S.S. internal note

Acknowledgements / Danksagungen

An dieser Stelle möchte ich einigen Personen, die auf die eine oder andere Art und Weise zum Gelingen meiner Doktorarbeit beigetragen haben, meinen Dank aussprechen:

- Meinem Chef und Doktorvater, Werner Hofmann, für die Möglichkeit der Promotion in Heidelberg, für den gewährten Freiraum, nicht zuletzt während meines Aufenthalts in Paris, und für die stets konstruktive und gute Zusammenarbeit.
- Der Wernher von Braun-Stiftung, die mich mit einem Promotions Stipendium finanziell unterstützt und gefördert hat, und meinem Onkel Klaus Berge, durch den ich von der Stiftung und den Förderungsmöglichkeiten erst erfahren habe.
- Jim Hinton, als Freund und Kollegen, für die stets sehr gute und kreative Zusammenarbeit, von der ich stark profitiert habe während der gesamten Zeit.
- Felix Aharonian, für die Gelegenheit in einer frühen Phase meiner Promotion schon sehr viel Verantwortung zu übernehmen als *corresponding author* der ersten RX J1713.7−3946 Publikation. Er hatte stets ein offenes Ohr für mich, und ich habe sehr viel über die Physik der Gammastrahlung von Supernova Überresten in unseren Diskussionen gelernt.
- Der gesamten Heidelberger H.E.S.S.-Gruppe für die gute Zusammenarbeit und die angenehme Arbeitsatmosphäre. Unter vielen anderen habe ich immer gerne mit German Hermann, Conor Masterson, Wystan Benbow, Bruno Khelifi und Gavin Rowell gearbeitet.
- Auch der Berliner H.E.S.S.-Gruppe um Thomas Lohse, Christian Stegmann und Schlenk gebührt besonderer Dank. Ich bin froh, dass die alten Kontakte immer erhalten geblieben sind.
- Stefan Funk für seine Freundschaft und die sehr gute Zusammenarbeit. Ohne ihn wäre ich wohl nicht so schnell nach Heidelberg zur Promotion gekommmen.
- Meiner Familie, Assel und Pu, Bernd und Brigitte, Johanna und Ali, sowie Rainer und Hendrik, die mir grossen Rückhalt gaben.
- Zuletzt möchte ich der wichtigsten Person danken, Verena, die mich immer bestärkt und unterstützt hat und für mich da war. Meine Sonne, die mir das Leben erleuchtet. Schön dass wir uns in Heidelberg gefunden haben.